

SPECIAL EDITION

www.ScienceRobotics.org

# Science Robotics



# 10 ways that Science Careers can help advance your career

1. Register for a free online account on **ScienceCareers.org**.
2. Search thousands of job postings and find your perfect job.
3. Sign up to receive e-mail alerts about job postings that match your criteria.
4. Upload your resume into our database and connect with employers.
5. Watch one of our many webinars on different career topics such as job searching, networking, and more.
6. Download our career booklets, including Career Basics, Careers Beyond the Bench, and Developing Your Skills.
7. Complete an interactive, personalized career plan at “my IDP.”
8. Visit our Employer Profiles to learn more about prospective employers.
9. Research graduate program information and find a program right for you.
10. Read relevant career advice articles from our library of thousands.

Visit **ScienceCareers.org**  
today — all resources are free



**ScienceCareers**

FROM THE JOURNAL SCIENCE 

SCIENCECAREERS.ORG

## SPECIAL EDITION: *Science Robotics*



This booklet features eleven articles published in *Science Robotics*. They include research advances in bio-inspired, space, medical, and soft robotics as well as commentary on related issues. The journal covers the traditional disciplines of robotics as well as emerging trends and seeks to transform the future of robotics for the benefit of all.

Credit: adobestocks.com/sdecoret

## Science Robotics | AAAS

*Science Robotics* publishes original, peer-reviewed, science and engineering-based research articles that advance the field of robotics bearing the quality hallmark of the *Science* family of journals.

### Editor-in-Chief

Jeremy Berg, Ph.D.  
*Science* family of journals  
AAAS, Washington, DC

### Editor

Guang-Zhong Yang, Ph.D.  
Hamlyn Centre,  
Imperial College London  
London, UK

### Editorial Team

Trista Wagoner  
Rachel Kline  
Cait Phillips

### Editorial Board

#### Howie Choset

Robotics Institute, Carnegie Mellon University

#### Steven Collins

Department of Mechanical Engineering,  
Stanford University

#### Paolo Dario

Scuola Superiore Sant'Anna, Pisa, Italy

#### Peer Fischer

Max Planck Institute for Intelligent Systems,  
and Institute of Physical Chemistry,  
University of Stuttgart, Germany

#### Ken Goldberg

Industrial Engineering & Operations  
Research, University of California Berkeley

#### Neil Jacobstein

Singularity University, NASA Research Park,  
Moffett Field and MediaX Program,  
Stanford University

#### Danica Kragic

Royal Institute of Technology,  
Stockholm, Sweden

#### Cecilia Laschi

BioRobotics Institute, Scuola Superiore  
Sant'Anna, Pisa, Italy

#### Robin R. Murphy

Department of Computer Science and  
Engineering, Texas A&M University

#### Bradley Nelson

ETH Zurich, Switzerland

#### Robert J. Wood

Wyss Institute for Biologically Inspired  
Engineering and School of Engineering  
and Applied Sciences, Harvard University

## IN THIS BOOKLET:

### EDITORIAL

**4 Science for robotics and robotics for science**  
Guang-Zhong Yang *et al.*

**6 Ten robotics technologies of the year**  
Guang-Zhong Yang *et al.*

### PERSPECTIVE

**10 The grand challenges of *Science Robotics***  
Guang-Zhong Yang *et al.*

### REVIEW

**24 Review on space robotics: Toward top-level science through space exploration**  
Yang Gao and Steve Chien

### FOCUS

**35 The uncanny valley of haptics**  
Christopher C. Berger *et al.* (Ken Hinckley)

### RESEARCH ARTICLES

**37 Optimized flocking of autonomous drones in confined environments**  
Gábor Vásárhelyi *et al.* (Tamás Vicsek)

**50 Prosthesis with neuromorphic multilayered e-dermis perceives touch and pain**  
Luke E. Osborn *et al.* (Nitish V. Thakor)

**61 Peano-HASEL actuators: Muscle-mimetic, electrohydraulic transducers that linearly contract on activation**  
Nicholas Kellaris *et al.* (Christoph Keplinger)

**72 A biorobotic adhesive disc for underwater hitchhiking inspired by the remora suckerfish**  
Yueping Wang *et al.* (Li Wen)

**81 Design principles of a human mimetic humanoid: Humanoid platform to study human intelligence and internal body system**  
Yuki Asano *et al.* (Masayuki Inaba)

**92 A soft robot that navigates its environment through growth**  
Elliot W. Hawkes *et al.* (Allison M. Okamura)

### Science Robotics Scientific Advisory Board

#### James G. Bellingham

Center for Marine Robotics  
Woods Hole Oceanographic Institution

#### Henrik I. Christensen

Contextual Robotics Institute  
Jacobs School of Engineering,  
University of California, San Diego

#### Pierre E. Dupont

Boston Children's Hospital,  
Harvard Medical School

#### Toshio Fukuda

Nagoya University, Meijo University,  
Japan and Beijing Institute of  
Technology, China

#### Robert J. Full

Center for Interdisciplinary  
Bio-Inspiration in Education and  
Research (CiBER), University of  
California at Berkeley

#### Hugh Herr

Harvard-MIT Division of Health  
Sciences and Technology and  
MIT Media Lab

#### Robert D. Howe

BioRobotics Laboratory,  
Harvard University

#### Koji Ikuta

University of Tokyo, Japan

#### Vijay Kumar

University of Pennsylvania

#### Marcia McNutt

National Academy of Science  
National Research Council

#### Yoshihiko Nakamura

University of Tokyo

#### Stuart Russell

University of California, Berkeley

#### Russell H. Taylor

Johns Hopkins University

Publisher/*Science* family of journals: **Bill Moran**  
AD/Business Development: **Justin Sawyers**  
Marketing Manager: **Shawana Arnold**  
Layout/Design: **Kim Huynh**

### Sponsorship Opportunities:

**Laurie Faraday**, *Science*  
lfaraday@aaas.org | +1.508.747.9395  
1200 New York Ave NW, Washington DC 20005

© 2019 by The American Association for the Advancement of Science. All Rights Reserved.

Learn more and submit your research today: [ScienceRobotics.org](https://www.sciencerobotics.org)

## ROBOTICS

## Science for robotics and robotics for science

Guang-Zhong Yang, James Bellingham, Howie Choset, Paolo Dario, Peer Fischer, Toshio Fukuda, Neil Jacobstein, Bradley Nelson, Manuela Veloso, Jeremy Berg

2016 © The Authors,  
some rights reserved;  
exclusive licensee  
American Association  
for the Advancement  
of Science.

From molecular machines to large-scale systems, from outer space to deep-sea exploration, robots have become ubiquitous, and their impact on our lives and society is growing at an accelerating pace. *Science Robotics* has been launched to cover the most important advances in robot design, theory, and applications. *Science Robotics* promotes the communication of new ideas, general principles, and original developments. Its content will reflect broad and important new applications of robots (e.g., medical, industrial, land, sea, air, space, and service) across all scales (nano to macro), including the underlying principles of robotic systems covering actuation, sensor, learning, control, and navigation. In addition to original research articles, the journal also publishes invited reviews. There are also plans to cover opinions and comments on current policy, ethical, and social issues that affect the robotics community, as well as to engage with robotics educational programs by using *Science Robotics* content. The goal of *Science Robotics* is to move the field forward and cross-fertilize different research applications and domains.

With this inaugural issue of *Science Robotics*, we are delighted to bring you a set of papers covering several key aspects of robotics. The Review by Laschi *et al.* (1) explores the evolution of soft robotics. Soft materials and fabrication techniques have led to deformable structures that give robots the ability to stretch, squash, climb, and morph, with the potential for biodegradability and self-healing. Although

a relatively new topic in robotics, soft robotics is changing how actuation, control, and dynamic adaptation are achieved by leveraging parallel advances in material science, chemistry, engineering, biology, and many other disciplines. An example embodiment of soft robotics is a prosthetic hand with stretchable optical waveguides, presented by Zhao *et al.* (2) in this issue. They used photonic strain sensors to allow for the capture of curvature, elongation, and force, thus permitting active sensation of the proposed optoelectronically innervated prosthetic hand.

One of the ambitions of *Science Robotics* is to root robotics research deeply into basic science. Biorobotics represents such an ambition: It keeps the living world (and thus life sciences) at its core, investigates different applications of bioinspired machines and robots, and validates scientific hypotheses. Our attempts to mimic animal motion have already devised many technological advances that have revolutionized how man-made machines move through air, in water, and over land. Despite numerous achievements, engineers and scientists have yet to closely replicate the grace and fluidity of animal movement. This suggests that the biological world still has much to teach, in terms of design inspiration and programming robotic systems with abilities that will far exceed current capabilities.

An example of this innovative thinking can be found in the work of Haldane *et al.* (3), who

devised a metric to quantify vertical jumping agility for both animals and robots. The extracted principles led to a new approach to power modulation, allowing the creation of a much more agile robot that achieves 78% of the vertical jumping agility of a galago.

Advances in robotics have also extended human sensory experience, cognition, and physical abilities. Direct brain control has offered disabled individuals a possibility to restore basic motor function. Soekadar *et al.* (4) give an example on how a noninvasive, hybrid electroencephalography and electrooculography-based brain and neural hand exoskeleton can restore intuitive control of grasping motions for quadriplegia patients, allowing them to perform basic daily living activities. As noted by H. Herr, an advisory board member of *Science Robotics*, “Future technologies will not only compensate for human disability but will drive human capacities beyond innate physiological levels, enabling humans to perform a diverse set of tasks with both anthropomorphic and nonanthropomorphic extended bodies.” Such augmentative technologies “will have a transformative influence on broad social, political, and economic spheres, affecting the future of sport, labor productivity, human longevity, and disability.”

For roboticists and the general public, the debate over autonomous driving concerns both the technical challenges and, perhaps more importantly, the potential social, ethical, safety, and legal considerations that must be addressed for widespread adoption to occur. Perhaps less explored is the situation where there is a transition between autonomous driving and full human control. Russell *et al.* (5), in studying motor learning effects during car-to-driver handover in automated vehicles, found that when a human driver retakes control, an extensive period of motor adaptation may be required to resume normal steering behavior. Designers of automated vehicles may thus need to carefully consider this period of compromised steering behavior when developing methods for control handover.

---

Guang-Zhong Yang is the Editor of *Science Robotics* and the Director and Co-founder of the Hamlyn Centre for Robotic Surgery, Imperial College London, U.K. Email: g.z.yang@imperial.ac.uk James Bellingham is the Director of the Center for Marine Robotics, Woods Hole Oceanographic Institution, Woods Hole, MA 02543, USA. Howie Choset is a Professor at the Robotics Institute, Carnegie Mellon University, Pittsburgh, PA 15213, USA. Paolo Dario is the Director of the BioRobotics Institute and a Professor of Biomedical Robotics at the Scuola Superiore Sant’Anna, Pisa, Italy. Peer Fischer is a Professor of Physical Chemistry, University of Stuttgart, and heads the Micro, Nano, and Molecular Systems Laboratory at the Max Planck Institute for Intelligent Systems, Stuttgart, Germany. Toshio Fukuda is an Emeritus Professor at Nagoya University, Nagoya, Japan, and a Professor at Meijo University, Nagoya, Japan, and at Beijing Institute of Technology, Beijing, China. Neil Jacobstein is the Chair of the Artificial Intelligence and Robotics Track, Singularity University, Moffett Field, CA 94035, USA, and a Distinguished Visiting Scholar, mediaX, Stanford University, Stanford, CA 94305, USA. Bradley Nelson is the Professor of Robotics and Intelligent Systems, ETH Zürich, Switzerland. Manuela Veloso is a Herbert A. Simon University Professor and the Head of the Department of Machine Learning, with courtesy appointments in the Department of Computer Science, the Robotics Institute, and the Department of Electrical and Computer Engineering, Carnegie Mellon University, Pittsburgh, PA 15213, USA. Jeremy Berg is the Editor-in-Chief of *Science* journals.



CREDITS: CORR/ISTOCKPHOTO; KEVIN MA AND PAKPONG CHIRARATTANANON/ HARVARD UNIVERSITY; NASA AMES; CHRIS GUNN/ NASA; KOSTAS KARAKASILIOTIS, BIROBOTICS LABORATORY, EPFL

It is our intention that *Science Robotics* will bear the quality hallmark of the *Science* family of journals and cover both the traditional disciplines of robotics and emerging trends, such as advanced materials and bioinspired designs. It will also cover all scales, from very large systems to micro- and nanorobots. The 2016 Nobel Prize in Chemistry honors three pioneers in this field who designed and built some of the first molecular machines. Despite the progress in crafting structures of increasing complexity at such a small scale, truly functional dynamic nanorobots that are autonomous and that can undertake useful tasks are still in their infancy. This is in contrast to any living organism, where dynamic biological nanomachines are ubiquitous and where they accomplish functions that are readily observed at the macroscopic scale. The challenges faced in realizing synthetic autonomous nanorobots that can rival their

biological counterparts, and that perhaps ultimately lead to medically useful applications, are manifold. We hope to see many original papers on nanorobots submitted to *Science Robotics* in the future because they truly require the combination of basic science and robotics to develop suitable fabrication and assembly strategies, to address questions of control and communication, and to solve the difficulty of power transfer to small scales.

We hope that you enjoy the first issue of *Science Robotics* and join us in this exciting robotics venture as we strive to transform the future of robotics for the benefit of all.

## REFERENCES

1. C. Laschi, B. Mazzolai, M. Cianchetti, Soft robotics: Technologies and systems pushing the boundaries of robot abilities. *Sci. Robot.* **1**, eaah3690 (2016).
2. H. Zhao, K. O'Brien, S. Li, R. F. Sheperd, Optoelectronically innervated soft prosthetic hand via stretchable optical waveguides. *Sci. Robot.* **1**, eaai7529 (2016).
3. D. W. Haldane, M. M. Plecnik, J. K. Yim, R. S. Fearing, Robotic vertical jumping agility via series-elastic power modulation. *Sci. Robot.* **1**, eaag2048 (2016).
4. S. R. Soekadar, M. Witkowski, C. Gómez, E. Opisso, J. Medina, M. Cortese, M. Cempini, M. C. Carozza, L. G. Cohen, N. Birbaumer, N. Vitiello, Hybrid EEG/EOG-based brain/neural hand exoskeleton restores fully independent daily living activities after quadriplegia. *Sci. Robot.* **1**, eaag3296 (2016).
5. H. E. B. Russell, L. K. Harbott, I. Nisky, S. Pan, A. M. Okamura, J. C. Gerdes, Motor learning affects car-to-driver handover in automated vehicles. *Sci. Robot.* **1**, eaah5682 (2016).

10.1126/scirobotics.aal2099

**Citation:** G.-Z. Yang, J. Bellingham, H. Choset, P. Dario, P. Fischer, T. Fukuda, N. Jacobstein, B. Nelson, M. Veloso, J. Berg, Science for robotics and robotics for science. *Sci. Robot.* **1**, eaal2099 (2016).

## Ten robotics technologies of the year

Guang-Zhong Yang is the Editor of *Science Robotics* and Director and Co-founder of the Hamlyn Centre, Imperial College London, London, UK. Email: g.z.yang@imperial.ac.uk

Robert J. Full is the Director of the Center for Interdisciplinary Bio-Inspiration in Education and Research (CiBER) and a Professor, Department of Integrative Biology, University of California Berkeley, Berkeley, CA, USA.

Neil Jacobstein is a Chair, Artificial Intelligence and Robotics, Singularity University, NASA Research Park, Moffett Field, CA, USA, and a Distinguished Visiting Scholar, MediaX Program, Stanford University, Stanford, CA, USA.

Peer Fischer is a Professor at the Max Planck Institute for Intelligent Systems and the Institute of Physical Chemistry, University of Stuttgart, Stuttgart, Germany.

James Bellingham is the Director of the Center for Marine Robotics, Woods Hole Oceanographic Institution, Woods Hole, MA, USA.

Howie Choset is a Professor at Carnegie Mellon University and the Robotics Institute, Pittsburgh, PA, USA.

Henrik Christensen is the Director of the Contextual Robotics Institute and Professor of Computer Science and Engineering, Jacobs School of Engineering, University of California San Diego, San Diego, CA, USA.

Paolo Dario is a Professor at Scuola Superiore Sant'Anna, Pisa, Italy.

Bradley J. Nelson is a Professor at ETH Zurich, Zurich, Switzerland.

Russell Taylor is the Director of the Laboratory for Computational Sensing and Robotics and a Professor at Johns Hopkins University, Baltimore, MD, USA.

The Authors, some rights reserved; exclusive licensee American Association for the Advancement of Science. No claim to original U.S. Government Works

In this Editorial, we identify 10 exciting robotics developments and technologies, ranging from original research that may change the future of robotics to commercial products

that enable basic science and drive industrial and medical innovations.

–Guang-Zhong Yang, Robert J. Full,

Neil Jacobstein, Peer Fischer,  
James Bellingham, Howie Choset,  
Henrik Christensen, Paolo Dario,  
Bradley J. Nelson, Russell Taylor

### 1. Boston Dynamics' Atlas doing parkour.



The performance of the 1.5-m, 75-kg Atlas keeps surprising us, jumping over a log in stride with one leg while jogging and jumping over wooden boxes with no break in pace. These feats add to walking on challenging terrain, keeping its balance when disturbed, standing up, lifting and manipulating objects, and executing a back flip like a gymnast (1). Marc Raibert's Boston Dynamics team remains the masters of robotic balance and propulsion. Raibert observes that "the mechanical system has a mind of its own, governed by the physical structure and laws of physics." Atlas uses its vision system to align itself and to measure distances to the parkour obstacles. Although Raibert admits that not all trials could be successfully mastered, he hopes that the demonstrations serve as an inspiration for what robots can do in the near future.

IMAGE CREDITS: 1, ATLAS ROBOT IMAGE COURTESY OF BOSTON DYNAMICS; 2, INTUITIVE SURGICAL INC.; 3, L. A. CICERO/STANFORD NEWS SERVICE; 4, (4); 5, (6); 6, C. BICKEL/SCIENCE, DATA: E. KOPFERGER AND F. C. SIMMEL/TECHNICAL UNIVERSITY OF MUNICH; 7, SKOPEI FILMS/@TU DELFT; 8, BIODESIGN LAB/HARVARD UNIVERSITY; 9, UNIVERSAL ROBOTS A/S; 10, SONY ELECTRONICS.

Robotic surgery represents one of the most important surgical innovations in recent years, and procedures such as radical prostatectomy are increasingly performed by using a robotic approach, implying many benefits. More robotic platforms are emerging, and increased clinical uptake depends on whether issues such as cost effectiveness and barriers to wider clinical accessibility will be further addressed. Da Vinci is an early pioneer and a global market leader, and Intuitive Surgical continues to push the boundaries of surgical robotics. Through a single 2.5-cm cannula and small incision, the newly launched da Vinci single-port system allows the surgeon to control three fully wristed, elbowed instruments, combined with an articulated endoscope for deep-seated lesions (2).

**2. Intuitive Surgical's da Vinci SP platform.**



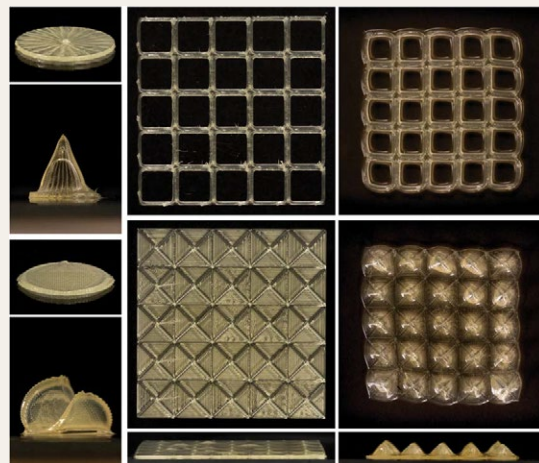
**3. Soft robot that navigates through growth.**



Navigation by growth at the tip opens a new direction for robots. Imagine if the growth of a vine, neuron, or fungal hyphae could be scaled up, sped up, and made steerable. The investigators took a tube of soft material that is folded inside itself but, when pressurized, grows outward as material at the front of the tube is pushed outward (3). This brilliant design idea addresses several grand challenges in robotics and exemplifies the use of bioinspired design by extracting a general biological principle and using it as an analogy to advance engineering beyond what is possible in nature. The soft robotic design allows obstacle avoidance in complex, unstructured environments, which holds promise for navigation in pipes and conduits, medical devices, and in exploration and search-and-rescue robots.

One of the grand challenges of robotics is to explore new materials and fabrication schemes for developing power-efficient, multifunctional and compliant actuators. 2018 saw many new developments in this burgeoning research area across different disciplines. Versatile shape-morphing liquid crystal elastomeric actuators have been used before, but this publication shows how the elastomers can be fabricated with 3D printing using high operating temperature direct ink writing with spatially programmed nematic order (4). These actuators demonstrated the ability to lift significantly more weight than other liquid crystal elastomers reported to date. The technique promises large area designs and dynamic functional architectures for soft robots.

**4. 3D-printed liquid crystal elastomers for soft robotics.**



**5. Muscle-mimetic, self-healing, and hydraulically amplified actuators.**

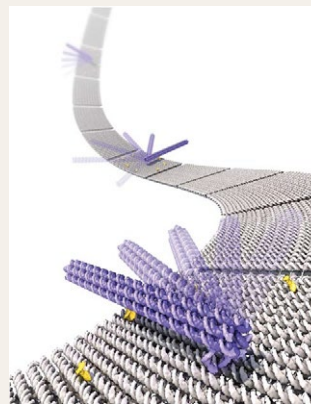


Peano-HASEL provides a soft actuator that is transparent and self-sensing, with controllable linear contractions up to 10%, a strain rate of 900% per second, and actuation at 50 Hz (5). The actuator uses both electrostatic and hydraulic principles to provide linear contraction upon application of a voltage without the need for pre-stretching the material or any rigid frames. The HASEL (hydraulically amplified self-healing electrostatic) actuator (6) is strong and versatile but cheap to produce, according to the authors, who only used a facile heat-sealing method with inexpensive commercially available materials to produce this promising technology. Remarkably, this actuator is able to lift more than 200 times its weight.

IMAGE CREDITS: 1, ATLAS ROBOT IMAGE COURTESY OF BOSTON DYNAMICS; 2, INTUITIVE SURGICAL INC.; 3, L. A. CICERO/STANFORD NEWS SERVICE; 4, (4); 5, (6); 6, C. BICKEL/SCIENCE, DATA: E. KÖPPERGER AND F. C. SIMMEL/TECHNICAL UNIVERSITY OF MUNICH; 7, SKOPEI FILMS@TU DELFT; 8, BIODESIGN LAB/HARVARD UNIVERSITY; 9, UNIVERSAL ROBOTS A/S; 10, SONY ELECTRONICS.

DNA origami can form different shapes at the nanoscale. By controlling a self-assembling DNA origami structure combined with a system of latches formed by single-stranded DNAs, precise nanoscale movement is now possible under an externally applied tunable electric field (7). These nanoscale robotic systems can be used in parallel for electrically driven transport of molecules or nanoparticles over tens of nanometers or more. The robot enables programmable synthesis and assembly of materials from the bottom up. Its positioning state may also be used as a molecular mechanical memory.

**6. Self-assembled nanoscale robot from DNA.**



**7. DelFly nimble bioinspired robotic flapper.**



Many bioinspired robots serve a dual purpose, namely, developing advanced technologies with practical applications and unveiling the principles used by nature to build and program living beings. Here, we see the design of a remarkable, tailless, untethered, autonomous, programmable, small (28 g), flapping aerial vehicle with exceptional agility capable of performing 360° roll and pitch flips with angular accelerations up to  $5000^{\circ} \text{ s}^{-2}$  (8). Although it is over 50 times the size of a fruit fly and does not mimic the wing morphology or kinematics of any specific natural flyer, the robot can serve as a novel physical model to test how flying organisms perform flight control. Surprisingly, the DelFly Nimble could accurately reproduce the rapid escape maneuvers of fruit flies even with no explicit control of all its rotation axes. We consider it a paradigmatic example of “science for robotics and robotics for science” and expect that it will advance the development of flying robots.

When it comes to wearing an exoskeleton for everyday life, most people do not want to resemble Iron Man. A lightweight, stretchy exosuit offers new ways of integrating fabric design, sensing, robotic control, and actuation to increase a wearer’s strength, balance, and endurance. Potential applications include assisting the elderly in enhancing their muscular strength, supporting their mobility and independence, and rehabilitating children and adults with movement disorders due to stroke, multiple sclerosis, or Parkinson’s disease. Human-in-the-loop control optimization further allows seamless integration of the robot with human, providing personalized control strategies and adaptation (9).

**8. Soft exosuit wearable robot.**



**9. Universal Robots (UR) e-Series Cobots.**



From research laboratories to assembly lines and logistics to surgical guidance, the UR robotic arms are becoming ubiquitous despite their unassuming appearance. The company is developing an ecosystem around its core products, and their new e-Series collaborative robot launched in 2018 echoes the general trend in collaborative automation and learning from hands-on demonstration rather than specialized programming (10). With enhanced safety features and force/torque sensing, we expect to see more intelligent human-robot interactions in a diverse range of environments where robots can seamlessly learn and collaborate with human operators.

The return of aibo, Sony’s toy dog first introduced nearly 20 years ago, is welcomed by many, and not just because of its new appearance, enhanced voice understanding, and its improved ability to learn from its owners (11). In addition, the robot has been developed with Sony’s increasing awareness of the role robots can play in childhood learning or as a companion for the aged, particularly those with neurodegenerative diseases. Understanding the perception, interaction, and expectations of the people around the robot and developing robot behavior and personality that are context aware (not dependent on pre-scripted programs and with personalization and adaptation) are interesting topics in social robotics.

**10. Sony’s aibo.**



IMAGE CREDITS: 1, ATLAS ROBOT IMAGE COURTESY OF BOSTON DYNAMICS; 2, INTUITIVE SURGICAL INC.; 3, L. A. CICERO/STANFORD NEWS SERVICE; 4, (4); 5, (6); 6, C. BICKEL/SCIENCE, DATA: E. KOPFERGER AND F. C. SIMMEL/TECHNICAL UNIVERSITY OF MUNICH; 7, SKOPEI FILMS@TU DELFT; 8, BIODESIGN LAB/HARVARD UNIVERSITY; 9, UNIVERSAL ROBOTS A/S; 10, SONY ELECTRONICS.

## REFERENCES

1. M. H. Raibert, J. A. Hodgins, Legged robots, in *Biological Neural Networks in Invertebrate Neuroethology and Robotics*, R. Beer, R. Ritzmann, T. McKenna, Eds. (Academic Press, 1993), pp. 319–354.
2. Intuitive Surgical announces innovative single port platform—the da Vinci SP Surgical System (2018); <https://globenewswire.com/news-release/2018/05/31/1515229/0/en/Intuitive-Surgical-Announces-Innovative-Single-Port-Platform-the-da-Vinci-SP-Surgical-System.html>.
3. E. W. Hawkes, L. H. Blumenschein, J. D. Greer, A. M. Okamura, A soft robot that navigates its environment through growth. *Sci. Robot.* **2**, eaan3028 (2017).
4. A. Kotikian, R. L. Truby, J. W. Boley, T. J. White, J. A. Lewis, 3D printing of liquid crystal elastomeric actuators with spatially programmed nematic order. *Adv. Mater.* **30**, 1706164 (2018).
5. N. Kellaris, V. Gopaluni Venkata, G. M. Smith, S. K. Mitchell, C. Keplinger, Peano-HASEL actuators: Muscle-mimetic, electrohydraulic transducers that linearly contract on activation. *Sci. Robot.* **3**, eaar3276 (2018).
6. E. Acome, S. K. Mitchell, T. G. Morrissey, M. B. Emmett, C. Benjamin, M. King, M. Radakovitz, C. Keplinger, Hydraulically amplified self-healing electrostatic actuators with muscle-like performance. *Science* **359**, 61–65 (2018).
7. E. Kopperger, J. List, S. Madhira, F. Rothfischer, D. C. Lamb, F. C. Simmel, A self-assembled nanoscale robotic arm controlled by electric fields. *Science* **359**, 296–301 (2018).
8. M. Karásek, F. T. Muijres, C. De Wagter, B. D. W. Remes, G. C. H. E. de Croon, A tailless aerial robotic flapper reveals that flies use torque coupling in rapid banked turns. *Science* **361**, 1089–1094 (2018).
9. Y. Ding, M. Kim, S. Kuindersma, C. J. Walsh, Human-in-the-loop optimization of hip assistance with a soft exosuit during walking. *Sci. Robot.* **3**, eaar5438 (2018).
10. Universal Robotics launches e-Series; [www.universal-robots.com/about-universal-robots/news-centre/universal-robots-launches-e-series-setting-a-new-standard-for-collaborative-automation-platforms/](http://www.universal-robots.com/about-universal-robots/news-centre/universal-robots-launches-e-series-setting-a-new-standard-for-collaborative-automation-platforms/).
11. Entertainment robot “aibo” announced (2017); [www.sony.net/SonyInfo/News/Press/201711/17-105E/index.html](http://www.sony.net/SonyInfo/News/Press/201711/17-105E/index.html).

10.1126/scirobotics.aaw1826

**Citation:** G.-Z. Yang, R. J. Full, N. Jacobstein, P. Fischer, J. Bellingham, H. Choset, H. Christensen, P. Dario, B. J. Nelson, R. Taylor, Ten robotics technologies of the year. *Sci. Robot.* **4**, eaaw1826 (2019).

## ROBOTICS

The grand challenges of *Science Robotics*

Guang-Zhong Yang,<sup>1\*</sup> Jim Bellingham,<sup>2</sup> Pierre E. Dupont,<sup>3</sup> Peer Fischer,<sup>4,5</sup> Luciano Floridi,<sup>6,7,8,9,10</sup> Robert Full,<sup>11</sup> Neil Jacobstein,<sup>12,13</sup> Vijay Kumar,<sup>14</sup> Marcia McNutt,<sup>15</sup> Robert Merrifield,<sup>1</sup> Bradley J. Nelson,<sup>16</sup> Brian Scassellati,<sup>17,18</sup> Mariarosaria Taddeo,<sup>7,8,9</sup> Russell Taylor,<sup>19</sup> Manuela Veloso,<sup>20</sup> Zhong Lin Wang,<sup>21</sup> Robert Wood<sup>22,23</sup>

Copyright © 2018  
The Authors, some  
rights reserved;  
exclusive licensee  
American Association  
for the Advancement  
of Science. No claim  
to original U.S.  
Government Works

One of the ambitions of *Science Robotics* is to deeply root robotics research in science while developing novel robotic platforms that will enable new scientific discoveries. Of our 10 grand challenges, the first 7 represent underpinning technologies that have a wider impact on all application areas of robotics. For the next two challenges, we have included social robotics and medical robotics as application-specific areas of development to highlight the substantial societal and health impacts that they will bring. Finally, the last challenge is related to responsible innovation and how ethics and security should be carefully considered as we develop the technology further.

## INTRODUCTION

Just over a year ago, we published the first issue of *Science Robotics*. Even within this relatively short period of time, remarkable progress has been made in many aspects of robotics—from micromachines for biomedicine (1) to large-scale systems for robotic construction (2) and from robots for outer space to those involved in deep-sea exploration (3). We have seen the evolution of soft robots and how new materials and fabrication schemes have led to deformable actuators that are compliant, versatile, and self-healing (4–6). We have also seen many examples of bioinspired designs, from the power-modulated jumping robot with agility and power that approach those of galagos (the animal with the highest vertical jumping agility) (7) to a biomimetic robotic platform to study flight specializations of bats (8) and a biorobotic adhesive disc for underwater hitchhiking inspired by the remora suckerfish (9). We also celebrated the 10th anniversary of the Robot Operating System (ROS) (10), the open-source robotics middleware that is making

great strides in realizing its mission of powering the world's robots, from space robot challenges to autonomous driving, industrial assembly, and surgery.

Given all these advances, what does the future hold for the field of robotics? Recently, we conducted an open online survey on major unsolved challenges in robotics. On the basis of the feedback and submissions received, an invited online expert panel was convened, and the panel shortlisted the 30 most important topics and research directions. These are further grouped into 10 grand challenges (Fig. 1) that may have major breakthroughs, significant research, and/or socioeconomic impact in the next 5 to 10 years:

(i) **New materials and fabrication schemes** for developing a new generation of robots that are multifunctional, power-efficient, compliant, and autonomous in ways akin to biological organisms.

(ii) **Biohybrid and bioinspired robots** that translate fundamental biological principles into engineering design rules or integrate liv-

ing components into synthetic structures to create robots that perform like natural systems.

(iii) **New power sources, battery technologies, and energy-harvesting schemes** for long-lasting operation of mobile robots.

(iv) **Robot swarms** that allow simpler, less expensive, modular units to be reconfigured into a team depending on the task that needs to be performed while being as effective as a larger, task-specific, monolithic robot.

(v) **Navigation and exploration in extreme environments** that are not only unmapped but also poorly understood, with abilities to adapt, to learn, and to recover and handle failures.

(vi) **Fundamental aspects of artificial intelligence (AI) for robotics**, including learning how to learn, combining advanced pattern recognition and model-based reasoning, and developing intelligence with common sense.

(vii) **Brain-computer interfaces (BCIs)** for seamless control of peripheral neuroprostheses, functional electric stimulation devices, and exoskeletons.

(viii) **Social interaction** that understands human social dynamics and moral norms and that can be truly integrated with our social life showing empathy and natural social behaviors.

(ix) **Medical robotics** with increasing levels of autonomy but with due consideration of legal, ethical, and technical challenges, as well as microrobotics tackling real demands in medicine.

(x) **Ethics and security** for responsible innovation in robotics.

The field of robotics is broad and covers many underpinning and allied technological areas. The identification of these challenges was a difficult task, and there are many sub-topics not listed that are equally important to future development. The above list is therefore neither exclusive nor exhaustive.

One of the ambitions of *Science Robotics* is to deeply root robotics research in science

<sup>1</sup>Hamlyn Centre for Robotic Surgery, Imperial College London, London, UK. <sup>2</sup>Center for Marine Robotics, Woods Hole Oceanographic Institution, Woods Hole, MA 02543, USA. <sup>3</sup>Department of Cardiovascular Surgery, Boston Children's Hospital, Harvard Medical School, Boston, MA 02115, USA. <sup>4</sup>Institute of Physical Chemistry, University of Stuttgart, Stuttgart, Germany. <sup>5</sup>Micro, Nano, and Molecular Systems Laboratory, Max Planck Institute for Intelligent Systems, Stuttgart, Germany. <sup>6</sup>Centre for Practical Ethics, Faculty of Philosophy, University of Oxford, Oxford, UK. <sup>7</sup>Digital Ethics Lab, Oxford Internet Institute, University of Oxford, Oxford, UK. <sup>8</sup>Department of Computer Science, University of Oxford, Oxford, UK. <sup>9</sup>Data Ethics Group, Alan Turing Institute, London, UK. <sup>10</sup>Department of Economics, American University, Washington, DC 20016, USA. <sup>11</sup>Department of Integrative Biology, University of California, Berkeley, Berkeley, CA 94720, USA. <sup>12</sup>Singularity University, NASA Research Park, Moffett Field, CA 94035, USA. <sup>13</sup>MediaX, Stanford University, Stanford, CA 94305, USA. <sup>14</sup>Department of Mechanical Engineering and Applied Mechanics, University of Pennsylvania, Philadelphia, PA 19104, USA. <sup>15</sup>National Academy of Sciences, Washington, DC 20418, USA. <sup>16</sup>Institute of Robotics and Intelligent Systems, Department of Mechanical and Process Engineering, ETH Zürich, Zurich, Switzerland. <sup>17</sup>Department of Computer Science, Yale University, New Haven, CT 06520, USA. <sup>18</sup>Department Mechanical Engineering and Materials Science, Yale University, New Haven, CT 06520, USA. <sup>19</sup>Department of Computer Science, Johns Hopkins University, Baltimore, MD 21218, USA. <sup>20</sup>Machine Learning Department, School of Computer Science, Carnegie Mellon University, Pittsburgh, PA 15213, USA. <sup>21</sup>School of Materials Science and Engineering, Georgia Institute of Technology, Atlanta, GA 30332, USA. <sup>22</sup>John A. Paulson School of Engineering and Applied Sciences, Harvard University, Cambridge, MA 02138, USA. <sup>23</sup>Wyss Institute for Biologically Inspired Engineering, Harvard University, Cambridge, MA 02138, USA.

\*Corresponding author. Email: g.z.yang@imperial.ac.uk

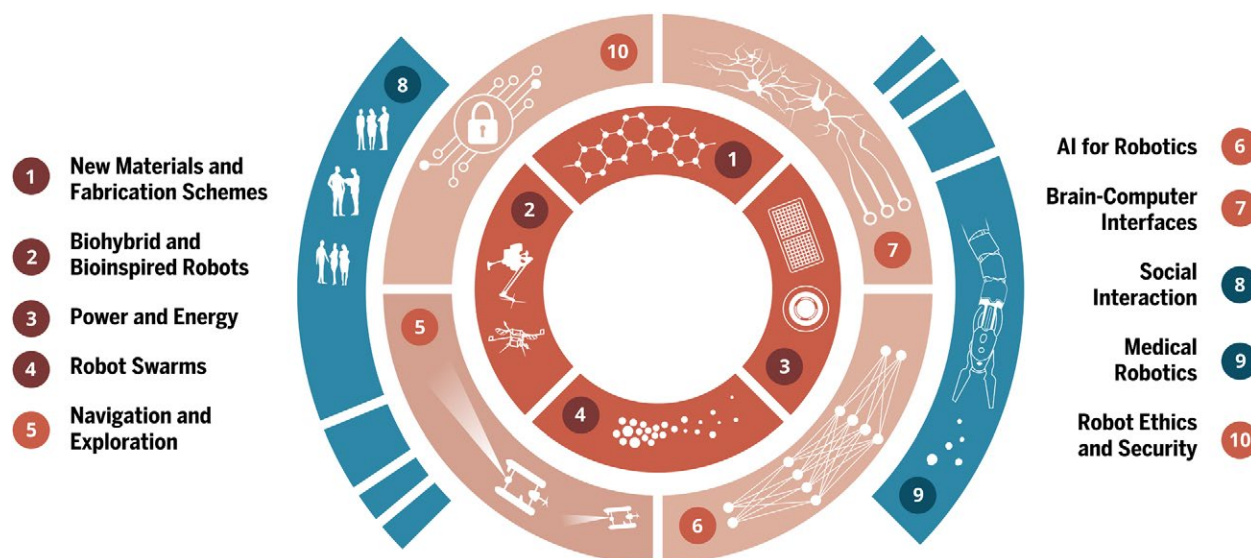


Fig. 1. Ten grand challenges of Science Robotics.

while developing novel robotic platforms that will enable new scientific discoveries. Of the 10 grand challenges listed here, the first seven represent underpinning technologies that have a wider impact on all application areas of robotics. For the next two challenges, we have included social robotics and medical robotics as application-specific areas of development to highlight the substantial societal and health impacts that they will bring. Finally, the last challenge is related to responsible innovation and how ethics and security should be carefully considered as we develop the technology further.

### CURRENT STATE OF THE ART AND 10 GRAND CHALLENGES

**New materials and fabrication schemes**  
Gears, motors, and electromechanical actuators are fundamental to many of the robotic platforms in use today, but laboratories around the world have begun to explore new materials including artificial muscles (11), compliant materials for soft robots (12), and emerging advanced manufacturing and assembly strategies (13). As illustrated in Fig. 2, these promise a new generation of robots that are power-efficient, multifunctional, compliant, and autonomous in ways that are similar to biological organisms. However, most demonstrations using new materials and fabrication strategies have been “one-offs” and must still overcome basic hurdles to achieve wide-scale adoption. These hurdles include improved portable energy storage and harvesting, new materials with

tunable properties, and new fabrication strategies to embody these functional materials as new capabilities for future robots, including the robot building and repairing itself.

New materials that combine sensing and actuation challenge the physical limitations of traditional mechatronic systems and offer a range of opportunities for the design of new robots (14). Many of the design principles draw inspiration from nature. In vertebrates, one finds a wide range of material properties from soft tissue to bone—over seven orders of magnitude in modulus—that is mediated by a continuous gradient of compliance. As opposed to the more “nuts-and-bolts” assembly approaches currently used to combine basic components into complete robots, a seamless integration of dissimilar material properties (e.g., rigid with soft, conductive with dielectric, etc.), spatially patterned with resolution several orders of magnitude smaller than the characteristic dimension of the robot, could obviate the need for complex assembly and lead to distributed function.

Similar to functionally graded materials, multifunctional materials can increase the efficiency of robot design and simultaneously offer distributed networks of hierarchically structured sensors and actuators. Opportunities exist to leverage breakthroughs in folding-based metamaterials that have demonstrated tunable electromagnetic (15) or mechanical (16) properties beyond what is possible with the base material itself. Similarly, multiphase composites may be used for simultaneous fluidic actuation or sensing (17, 18). Textiles are

a promising material for soft and wearable robotics, generating significant interest in embedding electrical functionality into fabrics. Finally, bidirectional transducers can enable sensors and actuators to behave as materials for energy harvesting or storage. While developing new materials for the future of robotics, it will be important to consider the biodegradability issues or as part of the circular economy paradigm to ensure their eco-sustainability. This is particularly relevant given the ubiquitous nature of robotic platforms in future (19, 20).

Fabrication and assembly is typically a serial process that is slow and difficult to scale to very large or very small scales. The 2016 Nobel Prize in Chemistry was awarded to three pioneers in the field of mechanochemistry who created the first synthetic molecular machines. A major remaining challenge that has thus far not been realized, despite Feynman’s prophecy (21), is to develop materials by integrating these molecular machines, or other force-generating molecules or biological motor proteins, into hierarchical materials. Substantial opportunity exists in the convergence of additive and subtractive methods, with emerging technologies involving two-dimensional (2D) to 3D transformations to generate new architectures that can simplify the need for specialized hardware and enhance the robot’s function. For example, 3D printing (or similar techniques such as multiphoton lithography or selective laser sintering) can create features and structures over nine orders of magnitude in size. However, there is no single technique

or machine that can cover this range—the best additive manufacturing strategy covers roughly three or four orders of magnitude in scale range—and none offers more than a handful of materials choices. Alternative methods should be explored that combine techniques from micro-/nanoscale fabrication (e.g., surface and bulk micromachining; physical and chemical deposition; and microscale molding, stamping, and functionalization used in soft lithography), mesoscale methods such as layering and lamination common in multilayer printed circuit boards, and the myriad macroscale multi-axis subtractive methods. Another challenge that requires much more investigation is the development of multiscalar materials able to adapt and heal over time, thus providing 4D robots that achieve the complexity found in natural systems (22).

### Bioinspired and biohybrid robots

As human technologies take on more of the characteristics of nature, nature becomes a more useful teacher (23).

By bioinspired robotics, we mean the use of fundamental biological principles that are translated into engineering design rules for creating a robot that performs like a natural system. If the biological understanding results in the direct use of biological material to design synthetic machines, then we refer to this as a biohybrid robot. Specific grand challenge lists for biorobotics have remained largely unchanged for the past 30 years—a battery to match metabolic conversion, muscle-like actuators, self-healing material that manufactures itself, autonomy in any environment, human-like perception, and, ultimately, computation and reasoning. For recent progress on these and other specific challenges, we refer readers to a few of the many outstanding perspectives and reviews (4, 24–31). Here, we identify major goals that, if met, would accelerate the design and implementation of bioinspired and biohybrid robots at an unprecedented pace.

Major challenges remain for nearly all component technologies (Fig. 3) that could enable bioinspired behavior. Materials that couple sensing, actuation, computation, and

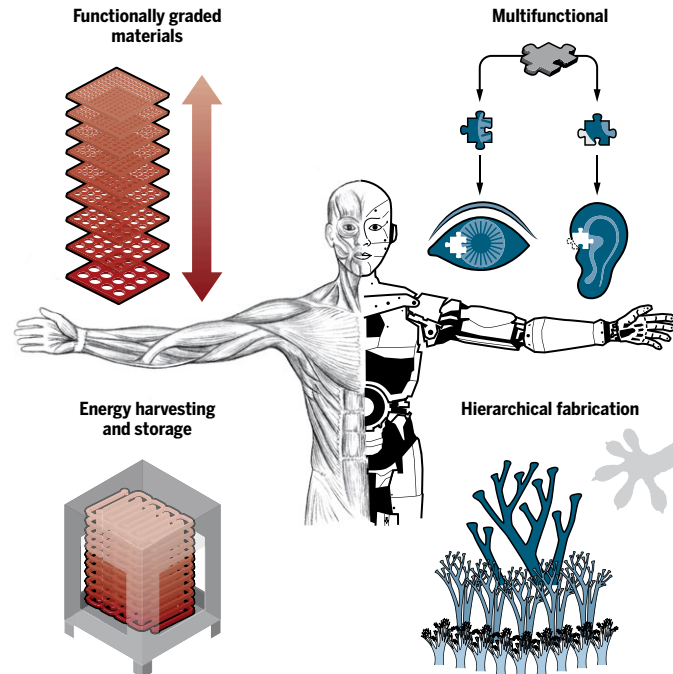


**Fig. 2. Multifunctional materials.** New materials and fabrication schemes promise a new generation of robots that are power-efficient, multifunctional, compliant, and autonomous in ways that are similar to biological organisms.

communication are critical and must be shared as developed (32). Novel designs of heterogeneous, anisotropic, hierarchical, multifunctional materials have used differing designs of structural elements to increase material strength, stiffness, and flexibility; fracture toughness; wear resistance; and energy absorption (33). These advances promise to provide robots with features such as body support, weight reduction, impact protection, morphological computation, and mobility. Techniques newly available to fabricate architectures at the micro-, meso-, and macroscales include recombinant technologies, biomineralization, layer-by-layer deposition, ori- and kirigami, self-assembly, bio-templating, magnetic manipulation, freeze-casting, vacuum-casting, extrusion and roll compaction, laser engraving, additive manufacturing, actuator-embedded molding, and soft lithography (33).

For biohybrid and bioinspired robots, actuation and energy remain major bottlenecks compared with performance seen in animals (34). Electromagnetic motors are adequate actuators for large robots but inefficient at small scales or in soft systems. New artificial muscles could revolutionize bioinspired robots; current versions that have muscle-like function and operate by shrinkage or expansion of material—such as shape-memory materials and electro-active polymers—lack robustness, efficiency, and energy and power

density. No battery can yet match metabolic energy generation in organisms, so highly miniaturized, biohybrid robots actuated by biological muscle become advantageous (28). Biohybrid robots can exploit the unique features of living cells that include self-healing (35), embedded sensors, dynamic response to changing environmental conditions, and use of inexpensive and eco-friendly fuel (28).

A major challenge remains as to how these components are effectively integrated and embodied to perform system-level behaviors (Fig. 3). The field of bioinspired robotics must address different challenges, mainly due to the synthesis/fabrication of efficient and scalable artificial components. However, biology has made progress toward providing principles, especially for mobility and manipulation. New discoveries in hydro-, aero-, and terradynamics have led to an impressive “robo-zoo” of bioinspired robots (24, 25) benefiting from the nonlinear, unsteady, self-stabilizing, energy storage, and return principles quantified in animals. Further development is required to understand transitions and multimodal performance (36) within the same platform. Significant progress has been made in bioinspired, quasi-static, pick-and-place manipulation, and grasping, but no system has integrated components sufficiently to match the flexibility and dexterity of human hands (37).

As bioinspired robots venture beyond the laboratory, models of real-world, unstructured environments will be required, but none can yet adequately represent our complex, dynamic world. Although first-principle models exist for hydro- and aerodynamic systems (i.e., the Navier-Stokes equations), a similar framework for terradynamics (38) is required to understand how bioinspired robots effectively interact with the ground. Because of their staggering complexity, one of the greatest challenges to extracting fundamental principles from biological systems involves model abstraction and dimensional reduction (39). Internal models can allow us to test hypotheses and simplify control, especially when placed into a dynamical systems theory framework (40). These models become even more important as we require simple representations for use in reinforcement, supervised,

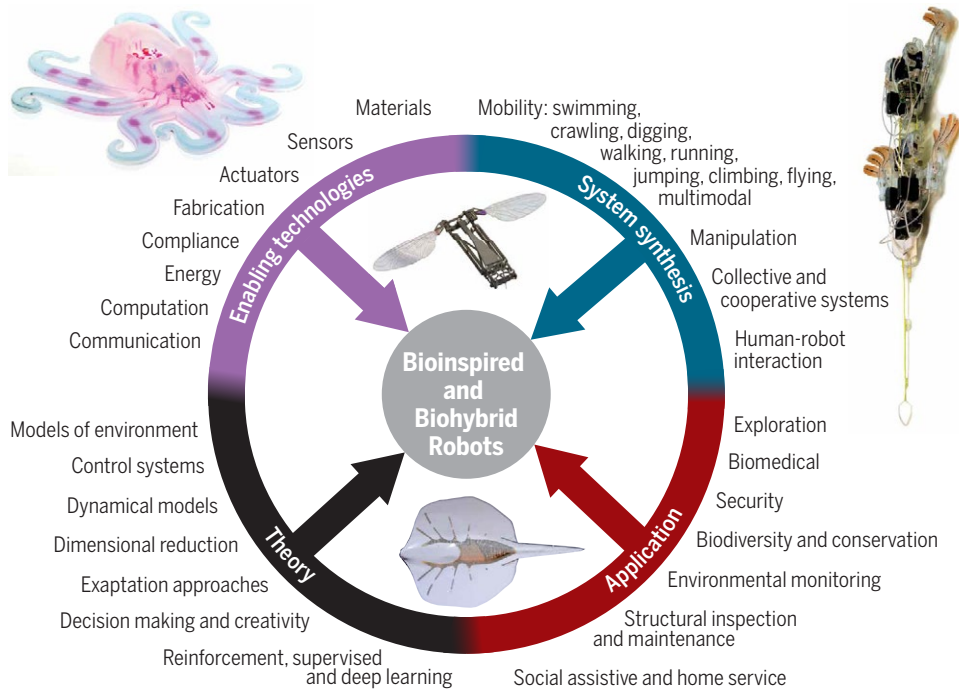


**Fig. 3. Convergence of conditions accelerating opportunities for design of bioinspired and biohybrid robots.** Enabling technologies, development of theory, a synthesis of systems, and application drivers all provide a foundation for a frontier. [Adapted by N. Cary/*Science Robotics*. Image credits: Octobot (4); RoboBee, Wyss Institute at Harvard University; StickyBot, PolyPEDAL Laboratory-Pauline Jennings, robot from M. Cutkosky, Stanford University; ray (105)].

and deep learning for adaptability, decision-making, and even creativity.

**Power and energy**

As for any electronic system, power and energy sources represent one of the most challenging areas of robotics research and deployment, especially for mobile robotics (Fig. 4). Underwater and particularly deep-sea exploration requires compact, stable, high-energy density batteries to support robots working in challenging conditions and extreme environments. The increasing adoption of drones and autonomous vehicles is fueling the development of new battery technologies that are safe and affordable, with longer cycle lives, robust temperature tolerance, higher energy densities, and relatively low weight. Beyond the currently available commercial technologies such as lead-acid, nickel-metal hydride, and lithium-ion batteries, there has already been extensive research on developing next-generation technologies, such as fuel cells and supercapacitors. These new areas include the development of silicon anodes with smart electrodes through conductive nanoporous structures and binder designs, which greatly enhances cyclability and minimizes pulverization. Other emerging electrode designs for achieving enhanced ca-

pacities use Ni-, Li-, and Mn-rich, layered materials (41). Although many new ideas are being developed, the fundamental issues being addressed remain the same for many historical technologies: irreversible phase transitions of active materials and/or unstable electrode-electrolyte solution interfaces (41).

Metal-oxygen, lithium-sulfur, aluminum-ion, and sodium-ion batteries are some of the key technologies being actively pursued. The potential of lithium-sulfur batteries combined with solar panels has already been demonstrated with the Zephyr-6 unmanned aerial vehicle in its record-setting, high-altitude, long-endurance flights (42). Although most battery research is focused on liquid electrolytes because of high ion conductivity and good surface-wetting properties, they often suffer from electrochemical and thermal instabilities, as well as low ion selectivity. Advanced battery systems based on solid electrolytes could bring advantages because of their safety, excellent stability, long cycle lives, and low cost (43). The advent of flow-based, lithium-ion, lithium-sulfur, and lithium-organic batteries also promises new opportunities (44). The future will also see new improvements to the current radioisotope power systems used for space exploration.

In practice, the operational longevity of a mobile, autonomous system is typically dictated by the battery power, its size, and its weight. Efforts continue to minimize power utilization through development of power-efficient electronics and actuators, but for robots to operate wirelessly for appreciable times in unstructured environments, they must extract useful energy from their surroundings and use radical new solutions for highly energy-dense storage, such as solar light, vibration, and mechanical movement. Compared with biological machines at any scale, robots are typically very energy-inefficient [e.g., the 100-horsepower (75 kW) consumption of Boston Dynamic’s horse-sized LS3]. Whereas the quintessential robot arm bolted to the factory floor and tethered to an unlimited power supply works well in industrial settings, mobile robots lack a standard fuel source, storage, and distribution system. Batteries, of course, are ubiquitous, although their energy density remains low compared with hydrocarbons (about 1 MJ/kg and 50 MJ/kg, respectively). One benchmark comes from biology, where carbohydrates (about 17 MJ/kg) power the effective running, swimming, and flying of organisms over a huge range of physical scales (45). Robotics will require a shift in energy storage technologies to produce similar behavior. Electrochemical storage technologies are attractive for numerous reasons, although many autonomous robots leverage combustion (13) or monopropellant decomposition (46) as alternatives. Developments in energy-harvesting techniques (e.g., mechanical, thermoelectric, photovoltaic, and electrochemical) and wireless power transmission (47) are expected to play a key role in addressing the power and energy challenges of robotics. Different mechanisms have been established for harvesting mechanical energy, including electromagnetic and electrostatic generators, as well as piezoelectric nanogenerators and triboelectric nanogenerators (based on the coupled effect of contact electrification and electrostatic induction) (48). Besides serving as a small power supplies, nanogenerators can be self-powered sensors and flexible actuators with the use of a range of materials from functional polymers, fabrics, and nanomaterials to traditional metal foils and ceramic thin films (49). The most important characteristic of a nanogenerator is its high response to low-frequency mechanical triggering, with complementary applications

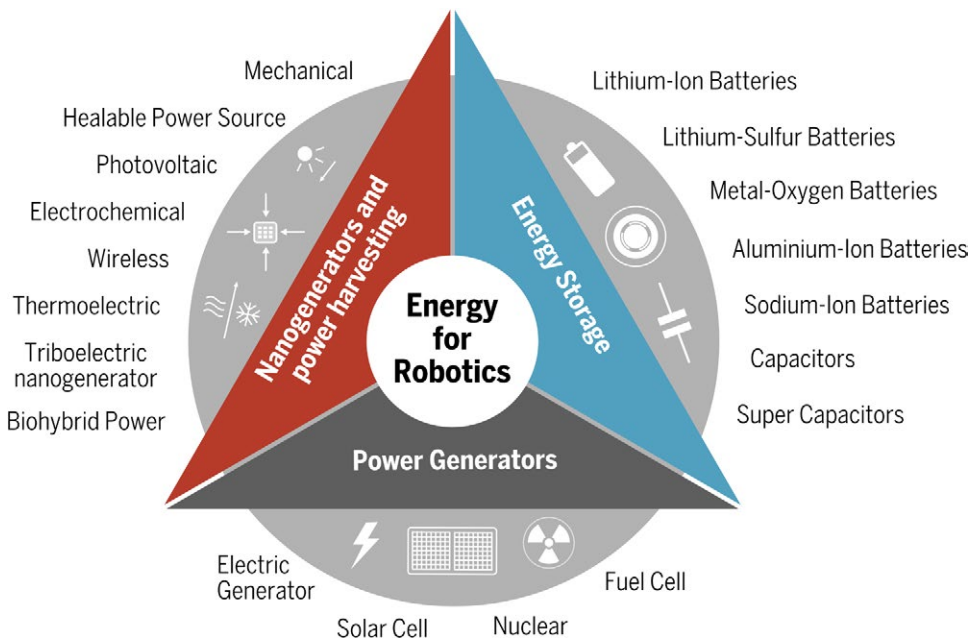


**Fig. 4. A summary of different energy sources for robotics.** Power generators, which include fuel cells, classical electromagnetic generators, and solar cells. Energy storage, including batteries and capacitors/supercapacitors. Power harvesting and newly developed nanogenerators, as micro-/nano-energy sources, self-powered sensors, and flexible transducers.

with an electromagnetic generator that usually works well at high operation frequency. In the working environment of a robotics, low-frequency mechanical stimulation is fairly popular, which can be effectively converted into electric output using a triboelectric nanogenerator.

As stated in the previous section, no battery can yet match metabolic energy generation in organisms. Biohybrid robots could use the unique features of living cells for potential solutions (28).

### Robot swarms

Robot swarms allow simpler, less expensive, modular robotic units to be reconfigured into a team (Fig. 5) depending on the task at hand while being as effective as a larger, task-specific, monolithic robot, which may be more expensive and have to be rebuilt depending on the task. Nature provides a repertoire of examples that illustrate this idea (50). Independently acting organisms cannot achieve a goal by themselves but, in coordination with other organisms, can solve complex problems and complete a mission. This “force multiplication” requires individuals to sense not only the environment but also their neighbors and to communicate with other individuals in their team while acting independently. This paradigm has been seen in fish, birds, and insects and is

fundamental to navigating as a flock or horde, foraging, hunting, building nests, and surviving harsh environments. Similarly, a group of relatively unsophisticated robots can form a networked team that realizes a range of behaviors well beyond the capabilities of the individuals by communicating and cooperating with team members. The swarm principle can be used at macro-, micro-, and nanoscales with a plethora of application areas.

There are three technology drivers suggesting that robot swarms will have an impact in the next 5 to 10 years that stem from falling prices and increasing performances of sensors, processors, storage devices, and communications hardware. First, the integration of components for computation and storage is resulting in a software-centric architecture that tightly couples computation, storage, networking, and virtualization resources—a framework that is being called “hyper-convergence” (51). Soon, sensors and wireless communication devices will be part of this hyper-convergence. Second, we are seeing the convergence of the hardware for consumer electronics (smart phones, tablets, and virtual reality devices) and intelligent autonomous systems (drones, robots, and self-driving vehicles), with concurrent advances in 5G wireless technologies. Third, cognitive systems relying on statistical machine learning and AI are becoming

mainstream. Tools from data science, machine learning, and predictive analytics are now being routinely used to extract information from text and speech and to recognize objects from imagery (pictures and videos).

As we think about swarms, it is useful to consider different forms of collective behavior. Coordination and cooperation can be seen in groups that are homogeneous, but heterogeneity is powerful because it allows for collaboration (52, 53). For example, a large robot may be able to carry more powerful sensors or have more powerful computational resources or radios, but it may be less agile than its smaller counterparts. Scale is particularly important in robot swarms where small groups lend themselves to centralized control, and information across the group can, in principle, be shared via communication and sensing. The analysis of group behaviors in these settings or the synthesis of group behaviors for a given task is easier for smaller groups with centralized architecture than for larger groups like swarms, where it is impractical to efficiently share information across the swarm and architecture because these systems are necessarily decentralized. From a mathematical perspective, the state space, which is the Cartesian product of the individual state spaces, grows linearly, and the types of interactions that can occur across individuals grow combinatorially. Thus, it is necessary to develop stochastic models for predicting collective behavior in large-scale swarms. However, we lack mathematical models of flock- or herd-like groups that elude the enumeration in small-scale groups yet do not justify ensemble-averaged models seen in large-scale swarms.

Robotic systems are equipped with sensors that allow them to perceive the environment. They reason about the environment and take actions, forming a feedback loop that is called a perception-action loop. Designing perception-action loops is fundamental to creating autonomous robots that function in unstructured environments. Robot swarms require their communication ability to be embedded in this feedback loop. Thus, perception-action-communication loops are key to designing multifunctional, adaptive robot swarms. There are currently no systematic approaches for designing such multidimensional feedback loops across large groups.

Whether we think of smaller robot groups, in which the combinatorics do not pose formidable challenges, or larger swarms, much of the literature addressing the problem of coordination makes use of simpler mathematical models; algorithms for perception, estimation, planning, and control; and robot deployments (54). The dynamics and control of cooperation have been addressed in cooperative manipulation, multi-fingered grasping, and legged locomotion, but systematic approaches to questions of synthesis do not exist. Similarly, although there is interesting work on collaboration between humans and robots (55) and between aerial and ground robots (56), a general framework for modeling heterogeneity and the design of heterogeneous groups and desired behaviors does not exist.

As we develop robot swarms, one must also develop the tools to create teams that can be responsive to human commands, can adapt to changing conditions, are robust to disturbances (to the extent that is possible given the constraints on resources), and are resilient to adversarial, disruptive changes caused by large-scale failures or damage to the swarm infrastructure. Responsiveness is generally characterized by the time a system takes to respond to input or meet input-output (task) specifications. Robustness is the property of the system to be responsive even in the presence of disturbances and modeling errors (and failures), although the majority of the literature addresses robustness with carefully constructed bounds on those disturbances and modeling errors. As pointed out by Rodin (57) in the context of similar challenges that confront urban societies today, resilience is a fundamentally different property that is about systems that can bend without breaking. Resilient systems are self-aware and self-regulating and can recover from large-scale disruptions to the network. Thus, a science of resilient robot swarms must focus beyond robust individual agents to resilient integration across diverse elements of the group that leverage new mechanisms (e.g., mobility, reconfiguration, sensing, communication, platform diversity, and involvement of human peers) for achieving macroscale resilience.

Robot networks integrated with our infrastructure have tremendous potential for solving the most pressing problems facing



**Fig. 5. Robot swarms.** New opportunities and research challenges.

human civilization. They can provide solutions to feed an ever-increasing population with limited resources by increasing the efficiency of food production and decreasing water consumption by an order of magnitude (58). They can respond to natural disasters and adversarial attacks by enabling resilience in our infrastructure (59). They are a part of any practical solution to space colonization. We are poised to see great advances and impacts in this area in the next 5 to 10 years.

### Navigation and exploration

Path planning, obstacle avoidance, localization, and environment mapping are ubiquitous requirements of robot navigation and exploration. Advances in sensing, machine vision, and embedded computation have underpinned the remarkable progress of autonomous vehicles roaming complex terrains at speed, drones forming swarms for completing collaborative tasks, and surgical robots delivering targeted therapy while negotiating complex, delicate anatomical structures. Many robots we deploy are intrinsic explorers that we send to the far reaches of the planet—the deep oceans, under the Arctic ice pack, into volcanoes—and go where no human has yet tread, often under unknown and extreme conditions. The associated challenges are therefore much greater than those encountered today.

Foremost, the robots must operate in environments that are not only unmapped, but, at times, their very nature is not understood. Adding to this are challenges associated with communications and navigation. Robots

in tunnels or mines must cope with rough terrain, narrow passageways, and degraded perception. Robots undertaking nuclear decommissioning must withstand radiation and restricted access, and those used to construct and assemble infrastructure must be able to resist chemicals and materials used in the construction process as well as being resistant to dirt, dust, and large impact forces. Undersea robots operate in an environment where radio does not penetrate and our usual forms of communication and navigation disappear; untethered undersea vehicles must be autonomous. As robotic spacecraft take on tasks like roaming distant planetary surfaces and, in the not-so-distant

future, possibly landing on the icy moons of the outer planets, they enter a regime where long latency and low bandwidths of communications not only greatly reduce productivity but also put the survival of the robot itself at risk.

Undoubtedly, current mapping and navigation techniques will continue to evolve. For example, techniques such as SLAM (simultaneous localization and mapping) will go beyond the current rigid and static assumptions of the world and will effectively deal with time-varying, dynamic environments with deformable objects (60). With resource constraints, specific challenges include how to learn, forget, and associate memories of scene content both qualitatively and semantically, similar to how human perception works; how to surpass purely geometric maps to have semantic understanding of the scenes; how to reason about new concepts and their semantic representations and discover new objects or classes in the environment through learning and active interactions; and how to evolve through online, prospective, and lifelong continuous learning.

For navigation, the grand challenge is to handle failures and being able to adapt, learn, and recover (Fig. 6). For exploration, it is developing the innate abilities to make and recognize new discoveries. From a system perspective, this requires the physical robustness to withstand harsh, changeable environments, rough handling, and complex manipulation. The robots need to have significant levels of autonomy leading to complex self-monitoring, self-reconfiguration, and repair such that there is no single point of complete failure but rather

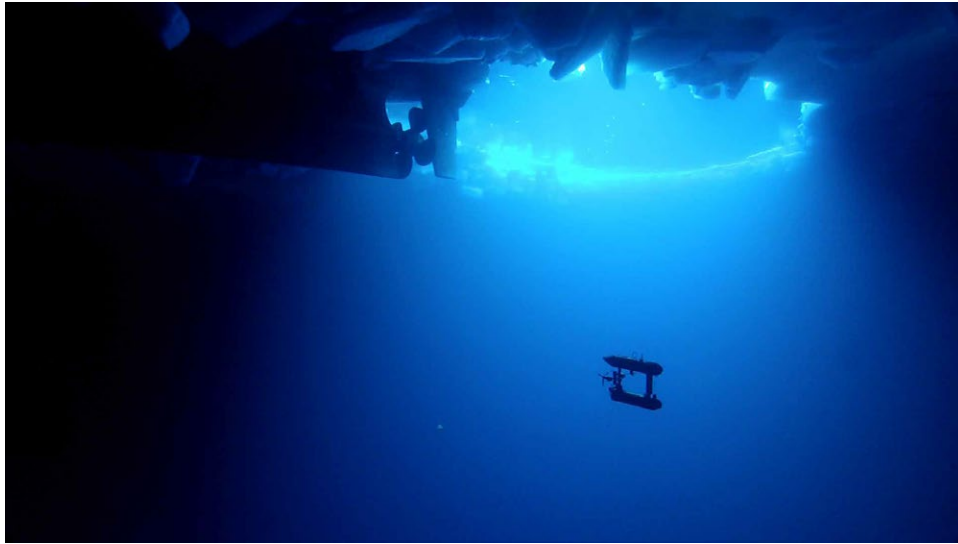


**Fig. 6. Intelligent explorers.** Handling failures and being able to adapt, learn, and recover are major challenges for navigation and exploration, especially for robots operating in extreme environments. [Reproduced from (106) with permission].

graceful system degradation. When possible, solutions need to involve control of multiple heterogeneous robots; adaptively coordinate, interface, and use multiple assets; and share information from multiple data sources of variable reliability and accuracy.

### AI for robotics

As the underpinning technology for robotics, AI is undergoing a renaissance after more than 60 years of ongoing development. There is a widespread myth that AI did not work for the first 50 years, but the truth is that for certain classes of domain- and task-specific problems, given enough development time as well as computing and data resources, the applications could be made to work. The advent of deep learning methods resulted in remarkable levels of object recognition accuracy (61) using hierarchical pattern recognition that retained information coherence at each level of the hierarchy. The new machine-learning algorithms were combined with unprecedented access to data, as well as inexpensive and powerful computing hardware. The resulting progress in solving narrow classes of AI problems has led many to think that we are on the verge of solving intelligence—in all its multifaceted and (still) poorly understood dimensions.

However, we still have a long way to go to replicate and exceed all the facets of intelligence that we see in humans. Combining advanced pattern recognition and model-based reasoning is critical for building systems that can go beyond statistical correlation and

begin to reason about underlying interdisciplinary mechanisms and systems dynamics. Meta-learning, or learning how to learn new things, is a critical new AI capability not only with large training data sets but also with limited data. The challenge is to be able to learn on the fly, adapting to dynamic and uncertain environments. One promising approach in this area has been developed based on neuroscience insights about the human hippocampus as a predictive map of novel situations (62).

AI systems that know their own limitations and know how to seek help could go beyond the current methods of training and knowledge acquisition. These systems will know how to interact, how to seek help, how to recover from failure, and how to become smarter. AI systems and robots that can model their own components and operations are critical for adaptation and evolution. We need AIs that are able to detect their own subcomponents, model their operations, and modify those models if their structure changes. Work by Bongard *et al.* (63) provides an early example of this type of robotic system, which can discover its own components and learn to use them dynamically in locomotion.

AI that can learn complex tasks on its own and with a minimum of initial training data will prove critical for next-generation systems. Most machine-learning systems are data-intensive and require massive data in order to learn complex tasks. DeepMind's AlphaGo Zero system that taught itself to play Go significantly better than the world champion in Go (64) was an impressive example of this.

However, we do not yet have systems that can do this easily across heterogeneous tasks and domains. AI systems that can comprehend deeply and synthesize across complex texts and narratives will prove useful in a variety of applications. We have already seen some initial examples, but the real world is both interdisciplinary and complex, and building robust systems of this class will prove extremely challenging.

One of the enduring grand challenges in AI is to provide a coherent and comprehensive mapping of the key mechanisms of human intelligence in a software system. The first key step in doing this is to produce a thorough account of how the neocortex actually works, including learning to learn and learning from limited examples. A recent paper on this provides some detailed and testable predictions concerning how columns in the neocortex provide location signals that enable

learning the structure of the world (65). We need to test theories of this type rigorously, both in terms of neuroscience data and in the operation of AI software (66). In addition, much progress has been made recently in building AI systems that understand natural language. A key set of targets is to build systems that maintain coherent conversations and deal with unknown environments and contexts.

Ambient intelligence and ubiquitous and networked AI and robotics (cloud robotics) will be critical in the development of integrated heterogeneous AI and robotic services. There are many initial examples of cloud AIs that update situation assessments and share knowledge but few working examples of heterogeneous AI or robotic services that integrate smoothly and reliably over time. DeepMind's PathNet architecture points to systems that allow for new contexts to be learned at the same time, leveraging knowledge of training in other contexts to learn much faster.

One of the big questions for AI is its ability to perform deep moral and social reasoning about real-world problems. As AI and robotic systems undergo accelerating growth in power and capabilities, there will be an increasing premium on systems that can demonstrate moral and social reasoning. Although human-in-the-loop may be a preferred design constraint for systems that touch life-or-death situations, in autonomous driving and aerospace applications, the relevant decision loops may well be too fast for the human brain, hence the need for embedded moral and

social reasoning. These challenges need to be framed in the context of baseline risks that humans have already habituated to, such as 1.2 million people dying worldwide as a result of largely avoidable driver errors committed by humans. We can expect to see considerable and rapid operational progress on this front.

### Brain-computer interfaces

A BCI forges a direct, online communication between brain and machine, independent from the user's physical abilities, and represents a new way to augment human capabilities and restore patient function (Fig. 7). Direct use of brain activity to control a computer or external device without the mediation of the peripheral, somatomotor nervous system has major applications in enabling paralyzed patients to communicate and control robotic prosthetics and in rehabilitation for restoring neural function (67–71). BCIs translate the user's intentions into outputs or actions by means of machine-learning techniques, operating by either presenting a stimulus to the operator and waiting for his/her response (synchronous) or continuously monitoring the operator's cognitive activity and responding accordingly (asynchronous). Beyond their clinical use, BCIs also have emerging applications in neuroergonomics, communication and control, education and self-regulation, as well as games and entertainment (72). Despite being a relatively new field, recent advances in BCIs have been accelerated by allied technologies, including neuroscience, sensor technologies and com-

ponent miniaturization, biocompatibility of materials, and embedded computing.

For practical use, a BCI can be classified as active, reactive, or passive (73). Active BCI derives its outputs from brain activity, which is directly and consciously controlled by the user, not necessarily depending on external events, for controlling an application. In reactive BCI, the outputs are derived from brain activities arising in response to specific external stimuli. Passive BCI is a relatively newer concept, which derives its outputs from arbitrary brain activity arising without the purpose of voluntary control, for enriching human-machine interaction with implicit information on the actual user state.

Both invasive and noninvasive methods are used to record brain activity. Invasive approaches measure the neural activities of the brain by either intracortical neural interfaces with microelectrode arrays, which capture spike signals and local field potentials, or cortical surface electrocorticography, providing both high temporal and spatial resolution with good immunity to artifacts (70). Noninvasive BCIs require no surgical implantation; typical signals used include slow cortical potentials, sensorimotor rhythms, P300 event-related potentials, steady-state visual evoked potentials, error-related negative evoked potentials, blood oxygenation levels, and cerebral hemodynamic changes. Common assessment methods include fMRI (functional magnetic resonance imaging), fNIRS (functional near-infrared spectroscopy), MEG (magnetoencephalography), and EEGs (electroencephalograms) (70).

Despite the success of BCI for patients with amyotrophic lateral sclerosis (also known as motor neuron disease), spinal cord injury, and rehabilitation of motor function after stroke, there remain significant challenges for the wider adoption of BCI (74). The first is in sensing and data acquisition because current modalities are expensive and cumbersome. Parallel developments in implantable sensing with new microfabrication, packaging, and flexible electronics, combined with ultralow-power local processing and wireless data paths, would bring new opportunities for completely untethered implants, providing improved patient experience and uptake in both clinical and home environments. For noninvasive techniques, newly emerging, low-cost, and ergonomically designed wireless EEG and fNIRS systems have shown promise for general BCI-based robotic control.

The second challenge is in data processing and dealing with artifacts of noncerebral origin, particularly for wearable approaches. The data-processing challenge is also associated with the fact that cortex folding differs between individuals, as do relevant functional maps. Furthermore, sensor locations may differ across different recording sessions, and brain dynamics can be intrinsically nonstationary. Current methods often involve extended periods of training, calibration, learning, and adaptation, thus making it prohibitive for general use.

Third, it remains to be seen whether BCI will always outperform simpler techniques, such as those using eye tracking or muscle-based devices. The development of hybrid BCIs may represent a viable way forward by combining with other, more mature assistive technologies. This would allow more reliable and seamless interfacing with peripheral neuroprostheses, functional electric stimulation devices, and exoskeletons.

A further challenge is dealing with tasks with high degrees of freedom. Current multiclass BCI classification generalizes poorly across individuals and tasks. In such cases, it may be more appropriate to rely on BCI for intention detection and task initiation and on autonomous robot manipulation for task completion.

Continuing development of BCIs will bring exciting new research opportunities not only in robot control and functional rehabilitation but also in knowledge exchange and cross-fertilization between neuroscience and robotics. It will also play an important role in

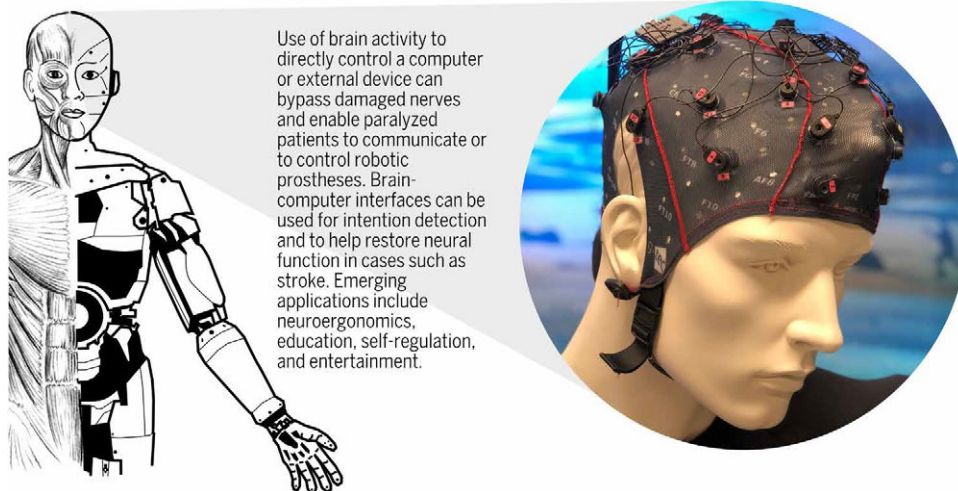


**Fig. 7. Brain-computer interfaces.** BCIs have extensive applications in enabling paralyzed patients to communicate with and control robotic prosthetics and in rehabilitation for restoring neural function. Continuing development of BCIs will also see applications in performing mission- or safety-critical tasks.

performing mission- or safety-critical tasks, whereby adaptive levels of automation, context-sensitive decision support, and motion constraints are provided depending on mental workload, task engagement, hypovigilance, mood or emotion, and precursors to human errors (e.g., hesitation and disorientation).

### Social interaction

Robotics and AI have often underestimated the difficulty of replicating capabilities that humans find particularly easy. Perhaps most notorious was the early belief that computer vision was a simple problem suitable for an undergraduate research project (what could be simpler than seeing a table as a table?) (75), but similar stories can be told for locomotion, manipulation, and understanding language. Social interaction has the same status: Because humans are so adept at recognizing and interpreting social behavior, we often underestimate the complexity of the challenge that this represents for a robot (Fig. 8).

As common as social interactions are in our daily lives, we have very few comprehensive, quantitative analyses of human social responses; our understanding of human social behavior is not nearly as advanced as our knowledge of Newtonian mechanics or even human visual perception. Although this alone might make some believe that building social interactions for robots is premature, the practicality of putting robots into our human environments—our schools, hospitals, shops, and homes—necessitates addressing social interaction. The three most significant challenges that stem from building robots that interact socially with people are modeling social dynamics, learning social and moral norms, and building a robotic theory of mind.

Social interaction is a major challenge for robotics in part because the perceptual demands are so significant. Social cues—such as gaze direction, facial expressions, or vocal intonation—are often extremely detailed, rapid, and nuanced signals that are embedded within other activity; the difference between an enthusiastic greeting and a sarcastic scolding might depend on a single wink, or rising inflection on just one phoneme. The temporal patterning of these signals is also frequently significant—a small delay when answering a question may be inter-

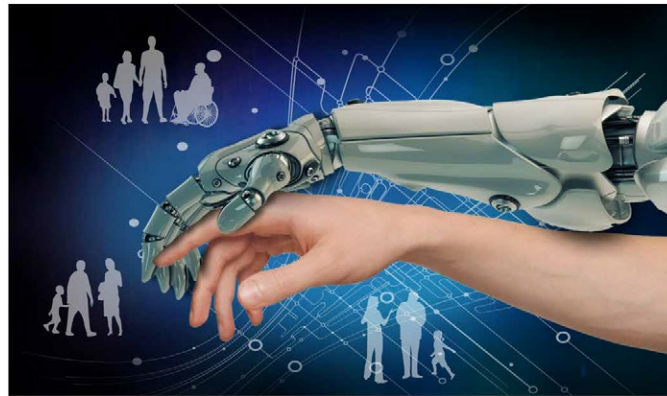


**Fig. 8. Social robotics.** Social interaction requires building and maintaining complex models of people, including their knowledge, beliefs, goals, desires, and emotions.

preted as a sign of uncertainty or mistrust. Although we have made substantial advances in machine perception in the last decade, especially in object recognition (76), action recognition (77), and human gaze analysis (78), we still lack systems that operate under the diverse natural conditions and real-world time constraints that social interactions demand. Next-generation systems will need to richly mix elements from multiple input modalities and combine these perceptual systems with predictive models of social intention to more fully capture the rich, dynamic nature of social interactions.

Social signals are also very context-dependent and culturally determined. Two individuals standing nearly nose to nose in a conversation might be typical in Argentina, but could be an indication that they are either close friends or about to have an argument in the United States. Robots that are deployed in human environments must be able not only to adapt to these cultural differences but also to learn the appropriate social and moral norms for their setting. A robot that expresses excitement when the death of a family member is being discussed, one that shouts at inappropriate times, or one that takes a coffee mug before it is empty will not find itself welcome in home or workplace. The development of robots capable of understanding empathy, ownership, and the need to keep a promise will be essential to building the long-term trust and relationships necessary for operating side by side with people. To take the next step in this domain, new tools are required for modeling the expectations of the people around the robot and expanding the robot's understanding of the consequences of its own actions.

Social interaction also requires building and maintaining complex models of people, including their knowledge, beliefs, goals, desires, and emotions. We routinely simplify our language based on what we know our partners understand, coordinate our actions to match the preferences of our collaborators, and interpret the actions of others as representing their inner goals. These “hidden” states allow us not only to understand why someone has taken a particular action but also to predict their likely future behavior. Modern work on intent recognition (79), user modeling in intelligent tutoring systems

(80), collaboration models in human-machine interaction (81), emotion recognition via facial feature analysis (82), and other domains touch on single aspects of this problem, but none of these domains has yet produced comprehensive or integrated models that allow robots to begin to have rich, usable models of human mental states (83). Advancing the state of the art in this domain will require integration of models of episodic memory, hierarchical models of tasks and goals, and robust models of emotion to create detailed cognitive models that capture the naïve psychology that we effortlessly apply to understanding human behavior.

Solutions should also work for long-term interactions and relationships: A joke told once might be funny, but the same joke told every day for a month is not. Most of our current social robots have been designed for interaction that lasts on the order of a few minutes or hours, but our human-human social interactions often span months, years, and even decades. Just as machine learning struggles to scale to continuous, long-term adaptation models (84), social robotics must expand from moment-to-moment engagements to long-term relationships. This expansion will require models of robot behavior and personality that distinguish between changes that are appropriate at different time scales, the capability to autonomously generate interaction content (both verbal and nonverbal) rather than relying on prescribed components, and personalization and adaptation mechanisms that adjust both short-term responses and long-term tendencies based on current interactions.

## Medical robotics

From minimally invasive surgery, targeted therapy, hospital optimization, to emergency response, prosthetics, and home assistance, medical robotics represents one of the fastest growing sectors in the medical devices industry (85).

The impact of robotics on medicine is undeniable. The therapeutic and commercial success of Intuitive Surgical's da Vinci system has spurred a number of commercial ventures targeting surgical applications, which echo the emerging trend in precision surgery, focusing on early malignancies with minimally invasive intervention and greater consideration of patient recovery and quality of life (86, 87). These efforts will continue to improve health-care in terms of both outcomes and cost. Other research and commercial efforts are focusing on what many see as an inevitable future in which intelligent robotic devices assist health-care workers in a variety of ways. As we move toward this future, however, many grand challenges remain. One of the primary challenges in surgical and interventional robotics is a move toward systems that exhibit increasingly higher degrees of autonomy (85). A second grand challenge is the creation of fully implantable robots that replace, restore, or enhance physiological processes. A third grand challenge is in the realization of micro- and nanorobotic devices of clinical relevance (Fig. 9).

In those industries in which robots are most successful (e.g., manufacturing and warehouse

automation), teleoperation has been replaced by semiautonomous or autonomous operation. Autonomy in medical robotics is incredibly challenging (88); whereas products and assembly lines can be designed to fit the capabilities of robots, this is not possible with the human body. Consequently, autonomy in existing medical robots remains limited. In most cases, the contribution of the robot has been to enhance the skill level of the surgeon. For example, Intuitive Surgical's da Vinci robot makes laparoscopy easy (89); routine procedures can be performed at a higher level of proficiency, and difficult cases that would otherwise be treated with open surgery can be performed laparoscopically. Similarly, Stryker's Mako robotic arm enhances hip and knee replacement by enabling more precise bone drilling than the surgeon can perform on his or her own. In both these examples, the robot acts as an extension of the surgeon's hand, and its motion is continuously under the surgeon's control. Other systems, such as Think Surgical's Robodoc system, execute precomputed and surgeon-approved cutting paths based on medical images. All these systems exercise some degree of "autonomy" in translating a surgeon's intentions (expressed in joystick motions or in preoperative planning) into the actual motions of the robot's actuators. The challenge arises when the controller needs to make more complex decisions in interpreting the clinician's intentions. Thus, we anticipate that the development of autonomy in medicine satisfying regulatory and ethical concerns will progress in stages. Two examples are described below.

Although medical robot autonomy is often discussed within the context of surgery, emergency medicine provides another set of challenges and opportunities. In this case, an emergency medical technician (EMT) needs to assess the condition of a patient quickly, prioritize problems, and often take time-urgent steps to stabilize the patient. Intelligent robotic systems that could assist with such tasks as placing and monitoring sensors, inserting intravenous lines or breathing tubes, and preparing a patient for transport could significantly improve the ability of an EMT to provide urgent care. In addition to obvious challenges in dexterity and device development, there are also difficult computational challenges. The robot assistant will need to recognize relevant patient anatomy in what is often a highly unstructured environment. It will need to use its situational understanding to perform tasks appropriately under direction of the EMT, who is likely to rely primarily on spoken commands, supplemented with gestures, to explain what needs to be done.

A long-term challenge is to enable one surgeon to supervise a set of robots that can perform routine procedure steps autonomously and only call on the surgeon to take control during critical, patient-specific steps. For example, intracardiac interventions involve navigating from percutaneous entry in the peripheral vasculature to specific locations inside the heart using a combination of pre- and intraoperative imaging. The theory of image-based robot navigation is well developed, so developing safe navigation algorithms seems quite feasible. As clinical experience with intracardiac devices (e.g., transcatheter valves) grows, the deployment of these devices may become sufficiently standardized to enable automated deployment. Furthermore, miniaturized and multifunctional fully implantable robots represent an emerging area of development (90, 91). Issues related to biocompatibility, packaging, power efficiency, and harvesting are important to be addressed (92). Perhaps the most significant challenge of automating any clinical task is to be able to anticipate, detect, and respond to all possible failure modes. Medical device regulation of autonomous robots will likely need to develop in a manner that balances the requirements for provably safe algorithms with compliance costs.

An emerging area of medical robotics is implantable robotic devices. These

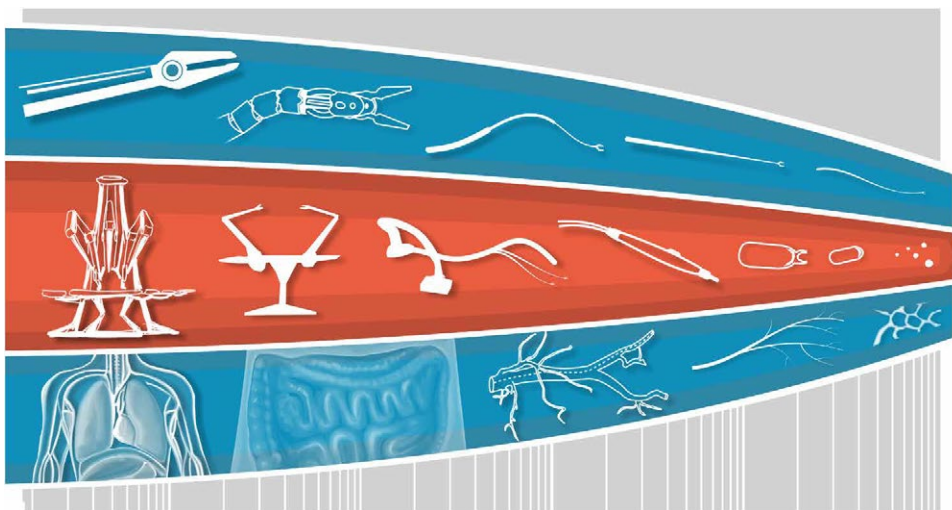


**Fig. 9. Medical robotics.** From macro to micro and from large systems to small, smarter devices that can support the future development of precision medicine.

bionic systems are being proposed as replacement organs, e.g., for the pancreas (91); as assist devices for damaged organs, e.g., for the heart (90); and to induce organ growth, e.g., of the esophagus and bowel (93). There are a number of challenges that must be addressed to advance this field. These include biocompatibility, reliability, adaptability, security, and providing power. Full biocompatibility is important in order to maintain long-term functionality. Furthermore, for those implants that provide temporary physiological support, designing the implant to be resorbable could eliminate the need for surgery to remove the device. Implants must also be designed to react to changing conditions, such as exercise, and extreme reliability is a necessity because malfunction could quickly lead to death. Although remote programming to provide software updates is advantageous, security is critically important to prevent one's organ from being hacked. Last, because the power requirements of a robotic device are high in comparison to, e.g., a pacemaker, the capability for wireless power transfer will be crucial.

An other emerging area of medical robotics is micro- and nanorobotics, with increasing numbers of groups maintaining high-profile research efforts. The field has made impressive strides over the past decade as researchers have created a variety of small devices capable of locomotion within liquid environments (94). Robust fabrication techniques have been developed, some devices have been functionalized for potential applications (95), and therapies are being actively considered (96). Although excitement remains high for this field, it faces a number of significant challenges that must be addressed head-on to make continued progress toward clinical relevance. The primary roadblocks to overcome include the development of biodegradable and noncytotoxic microrobots, development of autonomous devices capable of self-directed targeting, catheter-based delivery of microrobots near the target, tracking and control of swarms of devices in vivo, and the pursuit of clinically relevant therapies.

### Robot ethics and security

With increasing levels of autonomy and human-robot interaction, there needs to be careful consideration of potential regulatory, ethical, and legal barriers and the context of how robots are deployed. Because robotics and AI are fueled by data, some challenges are rooted in human-environment interactions and data governance (97), especially consent, discrimination, fair-

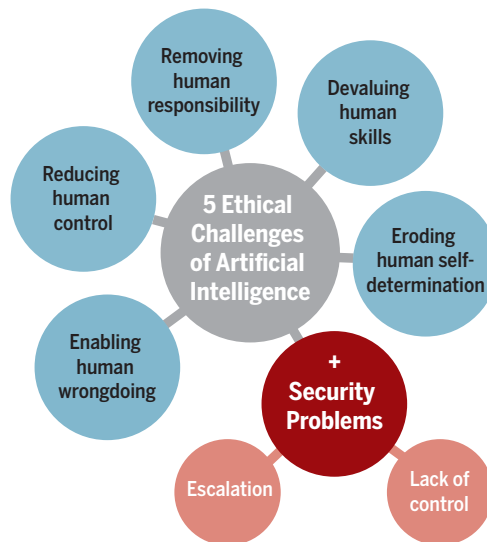


**Fig. 10. Ethical and security risks of robotics and AI developments.**

ness, ownership, privacy, surveillance, and trust (98). In terms of ethics, robotics and AI pose five increasingly pressing topics (Fig. 10).

First, excessive reliance on robotics and AI may lead to the delegation of sensitive tasks to autonomous systems that should remain at least partly subject to human supervision, either “in the loop” for monitoring purposes or “post-loop” for redressing. Thus, it is problematic that the European Union (EU) General Data Protection Regulation does not include an explicit right to an explanation when decisions affecting people are reached “solely” algorithmically (99).

Second, robotics and AI may de-responsibilize people whenever an autonomous system could be blamed for a failure. A recent EU proposal to treat forms of AI as “electronic persons” would only exacerbate this problem. Instead, new forms of distributed responsibility need to be developed, learning from the legal analysis of strict liability (100).

Third, unemployment is an ethical problem, not just an economic one. Robotics and AI could change the workforce structure, cause a shift in the skills base, and potentially facilitate a complete de-skilling of the work force even in safety-critical contexts; however, this would be imprudent. Radiologists need to keep studying images for the same reason pilots need to keep landing airplanes so that they still can even if the AI cannot, or if the AI gets it wrong. According to a recent report, AI could displace between 400 and 800 million jobs. Fairness dictates sharing the economic benefits of this huge and rapid transformation,

thus lowering inequality, whereas social solidarity should ensure that AI's costs are shouldered by future generations, too, because they will profit enormously from it.

Fourth, AI may erode human freedom, because it may lead to unplanned and unwelcome changes in human behaviors to accommodate the routines that make automation work and people's lives easier. AI's predictive power and relentless nudging, even if unintentional, should foster and not undermine human dignity and self-determination.

Finally, there is straightforward misuse. Strictly speaking, this is not a problem with AI's smart agency, but with the unethical application of AI by those who control it. The issues under this heading refer to “the human use of human beings,” to cite the title of Wiener's far-sighted book (101). Examples range from scanning citizens' faces in illiberal regimes to discriminating among applicants for a job or punishing law offenders unfairly.

In this case, Kant provides the right antidote: AI should be designed and used to treat every human being always as an end and never only as a means.

In terms of security, AI can improve security by increasing systems' resilience (enduring attacks) and robustness (averting attacks) and combining both with counterthreat strategies. Thanks to its autonomy, fast-paced threat analysis, and decision-making capabilities, AI can enable systems verification and patching and counter incoming threats by exploiting the vulnerabilities of antagonist systems. However, two challenges may hamper AI's potential for security. One is escalation: Robotics and AI can refine strategies and launch more aggressive counteroperations. This may snowball into an intensification of attacks and responses, which, in turn, may threaten key infrastructures of our societies (102). The solution may be to use AI to strengthen deterring strategies and discourage opponents before they attack, rather than mitigating the consequences of successful attacks afterward. The other challenge is lack of control. Pervasive distribution, multiple interactions, and fast-paced execution will make control of AI systems progressively less effective while increasing the risks for unforeseen consequences and errors. Regulations may mitigate the lack of control by ensuring proportionality of responses, the legitimacy of targets, and a higher degree of responsible behavior, but it is crucial to start shaping and enforcing

policies and norms for the use of AI in security as soon as possible while the technology is still nascent.

### DISCUSSION AND CONCLUSIONS

The general field of robotics is quickly evolving, which makes the identification of key grand challenges particularly difficult. In this article, we have focused mainly on underpinning technologies that may have wider impacts across different application domains in the next 5 to 10 years. There are, of course, many domain-specific robotics challenges that need to be addressed, such as those related to space and marine sciences, digital architecture and construction, humanoids, human assistance, rehabilitation, agrifood, infrastructure, and robots designed for emergency response and disaster relief. However, truly addressing these grand challenges requires scientists and researchers from many disciplines to form ongoing collaborations.

When Scott, the legendary polar explorer, died of exhaustion in the Antarctic, he and his team were within sight of their supply tent. Their ponies had died early in the expedition, and his team had to pull their heavy sleds across the frozen landscape acting as human pack animals. What did they carry that was so important it could not be left behind? Buried under the canvas of their sled were rocks containing fossils of leaves, showing that the barren Antarctic continent had at one time been much warmer and had once had forests. Although Scott and his team lost the race to be first to the South Pole, they made one of the great discoveries of Antarctic exploration. What is notable, besides their determination to bring back the fossils, is that they recognized their significance. Such is the spirit we should bear in mind while pursuing these challenges: The ability to recognize discoveries as we progress is as important as conquering these academic missions.

Addressing these grand challenges also requires a major cultural shift. For example, to meet the challenges of bioinspired and biohybrid robot design, engineers, physicists, applied mathematicians, and biologists must form mutually beneficial interdisciplinary collaborations. To extract principles, understand a biological design, and use biological material effectively, it is first necessary to understand that evolution is not engineering. Evolution works on the principle of sufficiency, not optimality, and organisms are severely constrained by their complex histories, development, and multifunctionality. Therefore, engineered mim-

icry in the absence of guiding principles is discouraged. Breathtaking progress is being made on relevant grand challenges in organismal biology, but much remains unknown given the complexity and constraints. Biologists should not only share these advances but also reveal how direct, comparative, and phylogenetic experiments using biodiversity are used to extract a principle. Particularly important for robotics is the development of a synergy where biological principles inspire novel robot or component design, and these robots (or their parts) are then used by biologists as physical models to further test hypotheses of biological structure-function relationships. This realization in biology—that bioinspired robots are invaluable physical models for pursuing further advances in understanding structure-function, ecology, neuroethology, etc.—is also found in physics: The term “robophysics” first emerged (103) for the use of robots as tools to study concepts in the terramechanics of locomotion, particularly on complex granular media.

If bioinspired and biohybrid robots are to move beyond proofs of concept and one-off laboratory demonstrations into real-world applications, then we must match robot capability with need while not compromising curiosity-based research. Bioinspired and biohybrid robots will be uniquely situated for exploration, environmental monitoring, biodiversity conservation, structural inspection and maintenance, security, social assistance and home service, and a wide range of biomedical applications. Market estimates forecast that bioinspired designs could account for a substantial part of U.S. and global gross domestic product (GDP) and result in millions of future jobs. If we can meet the grand challenge of developing bioinspired and biohybrid robots—and if we can establish a strong partnership between basic research in bioinspired engineering and industry—then the impact will be felt far beyond consumers and affect many areas of engineering, science, and social science as our human and natural technologies converge.

In this article, we have also highlighted the importance of robot ethics and security. Given the rapid pace of development in robotics and general public concerns, it is timely that this challenge is addressed in synchrony by basic science researchers, engineers, legal professionals and policy makers. Initiatives like AI4People, the IEEE (Institute of Electrical and Electronics Engineers) Global Initiative on Ethics of Autonomous and Intelligent Systems, and the Partnership on Artificial In-

telligence to Benefit People and Society are working on the ethics of robotics and AI.

As with any technological innovation, the advantages of robotics and AI enable us to not do (or do less of) things that we do not want to do, like driving a car, and to do (either at all or better) things that we want to do, like enjoying a safe and secure life. In both cases, robotics and AI can help us tackle the many concrete evils oppressing humanity and our planet, from environmental disasters to financial crises and from crime, terrorism, and war to famine, poverty, ignorance, inequality, and appalling living standards. Robotics and AI can and will help us manage the increasing complexity of our societies, from megacities to industrial production. Yet, the risk remains that we may misuse or underuse robotics and AI. We should be worried about real human ignorance, not fanciful artificial superintelligence. Churchill once said that “we shape our buildings and afterwards our buildings shape us” (104); this applies to robotics and AI as well. We must design and use robotics and AI ethically and securely and do so now. Humans, not technology, are both problem and solution and shall remain so for any foreseeable future.

### REFERENCES AND NOTES

1. J. Li, B. E.-F. de Ávila, W. Gao, L. Zhang, J. Wang, Micro/nanorobots for biomedicine: Delivery, surgery, sensing, and detoxification. *Sci. Robot.* **2**, eaam6431 (2017).
2. S. J. Keating, J. C. Leland, L. Cai, N. Oxman, Toward site-specific and self-sufficient robotic fabrication on architectural scales. *Sci. Robot.* **2**, eaam8986 (2017).
3. N. Jacobstein, J. Bellingham, G.-Z. Yang, Robotics for space and marine sciences. *Sci. Robot.* **2**, eaan5594 (2017).
4. C. Laschi, B. Mazzolai, M. Cianchetti, Soft robotics: Technologies and systems pushing the boundaries of robot abilities. *Sci. Robot.* **1**, eaah3690 (2016).
5. E. W. Hawkes, L. H. Blumenschein, J. D. Greer, A. M. Okamura, A soft robot that navigates its environment through growth. *Sci. Robot.* **2**, eaan3028 (2017).
6. S. Terryn, J. Brancart, D. Lefebvre, G. Van Assche, B. Vanderborght, Self-healing soft pneumatic robots. *Sci. Robot.* **2**, eaan4268 (2017).
7. D. W. Haldane, M. M. Plecnik, J. K. Yim, R. S. Fearing, Robotic vertical jumping agility via series-elastic power modulation. *Sci. Robot.* **1**, eaag2048 (2016).
8. A. Ramezani, S.-J. Chung, S. Hutchinson, A biomimetic robotic platform to study flight specializations of bats. *Sci. Robot.* **2**, eaal2505 (2017).
9. Y. Wang, X. Yang, Y. Chen, D. K. Wainwright, C. P. Kenaley, Z. Gong, Z. Liu, H. Liu, J. Guan, T. Wang, J. C. Weaver, R. J. Wood, L. Wen, A biorobotic adhesive disc for underwater hitchhiking inspired by the remora suckerfish. *Sci. Robot.* **2**, eaan8072 (2017).
10. L. Zhang, R. Merrifield, A. Deguet, G.-Z. Yang, Powering the world's robots—10 years of ROS. *Sci. Robot.* **2**, eaar1868 (2017).
11. T. Mirfakhrai, J. D. W. Madden, R. H. Baughman, Polymer artificial muscles. *Mater. Today* **10**, 30–38 (2007).

12. C. Majidi, Soft robotics: A perspective—Current trends and prospects for the future. *Soft Robot.* **1**, 5–11 (2013).
13. N. W. Bartlett, M. T. Tolley, J. T. B. Overvelde, J. C. Weaver, B. Mosadegh, K. Bertoldi, G. M. Whitesides, R. J. Wood, A 3D-printed, functionally graded soft robot powered by combustion. *Science* **349**, 161–165 (2015).
14. G.-Z. Yang, P. Fischer, B. Nelson, New materials for next-generation robots. *Sci. Robot.* **2**, eaap9294 (2017).
15. S. Yao, X. Liu, S. V. Georgakopoulos, M. M. Tentzeris, A novel tunable origami accordion antenna, *Proceedings of the 2014 IEEE Antennas and Propagation Society International Symposium (APSURS)*, Memphis, TN, 6 to 11 July 2014 (IEEE, 2014).
16. J. L. Silverberg, A. A. Evans, L. McLeod, R. C. Hayward, T. Hull, C. D. Santangelo, I. Cohen, Using origami design principles to fold reprogrammable mechanical metamaterials. *Science* **345**, 647–650 (2014).
17. P. Polygerinos, N. Correll, S. A. Morin, B. Mosadegh, C. D. Onal, K. Petersen, M. Cianchetti, M. T. Tolley, R. F. Shepherd, Soft robotics: Review of fluid-driven intrinsically soft devices; manufacturing, sensing, control, and applications in human-robot interaction. *Adv. Eng. Mater.* **19**, 1700016 (2017).
18. H.-W. Huang, M. S. Sakar, A. J. Petruska, S. Pané, B. J. Nelson, Soft micromachines with programmable motility and morphology. *Nat. Commun.* **7**, 12263 (2016).
19. J. Rossiter, J. Winfield, I. Ieropoulos, Here today, gone tomorrow: Biodegradable soft robots. *Proc. SPIE* **9798**, 97981S (2016).
20. M. Irimia-Vladu, “Green” electronics: Biodegradable and biocompatible materials and devices for sustainable future. *Chem. Soc. Rev.* **43**, 588–610 (2014).
21. R. Feynman, Infinitesimal machinery. *J. Microelectromech. Syst.* **2**, 4–14 (1993).
22. A. S. Gladman, E. A. Matsumoto, R. G. Nuzzo, L. Mahadevan, J. A. Lewis, Biomimetic 4D printing. *Nat. Mater.* **15**, 413–418 (2016).
23. S. Vogel, *Cats’ Paws and Catapults: Mechanical Worlds of Nature and People* (WW Norton & Company, 1998).
24. R. Pfeifer, M. Lungarella, F. Iida, Self-organization, embodiment, and biologically inspired robotics. *Science* **318**, 1088–1093 (2007).
25. A. J. Ijspeert, Biorobotics: Using robots to emulate and investigate agile locomotion. *Science* **346**, 196–203 (2014).
26. S. Kim, C. Laschi, B. Trimmer, Soft robotics: A bioinspired evolution in robotics. *Trends Biotechnol.* **31**, 287–294 (2013).
27. D. Rus, M. T. Tolley, Design, fabrication and control of soft robots. *Nature* **521**, 467–475 (2015).
28. L. Ricotti, B. Trimmer, A. W. Feinberg, R. Raman, K. K. Parker, R. Bashir, M. Sitti, S. Martel, P. Dario, A. Mencias, Biohybrid actuators for robotics: A review of devices actuated by living cells. *Sci. Robot.* **2**, eaaq0495 (2017).
29. Y. Mengüç, N. Correll, R. Kramer, J. Paik, Will robots be bodies with brains or brains with bodies? *Sci. Robot.* **2**, eaar4527 (2017).
30. R. Raman, R. Bashir, Biomimicry, biofabrication, and biohybrid systems: The emergence and evolution of biological design. *Adv. Healthc. Mater.* **6**, 1700496 (2017).
31. S. Kim, M. Spenko, S. Trujillo, B. Heyneman, V. Mattoli, M. R. Cutkosky, Whole body adhesion: Hierarchical, directional and distributed control of adhesive forces for a climbing robot, *2007 IEEE International Conference on Robotics and Automation*, Rome, Italy, 10 to 14 April 2007 (IEEE, 2007).
32. M. A. McEvoy, N. Correll, Materials that couple sensing, actuation, computation, and communication. *Science* **347**, 1261689 (2015).
33. S. E. Naleway, M. M. Porter, J. McKittrick, M. A. Meyers, Structural design elements in biological materials: Application to bioinspiration. *Adv. Mater.* **27**, 5455–5476 (2015).
34. M. H. Dickinson, C. T. Farley, R. J. Full, M. A. R. Koehl, R. Kram, S. Lehman, How animals move: An integrative view. *Science* **288**, 100–106 (2000).
35. D. L. Taylor, Self-healing hydrogels. *Adv. Mater.* **28**, 9060–9093 (2016).
36. K. H. Low, T. Hu, S. Mohammed, J. Tangorra, M. Kovac, Perspectives on biologically inspired hybrid and multi-modal locomotion. *Bioinspir. Biomim.* **10**, 020301 (2015).
37. F. J. Valero-Cuevas, M. Santello, On neuromechanical approaches for the study of biological and robotic grasp and manipulation. *J. Neuroeng. Rehabil.* **14**, 101 (2017).
38. C. Li, T. Zhang, D. I. Goldman, A terradynamics of legged locomotion on granular media. *Science* **339**, 1408–1412 (2013).
39. R. J. Full, D. E. Koditschek, Templates and anchors: Neuromechanical hypotheses of legged locomotion on land. *J. Exp. Biol.* **202**, 3325–3332 (1999).
40. P. Holmes, R. J. Full, D. Koditschek, J. Guckenheimer, The dynamics of legged locomotion: Models, analyses, and challenges. *SIAM Rev.* **48**, 207–304 (2006).
41. J. W. Choi, D. Aurbach, Promise and reality of post-lithium-ion batteries with high energy densities. *Nat. Rev. Mater.* **1**, 16013 (2016).
42. X. Zhu, Z. Guo, Z. Hou, Solar-powered airplanes: A historical perspective and future challenges. *Prog. Aerospace Sci.* **71**, 36–53 (2014).
43. A. Manthiram, X. Yu, S. Wang, Lithium battery chemistries enabled by solid-state electrolytes. *Nat. Rev. Mater.* **2**, 16103 (2017).
44. M. Park, J. Ryu, W. Wang, J. Cho, Material design and engineering of next-generation flow-battery technologies. *Nat. Rev. Mater.* **2**, 16080 (2016).
45. V. A. Tucker, The energetic cost of moving about: Walking and running are extremely inefficient forms of locomotion. Much greater efficiency is achieved by birds, fish—and bicyclists. *Am. Sci.* **63**, 413–419 (1975).
46. M. Wehner, R. L. Truby, D. J. Fitzgerald, B. Mosadegh, G. M. Whitesides, J. A. Lewis, R. J. Wood, An integrated design and fabrication strategy for entirely soft, autonomous robots. *Nature* **536**, 451–455 (2016).
47. M. Boyvat, J.-S. Koh, R. J. Wood, Addressable wireless actuation for multijoint folding robots and devices. *Sci. Robot.* **2**, eaan1544 (2017).
48. Z. L. Wang, Triboelectric nanogenerators as new energy technology for self-powered systems and as active mechanical and chemical sensors. *ACS Nano* **7**, 9533–9557 (2013).
49. Z. L. Wang, L. Lin, J. Chen, S. Niu, Y. Zi, *Triboelectric Nanogenerators* (Springer, 2016).
50. J. K. Parrish, L. Edelstein-Keshet, Complexity, pattern, and evolutionary trade-offs in animal aggregation. *Science* **284**, 99–101 (1999).
51. [https://en.wikipedia.org/wiki/Hyper-converged\\_infrastructure](https://en.wikipedia.org/wiki/Hyper-converged_infrastructure).
52. J. P. Desai, J. P. Ostrowski, V. Kumar, Modeling and control of formations of nonholonomic mobile robots. *IEEE Trans. Rob. Autom.* **17**, 905–908 (2001).
53. A. Jadbabaie, J. Lin, A. S. Morse, Coordination of groups of mobile autonomous agents using nearest neighbor rules. *IEEE Trans. Automat. Contr.* **48**, 988–1001 (2003).
54. S. Berman, Q. Lindsey, M. S. Sakar, V. Kumar, S. C. Pratt, Experimental study and modeling of group retrieval in ants as an approach to collective transport in swarm robotic systems. *Proc. IEEE* **99**, 1470–1481 (2011).
55. A. Bauer, D. Wollherr, M. Buss, Human–robot collaboration: A survey. *Int. J. Human. Robot.* **5**, 47–66 (2008).
56. A. Prorok, M. A. Hsieh, V. Kumar, The impact of diversity on optimal control policies for heterogeneous robot swarms. *IEEE Trans. Robot.* **33**, 346–358 (2017).
57. J. Rodin, *The Resilience Dividend: Being Strong in a World Where Things Go Wrong* (Public Affairs, 2014).
58. T. Kozai, G. Niu, M. Takagaki, *Plant Factory: An Indoor Vertical Farming System for Efficient Quality Food Production* (Academic Press, 2015).
59. Q. Zhu, T. Başar, Robust and resilient control design for cyber-physical systems with an application to power systems, *2011 50th IEEE Conference on Decision and Control and European Control Conference (CDC-ECC)*, Orlando, FL, 12 to 15 December 2011 (IEEE, 2012).
60. C. Cadena, L. Carlone, H. Carrillo, Y. Latif, D. Scaramuzza, J. Neira, I. Reid, J. J. Leonard, Past, present, and future of simultaneous localization and mapping: Toward the robust-perception age. *IEEE Trans. Robot.* **32**, 1309–1332 (2016).
61. A. Krizhevsky, I. Sutskever, G. Hinton, Imagenet classification with deep convolutional neural networks, in *Advances in Neural Information Processing Systems 25*, P. Bartlett, K. Q. Weinberger, C. J. C. Burges, L. Bottou, F. C. N. Pereira, Eds. (Neural Information Processing Systems, 2012), pp. 1097–1105.
62. K. L. Stachenfeld, M. M. Botvinick, S. J. Gershman, The hippocampus as a predictive map. *Nat. Neurosci.* **20**, 1643–1653 (2017).
63. J. Bongard, V. Zykov, H. Lipson, Resilient machines through continuous self-modeling. *Science* **314**, 1118–1121 (2006).
64. D. Silver, J. Schrittwieser, K. Simonyan, I. Antonoglou, A. Huang, A. Guez, T. Hubert, B. Baker, M. Lai, A. Bolton, Y. Chen, T. Lillicrap, F. Hui, L. Sifre, G. van den Driessche, T. Graepel, D. Hassabis, Mastering the game of Go without human knowledge. *Nature* **550**, 354–359 (2017).
65. J. Hawkins, S. Ahmad, Y. Cui, A theory of how columns in the neocortex enable learning the structure of the world. *Front. Neural Circuits* **11**, 81 (2017).
66. B. M. Lake, T. D. Ullman, J. B. Tenenbaum, S. J. Gershman, Building machines that learn and think like people. *Behav. Brain Sci.* **40**, e253 (2017).
67. J. P. Donoghue, Connecting cortex to machines: Recent advances in brain interfaces. *Nat. Neurosci.* **5**, 1085–1088 (2002).
68. M. D. Serruya, N. G. Hatsopoulos, L. Paninski, M. R. Fellows, J. P. Donoghue, Brain-machine interface: Instant neural control of a movement signal. *Nature* **416**, 141–142 (2002).
69. M. Velliste, S. Perel, M. C. Spalding, A. S. Whitford, A. B. Schwartz, Cortical control of a prosthetic arm for self-feeding. *Nature* **453**, 1098–1101 (2008).
70. U. Chaudhary, N. Birbaumer, A. Ramos-Murguialday, Brain–computer interfaces for communication and rehabilitation. *Nat. Rev. Neurol.* **12**, 513–525 (2016).
71. J. N. Mak, J. R. Wolpaw, Clinical applications of brain-computer interfaces: Current state and future prospects. *IEEE Rev. Biomed. Eng.* **2**, 187–199 (2009).
72. L. F. Nicolas-Alonso, J. Gomez-Gil, Brain computer interfaces, a review. *Sensors* **12**, 1211–1279 (2012).
73. T. O. Zander, C. Kothe, S. Jatzew, M. Gaertner, Enhancing human-computer interaction with input from active and passive brain-computer interfaces, in *Brain-Computer Interfaces*, D. S. Tan, A. Nijholt, Eds., (Springer, 2010), pp. 181–199.
74. E. Vaadia, N. Birbaumer, Grand challenges of brain computer interfaces in the years to come. *Front. Neurosci.* **3**, 151–154 (2009).
75. S. A. Papert, The summer vision project (1966); <http://hdl.handle.net/1721.1/6125>
76. P. Loncomilla, J. Ruiz-del-Solar, L. Martínez, Object recognition using local invariant features for robotic

- applications: A survey. *Pattern Recogn.* **60**, 499–514 (2016).
77. S. Herath, M. Harandi, F. Porikli, Going deeper into action recognition: A survey. *Image Vis. Comput.* **60**, 4–21 (2017).
  78. H. Admoni, B. Scassellati, Social eye gaze in human-robot interaction: A review. *J. Hum. Robot Interact.* **6**, 25–63 (2017).
  79. G. Sukthankar, C. Geib, H. H. Bui, D. Pynadath, R. P. Goldman, *Plan, Activity, and Intent Recognition: Theory and Practice* (Elsevier, 2014).
  80. S. Rossi, F. Ferland, A. Tapus, User profiling and behavioral adaptation for HRI: A survey. *Pattern Recognit. Lett.* **99**, 3–12 (2017).
  81. B. Hayes, B. Scassellati, Autonomously constructing hierarchical task networks for planning and human-robot collaboration, *2016 IEEE International Conference on Robotics and Automation (ICRA)*, Stockholm, Sweden, 16 to 21 May 2016 (IEEE, 2016).
  82. C. A. Corneanu, M. O. Simón, J. F. Cohn, S. E. Guerrero, Survey on RGB, 3D, thermal, and multimodal approaches for facial expression recognition: History, trends, and affect-related applications. *IEEE Trans. Pattern Anal. Mach. Intell.* **38**, 1548–1568 (2016).
  83. B. Scassellati, Theory of mind for a humanoid robot. *Auton. Robot.* **12**, 13–24 (2002).
  84. M. I. Jordan, T. M. Mitchell, Machine learning: Trends, perspectives, and prospects. *Science* **349**, 255–260 (2015).
  85. G.-Z. Yang, J. Cambias, K. Cleary, E. Daimler, J. Drake, P. E. Dupont, N. Hata, P. Kazanzides, S. Martel, R. V. Patel, V. J. Santos, R. H. Taylor, Medical robotics—Regulatory, ethical, and legal considerations for increasing levels of autonomy. *Sci. Robot.* **2**, eaam8638 (2017).
  86. C. Bergeles, G.-Z. Yang, From passive tool holders to microsurgions: Safer, smaller, smarter surgical robots. *IEEE Trans. Biomed. Eng.* **61**, 1565–1576 (2014).
  87. V. Vitiello, S.-L. Lee, T. P. Cundy, G.-Z. Yang, Emerging robotic platforms for minimally invasive surgery. *IEEE Rev. Biomed. Eng.* **6**, 111–126 (2013).
  88. A. Shademan, R. S. Decker, J. D. Opfermann, S. Leonard, A. Krieger, P. C. W. Kim, Supervised autonomous robotic soft tissue surgery. *Sci. Transl. Med.* **8**, 337ra64 (2016).
  89. K. P. Sajadi, H. B. Goldman, Robotic pelvic organ prolapse surgery. *Nat. Rev. Urol.* **12**, 216–224 (2015).
  90. C. J. Payne, I. Wamala, D. Bautista-Salinas, M. Saeed, D. Van Story, T. Thalhoffer, M. A. Horvath, C. Abah, P. J. del Nido, C. J. Walsh, N. V. Vasilyev, Soft robotic ventricular assist device with septal bracing for therapy of heart failure. *Sci. Robot.* **2**, eaan6736 (2017).
  91. V. Iacovacci, L. Ricotti, P. Dario, A. Menciasci, Design and development of a mechatronic system for noninvasive refilling of implantable artificial pancreas. *IEEE ASME Trans. Mechatron.* **20**, 1160–1169 (2015).
  92. G.-Z. Yang, *Implantable Sensors and Systems—From Theory to Practice* (Springer, 2018).
  93. D. D. Damian, K. Price, S. Arabagi, I. Berra, Z. Machaidze, S. Manjila, S. Shimada, A. Fobozzo, G. Arnal, D. Van Story, J. D. Goldsmith, A. T. Agoston, C. Kim, R. Jennings, P. D. Ngo, M. Manfredi, P. E. Dupont, In vivo tissue regeneration with robotic implants. *Sci. Robot.* **3**, eaaq0018 (2018).
  94. B. J. Nelson, I. K. Kaliakatsos, J. J. Abbott, Microrobots for minimally invasive medicine. *Annu. Rev. Biomed. Eng.* **12**, 55–85 (2010).
  95. A. Servant, F. Qiu, M. Mazza, K. Kostarelos, B. J. Nelson, Controlled in vivo swimming of a swarm of bacteria-like microrobotic flagella. *Adv. Mater.* **27**, 2981–2988 (2015).
  96. O. Felfoul, M. Mohammadi, S. Taherkhani, D. de Lanauze, Y. Zhong Xu, D. Loghini, S. Essa, S. Jancik, D. Houle, M. Lafleur, L. Gaboury, M. Tabrizian, N. Kaou, M. Atkin, T. Vuong, G. Batist, N. Beauchemin, D. Radzioch, S. Martel, Magneto-aerotactic bacteria deliver drug-containing nanoliposomes to tumour hypoxic regions. *Nat. Nanotechnol.* **11**, 941–947 (2016).
  97. C. Cath, S. Wachter, B. Mittelstadt, M. Taddeo, L. Floridi, Artificial Intelligence and the ‘Good Society’: The US, EU, and UK approach. *Sci. Eng. Ethics* **2017**, 1–24 (2017).
  98. L. Floridi, M. Taddeo, What is data ethics? *Philos. Trans. A Math. Phys. Eng. Sci.* **374**, 20160360 (2016).
  99. S. Wachter, B. Mittelstadt, L. Floridi, Transparent, explainable, and accountable AI for robotics. *Sci. Robot.* **2**, eaan6080 (2017).
  100. L. Floridi, Distributed morality in an information society. *Sci. Eng. Ethics* **19**, 727–743 (2013).
  101. N. Wiener, *The Human Use of Human Beings* (Houghton Mifflin, 1954).
  102. M. Taddeo, The limits of deterrence theory in cyberspace. *Philos. Technol.* **2017**, 1–17 (2017).
  103. J. Aguilar, T. Zhang, F. Qian, M. Kingsbury, B. McInroe, N. Mazouchova, C. Li, R. Maladen, C. Gong, M. Travers, R. L. Hatton, A review on locomotion robotics: The study of movement at the intersection of robotics, soft matter and dynamical systems. *Rep. Prog. Phys.* **79**, 110001 (2016).
  104. House of Commons Rebuilding, <http://hansard.millbanksystems.com/commons/1943/oct/28/house-of-commons-rebuilding>.
  105. S.-J. Park, M. Gazzola, K. S. Park, S. Park, V. Di Santo, E. L. Blevins, J. U. Lind, P. H. Campbell, S. Dauth, A. K. Capulli, F. S. Pasqualini, S. Ahn, A. Cho, H. Yuan, B. M. Maoz, R. Vijaykumar, J.-W. Choi, K. Deisseroth, G. V. Lauder, L. Mahadevan, K. K. Parker, Phototactic guidance of a tissue-engineered soft-robotic ray. *Science* **353**, 158–162 (2016).
  106. H. Singh, T. Maksym, J. Wilkinson, G. Williams, Inexpensive, small AUVs for studying ice-covered polar environments. *Sci. Robot.* **2**, eaan4809 (2017).
- Acknowledgments:** We thank all those who have responded to our online survey. In particular, we thank H. Choset, P. Dario, P. Fiorini, T. Fukuda, D. Leff, and S. Russell, who provided detailed comments, review, and original materials for this article.
- 10.1126/scirobotics.aar7650
- Citation:** G.-Z. Yang, J. Bellingham, P. E. Dupont, P. Fischer, L. Floridi, R. Full, N. Jacobstein, V. Kumar, M. McNutt, R. Merrifield, B. J. Nelson, B. Scassellati, M. Taddeo, R. Taylor, M. Veloso, Z. L. Wang, R. Wood, The grand challenges of *Science Robotics*. *Sci. Robot.* **3**, eaar7650 (2018).

## SPACE ROBOTS

# Review on space robotics: Toward top-level science through space exploration

Yang Gao<sup>1\*</sup> and Steve Chien<sup>2</sup>

Robotics and autonomous systems have been instrumental to space exploration by enabling scientific breakthroughs and by fulfilling human curiosity and ambition to conquer new worlds. We provide an overview of space robotics as a rapidly emerging field, covering basic concepts, definitions, historical context, and evolution. We further present a technical road map of the field for the coming decades, taking into account major challenges and priorities recognized by the international space community. Space robotics represents several key enablers to a wide range of future robotic and crewed space missions as well as opportunities for knowledge and technology transfer to many terrestrial sectors. In the greater humanitarian context, space robotics inspires both current and future generations to exploration and critical study of science, technology, engineering, and mathematics.

## INTRODUCTION

Space exploration of our solar system and distant galaxies in the furthest reaches of the universe is important to top-level science and to answer many fundamental scientific questions, including the formation of the universe, the origin of Earth, the evolution of life, and the existence of life beyond Earth. Space robotics plays a critical role in current and future space exploration missions and enables mission-defined machines that are capable of surviving in the space environment and performing exploration, assembly, construction, maintenance, or service tasks. Modern space robotics represents a multidisciplinary emerging field that builds on and contributes to space engineering, terrestrial robotics, and computer science, as well as related specialties such as materials and mechanisms (1).

Robotics improves humanity's ability to explore and to operate by providing access beyond human limitations in the harsh environment of space and supporting operations that extend astronauts' capabilities. Autonomous systems are capable of reducing the cognitive load on humans given the abundance of information that has to be reasoned in a timely fashion and are critical for improving human and system safety. Robotics can also enable the deployment and operation of multiple assets without the same order-of-magnitude increase in ground support. Given the potential reduction in cost and the risk of spaceflight, both crewed and robotic, space robotics and autonomous systems are deemed relevant across all mission phases, such as development, flight system production, launch, and operation.

Space robotics covers all types of robotics for the exploration of a planet surface, as well as those used in orbit around the bodies, and the sensors needed by the platform for navigation or control. Orbital robots can be envisaged for repairing satellites, assembling large space telescopes, capturing and returning asteroids, deploying assets for scientific investigations, etc. Planetary robots play a key role in surveying, observation, extraction, and close examination of extraterrestrial surfaces (including natural phenomena, terrain composition, and resources); constructing infrastructure on a planetary surface for subsequent human arrival; mining planetary resources; etc.

Two attributes are often deemed essential for a spacecraft to be classified as a space robot, namely, locomotion and autonomy (2). Depending

on its application (either orbital or planetary), a space robot is designed to have locomotion (or mobility) to manipulate, grip, rove, drill, and/or sample. Driven similarly by the nature of the mission and distance from Earth, the robot is expected to have varying levels of autonomy, ranging from teleoperation by a human to fully autonomous operation by the robots themselves (3, 41). Depending on the level of autonomy, a space robot can act as (i) an agent (or human proxy) in space to perform various tasks using teleoperation up to semi-autonomous operation; (ii) an assistant that can help human astronauts perform tasks quickly and safely, with higher quality and cost efficiency using semi-autonomous to fully autonomous operation; or (iii) an explorer that is capable of exploring unknown territories in space using fully autonomous operation (4).

Here, we survey past, current, and planned robotic spacecraft missions as well as describe some developmental work targeting future mission concepts. Because of the breadth and depth of the field, we acknowledge that this cannot be a comprehensive technical survey; it is rather intended to provide the reader with the flavor of this diverse and rapidly evolving field. We acknowledge previous surveys by Yoshida (5) in 2009 and Flores-Abad *et al.* (6) in 2014 that focus on on-orbit robotic servicing. In addition, for a more technically detailed coverage of space robotics, we refer the reader to (7, 8).

## HISTORY AND EVOLUTION OF SPACE ROBOTICS

### Past and current space exploration using robots

Outer space has provided real, new exploration frontiers for mankind since the 1950s. With the capability and the irresistible attraction to go beyond our planet Earth, minimizing the impact of mankind on other extraterrestrial bodies (be it a planet, a moon, a comet, or an asteroid) is paramount. The onset of space exploration in the late 1950s to early 1960s focused on sending humans into Earth's orbit and to the Moon as a result of the space race between the Soviet Union and the United States. In parallel to the expensive development of crewed space programs, the use of cheaper robotic proxies was critical to understand the space environment where the astronauts would be operating and to further explore our solar system. Across the existing robotic missions, a range of mobility or locomotion systems has played a substantial role, including the surface rovers, robotic arms or manipulators, subsurface samplers, and drills.

For example, the first genuine robotic locomotion system successfully operated on an extraterrestrial body was a scoop (i.e., a manipulation

<sup>1</sup>Surrey Technology for Autonomous systems and Robotics (STAR) Lab, Surrey Space Centre, University of Surrey, Guildford GU2 7XH, UK. <sup>2</sup>Jet Propulsion Laboratory, California Institute of Technology, Pasadena, CA 91109-8099, USA.

\*Corresponding author. Email: yang.gao@surrey.ac.uk

cum sampling device) onboard the Surveyor 3 lander launched in 1967 to the Moon. After that, Luna 16 succeeded with the first planetary robotic arm-mounted drill in 1970, and Luna 17 succeeded with the first planetary rover called Lunokhod 1 in 1970. These “firsts” led to incredible mission successes and science discoveries as a result of unabated and relentless launch attempts during the space race between the superpowers (4).

Table 1 summarizes the missions and robots successfully flown on Earth’s orbit, the Moon, Mars, and small bodies as of 2017. Within the orbital missions, robotic arms have been the major mechanism for extended mobility. For the planetary case, most existing missions have used either wheeled rovers or stationary landers but equipped with a robotic arm, a drill, or a sampler to achieve mobility. Many of the existing missions, particularly for planetary exploration, have achieved remarkable science; for example, much of what we know

about the Moon and Mars has been the direct result of robotic in situ exploration.

National Aeronautics and Space Administration (NASA) has been at the frontier of Mars science through a series of successful planetary rover missions, for example, Mars Pathfinder (MPF), Mars exploration rovers (MERs), and Mars Science Laboratory (MSL) as introduced in Table 2. Instrumentation carried by the NASA Mars rovers has been substantially increasing with time. As a reference point, the MPF rover Sojourner was a relatively small, limited-lifetime mobile robot, yet its key discoveries in geology (i.e., likelihood of previous water on Mars, magnetic properties of Martian dust, and current Mars climate) rewrote our understanding of Mars (9). The two identical MERs were much larger and hence could carry a much more capable science payload, including enhanced remote sensing, and a more advanced robotic arm carrying instruments for close-in/surface measurement including the

**Table 1. Successfully flown robots on Earth’s orbit, the Moon, Mars, and small bodies as of 2016.**

Launch year	Mission name	Country	Target	Rover	Arm	Sampler	Drill
1967	Surveyor 3	United States	Moon			x	
1970/1972/1976	Luna 16/20/24	Soviet Union	Moon		x	x	x
1970/1973	Luna 17/21	Soviet Union	Moon	x			
1975	Viking	United States	Mars		x	x	
1981/2001/2008	Canadarm1/2/Dextre	Canada	ISS		x		
1993	Rotex	Germany	Earth’s orbit		x		
1996	MPF	United States	Mars	x			
1997	ETS-VII	Japan	Earth’s orbit		x		
2003	Hayabusa	Japan	Asteroid			x	
2003	MERs	United States	Mars	x	x	x	
2004	ROKVISS	Germany	ISS		x		
2007	Orbital Express	United States	Earth’s orbit		x		
2008	JEMRMS	Japan	ISS		x		
2008	Phoenix	United States	Mars		x	x	
2012	Robonaut	United States	ISS		x		
2011	MSL	United States	Mars	x	x	x	
2013	Chang’E 3	China	Moon	x			
2004 (arrived in 2014)	Rosetta	Europe	Comet		x	x	x
2016	Aolong-1	China	Earth’s orbit		x		

**Table 2. Growing science capabilities of NASA’s Mars robotic missions as exemplified by each generation of Mars rover.**

Mars rover	Mass (kg)	Lifetime (sol)	Distance traveled (km) (as of April 2017)	Maximum traverse speed (cm/s)	Science payload mass (kg)	Science results reported
MPF’s Sojourner	10	83	0.1	0.6	<1	(9)
MER’s Opportunity	185	4500*	>44	1	6	(10–12)
MSL’s Curiosity	899	1667*	>15.98	5	75	(13)

\*Still in operation as of 2017.

Rock Abrasion Tool, the Microscopic Imager, the Alpha Proton X-Ray Spectrometer, and the Mossbauer Spectrometer. The rovers also had significantly more advanced mobility and navigation capabilities that enabled the Opportunity rover to travel more than 44 km in more than 4700 sols (i.e., Martian days) as of 2017. The MER rovers achieved even more impressive scientific progress in the fields of geology, atmospheric science, and much more (10–12). The MSL rover Curiosity is the largest among the three rover missions and is more capable, with the help of next-generation instruments, of studying geology, the atmosphere, environmental conditions, and potential biosignatures. From a robotic perspective, Curiosity has a number of instruments that use the robotic arm to take close-in measurements, namely, the Mars Hand Lens Imager, the Alpha Particle X-ray Spectrometer, and sample acquisition analysis (13).

Another notable project is the Japanese Hayabusa robotic mission that studied and sampled the near-Earth asteroid Itokawa in 2005

and returned these samples to Earth in 2010. The Hayabusa mission received considerable attention with special issues in *Science* on Itokawa (14) and the findings from the returned sample (15).

As an alternate data point, the Rosetta mission of the European Space Agency (ESA) made an extremely bold attempt for a controlled landing on a comet nucleus. The Rosetta lander called Philae (Fig. 1) had a number of remote sensing and in situ instruments for compositional/gas analysis (e.g., Cometary Sampling and Composition and Ptolemy), drilling and sample retrieval (i.e., SD2), and surface measurement (i.e., Surface Electrical Sounding and Acoustic Monitoring Experiment). Unfortunately, the lander bounced, and its subsequently canted resting location prevented application of the arm, sampler, and drill and limited Philae’s measurements and lifetime. Despite these challenges, Philae made possible numerous scientific achievements, including the discovery of organic molecules on the nucleus of 67P/Churyumov-Gerasimenko (16, 17).



Fig. 1. Artistic depiction of Philae lander at landing (courtesy of ESA).

**FUTURE SPACE ROBOTIC MISSIONS**

**Mid-term planned missions**

A list (Table 3) of upcoming robotic missions planned by various international space agencies in the medium term makes evident that what was historically the domain of relatively few nations/organizations now includes a much greater rate of launches and diversity of players. Space-faring nations like China and India are more active in promoting robotic missions, targeting the Moon first as a test-bed. NASA and ESA have their focus on Mars and small bodies and are also advancing space robotics to tackle sample return missions.

**Orbital robotic missions**

A number of on-orbit applications envisaged for the 2025 to 2035 time frame require advanced robotics capabilities.

Table 3. Medium-term space robotic missions in the pipeline.

Launch year	Mission	Country	Target	Rover	Arm	Sampler	Drill
2017	Chang'E 5	China	Moon	x	x	x	x
2018	Chandrayaan 2	India	Moon	x			
2018 (to arrive)	OSIRIS-REx Sample Return	United States	NEA		x	x	
2018	InSight	United States	Mars		x	x	x
2018	Chang'E 4	China	Moon (farside)	x			
2019	SLIM	Japan	Moon	x	x	x	x
2020	Mars 2020	United States	Mars				
2020	ExoMars 2020	Europe	Mars	x		x	x
2020+	Chinese Space Station	China	Earth's orbit		x		
2025	Phobos sample return	Europe and Russia	Phobos		x	x	

Mission operators may range from space administrations to national governments to businesses. The following mission foci are envisaged: space debris removal, rescue, planned orbit raising, inspection and support to deployment, deployment and assembly aid, repair, refueling and orbit maintenance, mission evolution and adaptation, lifetime extension, and re- and deorbiting. The International Space Station (ISS) continues to represent an excellent opportunity for scientific experiments to be conducted in space, amid the unique characteristics, constraints, and pressures that environment brings. China is also actively developing its own space station program that will be gradually established in the next decade, providing a new space platform for robotic solutions. These orbital robotic missions can directly and indirectly support scientific exploration from Earth's orbit.

### Planetary robotic missions

Newly planned planetary missions typically aim to deliver more exciting, ambitious scientific goals, building on the results gained from past

missions to the Moon, Mars, and small bodies. In particular, missions planned by NASA and ESA in the medium term will demonstrate advanced science and robotic technologies compared with past missions.

**NASA's OSIRIS-REx mission.** OSIRIS-REx (Fig. 2) was launched in 2016 and will arrive at the near-Earth carbonaceous asteroid 101955 Benu in 2018. It will map the target for 500 days and then approach and capture a small sample (<2 kg) to return to Earth in 2023. Its Touch-and-Go Sample Acquisition Mechanism (TAGSAM) uses a sampler head on the end of a robotic arm. When the sample head detects impact, it uses a nitrogen system to acquire a sample. TAGSAM can be used up to three times when attempting to acquire a sample. When the spacecraft returns to Earth in 2023, it will use a Sample Return Capsule (Stardust heritage) with reentry heat shield and parachute to land the sample.

**NASA's InSight mission.** InSight (Fig. 3) is a Mars lander that is scheduled for launch and landing on the surface of Mars in 2018.

InSight uses many of the same concepts as the previous Phoenix lander mission but uses different instruments to study the Martian interior. Its Instrument Deployment Arm and Instrument Deployment Camera will deploy two instruments: (i) the Seismic Experiment for Interior Structure (led by Centre national d'études spatiales, the French national space agency), a seismographic instrument used to study the Martian interior and seismic activity, and (ii) the Heat Flow and Physical Properties Probe (led by Deutsche Zentrum für Luft- und Raumfahrt, the German national space agency), a self-burrowing mole that penetrates up to 5 m below the planetary surface to measure heat escaping from the Martian interior (18).

**NASA's Mars 2020.** The United States' next rover to Mars, Mars 2020, shares considerable heritage with the MSL rover but carries entirely new instruments. The mission will use the Skycrane deployment method (Fig. 4), which uses a rocket-powered hovering carrier to lower the rover to the surface of Mars with a tether. However, the delivery method is enhanced with Terrain Relative Navigation to enable the system to avoid hazardous terrain in selecting a location to lower the rover. Another substantial improvement is that the rover will carry a drill that is capable of coring and caching samples for potential future retrieval to return to Earth. The new rover will also have increased autonomy, including (i) an onboard scheduler to better use available time, energy, and data volume (19) and (ii) the ability to autonomously target instruments, such as SUPERCAM, based on scientist-provided criteria, which is an evolution of the AEGIS system currently on MER (20) and MSL (21).



Fig. 2. OSIRIS-REx spacecraft with the TAGSAM robotic sampling arm (courtesy of NASA).

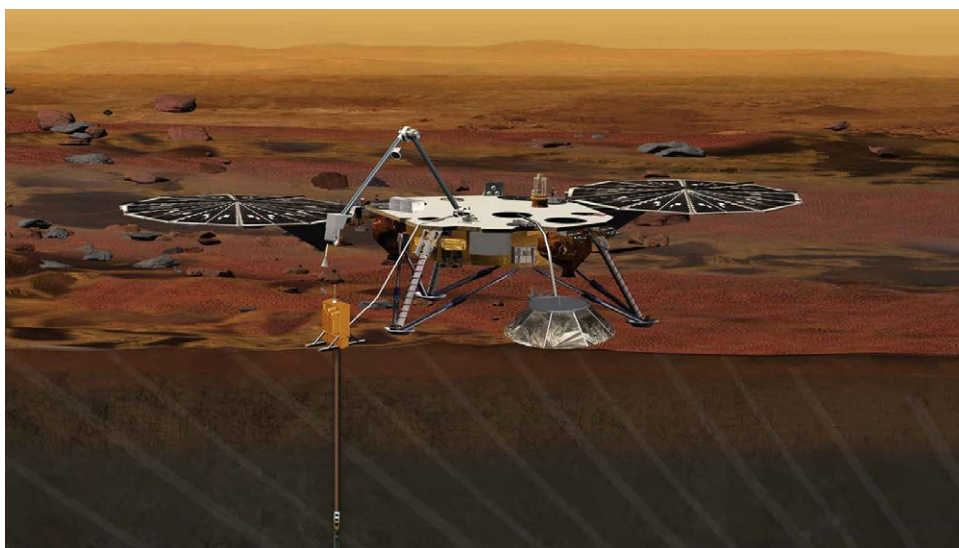


Fig. 3. InSight lander with a robotic instrument deployment arm and a seismic sensor and a heat flow sensor deployed (courtesy of JPL/NASA).



Fig. 4. Mars 2020 rover being deployed by Skycrane (courtesy of JPL/NASA).

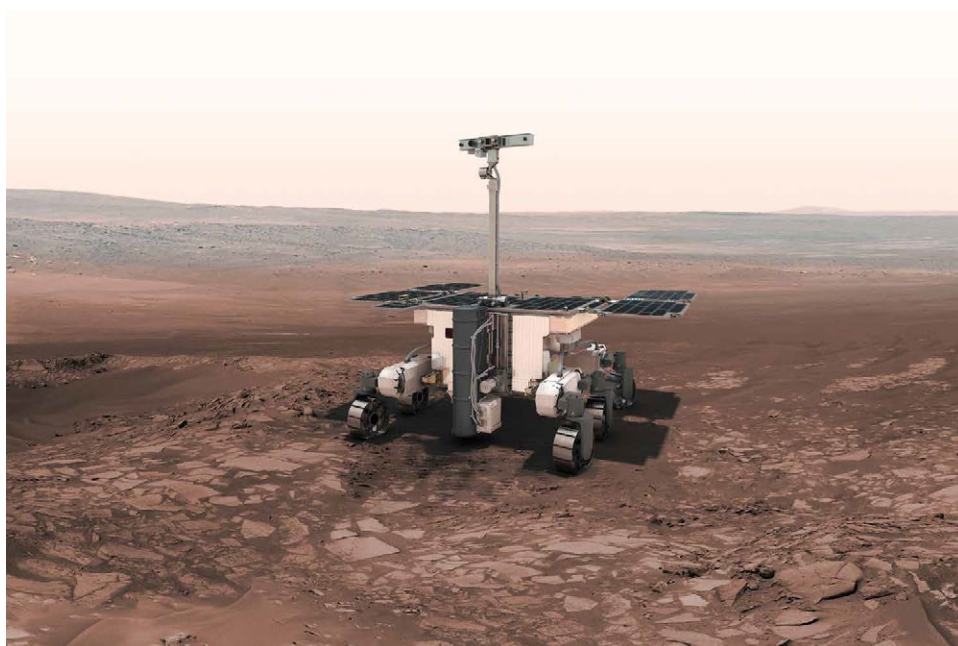


Fig. 5. ExoMars 2020 with rover and deep drill assembly (courtesy of ESA).

ESA's *ExoMars 2020*. Presently, ExoMars (Fig. 5) is the only European-funded mission to make substantial use of robotics in the form of an autonomous rover, an automated exobiology laboratory, and a robotic drilling system; it is due to be launched in 2020 to complement the ExoMars Phase 1 launched in March 2016. Data from the novel suite of instruments onboard the ExoMars rover will help conduct accurate visual and spectral characterization of the surface of Mars, ranging from panoramic (meter) scales and smaller (submillimeter) studies to the molecular identification of organic compounds. The surface study is complemented by electromagnetic and neutron subsurface investigations, which will further help understand the depositional environment (e.g., sedimentary, volcanic, and Aeolian). The unique contribution on

exobiology from ESA's Mars robotic mission constitutes a step forward in the search for traces of past or present signatures of life on Mars.

*ESA-Roscosmos' Phobos sample return.* Another robotic mission in study is PHOOTPRINT (Fig. 6), which aims at the return of surface samples from Phobos (Mars' moon). The mission would make use of robotic elements to sample the surface in low gravity. The mission has been initially assessed in two ESA concurrent design facility (CDF) studies, in one industrial study, and, more recently, under the assumption that it could become a joint mission with Roscosmos (Russian Space Agency), by a further CDF study. The mission would need the relevant technologies by about 2022.

### Long-term mission concepts

To meet the long-term need for exploration and science, a variety of robotic mission concepts, encompassing efforts from both academia and industry, have been proposed and studied by the international space community. Table 4 attempts to summarize these ideas in an organized manner without having an exhaustive list.

### EVOLUTION OF SPACE ROBOTICS

The new generation of space exploration has traveled further into the solar system to tackle more ambitious scientific and exploration goals. Hence, it is anticipated to require more capable space robots with diversified locomotion (Table 5) and increased level of autonomy (Fig. 7). Most existing, successfully flown space robots are considered robotic agents that act as human proxies in space. Future space missions with increasingly challenging goals will require higher levels of autonomy, evolving toward robotic explorers and robotic assistants.

### Diversified mobility and access

Despite successful exploration performed to date, space robotic systems have literally only scratched the surface. To further advance our knowledge of Earth and other destinations, a cornucopia of robotic mobility solutions have been proposed by the space community to explore the vast swathes of unexplored landscapes. The exciting new work underway is intended to provide access to more extreme terrains, caves, and aerial exploration of extraterrestrial surfaces or to tackle challenging tasks in orbit. Table 5 gives an organized view and summary of many proposed ideas to date, examples from which are further described in Table 6 based on a number of NASA-funded studies.

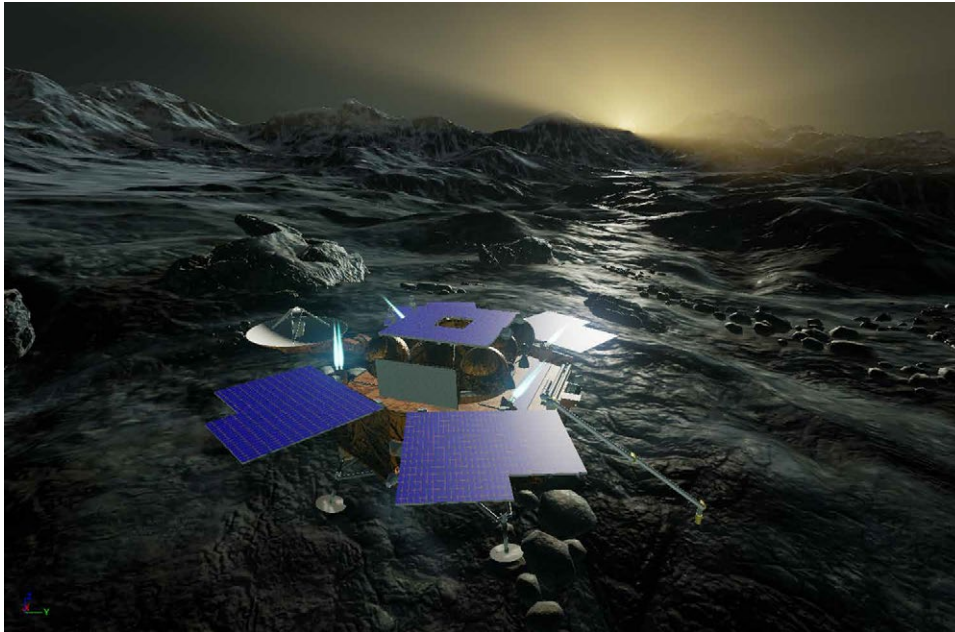


Fig. 6. Phobos sample return mission concept (courtesy of Airbus DS Ltd.).

the ISS. The mobile Robonaut Centaur participated in the human-robot Desert Rats demonstrations (22), which has also included the ATHLETE nonhumanoid limbed robot (23). DLR’s Justin platform (24) is another humanoid example.

**Increased level of autonomy**

Increasing robotic autonomy enables human interaction with or usage of robots at a greater level—as assistants/peers in mixed human-robot teams or goal-oriented fully autonomous explorers. Planning, scheduling, and resource management enable robotic agents to manage their own actions within resource limitations. Robust task execution systems allow autonomous robots to persist in uncertain execution environments. Navigation, mode, and state estimation and situational awareness capabilities, also called integrated vehicle health management and prognostics, enable autonomous robots to track their own state as well as their state within their locale and

immediate environment to operate appropriately. These technologies together enable space robots to have increased survivability, increased ability to achieve their desired missions, and more effective support for science.

Many research and development (R&D) efforts have focused on increasing the efficiency of traditional science measurements using new forms of closed-loop science (25), scientific goal-oriented planning (26), and reconfigurable autonomous onboard control (27). Spacecraft applications already flown on real-world missions include tracking dust devils on Mars (28); retargeting of Mars rover measurements for MER (14) and MSL (15); and monitoring of active volcanism (29), cryosphere (30), and flooding (31) from orbit (32). Future proposed applications include detection and tracking of plumes (33) or surface volatiles at primitive bodies (25).

Advancement in general artificial intelligence techniques (e.g., machine learning and adaptation) is relevant for improving autonomous functions of space robots in many areas. For example, machine learning is often applied to sensing and perception (e.g., machine vision) tasks. It has also been applied to locomotion to improve locomotion strategies, policies, and navigation. System-wide autonomy, planning, scheduling, and resource allocation are also areas of continuing work for machine learning. In human-robot interaction, learning for adaptation to individual users or specific tasks is an area of active work. Furthermore, in multi-agent systems, coordination and control, as well as data assimilation, are viable applications for machine learning.

**TECHNICAL DEMANDS AND CHALLENGES**

The current desire to explore space is as strong as ever. Past space powers have been gradually joined by a flurry of new nations eager to test and demonstrate their technologies and to contribute to an increasing body of knowledge. Commercial endeavors also have eyes on space and actively promote the Moon and Mars as possible destinations for long-term human presence or habitation. Whether future exploration missions be crewed or robotic, space robots are

**Table 4. Long-term space robotic mission concepts (4).** ISRU, in situ resource utilization.

Destination	Proposed mission concepts	Proposed robotic locomotion
Earth’s orbit	Space debris removal, on-orbit servicing, and assembly	Arm, hand/gripper, harpoon
Moon	Sample return, ISRU, exploration of permanently shaded craters, prepare for manned base	Rover, arm, sampler, drill
Mars	Sample return, ISRU, crewed base	Aeroshell, airplane, helicopter, balloon, hopper, swarms
Venus	Exploration	Balloon
Mercury	Exploration	Rover
Asteroid	Sample return, ISRU	Rover, hopper, arm, harpoon
Titan	Exploration	Aeroshell, aerobot, balloon, lake lander, submarine, ship, cooperative robots
Europa/Enceladus	Exploration	Subsurface, submarine, hopper
Gas giants	Exploration	Balloon

A more comprehensive and system-level mobility concept is humanoid robotics, particularly in the context of human exploration space missions and human-robot interaction. Extremely prominent in this area is NASA’s Robonaut program, which has been used onboard

always desired to deliver the robotic avatars and to perform in situ tasks to proxy, assist, or explore through their “eyes,” “ears,” “noses,” and “hands” (4).

In particular, the technical goals of robotics are to extend human’s reach or access into space, to expand our abilities to manipulate assets and resources, to prepare environments for human arrival, to support human crews in their space operations and the assets they leave behind, and to enhance efficiencies of mission operations across the board. Advances in robotic sensing and perception, mobility and manipulation, rendezvous and docking, onboard and ground-based autonomous capabilities, and human-robot integration will help achieve these goals.

NASA’s 2015 technology road map has identified several robotics areas needed by 2035 (34). Similarly, ESA has been developing technology road maps in space robotics through various European Commission-funded projects, such as PERASPERA and SpacePlan2020.

Other space-faring nations like Russia, China, India, and Japan have also announced their individual plans for future missions involving space robotics. Besides differences in mission timetables by different space players, there are numerous technological needs or challenges in robotics that are widely acknowledged by the international space community (see Table 7).

**NEW OPPORTUNITIES**

**Commercial entry into space robotics**

The competitive landscape of space robotics is changing. Traditionally, national space agencies have been the principal entities. More recently, commercial enterprises have declared their intent and are entering the area. Commercial enterprises are investigating and developing the means to exploit resources in the Moon and asteroids. Moon Express, Deep Space Industries, and Planetary Resources are working toward the long-term goal of exploiting key elements in the Moon and beyond. In the near term, exploitation of resources beyond Earth could include water-bearing substances to enable in situ production of rocket fuels (e.g., at the Moon or at Mars for a return vehicle). In the more distant future, the mining of helium-3 from the Moon and elsewhere could provide valuable fuel for fusion reactors. Last, rare metals (such as iron, nickel, cobalt, platinum, and titanium) can be found in many extraterrestrial bodies. As a nearer-term goal, some of these teams are competing for the Google Lunar X prize worth \$30 million for operating a rover on the lunar surface.

**Knowledge/technology transfer to nonspace sectors**

Exploration and Robotics is an area of the space industry that is driven heavily by technology and faces huge challenges to achieve the mission science goals. It is mainly concerned with upstream activities with very little direct downstream benefits to the space industry. However, it does have excellent potential for spin-along activities, allowing the spinning in of terrestrial technologies from other sectors and then spinning out the resulting technology advances. Early findings have revealed that current advances being made in R&D projects on space robotics could have significant knock-on effects in many sectors, including the following:

- (1) Nuclear facility decommissioning: for post-operational clearout, initial decommissioning, interim decommissioning, and final demolition.

**Table 5. Diversified locomotion for future space robots (4).**

Robotic platform	Robotic locomotion
Land surface	- Wheeled rover - Tracked rover - Legged rover - Rolling (e.g., ball or sphere) rover - Hopper - Hovercraft
Airborne	- Quadcopter, helicopter, or ornithopter - Plane or glider - Balloon, montgolfier, aerobot
Subsurface	- Drill (e.g., ice drilling or melting, rotary drilling, percussive drilling, dual reciprocating drilling) - Submarine, submersible
Manipulation	- Arm - Hand, gripper - Sampler (e.g., corer, scoop)
Water surface	- Vertical profiling float - Boat, ship

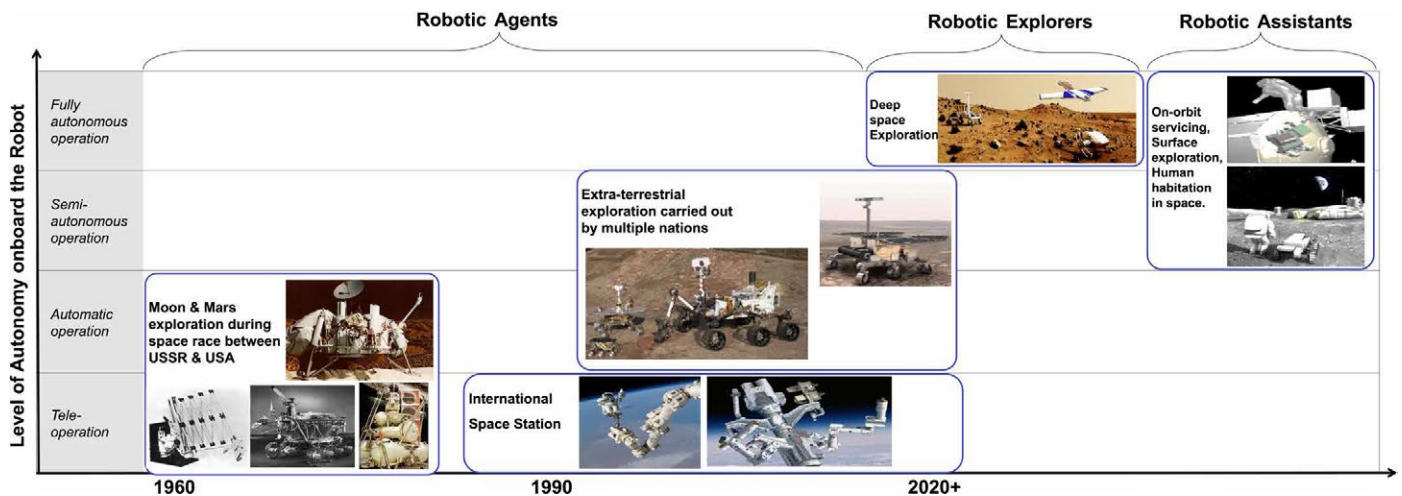


Fig. 7. Evolution of space robots in terms of level of autonomy (7).

Table 6. Examples of novel robotic locomotion concepts for future space exploration (all images courtesy of JPL/NASA).

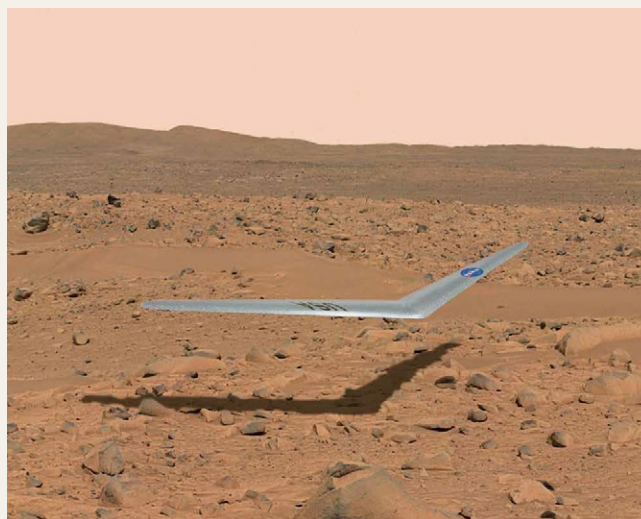


**Mars helicopter (36)**

Mars helicopter is proposed to facilitate surface rover operations. Despite the thin Martian atmosphere (only 0.6% that of Earth), the solar-powered Mars helicopter at 1 kg in mass and with a 1.1-m-long rotor, would scout ahead of a surface rover, providing critical imagery to enable the rover to drive up to three times as far per sol.

**Mars airplane (37)**

Whereas the extremely thin Martian atmosphere makes air vehicles challenging, a Mars airplane is proposed as the Preliminary Research Aerodynamic Design to Land on Mars (or Prandtl-m). A Mars airplane could be released as part of the entry, descent, and landing ballast for a future Mars-landed mission to acquire unique airborne imaging of the Martian surface.



**Titan aerobot (38)**

With a dense methane atmosphere providing strong lift and weak gravity, an aerobot is an ideal vehicle to explore Titan, a moon of Saturn. Titan is of great interest to scientists because of its abundant methane as a possible ingredient for life and its liquid methane lakes on the surface. Aerobots and montgolfiers have been proposed and tested to develop technologies for this ambitious robotic mission.



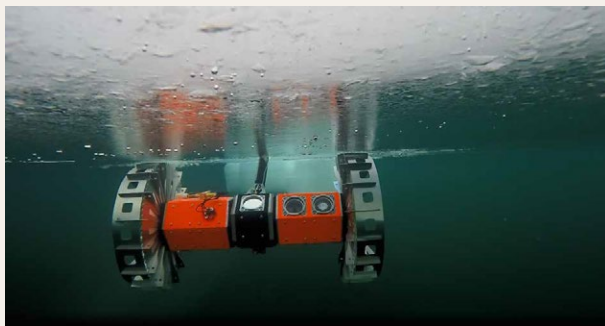
Test flight in the Mojave Desert, CA, USA

(Continued on next page)

Table 6. Continued

**Mars dual-axel rover (39)**

Recent interest in recurrent slope lineae as liquids on the surface of Mars has spurred interest in robotic access to extreme slopes to study these science phenomena. The axel robot is a single axle with tether designed to rappel down steep slopes. In a dual-axel rover configuration, one axel would remain at the top of the slope as an anchor to allow the other axel to rappel down the slope.



BRUIE Field trials in Alaska, USA

**Underwater vehicle (40)**

Scientists now believe that there are at least eight ocean worlds in our solar system. These liquid oceans may provide the best chance for life outside Earth in our solar system. BRUIE, Buoyant Rover for Under Ice Exploration underwater vehicle, is a rover designed to roam the underside of the icy shell at the top of an ocean (such as on Europa, Enceladus, or other ocean worlds). BRUIE could rove along the underside of ice—adjusting its buoyancy to maintain contact or hop at will. Its position at the water-ice interface offers it a great position to explore this unique surface where evidence of life may exist.

Table 7. Technological needs and challenges for space robotics in the coming decades.

Areas	Goals	Technological needs or challenges	Relevance to achieving top-level science
Sensing and perception	To provide situational awareness for space robotic agents, explorers, and assistants	<ul style="list-style-type: none"> <li>- New sensors</li> <li>- Sensing techniques</li> <li>- Algorithms for 3D perception, state estimation, and data fusion</li> <li>- Onboard data processing and generic software framework</li> <li>- Object, event, or activity recognition</li> </ul>	<p>The sensors provide the vast bulk of the direct science:</p> <ul style="list-style-type: none"> <li>-Increases in instruments, both remote sensing and in situ enable more precise measurements (e.g., spatial, spectral resolution, while reducing volume, mass, and power).</li> <li>- New types of instruments are emerging. Imaging spectroscopy to determine composition; lidar for 3D mapping; interferometric radar for change detection, structure; sample processing for life detection and astrobiology to enable new measurements for new types of science.</li> </ul>
Mobility or locomotion	To reach and operate at sites of scientific interest on extraterrestrial surfaces or free space environments	<ul style="list-style-type: none"> <li>- Mobility on, into, and above an extraterrestrial surface using locomotion like flying, walking, climbing, rappelling, tunneling, swimming, and sailing</li> <li>- Melting through the kilometers-thick ocean worlds' ice shells of Europa, Enceladus, or Pluto</li> <li>- Manipulations to make intentional changes in the environment or objects using locomotion like placing, assembling, digging, trenching, drilling, sampling, grappling, and berthing</li> </ul>	<p>Locomotion represents the ability to explore an environment, such as rovers, aerobots, and submarines. Melting through ocean worlds' ice shells enables access to habitable oceans underneath. Digging, trenching, and coring enable access to materials without atmospheric contamination (e.g., Mars geology) or radiation (e.g., Europa astrobiology).</p>

(Continued on next page)

Table 7. Continued

High-level autonomy for system and subsystems	To provide robust and safe autonomous navigation, rendezvous, and docking capabilities and to enable extended-duration operations without human interventions to improve overall performance of human and robotic missions. To enable closed-loop science for more efficient, novel science (e.g., tracking a dynamic plume at a comet)	<ul style="list-style-type: none"> <li>- GNC algorithms</li> <li>- Docking and capture mechanisms and interfaces</li> <li>- Planning, scheduling, and common autonomy software framework</li> <li>- Multi-agent coordination</li> <li>- Reconfigurable and adjustable autonomy</li> <li>- Automated data analysis for decision-making, fault detection, isolation and recovery/IVHM, and execution</li> </ul>	<ul style="list-style-type: none"> <li>- Enhanced guidance navigation and control means higher precision navigation for better science measurements. Scheduling, execution, and integrated vehicle health management enable more productive science time for vehicles.</li> <li>- Automated science analysis and scheduling enable closing the loop without ground in the loop, enabling more science cycles per mission (i.e., higher productivity and unique, opportunistic science).</li> </ul>
Human-robot interaction	To enable humans to accurately and rapidly understand the state of the robot in collaboration and act effectively and efficiently toward the goal state	<ul style="list-style-type: none"> <li>- Multimodal interaction; remote and supervised control</li> <li>- Proximate interaction</li> <li>- Distributed collaboration and coordination</li> <li>- Common human-system interfaces</li> </ul>	Virtual reality and augmented reality allow more natural interfaces to analyze vast acquired data streams. Virtual reality and augmented reality also allow for natural means of vehicle controlling such as by reach, touch, and gesture.
System engineering	To provide a framework for understanding and coordinating the complex interactions of robots and achieving the desired system requirements	<ul style="list-style-type: none"> <li>- Modularity, commonality, and interfaces</li> <li>- Verification and validation of complex adaptive systems</li> <li>- Robot modeling and simulation</li> <li>- Software architectures and frameworks</li> <li>- Safety and trust</li> </ul>	High stakes in billions require a reliable mission. As systems become increasingly complex, being able to characterize robotic behavior (especially for multivehicle swarms) becomes increasingly challenging.

(2) Health and care: for robotic surgery, diagnostics, independent living, nursing systems, prosthetics, and analysis and therapy.

(3) Emergency services: for improved responsiveness, reduced risk to life, and more efficient deployment.

(4) Deep mining: for exploration, excavation, and refinement in wind energy for turbine inspection and maintenance.

(5) Seabed robotics: for exploration and exploitation of oil, gas, and mineral resources on the ocean floor.

(6) Water industry: for asset inspection, maintenance, and health condition monitoring.

(7) Agriculture industry: for crop inspection and precision farming.

The markets associated with each of these sectors are expected to undergo huge growth in the coming years, and the adoption and insertion of robotics-based products and services into these applications are expected to deliver economic benefits of at least \$1.9 trillion by 2025 (35).

**CONCLUSIONS**

Robotics has demonstrated novel access capabilities for humans to extend their reach in space. Past robotic missions have enabled unique

science, increasing our knowledge in a wide range of science disciplines. Future robotics missions will continue to change the way space is explored in even more fundamental ways, enabling exploration more frequently, at a reduced cost, and in ever more challenging and dynamic environments. These missions will both continue our robotic exploration beyond Earth and play a key role in furthering human exploration beyond Earth.

**REFERENCES AND NOTES**

1. Y. Gao, UK-RAS White Paper on Space Robotics & Autonomous Systems: Widening the horizon of space exploration (2016); [http://hamlyn.doc.ic.ac.uk/uk-ras/sites/default/files/UK\\_RAS\\_wp\\_space.pdf](http://hamlyn.doc.ic.ac.uk/uk-ras/sites/default/files/UK_RAS_wp_space.pdf).
2. Noting this paper does not consider regular orbiting satellite or flyby spacecraft that only have mobility in their orbital trajectory. In addition, although these spacecrafts are technically “robotic,” they typically do not have intimate, unpredictable interactions with their environment that is more typical of the “robotics field,” such as driving mobility, sampling, manipulation or assembly, or atmospheric interactions as with an airplane, a helicopter, or an aerobot.
3. Level of autonomy onboard spacecraft defined by European Cooperation for Space Standardization (ECSS) [42]: Level E1: Execution mainly under real-time ground control, that is, remote or teleoperation; Level E2, execution of preplanned mission operations onboard, that is, automatic operation; Level E3, execution of adaptive mission operations

- onboard, that is, semi-autonomous operation; Level E4, execution of goal-oriented mission operations on board, that is, fully autonomous operation.
4. Y. Gao, Ed. *Contemporary Planetary Robotics—An Approach to Autonomous Systems* (Wiley-VCH, 2016), pp. 1–450, ISBN-13: 978-3527413256.
  5. K. Yoshida, Achievements in space robotics. *IEEE Robot. Autom. Mag.* **16**, 20–28 (2009).
  6. A. Flores-Abad, O. Ma, K. Pham, S. Ulrich, A review of robotics technologies for on-orbit services. *Prog. Aeronaut. Sci.* **68**, 1–26 (2014).
  7. K. Yoshida, D. Nenchev, G. Ishigami, Y. Tsumaki, Space robotics, in *The International Handbook of Space Technology*, M. Macdonald, V. Badescu, Eds. (Springer, 2014), chap. 19.
  8. K. Yoshida, B. Wilcox, G. Hirzinger, R. Lampariello, Space robotics, in *Springer Handbook of Robotics*, B. Siciliano, O. Khatib, Eds. (Springer, ed. 2, 2016), chap. 55.
  9. M. P. Golombek, R. A. Cook, T. Economou, W. M. Folkner, A. F. C. Haldemann, P. H. Kallemeyn, J. M. Knudsen, R. M. Manning, H. J. Moore, T. J. Parker, R. Rieder, J. T. Schofield, P. H. Smith, R. M. Vaughan, Overview of the Mars Pathfinder mission and assessment of landing site predictions. *Science* **278**, 1743–1748 (1997).
  10. J. A. Crisp, M. Adler, J. R. Matijevic, S. W. Squyres, R. E. Arvidson, D. M. Kass, Mars exploration rover mission. *J. Geophys. Res.* **108**, 8061 (2003).
  11. S. W. Squyres, R. E. Arvidson, D. Bollen, J. F. Bell III, J. Brückner, N. A. Cabrol, W. M. Calvin, M. H. Carr, P. R. Christensen, B. C. Clark, L. Crumpler, D. J. Des Marais, C. d’Uston, T. Economou, J. Farmer, W. H. Farrand, W. Folkner, R. Gellert, T. D. Glotch, M. Golombek, S. Gorevan, J. A. Grant, R. Greeley, J. Grotzinger, K. E. Herkenhoff, S. Hviid, J. R. Johnson, G. Klingelhöfer, A. H. Knoll, G. Landis, M. Lemmon, R. Li, M. B. Madsen, M. C. Malin, S. M. McLennan, H. Y. McSween, D. W. Ming, J. Moersch, R. V. Morris, T. Parker, J. W. Rice Jr., L. Richter, R. Rieder, C. Schröder, M. Sims, M. Smith, P. Smith, L. A. Soderblom, R. Sullivan, N. J. Tosca, H. Wänke, T. Wdowiak, M. Wolff, A. Yen, Overview of the opportunity mars exploration rover mission to meridiani planum: Eagle crater to purgatory ripple. *J. Geophys. Res.* **111**, E12512 (2006).
  12. R. E. Arvidson, S. W. Squyres, R. C. Anderson, J. F. Bell III, D. Blaney, J. Brückner, N. A. Cabrol, W. M. Calvin, M. H. Carr, P. R. Christensen, B. C. Clark, L. Crumpler, D. J. Des Marais, P. A. de Souza Jr., C. d’Uston, T. Economou, J. Farmer, W. H. Farrand, W. Folkner, M. Golombek, S. Gorevan, J. A. Grant, R. Greeley, J. Grotzinger, E. Guinness, B. C. Hahn, L. Haskin, K. E. Herkenhoff, J. A. Hurowitz, S. Hviid, J. R. Johnson, G. Klingelhöfer, A. H. Knoll, G. Landis, C. Leff, M. Lemmon, R. Li, M. B. Madsen, M. C. Malin, S. M. McLennan, H. Y. McSween, D. W. Ming, J. Moersch, R. V. Morris, T. Parker, J. W. Rice Jr., L. Richter, R. Rieder, D. S. Rodionov, C. Schröder, M. Sims, M. Smith, P. Smith, L. A. Soderblom, R. Sullivan, S. D. Thompson, N. J. Tosca, A. Wang, H. Wänke, J. Ward, T. Wdowiak, M. Wolff, A. Yen, Overview of the spirit Mars exploration rover mission to Gusev Crater: Landing site to Backstay Rock in the Columbia Hills. *J. Geophys. Res.* **111**, E02501 (2006).
  13. J. P. Grotzinger, J. Crisp, A. R. Vasavada, R. C. Anderson, C. J. Baker, R. Barry, D. F. Blake, P. Conrad, K. S. Edgett, B. Ferdowski, R. Gellert, J. B. Gilbert, M. Golombek, J. Gómez-Elvira, D. M. Hassler, L. Jandura, M. Litvak, P. Mahaffy, J. Maki, M. Meyer, M. C. Malin, I. Mitrofanov, J. J. Simmonds, D. Vaniman, R. V. Welch, R. C. Wiens, Mars Science Laboratory mission and science investigation. *Space Sci. Rev.* **170**, 5–56 (2012).
  14. J. Baker, The Falcon has landed. *Science* **312**, 1327 (2006).
  15. K. Matyjaszewski, Architecturally complex polymers with controlled heterogeneity. *Science* **333**, 1104–1105 (2011).
  16. F. Goesmann, H. Rosenbauer, J. H. Bredehöft, M. Cabane, P. Ehrenfreund, T. Gautier, C. Giri, H. Krüger, L. Le Roy, A. J. MacDermott, S. McKenna-Lawlor, U. J. Meierhenrich, G. M. M. Caro, F. Raulin, R. Roll, A. Steele, H. Steining, R. Sternberg, C. Szopa, W. Thiemann, S. Ulamec, Organic compounds on comet 67P/Churyumov-Gerasimenko revealed by COSAC mass spectrometry. *Science* **349**, aab0689 (2015).
  17. I. P. Wright, S. Sheridan, S. J. Barber, G. H. Morgan, D. J. Andrews, A. D. Morse, CHO-bearing organic compounds at the surface of 67P/Churyumov-Gerasimenko revealed by Ptolemy. *Science* **349**, aab0673 (2015).
  18. W. B. Banerdt, S. Smrekar, K. Hurst, P. Lognonné, T. Spohn, S. Asmar, D. Banfield, L. Boschi, U. Christensen, V. Dehant, W. Folkner, D. Giardini, W. Goetz, M. Golombek, M. Grott, T. Hudson, C. Johnson, G. Kargl, N. Kobayashi, J. Maki, D. Mimoun, A. Mocquet, P. Morgan, M. Panning, W. T. Pike, J. Tromp, T. van Zoest, R. Weber, M. Wiczorek; InSight Team, InSight: A discovery mission to explore the interior of Mars, in *Proceedings of Lunar and Planetary Science Conference (LPSC 2013)*, p. 1915.
  19. G. Rabideau, E. Benowitz, Prototyping an onboard scheduler for the mars 2020 rover, in *Proceedings of International Workshop on Planning and Scheduling for Space (IWSPSS, 2017)*.
  20. T. A. Estlin, B. J. Bornstein, D. M. Gaines, R. C. Anderson, D. R. Thompson, M. Burl, R. Castaño, M. Judd, Aegis automated science targeting for the MER opportunity rover. *ACM Trans. Intell. Syst. Technol.* **3**, 1–19 (2012).
  21. R. Francis, T. Estlin, G. Doran, S. Johnstone, D. Gaines, V. Verma, M. Burl, J. Frydenvang, S. Montaño, R. C. Wiens, S. Schaffer, O. Gasnault, L. DeFlores, D. Blaney, B. Bornstein, AEGIS autonomous targeting for ChemCam on Mars Science Laboratory: Deployment & results of initial science team use. *Sci. Robot.* **2**, ean4582 (2017).
  22. A. Ross, J. Kosmo, B. Janoiko, Historical synopses of Desert RATS 1997–2010 and a preview of desert RATS 2011. *Acta Astronaut.* **90**, 182–202 (2013).
  23. B. H. Wilcox, ATHLETE: A limbed vehicle for solar system exploration, in *Proceedings of IEEE Aerospace Conference* (2012), pp. 1–9.
  24. C. Borst, T. Wimbock, F. Schmidt, M. Fuchs, B. Brunner, F. Zacharias, P. R. Giordano, R. Konietschke, W. Sepp, S. Fuchs, C. Rink, A. Albu-Schaffer, G. Hirzinger, Rollin’ Justin-Mobile platform with variable base, in *Proceedings of IEEE International Conference on Robotics & Automation (IEEE, 2009)*, pp. 1597–1598.
  25. S. Chien, R. Knight, S. Schaffer, D. R. Thompson, B. Bue, M. Troesch, Agile science flight software—A new paradigm for space missions, Invited Talk, Flight Software Workshop, Pasadena, CA, USA, December 2016, <http://flightsoftware.jhuapl.edu/>.
  26. A. Ceballos, B. Bensalem, A. Cesta, L. de Silva, S. Fratini, F. Ingrand, J. Ocón, A. Orlandini, K. Rajan, R. Rasconi, M. van Winnendael, A goal-oriented autonomous controller for space exploration, in *Proceedings of ESA Symposium on Advanced Space Technologies in Robotics & Automation (ASTRA, 2011)*.
  27. G. Burroughes, Y. Gao, Ontology-based self-reconfiguring guidance, navigation, and control for planetary rovers. *J. Aerosp. Inf. Syst.* **13**, 316–328 (2016).
  28. A. Castano, A. Fukunaga, J. Biesiadecki, L. Neakrase, P. Whelley, R. Greeley, M. Lemmon, R. Castano, S. Chien, Automatic detection of dust devils and clouds on Mars. *Mach. Vis. Appl.* **19**, 467–482 (2008).
  29. A. G. Davies, S. Chien, V. Baker, T. Doggett, J. Dohm, R. Greeley, F. Ip, R. Castano, B. Cichy, G. Rabideau, D. Tran, R. Sherwood, Monitoring active volcanism with the autonomous sciencecraft experiment on EO-1. *Remote Sens. Environ.* **101**, 427–446 (2006).
  30. T. Doggett, R. Greeley, A. G. Davies, S. Chien, B. Cichy, R. Castano, K. Williams, V. Baker, J. Dohm, F. Ip, Autonomous on-board detection of cryospheric change. *Remote Sens. Environ.* **101**, 447–462 (2006).
  31. F. Ip, J. M. Dohm, V. R. Baker, T. Doggett, A. G. Davies, R. Castano, S. Chien, B. Cichy, R. Greeley, R. Sherwood, D. Tran, G. Rabideau, Flood detection and monitoring with the Autonomous Sciencecraft Experiment onboard EO-1. *Remote Sens. Environ.* **101**, 463–481 (2006).
  32. S. Chien, R. Sherwood, D. Tran, B. Cichy, G. Rabideau, R. Castano, A. Davies, D. Mandl, B. Trout, S. Shulman, D. Boyer, Using autonomy flight software to improve science return on Earth observing one. *J. Aerosp. Comput. Inf. Commun.* **2**, 196–216 (2005).
  33. K. L. Wagstaff, D. R. Thompson, B. D. Bue, T. J. Fuchs, Autonomous real-time detection of plumes and jets from moons and comets. *The Astrophys. J.* **794**, 43 (2014).
  34. NASA Technology Roadmaps—TA 4: Robotics and Autonomous Systems (2015).
  35. European Commission funded Space Robotics Strategic Research Cluster (SRC) report on knowledge & technology transfer for space robotics (2017).
  36. NASA/JPL Mars Helicopter, retrieved 17 April 2017; <https://jpl.nasa.gov/news/news.php?feature=4457>.
  37. R. D. Braun, H. S. Wright, M. A. Croom, J. S. Levine, D. A. Spencer, Design of the ARES Mars airplane and mission architecture. *J. Spacecraft Rockets* **43**, 1026–1034 (2006).
  38. J. L. Hall, V. V. Kerzhanovich, A. H. Yavrouian, J. A. Jones, C. V. White, B. A. Dudik, G. A. Plett, J. Mennella, A. Elfes, An aerobot for global in situ exploration of Titan. *Adv. Space Res.* **37**, 2108–2119 (2006).
  39. I. A. D. Nesnas, J. B. Matthews, P. Abad-Manterola, J. W. Burdick, J. A. Edlund, J. C. Morrison, R. D. Peters, M. M. Tanner, R. N. Miyake, B. S. Solish, R. C. Anderson, Axel, DuAxel rovers for the sustainable exploration of extreme terrains. *J. Field Robot.* **29**, 663–685 (2012).
  40. D. F. Berisford, J. Leichty, A. Klesh, K. P. Hand, Remote under-ice roving in Alaska with the buoyant rover for under-ice exploration, in *AGU Fall Meeting (AGU, 2013)*.
  41. Space Engineering: Space Segment Operability (ECSSE-70-11A), European Cooperation for Space Standardization (2005).

**Acknowledgments:** We thank the reviewers for many helpful comments to improve the article. **Funding:** We thank the UK-RAS Network and various space agencies and funding bodies such as NASA, ESA, and industrial companies who have sponsored and/or developed robotic technologies mentioned in the paper. Portions of this research were carried out by the Jet Propulsion Laboratory (JPL), California Institute of Technology, under a contract with NASA. **Competing interests:** The authors declare that they have no competing interests.

Submitted 23 April 2017  
 Accepted 7 June 2017  
 Published 28 June 2017  
 10.1126/scirobotics.aan5074

**Citation:** Y. Gao, S. Chien, Review on space robotics: Toward top-level science through space exploration. *Sci. Robot.* **2**, ean5074 (2017).

## HUMAN-ROBOT INTERACTION

## The uncanny valley of haptics

Christopher C. Berger,<sup>\*†</sup> Mar Gonzalez-Franco,<sup>†‡</sup> Eyal Ofek, Ken Hinckley

During teleoperation and virtual reality experiences, enhanced haptic feedback incongruent with other sensory cues can reduce subjective realism, producing an uncanny valley of haptics.

Copyright © 2018  
The Authors, some  
rights reserved;  
exclusive licensee  
American Association  
for the Advancement  
of Science. No claim  
to original U.S.  
Government Works

In the field of humanoid robotics, most people are familiar with the notion of an “uncanny valley” (1): the phenomenon whereby increasing the realism of a robot—its human-like appearance or movements—yields feelings of unease, or even revulsion, in people as its representation becomes more and more (but never quite fully) human-like.

We took this notion one step further by examining whether an uncanny valley also exists for human perception of forces (i.e., tactile sensations) that might be rendered during human-robot interaction, teleoperation, or other virtual manipulation tasks in virtual environments (2). That is, do enhancements of the “actual” forces applied by robots (or other devices) necessarily lead to an improved subjective experience by the human operator?

We argue that the answer is no: The subjective perception of haptic sensations by a human operator critically depends on the fusion of haptic and visual stimuli as a unitary percept in the human brain (3). If the fidelity of the haptic sensation increases but is not rendered in concordance with other sensory feedback (such as visual and auditory cues), the subjective impression of realism actually gets worse, not better. We refer to this degradation as the uncanny valley of haptics (Fig. 1A).

To demonstrate this effect and its implications, we used a virtual reality (VR) system as an experimental test bed, with haptic sensations delivered via a handheld controller in each hand. We elicit a phantom touch illusion using a technique known as funneling. Funneling provides the user with synchronous vibrotactile stimuli of different amplitudes from controllers that are physically (or, in our case, virtually) linked (Fig. 1C). When human participants hold a controller in each hand with vibrotactile haptics ren-

dered in this manner (Fig. 1D), they experience the haptic sensation as localized in space (“spatialized”). And paradoxically, it “feels like” it originates in the empty space between the two hands (4). What is happening is that, upon the arrival of two near-synchronous tactile cues, the human brain integrates the stimuli. That is, the brain assumes that the two stimuli have a common source—and not just in time, but also in space (5).

Note that this experimental setup serves as an ecologically valid proxy, carefully designed to sensitively probe the potential influence of haptic stimuli, for a variety of teleoperation tasks. This is important because augmenting such tasks with higher-fidelity haptic sensations may come with the (oft-unstated) assumption that such “improvements” will always yield more realistic and immersive virtual environments. Of course, realism and immersion are subjective perceptions (6), but we can formally assess and quantify them using scientifically established presence questionnaires (7).

We ran several experiments (see the Supplementary Materials) to better understand the dynamics of haptic perception and how to elicit the aforementioned uncanny valley of haptics—and perhaps more importantly, how to avoid it. These experiments studied passive haptic stimulation (i.e., when the participant passively receives a haptic stimulation without moving their arms) contrasted with dynamic haptic stimulation (triggered by the movements of the participant). Research on humanoid robotics has shown that the feelings of unease (or even revulsion) associated with the classic notion of an uncanny valley can be shifted or eliminated (1) by manipulating various aspects of the simulations. For example, cartoonish features can reduce the mismatch between the human-likeness of a robot and its perceived realism (8). To see if

a participant’s top-down expectations influenced the results, we also probed causal haptic stimulation with a condition in which users could plausibly attribute an external cause. This took the form of an animated cloud that partially obscured the view of the funneling effect’s location, thereby “explaining away” any discrepancy in haptic sensations.

Our results show that participants could localize the vibrotactile stimuli in different locations (4), establishing the spatial haptic effects. However, the experience—the overall sense of immersion—dipped as this increasing realism of the haptics exceeded the complementary cues (from other senses) in the simulation (Fig. 1B). These findings therefore support the existence of an uncanny valley of haptics.

Likewise, our results demonstrate techniques to reduce and recover from the uncanny valley of haptics. For example, in the dynamic haptic stimulation, asking the participants to perform a motor action was sufficient to provide a “reason” for the haptic sensation, bringing the subjective experience back into agreement with the perceived realism. In addition, in our probe of causal haptic stimulation, providing an animated feature (a moving cloud) that could plausibly “cause” the mismatch between senses was sufficient to preserve the subjective experience.

An uncanny valley of haptics means that designers of human-robot interactions cannot simply assume that more (or more realistic) haptics is better. As experiences move beyond purely visual displays and integrate richer feedback from multiple senses, including haptic and auditory sensations, mismatches become possible and may undermine “improvements” to haptic rendering.

Subjective incongruences produce conflicting percepts across multiple sensory channels. When the human brain subconsciously integrates these conflicting cues into a unified percept (3, 9), the result may be reduced subjective experience (i.e., a decreased sense of immersion). Our finding of an uncanny valley effect for haptics calls for a shift in focus in the design of human-robotic interactions

Microsoft Research, Redmond, WA 98052, USA.

<sup>\*</sup>Present address: Division of Biology and Biological Engineering/Computation and Neural Systems, California Institute of Technology, Pasadena, CA 91125, USA.

<sup>†</sup>These authors contributed equally to this work.

<sup>‡</sup>Corresponding author. Email: margon@microsoft.com

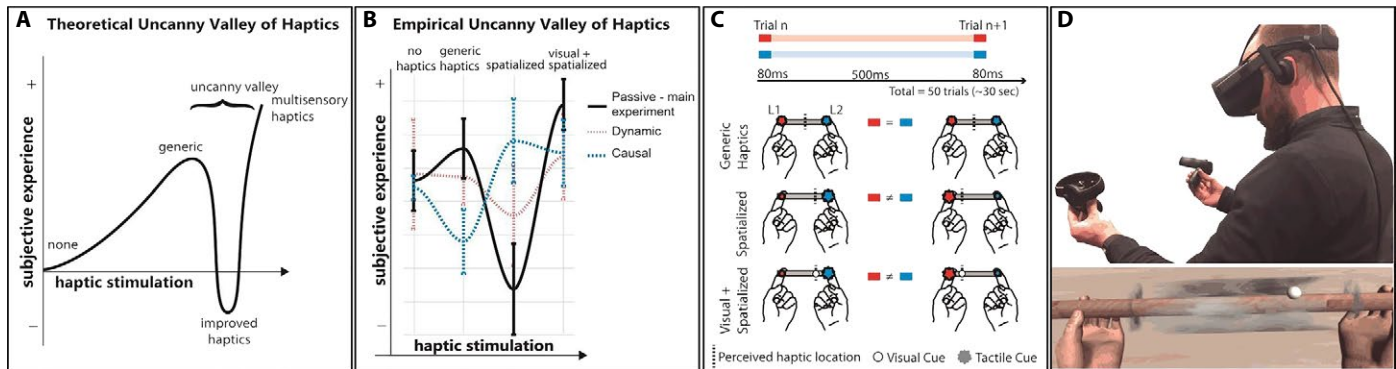


**Fig. 1. Uncanny valley of haptics.** (A) The theoretical uncanny valley of haptics as defined by studies from the classic humanoid robotic uncanny valley (1). (B) The empirical data from our experiments. The subjective experience corresponds to the Presence Questionnaire score. Error bars represent SEM. (C) A diagram showing the stimulation paradigm for producing the illusion of spatialized haptic feedback via funneling. In generic haptics stimulations, the same amplitude of vibrations was delivered for all trials to both controllers. No funneling occurs in such conditions. However, under the spatialized and visual + spatialized conditions, a funneling effect was achieved by varying the vibrotactile amplitude delivered at each controller, producing a change in the perceived haptic location. (D) Inside the VR headset, the participant sees a (virtual) wooden dowel that bridges their hands (as sensed by the position and orientation of the controllers). In the passive and causal experiments, the participant held the dowel in a specific “activation area” to receive the haptic stimuli (represented by a “cloud” that looked like a smoky cylinder). During the visual + spatialized stimulation, participants saw a white marble cue that visually reinforced the location of the haptic feedback.

from precision to context and suggests a need for a multi-modal approach to haptic feedback—a holistic approach that incorporates multiple human sensory channels into design, rendering, and evaluation of haptic sensations in the user experience.

Although demonstrated in a VR test bed, the effects are rooted in human perception and as such could affect the perceived realism and immersion manifest in many real-world applications, such as teleoperation scenarios, remote robotic manipulation, or even telesurgical tasks. Our study offers insights, methods, and results that may boost future endeavors to render haptic effects that improve (rather than detract from) the overall user experience.

## SUPPLEMENTARY MATERIALS

robotics.sciencemag.org/cgi/content/full/3/17/ear7010/DC1  
Materials and Methods  
Results  
Fig. S1. Reported spatial haptic perception.  
Table S1. Questionnaire and factor loadings.  
Table S2. Main experiment (passive) results.  
Table S3. Summary of learnings and recommendations from the uncanny valley of haptics.  
Movie S1. The uncanny valley of haptics.  
Data file S1. Anonymized questionnaire responses for all experiments and conditions.  
References (10–15)

## REFERENCES AND NOTES

- M. Mori, The uncanny valley. *Energy* **7**, 33–35 (1970).
- C. Duriez, F. Dubois, A. Kheddar, C. Andriot, Realistic haptic rendering of interacting deformable objects in virtual environments. *IEEE Trans. Vis. Comput. Graph.* **12**, 36–47 (2006).
- A. A. Ghazanfar, C. E. Schroeder, Is neocortex essentially multisensory? *Trends Cogn. Sci.* **10**, 278–285 (2006).
- J. Lee, Y. Kim, G. J. Kim, Funneling and saltation effects for tactile interaction with virtual objects, in *Proceedings of the SIGCHI Conference on Human Factors in Computing Systems* (ACM, 2012), pp. 3141–3148.
- G. v. Békésy, Funneling in the nervous system and its role in loudness and sensation intensity on the skin. *J. Acoust. Soc. Am.* **30**, 399–412 (1958).
- M. Gonzalez-Franco, J. Lanier, Model of illusions and virtual reality. *Front. Psychol.* **8**, 1125 (2017).
- T. Schubert, F. Friedmann, H. Regenbrecht, The experience of presence: Factor analytic insights. *Presence* **10**, 266–281 (2001).
- H. Chen, R. Russell, K. Nakayama, M. Livingstone, Crossing the “uncanny valley”: Adaptation to cartoon faces can influence perception of human faces. *Perception* **39**, 378–386 (2010).
- B. E. Stein, T. R. Stanford, Multisensory integration: Current issues from the perspective of the single neuron. *Nat. Rev. Neurosci.* **9**, 255–266 (2008).
- E. Kokkinara, R. McDonnell, Animation realism affects perceived character appeal of a self-virtual face, in *Proceedings of the 8th ACM SIGGRAPH Conference on Motion in Games* (ACM, 2015), pp. 221–226.
- M. González-Franco, P. Yuan, D. Zhang, B. Hong, S. Gao, Motor imagery based brain-computer interface: A study of the effect of positive and negative feedback, in *2011 Annual International Conference of the IEEE Engineering in Medicine and Biology Society* (IEEE, 2011), pp. 6323–6326.
- C. C. Berger, H. H. Ehrsson, Mental imagery changes multisensory perception. *Curr. Biol.* **23**, 1367–1372 (2013).
- C. C. Berger, H. H. Ehrsson, The content of imagined sounds changes visual motion perception in the cross-bounce illusion. *Sci. Rep.* **7**, 40123 (2017).
- M. J. Schuemie, P. van der Straaten, M. Krijn, C. A. P. G. van der Mast, Research on presence in virtual reality: A survey. *Cyberpsychol. Behav.* **4**, 183–201 (2001).
- I. T. Jolliffe, Principal component analysis and factor analysis, in *Principal Component Analysis*, I. T. Jolliffe, Ed. (Springer, 1986), pp. 115–128.

**Funding:** This study was funded by Microsoft Research. C.C.B. was supported by a grant from the Swedish Research Council (2017-00276). **Author contributions:** M.G.-F. and C.C.B. defined the studies, implemented the simulations, and analyzed the data. C.C.B. ran the user studies. E.O., K.H., M.G.-F., and C.C.B. wrote the paper and established the uncanny valley of haptics theory. **Competing interests:** The authors report their affiliation to Microsoft, an entity with a financial interest in the subject matter or materials discussed in this manuscript. However, the authors have conducted the studies following scientific research standards and declare that the current manuscript presents balanced and unbiased studies and theories. **Data and materials availability:** The anonymized data can be obtained from the Supplementary Materials. The principal component analysis was performed using <https://notebooks.azure.com/margon/libraries/QuestionnairePCA>.

10.1126/scirobotics.aar7010

**Citation:** C. C. Berger, M. Gonzalez-Franco, E. Ofek, K. Hinckley, The uncanny valley of haptics. *Sci. Robot.* **3**, ear7010 (2018).

## COLLECTIVE BEHAVIOR

# Optimized flocking of autonomous drones in confined environments

Gábor Vásárhelyi<sup>1,2\*</sup>, Csaba Virágh<sup>2</sup>, Gergő Somorjai<sup>1,2</sup>, Tamás Nepusz<sup>3</sup>, Agoston E. Eiben<sup>4</sup>, Tamás Vicsek<sup>1,2</sup>

Copyright © 2018  
The Authors, some  
rights reserved;  
exclusive licensee  
American Association  
for the Advancement  
of Science. No claim  
to original U.S.  
Government Works

We address a fundamental issue of collective motion of aerial robots: how to ensure that large flocks of autonomous drones seamlessly navigate in confined spaces. The numerous existing flocking models are rarely tested on actual hardware because they typically neglect some crucial aspects of multirobot systems. Constrained motion and communication capabilities, delays, perturbations, or the presence of barriers should be modeled and treated explicitly because they have large effects on collective behavior during the cooperation of real agents. Handling these issues properly results in additional model complexity and a natural increase in the number of tunable parameters, which calls for appropriate optimization methods to be coupled tightly to model development. In this paper, we propose such a flocking model for real drones incorporating an evolutionary optimization framework with carefully chosen order parameters and fitness functions. We numerically demonstrated that the induced swarm behavior remained stable under realistic conditions for large flock sizes and notably for large velocities. We showed that coherent and realistic collective motion patterns persisted even around perturbing obstacles. Furthermore, we validated our model on real hardware, carrying out field experiments with a self-organized swarm of 30 drones. This is the largest of such aerial outdoor systems without central control reported to date exhibiting flocking with collective collision and object avoidance. The results confirmed the adequacy of our approach. Successfully controlling dozens of quadcopters will enable substantially more efficient task management in various contexts involving drones.

## INTRODUCTION

Groups of gregarious animals often display an interesting and spectacular collective pattern (1): They establish ordered structures without collisions in a limited amount of time (2, 3). They can also react extremely fast to environmental changes, such as the sudden appearance of a predator or an obstacle (4, 5). Although these systems are enormously complex, they are also perfectly optimized, and thus, their expressed motion patterns remain gracefully natural (6). When these systems are modeled, one tends to focus on the replication of the smooth optimal motion patterns by making idealistic assumptions about the underlying complexity. This simultaneous simplification of the “input” and “output” explains why so many different statistical physical models of swarm behavior can be efficient in reproducing the same natural collective motion patterns with abstract mathematical formalism.

According to early microscopic agent-based models (7), establishing and maintaining collision-free cohesive flocking require only three simple interactions between idealistic agents: repulsion in short range, velocity alignment in middle range, and attraction in long range. On the basis of these general rules, hundreds of models have emerged to describe the synchronized collective motion of animals, humans, or even migrating cells (8–10). We call these systems self-organized because interactions in them are local and decisions are made by the agents themselves.

One of the recent applications of self-organizing flocking models is in collective robotics (11, 12), where decentralized control algorithms for groups of autonomous drones can be developed on the basis of these interactions, as a prerequisite for safe operation. Driving the behavior of such systems toward some desirable pattern is highly non-

trivial. First, the agents (robots and drones) are autonomous and imperfect. That is, every agent has (i) its own onboard computer for performing the calculations needed for controlling its own actions, (ii) its own sensor system for measuring relative positions and velocities, and (iii) its own communication device for data exchange with neighboring agents. These features reflect the current definition of sensory and reactive autonomy described in (13). Second, these systems should work without central control. That is, although agents can observe each other and may exchange information, they do not send and receive direct control commands because there is no leader within the group, nor is there an external supervisor such as a base station or human overseer.

In developing decentralized control algorithms for swarms of flying robots in stochastic environments where communication outages and delays are common, one soon faces a set of severe challenges that are rarely targeted by previous idealistic agent-based models. As an example, 32 representative microscopic flocking models were selected and compared out of more than 100 (9). Fine and Shell state that “there is no consensus on the precise details of the motions needed to produce rich flocking motions under realistic sensing models, actuation, and dynamics constraints”; most works lack completeness and precision in terms of repeatable modeling and validation; only a few included motion constraints and collision avoidance [e.g., (7, 14, 15)]; and none handled motion constraints explicitly. Finally, only one investigated bounded space with obstacles (16).

While aiming for a stable and scalable flocking model for real flying robots, some serious design challenges need to be addressed:

(1) Reality gap. Flocking models that are stable in simulation under idealistic conditions tend to oscillate and destabilize quickly under real-life conditions when delays, uncertainties, and kinematic constraints are present (17–21).

(2) Adaptivity. Flocking models developed for open space or periodic boundary conditions do not necessarily work in confined spaces and with obstacles in the way (9, 22).

<sup>1</sup>Statistical and Biological Physics Research Group of the Hungarian Academy of Sciences, Pázmány Péter sétány 1/A, 1117 Budapest, Hungary. <sup>2</sup>Department of Biological Physics, Eötvös Loránd University, Pázmány Péter sétány 1/A, 1117 Budapest, Hungary. <sup>3</sup>Molde University College, Britvegen 2, 6410 Molde, Norway. <sup>4</sup>Department of Computer Science, Vrije Universiteit Amsterdam, de Boelelaan 1081a, 1181HV Amsterdam, Netherlands.

\*Corresponding author. Email: vasarhelyi@hal.elte.hu

(3) Scalability. Flocking models that are developed for a specific speed or group size might not be scalable; that is, for higher velocities or larger groups, motion patterns may become unstable (16, 23, 24).

(4) High dimensionality. Flocking models that work well in real life generally have a substantial number of parameters with complex nonlinear interactions that need to be tuned for a wide range of conditions in reasonable time (6).

The largest drone swarms so far were developed for show business by Intel (25) and by Ehang (26) with more than 1000 drones each; however, these drones were individually programmed for predefined trajectories or were centrally controlled and did not satisfy the above criteria of autonomy. The music band Metallica recently included dozens of drones in their concerts that seemed to exhibit some kind of partially autonomous swarming behavior by using a dedicated indoor positioning system and central control mechanisms (27). The U.S. military is also experimenting with fixed-wing drone swarms called *Perdix* (28). The press release stated that the system of 103 autonomous drones performed adaptive formation flying. The published video suggests that the drones received a set of predefined targets, chose one with a collective decision, and followed that individually. Drones also loitered around a common point, although at different heights. Unfortunately, there are no public details about the control mechanism, the communication scheme, or possible collision avoidance behavior for a reliable assessment of the work.

Autonomous drone swarms also appear in the scientific literature, using indoor motion capture-based (29, 30), outdoor Global Positioning System (GPS)-based (24, 31–33), or even vision-assisted (34, 35) navigation. These systems typically have a much smaller flock size than preprogrammed drone swarms. Although motion capture-based indoor systems (with 20 minidrones and 49 nanodrones in the mentioned citations) are remarkably accurate and dynamic, they represent a very different type of system because they do not have to tolerate profound imperfections such as meter-level positioning, external wind turbulence, or long-range communication decay. The mentioned GPS-based outdoor swarms consisted of no more than 10 drones, except for (32), where 50 fixed-wing unmanned aerial vehicles (UAVs) were flown but at different altitudes, without any explicit collision avoidance mechanism. Vision-based solutions have used only a few drones as the state of the art.

In this article, we build on our previous results (24), where an outdoor drone swarm of 10 agents were presented as a proof of concept with flocking and formation flight capabilities. Although the previous work included preliminary results of closed-area flocking, trajectories were quite oscillatory even though they were executed in the simplest arena: a circular one that actually helped to develop smooth turns. Furthermore, the system—due to the improper treatment of acceleration limits—was not scalable to speeds higher than 4 m/s.

Creating a large decentralized outdoor drone swarm with synchronized flocking behavior using autonomous collision and object avoidance in a bounded area is as yet an unresolved task. We filled this gap by presenting real flights of 30 autonomous quadcopters performing tight and stable flocking in a bounded and cluttered environment. To achieve this goal we used a scalable, optimized control framework, based on realistic dynamic modeling and the explicit treatment of motion constraints in the flocking equations.

The overall descriptors that specified a given setup of our system were the number of drones and the predefined flocking speed. The desired swarm behavior was defined as being collision-free and coherent, that is, with strongly correlated velocity values of the individual

drones, and exhibiting a velocity close to the flocking speed. Furthermore, we aimed for stable swarm behavior with persistent global collective motion patterns resembling those of natural systems with collective intelligence.

The explicit treatment of motion constraints was based on a special concept for the velocity alignment interaction. The key idea was to abandon the generally used fixed spatial boundaries of the local interactions. Instead, the alignment interaction range (and magnitude) was determined dynamically, based on the expected optimal relation between distance and velocity difference. Because the acceleration of agents is limited, they need time and space to brake and avoid collisions. Consequently, the amount of allowed velocity difference must be distance-dependent: Close agents should align perfectly, whereas distant agents are allowed to have larger velocity difference up to a certain limit. To find the upper bound of velocity difference for a given distance, we used an acceleration-limited braking curve. The goal of the alignment was thus to reduce velocity difference below this distance-dependent threshold. This workflow was easy to calculate and provided optimal foundations of scalability in the velocity domain because it took into account the limited acceleration of agents, the source of many undesired oscillations.

The model has many independent parameters with which a broad range of emerging behaviors and visually pleasing collective patterns could be generated. However, our requirements of stability and coherence provide quantifiable criteria for the instantiation of the general model with suitable parameter values. This implies a highly nontrivial optimization problem because of the large number of parameters, their complex nonlinear interactions, and the noisy relations between parameter values and collective motion patterns.

An important element of our approach is the focus on model instances, that is, on models together with specific values of their parameters. The rationale is grounded in our interest in system behavior. Having a model is not enough to generate and study motion patterns; to make a model executable, it must be instantiated by parameter values. Blatantly disregarding theoretical benefits of models, we could say that any model is worth as much as its best instance. Therefore, we considered optimizing the parameter setup as an essential part of the model generation.

This view is missing from current flocking models and the realization of the corresponding robotic swarms, although it stands to reason that natural systems operate at the optimal values of their “tunable” parameters (in the spirit of the Darwinian theory). As the complexity of artificial intelligence increases, we will be forced to include more and more optimization into model design.

To solve the optimization problem, we used evolutionary algorithms, population-based stochastic search methods inspired by natural evolution that have proven competitive in solving hard problems in the face of challenging characteristics such as nondifferentiability, discontinuities, multiple local optima, noise, and nonlinear interactions among the variables (36). The family of evolutionary algorithms contains several variants of the main principles, including genetic algorithms, evolution strategies, differential evolution, and particle swarm optimization (37). Evolution strategies, particularly the covariance matrix adaptation evolution strategy (CMA-ES) (38), are considered to be excellent optimizers in continuous parameter spaces; therefore, we used this algorithm to find good settings for our model.

The main contributions of this paper are (i) a flocking model that explicitly treats motion constraints by maintaining an improved balance between distance and velocity difference; (ii) a method to design

individual drone controllers by optimizing self-organized group-level behavior in a complex, noisy, real-world system; (iii) simulations of this system for presenting its scalability for wide velocity ranges and group sizes; and (iv) the demonstration of the framework with a fleet of 30 quadcopters, performing fully autonomous, synchronized outdoor flights with collective collision and obstacle avoidance in a confined space.

**RESULTS**

**Flocking model instantiation through evolutionary optimization**

Our generic flocking model included proper evaluation metrics, that is, order parameters and fitness functions (see Materials and Methods for detailed equations). The model was instantiated with proper parameter values first in simulation. Evolutionary optimization has been used to find parameter values that maximize flock coherence and speed while minimizing collisions. First, we optimized the parameters under conditions suitable for real experiments: using a square-shaped obstacle-free arena with a side length of  $L^{\text{arena}} = 250$  m and three different flocking speed ( $v^{\text{flock}}$ ) values: 4, 6, and 8 m/s. The corresponding values for the maximum allowed speed ( $v^{\text{max}}$ ) were 6, 8, and 10 m/s, respectively. We examined the behavior of 100 simulated agents in all cases. For each of the  $v^{\text{flock}}$  values, we performed at least three independent, randomly initialized optimization processes to identify possible multiple local optima in the parameter space but found very similar solutions and convergence in the alternative evolutionary runs. Therefore, below, we will only refer to the best (highest fitness) evolutionary run for each flocking speed.

The populations in our evolutionary algorithm consisted of parameter vectors whose fitness was determined by a 10-min-long realistic simulation of the system. In all runs, we used a population size of 100 and terminated after 150 generations. The 15,000 fitness evaluations turned out to be sufficient in all cases. The optimization was performed on the Atlasz supercomputer cluster of Eötvös University,

Budapest, Hungary (39); the overall execution time of a single evolutionary run varied between 2 and 6 days.

The evaluation of the phenotypes was based on a single fitness value that was created as the product of six independent normalized partial fitness values (corresponding to minimized collision risk, minimized collision with walls, maximized velocity correlation, velocity magnitude as close as possible to flocking speed, maximized cluster size, and minimized number of disconnected agents). Each partial fitness, as well as the final fitness value, takes values between 0 (worst case) and 1 (ideal case).

The final fitness of the best solutions after optimization converged to 0.92, 0.87, and 0.8 for  $v^{\text{flock}} = 4, 6,$  and 8 m/s, respectively. In these best stochastic simulation instances, four of the six partial fitnesses were exactly 1 (corresponding to a perfectly collisionless and fully connected flock), and only the velocity correlation and the average velocity reduced the overall fitness. This is a natural and inevitable tendency because hitting the wall in a bounded area requires the flock to change direction, and this cannot be performed without temporarily reducing the speed and velocity correlation. It is worth noting that these high fitness values have been reached under harsh realistic conditions with a 1-s communication delay and substantial noise, which generally act against perfect synchronization. Optimized parameter values are given in table S1.

The stability of the optimized models was investigated next by executing 100 parallel stochastic simulations for each speed. Detailed results about the statistical evaluations can be found in table S2. The average fitnesses naturally became somewhat lower than the maxima:  $0.812 \pm 0.101$  (SD),  $0.776 \pm 0.086$ , and  $0.728 \pm 0.075$  for  $v^{\text{flock}} = 4, 6,$  and 8 m/s, respectively, with the appearance of occasional collisions. Note that in simulation, the partial fitness of collisions must be a continuous and not-too-steep function; otherwise, the optimizer cannot find the direction of gradients from suboptimal solutions. This means that having a few collisions can be banned only with a limited decrease of fitness, and the optimizer will not devote a special

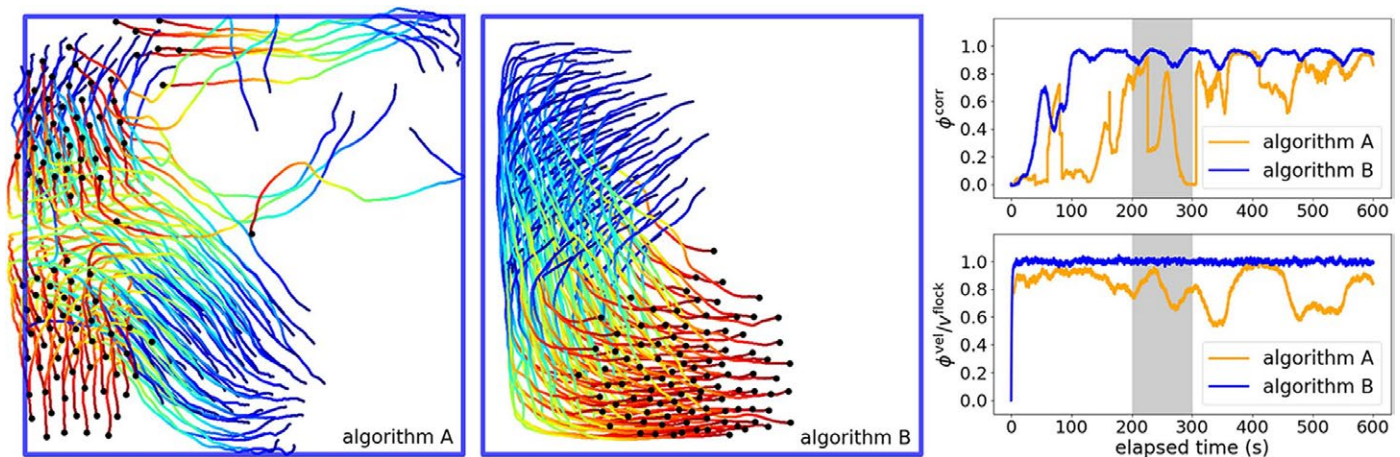


**Fig. 1. Comparing previous simulation work with current study.** Sample timelines of two order parameters (right, velocity correlation at top and normalized velocity magnitude at bottom) from our previous work (40) (algorithm A) and our novel flocking model (algorithm B). Trajectories corresponding to the gray sections of the timelines are shown for both models on the left, with color mapped to time. Corresponding motion can be seen in movies S1 and S2. Algorithm B performs much better and has a lower transient time. We used the following interaction parameter set for algorithm A:  $C^{\text{frict}} = 30 \text{ m}^2$ ,  $r_{\text{min}}^{\text{frict}} = 5 \text{ m}$ ,  $r_0^{\text{rep}} = 20 \text{ m}$ , and  $p^{\text{rep}} = 1 \text{ s}^{-1}$  [for details on parameters, see (40)]. For algorithm B, we used the optimized parameter set for  $v^{\text{flock}} = 4 \text{ m/s}$ . Using an average from 10 simulations with the same parameter setup, the order parameters averaged over time were  $\phi_A^{\text{corr}} = 0.63 \pm 0.07$  and  $\phi_A^{\text{vel}} = 3.37 \pm 0.15 \text{ m/s}$  for algorithm A and  $\phi_B^{\text{corr}} = 0.92 \pm 0.002$  and  $\phi_B^{\text{vel}} = 3.83 \pm 0.005 \text{ m/s}$  for algorithm B.

priority to entirely collisionless solutions; it will aim for a maximally dense flock implicitly to increase connectedness and velocity correlation, which narrows that stability range with regard to collisions. On the other hand, in reality, collisions have to be eliminated completely at all times as a first rule. Several workarounds exist for this problem: (i) running the optimizer with a larger radius of collision or a larger communication delay to optimize to a solution where minimum interagent distances become larger and (ii) increasing interagent distance (repulsion) manually after optimization with the harmless compromise of reducing overall velocity correlation in the enlarged flock. This time, we chose the second method because, in real flights, one needs to start from an oversecured parameter setup anyways, compared with the optimum with highest possible fitness but lower stability.

Evolutionary optimization produced a huge number of stochastic fitness evaluations, which also contain precious information about the reasonable parameter ranges where fitness is expected to be high. These working ranges are summarized in table S1 to provide tuning information for real drones as well. We also listed all model parameters in table S3 with a detailed explanation on meaning and usage.

Finally, let us note a surprising benefit of evolving parameter settings. The evolutionary algorithm found unexpected parameter settings in both the repulsive and alignment interactions between agents:

(1) Instead of a strong hard-core repulsion (as expected intuitively), a spatially more extended and smoother repulsion is preferable according to the evolutionary optimization.

(2) The velocity alignment between close-by agents should be maximal and mostly distance-independent, allowing only a certain, relatively small velocity difference slack, mainly to speed up the collective turning process.

Overall, we achieved our first goal: The general model could be instantiated well with suitable parameter values in simulation; the optimized setup displayed a stable and efficient flock in the investigated velocity regime, which can serve as the basis for the real field experiments. Comparing our new results to our previous work (40), we can see a substantial increase in flock stability and coherence (see Fig. 1). Movies S1 and S2 show corresponding motion of old and new simulations at 4 m/s.

### Scalability in velocity

The most important feature of the acceleration-limited velocity alignment term in the agent-agent and wall-agent interactions is its inherent scalability in the velocity regime. To demonstrate this, we performed

further optimizations with higher flocking speed values: 16 and 32 m/s, beyond most bird migration speeds (41). We changed two parameters in the environmental setup: We increased the communication range from 80 to 160 and 320 m and the size of the arena from 250 to 500 and 1000 m for the two speed values, respectively. The first change was needed because the communication delay remained at 1 s, which created a much larger positional uncertainty and braking distance at higher speeds. This can be compensated only if agents have information about each other at higher distances. The second change was a consequence of the first: With such a large communication delay and speed, the interagent distances became larger, and thus, the flock could not fit into a smaller arena with enough freedom for nice flocking behavior.

The optimized solutions obtained a high fitness again, with a maximum of 0.91 and 0.89 and a statistical average of  $0.79 \pm 0.12$  and  $0.63 \pm 0.23$  for 16 and 32 m/s, respectively. Detailed fitness values of the statistical evaluations are summarized in table S2. Note that for the highest speed of 32 m/s, the lower average of the fitness is mostly a result of the slightly increased number of collisions ( $3.53 \pm 3.61$ ). We investigated the role of communication range and delay in this case and found that collisions disappeared when we reduced the delay below 1 s, assuming that the communication range was large enough (see Fig. 2 for details). The first part of movie S3 shows the optimized and stable flocking behavior of 100 agents in simulation for 16 m/s.

### Scalability in agent number with collective obstacle avoidance

Because of the locality of the communication and the interactions, the proposed flocking model provides the foundations of scalability in agent number. However, when more agents synchronize in such a nonequilibrium system, the overall momentum of the flock also scales with flock size, which creates increased “pressure” of agents when the flock bumps into walls. In similar situations, human crowds are prone to injuries or even death during panic events (16) or, for example, around mosh pits at heavy metal concerts (42). To provide collisionless solutions with higher agent numbers, one needs to prevent accumulating pressure of agents, for example, using obstacles inside the arena. Obstacles can be introduced with the same type of interactions as surrounding walls (see Materials and Methods for details).

Without going into statistical details, movie S3 shows some examples of the realistic simulation with flock sizes between 30 and 1000 and flocking speeds between 4 and 32 m/s, with different types of obstacles in the way. Overall, we see that the presented flocking

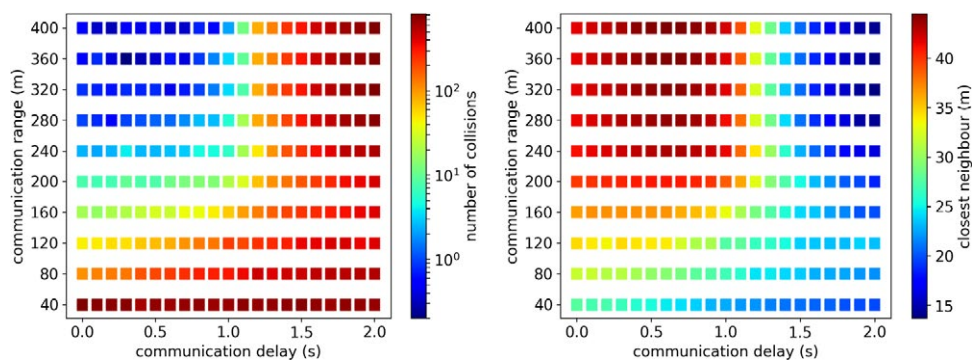


**Fig. 2. Distribution of the number of collisions and the average closest-neighbor distance as a function of communication range and delay.** Every bin is the average of 20 simulations with the optimized parameter setup for a flocking speed of 32 m/s. As can be seen, safe flocking can be achieved with small enough delay (<1 s) and large enough communication range (>240 m) for this setup.

model can be used as a general framework to handle flocking-type motion in a confined area, with a large number of agents, large flocking speeds, and obstacles.

**Experimental results with outdoor flying robots**

We implemented the described model in our custom-built multidrone framework as a control algorithm. Details of the drone setup are given in Materials and Methods.

We performed two-dimensional experiments with 30 drones flocking at the same altitude, with a horizontal speed of  $v^{\text{flock}} = 4, 6, \text{ and } 8 \text{ m/s}$  and  $L^{\text{arena}} = 200 \text{ to } 260 \text{ m}$ . Parameter values were initialized mostly within the working range of the corresponding evolutionary optimized results (table S1) with some notable changes from simulation optima based on the following precautions and preventive safety considerations: (i) repulsion strength was somewhat increased (larger gain) to minimize the chance of collisions (compromise: sparser flock); (ii) coefficient of alignment was increased to reduce possible oscillations (compromise: more sluggish motion); (iii) shill interaction strength was reduced (smaller shill velocity), but range was extended (larger distance offset) to avoid very high interaction terms at walls while maintaining overall strength. The final parameter values used in the experiments and detailed comments on their possible changes from simulation optima are summarized in table S4.

To assess the quality of the flights, we calculated a set of order parameters that describe different aspects of the motion. We calculated the cluster-dependent velocity correlation ( $\phi^{\text{corr}}$ ), the average velocity

( $\phi^{\text{vel}}$ ), the average and minimum of interagent distances ( $\text{min}(r_{ij})$  and  $\bar{r}_{ij}^{\text{min}}$ ), and the average normalized velocity expressed in local angle polar (LAP) coordinates (43):

$$\phi^{\text{LAP}} = \frac{v_y r_x - v_x r_y}{v^{\text{flock}} \sqrt{r_x^2 + r_y^2}} \tag{1}$$

where  $r_x$  and  $r_y$  represent the average position of agents in the horizontal plane relative to the center of the arena and  $v_x$  and  $v_y$  are the average velocity components of the agents in the horizontal plane.  $\phi^{\text{LAP}}$  is a simple descriptor of rotational behavior: An instantaneous value of zero means no correlated motion tangentially, whereas a value of 1 or -1 represents correlated circular flight in the counterclockwise and clockwise directions, respectively.

Figure 3 shows the order parameters as a function of time for a selection of full 10- to 15-min stable flights (flight time depended on battery and wind conditions, with a maximum tolerated wind of about 40 km/hour). Flights were selected to represent the most common emerging collective patterns, namely, repetitive circular and diagonal flights in an obstacle-free arena and a lively random collective flight with obstacles. Note that the emergent rotational pattern is a universal one (44), appearing in a large variety of flocking systems ranging from elongated rods (45) through locusts (2) and fish (5) to humans (46, 47). A 10-min part of the trajectories from the same flights can be seen in Fig. 4, a long-exposure photo of a shorter section is shown in Fig. 5,

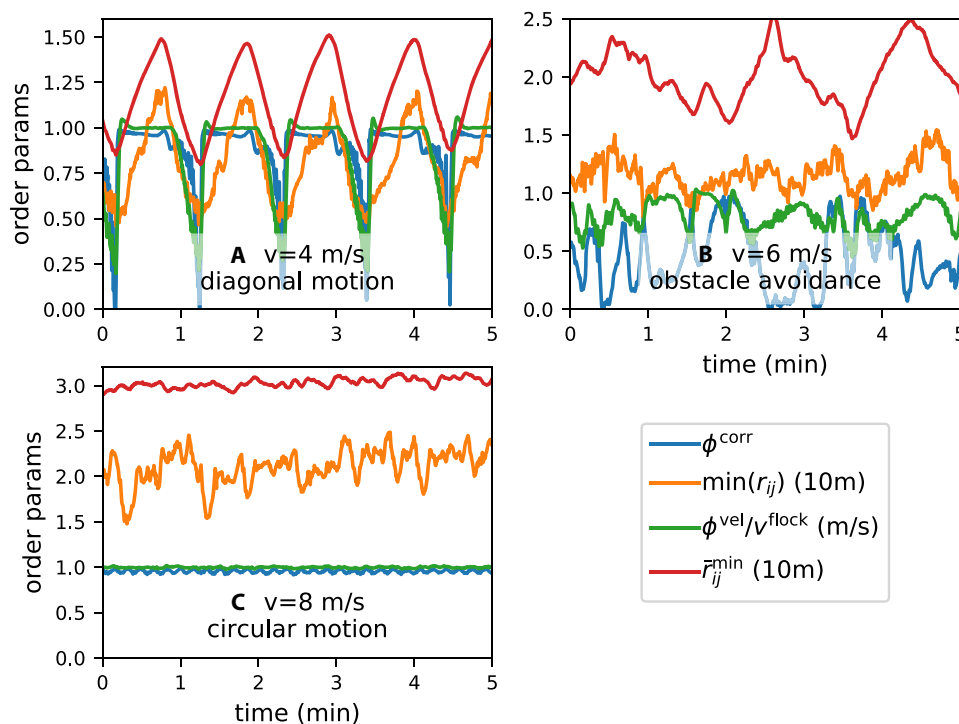


**Fig. 3. Order parameters as a function of time for different  $v^{\text{flock}}$  values during real experiments with 30 drones.**  $\phi^{\text{corr}}$  is the cluster-dependent velocity correlation,  $\phi^{\text{vel}}/v^{\text{flock}}$  is the average normalized velocity, and  $\bar{r}_{ij}^{\text{min}}$  represents the average of the closest neighbors, whereas  $\text{min}(r_{ij})$  is the minimum of the closest neighbors. The depicted region corresponds to the middle 5 min of Fig. 4. There are two typical, mostly stable behaviors in a square-shaped arena without obstacles: (A) shows mostly linear motion along the main diagonals with a cyclic expansion and shrinking of the flock (cyclic red and orange curves) and sudden turns at corners (blue and green curves dropping to zero), whereas (C) shows circular motion within the boundaries (nearly constant order parameters at all times). (B) The repetitive, trivial patterns were broken and became livelier due to obstacles in the way. Correspondingly, velocity correlation and average velocity magnitude drops, whereas minimal interagent distance remains the same, showing the stability of the flight even in this obstructed case.

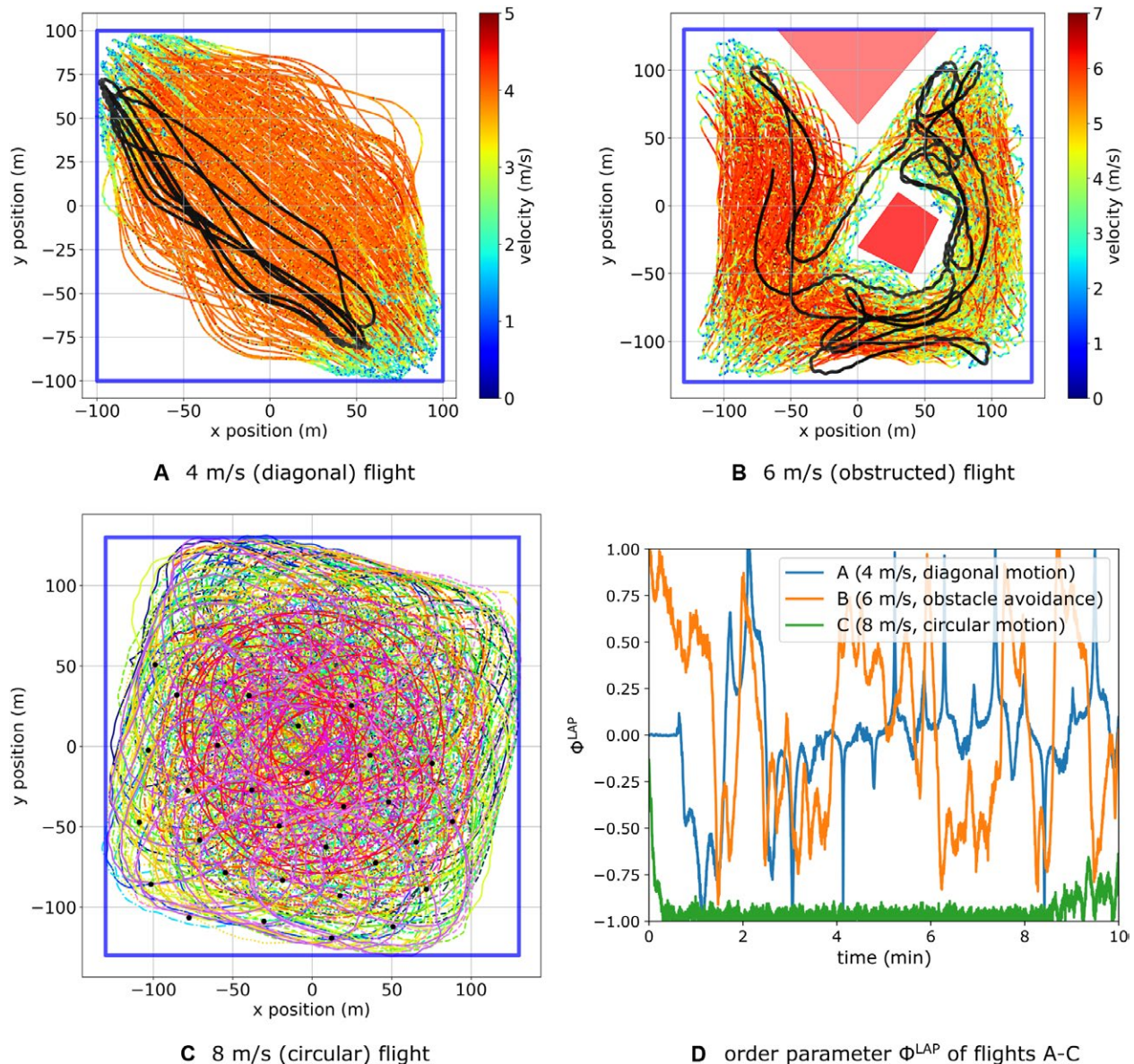


**Fig. 4. Multidrone flight trajectories and corresponding order parameters.** Ten-minute trajectory sections of 30 drones in the horizontal plane for (A) 4 m/s, (B) 6 m/s and (C) 8 m/s flights, representing a selection of typical flight patterns. Blue squares show the boundaries of the virtual arena. (A) The trajectories show diagonal linear motion of the flock, bouncing back from the right-angled corners. Trajectory colors represent speed in the horizontal plane, whereas a random single trajectory is highlighted in gray scale. (B) The motion is still locally correlated, but the obstacles (red shapes) induce a very rich dynamic pattern, resembling lively flocks of birds or other animals. (C) The trajectories show a highly correlated close-to-circular flight. Colors and line styles are mapped to individual drones here; black dots show terminal positions of drones. (D) Comparison of the three qualitatively different behaviors of (A) to (C) with the timeline of a dedicated order parameter: the average normalized velocity, expressed in local angle polar coordinates ( $\phi^{\text{LAP}}$ ).

whereas movies S4 to S6 show the corresponding dynamic flight log visualizations for the three selected flights. Finally, movie S7 shows a summary of the results including actual footage of the flights, too.

As can be seen from the experiments, real drones performed well within the whole tested flocking speed regime. Namely, there are no critical oscillations or collisions with each other, with the wall, or with obstacles. Furthermore, motion is smooth and lively during collective turns when the flock hits the walls, flies into the right-angled corner of the arena, or splits when obstacles are in the way. On the basis of Fig. 3, we can see that, for the flocking speed regime of 4 to 8 m/s, the average closest-neighbor distance varied between 12 and 30 m and the

minimum interagent distance remained between about 5 and 15 m. With Global Navigation Satellite System (GNSS) positioning errors in the range of 2 and 3 m and possible communication outages in the order of 1 s, we believe that these results show a tight and stable flock.

## DISCUSSION

We have presented a tunable distributed flocking model for a large group of autonomous flying robots with which they were capable of maintaining stable, collision-free collective motion in a closed space with or without obstacles, within a large velocity regime. The solution is based on the



**Fig. 5. Long-exposure photo of a flight with multiple drones.** [Credit: Zsolt Bézsényi]

simplest force-based rules presented by the earliest self-propelled particle models, repulsion and alignment, but uses a form of alignment that takes into account the desired acceleration regime of agents. The model works in a noisy environment, with inaccurate sensors and short-range communication devices, and in the presence of substantial communication delay and with possible local communication outages—these are usual features of current outdoor multidrone experimental setups. The model produces a very rich dynamic of motion, especially in an obstructed space, with a variety of emergent collective motion patterns, resembling lively natural flocks.

The model has 11 tunable parameters that call for automated and efficient optimization methods, such as the CMA-ES. With the introduced single-objective fitness function taking into account several important order parameters, we could instantiate our model to find working ranges and optimal parameter setups for a wide range of velocities. Both our optimized simulation results with 30 to 1000 drones and 4 to 32 m/s flocking speeds and our real experiments on 30 drones and 4 to 8 m/s flocking speeds showed stable flocking behavior of agents.

Because of the concept behind the new alignment term, we believe that much higher velocity regimes can be targeted with the same approach, if needed. For this, one would need to have larger interagent distances, larger radii of interactions, and thus proper large-distance communication methods.

Limitations of the general usage of the model could arise from further scaling in the velocity regime and in the number of drones. With 30 drones, we demonstrated an order-of-magnitude scalability relative to the smallest drone swarms of only a few agents; however, further scaling in numbers also implies an increase in emergent pressure among frontal agents facing walls and obstacles, such as that in human crowds, resulting in smaller, possibly dangerous interagent distances. This issue has to be solved in systems with a very high number of agents. A related limiting factor is the large number of necessary parameters that need to be optimized for every system separately. Although we have selected the parameters with special care to have independent meaning and significance, in such a complex system, a deep understanding of the rich dynamic behavior and substantial experience is needed before safely applying the results to other vehicles with different characteristics. A final shortcoming of the present study is the lack of rigorous quantitative analysis of stability, because it is not straightforward

to do in such a high-dimensional parameter space. We avoided this by analyzing the fitness evaluations statistically and gave approximate, independent ranges for the parameters above which fitness is expected to be high. For certain applications, though, a more sophisticated analysis would be more appropriate. Despite these limitations, we believe that the presented concept of velocity alignment, the model in general, together with the fitness evaluation method, can be used optimally in a wide range of multidrone scenarios requiring sophisticated cooperation and/or collaboration.

## MATERIALS AND METHODS

### A tunable self-propelled flocking model

On the basis of statistical-physical methods, a basic flocking model was introduced in (40) and (24). This is a minimal realistic approach of flocking behavior that was demonstrated to work with up to 10 flying robots with a maximum flocking speed of 4 m/s. In this model, the three interaction terms yield a momentary desired velocity vector  $\mathbf{v}^d$ , which has to be achieved by the agents. Of course, maintaining the desired velocity is generally hard due to several robot-specific deficiencies such as communication delays and reaction times, inaccuracy of the onboard sensors, effects of wind, sensor signal outages, inertia etc. The question we examine here is whether there are interactions that can guarantee more stable behavior than previously published attempts under these conditions for larger flocking speeds and also in confined spaces. In the subsections below, we present the exact mathematical formulation of our novel generic flocking model, taking into account the realistic limitations of autonomous flying agents with the explicit treatment of motion constraints in the equations.

### Repulsion

For local repulsion, we choose a simple half-spring model, that is, a linear distance-dependent central velocity term with a cutoff at a maximum interaction range,  $r_0^{\text{rep}}$ , under which agents start to repulse each other:

$$v_{ij}^{\text{rep}} = \begin{cases} p^{\text{rep}} \cdot (r_0^{\text{rep}} - r_{ij}) \cdot \frac{r_i - r_j}{r_{ij}} & \text{if } r_{ij} < r_0^{\text{rep}} \\ 0 & \text{otherwise} \end{cases} \quad (2)$$

In the equation above,  $p^{\text{rep}}$  is the linear gain of the pairwise repulsion and  $r_{ij} = |\mathbf{r}_i - \mathbf{r}_j|$  is the distance between agents  $i$  and  $j$ . The total repulsion term calculated for agent  $i$  with respect to the other agents is

$$\mathbf{v}_i^{\text{rep}} = \sum_{j \neq i} \mathbf{v}_{ij}^{\text{rep}} \quad (3)$$

where  $j$  is iterated for all other agents. Note that we have experimented with more complex repulsion functions in the  $v(r)$  plane (40, 48), but according to our experience, the half-spring model is sufficiently simple and effective at the same time.

### Velocity alignment

Pairwise velocity alignment can be obtained with a velocity term that depends on the difference of the velocity vectors of nearby agents. Previous works typically used a power law of the velocity difference of the interacting agents decaying in space asymptotically to zero (49, 50). These models work fine in some specific conditions, within a lower velocity regime. However, our objectives regarding the velocity alignment are complex. It is the very term that synchronizes motion to achieve collective flocking behavior, but it also has to serve as a damping medium, reducing self-excited oscillations emerging due to the delayed and noisy response to for example, repulsion. It has to be local, but it also has to be scalable for large velocities (and therefore large possible velocity differences) at the same time. This last condition implies that if the acceleration of the agents is limited, large velocity differences should be relaxed at larger distances to avoid collisions.

To fulfill all the requirements above, as a theoretical basis for the velocity alignment term, we have chosen an ideal braking curve, that is, a smooth velocity decay function in space [denoted by  $D(\cdot)$ ], with constant acceleration at high speeds and exponential approach in time at low speeds (51):

$$D(r, a, p) = \begin{cases} 0 & \text{if } r \leq 0 \\ rp & \text{if } 0 < rp < a/p \\ \sqrt{2ar - a^2/p^2} & \text{otherwise} \end{cases} \quad (4)$$

where  $r$  is the distance between an agent and an expected stopping point,  $a$  is the preferred acceleration, and  $p$  is a linear gain also determining the crossover point between the two phases of deceleration.

The rationale behind our velocity alignment term is to prohibit two agents having a larger velocity difference at a given distance than what is allowed by this ideal braking curve and, thus, to serve as kind of a motion planning term in the otherwise momentary force-based equations (see Fig. 6 for a visual representation):

$$v_{ij}^{\text{frictmax}} = \max\left(v_{ij}^{\text{frict}}, D(r_{ij} - r_0^{\text{frict}}, a^{\text{frict}}, p^{\text{frict}})\right), \quad (5)$$

$$v_{ij}^{\text{frict}} = \begin{cases} C^{\text{frict}}(v_{ij} - v_{ij}^{\text{frictmax}}) \cdot \frac{v_i - v_j}{v_{ij}} & \text{if } v_{ij} > v_{ij}^{\text{frictmax}} \\ 0 & \text{otherwise} \end{cases} \quad (6)$$

In the equations above,  $C^{\text{frict}}$  is a linear coefficient of the velocity alignment error reduction,  $v^{\text{frict}}$  is a velocity slack to allow for certain amount of velocity difference independently of interagent distance,  $r_0^{\text{frict}}$  is the distance of the stopping point for agent  $i$  relative to and in

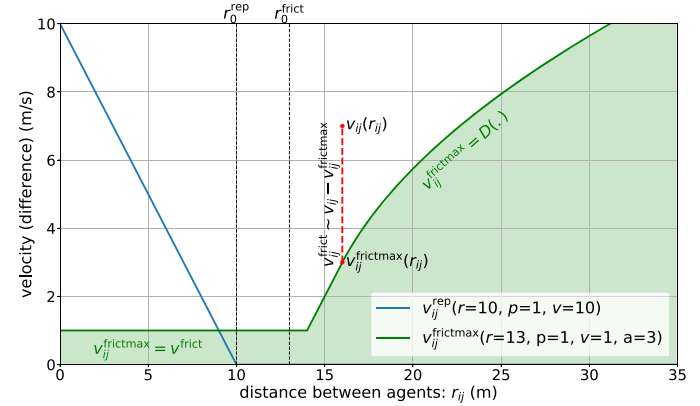


**Fig. 6. Visual explanation of the interaction terms.** The blue line depicts repulsion between agents as a function of interagent distance. The green line is the maximum allowed velocity difference between agents as a function of interagent distance. The velocity alignment term is proportional to the difference between this and the actual velocity difference between agents (red dashed line). All exemplary parameter values are in SI units.

front of agent  $j$ ,  $p^{\text{frict}}$  and  $a^{\text{frict}}$  are the linear gain and the acceleration parameters of the pairwise alignment, and  $v_{ij} = |\mathbf{v}_i - \mathbf{v}_j|$  is the amplitude of the velocity difference between agents  $i$  and  $j$ . The total velocity alignment term calculated for agent  $i$  with respect to the other agents—similarly to the repulsion term—is

$$\mathbf{v}_i^{\text{frict}} = \sum_{j \neq i} \mathbf{v}_{ij}^{\text{frict}} \quad (7)$$

where  $j$  is iterated for all other agents. Note that the superscript “frict” comes from the concept that velocity alignment should be a strong local velocity-damping term, analogous to viscous friction (24).

In addition, the locality condition of the velocity alignment in this form is only implicitly included: The interaction range is upper bounded by the distance where  $D(\cdot) = 2v^{\text{max}}$ . On the other hand, this solution allows for flexible scalability in the velocity domain. If the flocking speed is much higher, then it is obviously preferable to start reducing velocity difference at a much larger distance (as an analogy, compare the deceleration behavior and braking distances of a toy drone against an object and a large manned aircraft reaching its destination).

### Interaction with walls and obstacles

Long-range attraction (7) is not explicitly part of our flocking system. To keep agents together, we instead define a bounded flight arena for the agents surrounded with soft repulsive virtual walls. One of the ideal ways to define such repulsion is to define virtual “shill” agents near the arena walls (52). These virtual agents are heading toward the arena with a certain speed,  $v^{\text{shill}}$ . The real agents close to the walls should relax their velocity to the velocity of the shill agents. We do this here with the velocity alignment term introduced before:

$$v_{is}^{\text{shillmax}} = D(r_{is} - r_0^{\text{shill}}, a^{\text{shill}}, p^{\text{shill}}) \quad (8)$$

$$v_{is}^{\text{wall}} = \mathbf{v}_{is}^{\text{frict}}(C - 1) = \begin{cases} (v_{is} - v_{is}^{\text{shillmax}}) \cdot \frac{v_i - v_s}{v_{is}} & \text{if } v_{is} > v_{is}^{\text{shillmax}} \\ 0 & \text{otherwise} \end{cases} \quad (9)$$

These equations are very similar to Eqs. 5 and 6, with two simplifications: We do not allow velocity slack for the wall and keep the error proportional term ( $C^{\text{shill}}$ ) at 1 to have the strongest shill alignment possible. In the equations above, the index  $s$  refers to the shill agents defined for all wall polygon edges separately;  $r_{is} = |\mathbf{r}_i - \mathbf{r}_s|$ , where  $\mathbf{r}_s$  is the position of the shill agent, located at the closest point of the given edge of an arbitrarily shaped convex wall polygon relative to agent  $i$ ;  $v_{is} = |\mathbf{v}_i - \mathbf{v}_s|$ , where  $\mathbf{v}_s$  is the velocity of the shill agent, pointing perpendicularly to the wall polygon edge inward the arena, with magnitude  $v^{\text{shill}}$ .

Convex obstacles inside the arena can be avoided with the same concept, but with shill agents moving outward from the obstacle, not inward, as described above for the arena. Another difference is that, whereas all wall polygon edges generate a separate shill agent inside the arena, obstacles are represented with a single shill agent located at the closest point of the obstacle polygon relative to the agent. Thus, for every agent  $i$  and obstacle  $s$ , we can define a velocity component  $\mathbf{v}_{is}^{\text{obstacle}}$  similarly to Eq. 9, using the same shill parameters as for the wall.

**Self-propelling term**

Besides the agent-agent and agent-wall interactions introduced above, a simple self-propelling term is added to the desired velocity of the agents. For the  $i$ th agent, this term is parallel with the actual velocity vector,  $\mathbf{v}_i$ , and has a certain constant magnitude,  $v^{\text{flock}}$ .

**Final equation of desired velocity**

To calculate the desired velocity, we take the vectorial sum of all the interaction terms introduced before:

$$\tilde{\mathbf{v}}_i^d = \frac{\mathbf{v}_i}{|\mathbf{v}_i|} v^{\text{flock}} + \mathbf{v}_i^{\text{rep}} + \mathbf{v}_i^{\text{frict}} + \sum_s \mathbf{v}_{is}^{\text{wall}} + \sum_s \mathbf{v}_{is}^{\text{obstacle}} \quad (10)$$

After this superposition, we also introduced a cutoff at  $v^{\text{max}}$ , keeping the direction of the desired velocity but reducing its magnitude if it is over the limit:

$$\mathbf{v}_i^d = \frac{\tilde{\mathbf{v}}_i^d}{|\tilde{\mathbf{v}}_i^d|} \cdot \min\left\{|\tilde{\mathbf{v}}_i^d|, v^{\text{max}}\right\} \quad (11)$$

In the flocking model above, we have introduced a substantial number of parameters to give the necessary degree of freedom to the general model. To help readers understand complex model behavior, we provide an overview of the parameters with detailed descriptions on meaning and usage (table S3).

Tuning the above model means that we choose an optimal set of parameters for a fixed flocking speed  $v^{\text{flock}}$  and maximal speed  $v^{\text{max}}$  for a given arena with characteristic size  $L^{\text{arena}}$ . The other parameters (namely,  $r_0^{\text{rep}}, p^{\text{rep}}, r_0^{\text{frict}}, C^{\text{frict}}, v^{\text{frict}}, p^{\text{frict}}, a^{\text{frict}}, r_0^{\text{shill}}, v^{\text{shill}}, p^{\text{shill}}$ , and  $a^{\text{shill}}$ ) have to be optimized. Note that the parameter space is 11-dimensional; therefore, manual tuning, global optimization methods, or parameter sweeping would be generally too time-consuming.

**General model of a flying robot**

For testing any flocking algorithm in a realistic environment before actual flights, we used a simulation framework, which was originally developed for modeling special features of flying robots based on second-order ordinary differential equations. In this subsection, we

present only the main features of this framework, without details. For further details, see (40) or download the simulation framework from <https://github.com/csviragh/robotsim>. The following general features of flying robots can be taken into account with our framework:

(1) Communication delay. The position and velocity data received by an agent from neighboring agents are old due to the necessary time for data transmission and processing. In the simplest case, we modeled this effect with a constant time delay  $t^{\text{del}}$ .

(2) Inertia. A flying robot cannot change its velocity immediately because of its mass, aerodynamic effects, and specific features of its low-level control algorithm. We assumed that the real velocity  $\mathbf{v}_i$  converges to the desired velocity  $\mathbf{v}_i^d$  exponentially with a characteristic time  $\tau^{\text{CTRL}}$ . A maximal acceleration of the units ( $a^{\text{max}}$ ) is also assumed.

(3) Refresh rate of the sensors. The agents cannot update their sensory data continuously, only with a nonzero time period  $t^s$ . For simplicity, in the simulation framework, this parameter is constant and uniform for all agents.

(4) Locality of the communication. If two agents are too far from each other, they cannot exchange messages; that is, they do not see each other. This is a common feature of any decentralized, radio-based communication device. For modeling this effect, a maximum communication range  $r^c$  is defined in our approach.

(5) Inaccuracy of the onboard sensors. We also had to model the fluctuating behavior of measured positions and velocities. This behavior can be described as a stochastic process. For the  $i$ th agent, this process can be chosen as a fictive Langevin equation with a Gaussian noise term and a parabolic potential centered at  $\mathbf{r}_i$ . The noise can be characterized by its SD  $\sigma^s$ .

(6) Outer noises. To take into account the environmental effects such as wind compensation of the low-level control algorithm, we added a delta-correlated Gaussian noise term with SD  $\sigma$  to the acceleration of the robots.

According to the list above, one can define a simulated realistic homogeneous multirobot system by giving certain values to all elements of the set  $\{t^{\text{del}}, \tau^{\text{CTRL}}, a^{\text{max}}, r^c, t^s, \sigma^s, \sigma\}$ . We presented the optimization through a realistic example based on measurements performed with quadcopters [for further details, see (24, 40)]; we chose the values listed in table S5.

Note that we prefer and tend to overestimate the errors compared with their real mean value to simulate worst-case scenarios. This makes model selection and optimization harder, but once a proper solution is found, it will ensure a larger stability range in real experiments.

**Order parameters**

In this subsection, the quantitative requirements of stability and coherence of a flock will be discussed. To this end, we used three measures: coherence, collision avoidance, and obstacle avoidance. Coherence is frequently described by the spatial velocity correlation, which is a commonly accepted order parameter of collective motion. However, on a large area, correlated subflock clusters without global coherence can also be treated as a reasonably good solution for flocking. Therefore, it is practical to measure the correlation function only within connected clusters. To define clusters, we defined a communication graph that contains the agents as nodes. An edge exists between two nodes if the agents referred by the nodes are closer to each other than a given  $r^{\text{cluster}}$ , typically defined by the range of interactions. We used the value

$$r^{\text{cluster}} = \max\left(r_0^{\text{rep}}, r_0^{\text{frict}} + \tilde{D}(v^{\text{flock}}, a^{\text{frict}}, p^{\text{frict}})\right) \quad (12)$$

where  $\tilde{D}(v, a, p)$  is the braking distance  $r$  for which  $D(r, a, p) = v$ .

Let  $N$  be the number of agents,  $N_i$  be the number of agents in the cluster that contains the  $i$ th agent, and let  $J_i$  refer to the set of indices of agents that are in the same cluster as the  $i$ th agent. On the basis of these notations, the expression of cluster-dependent velocity correlation takes the following form:

$$\phi^{\text{corr}} = \frac{1}{T} \frac{1}{N} \int_0^T \sum_{i=1}^N \frac{1}{N_i - 1} \sum_{j \in J_i} \frac{\mathbf{v}_i \cdot \mathbf{v}_j}{|\mathbf{v}_i| |\mathbf{v}_j|} dt \quad (13)$$

This value needs to be maximized. Besides high velocity correlation inside clusters, one can characterize the flock with properties of the communication graph itself. For example, the number of disconnected points ( $N^{\text{disc}}$ , referring to agents that cannot communicate with any other agents) can be measured, or a minimum cluster size ( $N^{\text{min}}$ ) can be defined as an error threshold for avoiding the situation where only very small groups of agents are present in the system. Of course, the minimum cluster size should depend on the total number of agents. For intuitive reasons, we chose  $N^{\text{min}} > N/5$  as an experimentally good lower threshold.

The next important requirement is collision-free motion. We defined a characteristic distance  $r^{\text{coll}} = 3$  m, which refers to a dangerous zone around agents. If two agents are closer to each other than  $r^{\text{coll}}$ , a dangerous situation (collision) occurs. During algorithm tuning, the number of collisions should be minimized, which is similar to minimizing the following parameter, the so-called collision risk:

$$\phi^{\text{coll}} = \frac{1}{T} \frac{1}{N(N-1)} \int_0^T \sum_{i=1}^N \sum_{j \neq i} \Theta(r_{ij}(t) - r^{\text{coll}}) dt \quad (14)$$

where  $\Theta(\cdot)$  is the Heaviside step function.

With the wall-agent interaction velocity term defined as Eq. 9, one can restrict the motion of the flocking agents into a closed space, which can be viewed as a method for maintaining the cohesiveness of the group (this is a general criterion of flocking behavior) but also can be treated as a general approach of obstacle avoidance, which is a common task in collective robotics. Below, we define an order parameter for calculating the possible collisions with the walls of the arena or obstacles (this parameter has to be minimized):

$$\phi^{\text{wall}} = \frac{\int_0^T \sum_{i=1}^N \Theta(\tilde{r}_{is}(t)) \tilde{r}_{is}(t) dt}{\int_0^T \sum_{i=1}^N \Theta(\tilde{r}_{is}(t)) dt} \quad (15)$$

where  $\tilde{r}_{is}$  is the signed form of  $r_{is}$ , taking a positive value outside, and a negative value inside, the arena (and the opposite for obstacles), assuring that the calculation of the average is performed only at the points where the agents are outside of the arena (or inside obstacles).

With the parameters presented above, one can define a quantitative criterion for safe flocking behavior for the simulated (or real) robots, namely,  $\phi^{\text{corr}} \rightarrow 1$ ,  $\phi^{\text{coll}} \rightarrow 0$ ,  $\phi^{\text{wall}} \rightarrow 0$ , and  $N^{\text{min}} > N/5$ .

Finally, we also require the flock to move with a certain flocking speed:

$$\phi^{\text{vel}} := \frac{1}{T} \frac{1}{N} \int_0^T \sum_{i=1}^N |\mathbf{v}_i(t)| dt \rightarrow v^{\text{flock}} \quad (16)$$

### Fitness function

Instead of parameter sweeping or any relatively slow global optimization method, the search for the optimal values of the 11 model parameters

( $r_0^{\text{rep}}$ ,  $p^{\text{rep}}$ ,  $r_0^{\text{frict}}$ ,  $C^{\text{frict}}$ ,  $v^{\text{frict}}$ ,  $p^{\text{frict}}$ ,  $a^{\text{frict}}$ ,  $r_0^{\text{shill}}$ ,  $v^{\text{shill}}$ ,  $p^{\text{shill}}$ , and  $a^{\text{shill}}$ ) is known to be much more efficient by using evolutionary optimization. Within such a framework with the defined set of order parameters, one can choose between single- or multiobjective evolutionary algorithms. We chose using a single-valued fitness function that contains several criteria about the order parameters presented in the previous subsection. According to these assumptions, a global fitness function can be defined using three different types of transfer functions (the value of these functions should be between 0 and 1).

The first type is a monotonically growing function,  $F_1(\phi)$ , which converges to 1 with increasing  $\phi$ :

$$F_1(\phi, \phi_0, d) = 1 - S(\phi, \phi_0, d) \quad (17)$$

where  $S(x, x_0, d)$  is a sigmoid function with a smooth sinusoidal decay from  $x_0 - d$  to  $x_0$ :

$$S(x, x_0, d) = \begin{cases} 1 & \text{if } x < x_0 - d, \\ \frac{1}{2} \left( 1 - \cos\left(\frac{\pi}{d}(x - x_0)\right) \right) & \text{if } x_0 - d < x < x_0 \\ 0 & \text{otherwise} \end{cases} \quad (18)$$

The second transfer function is derived from the probability density of the normal distribution, with a single maximum at  $\phi = 0$  and a smooth decay around it:

$$F_2(\phi, s) = \exp\left(-\frac{\phi^2}{s^2}\right) \quad (19)$$

Finally, the third transfer function is a sharp peak, which gives a harsh constraint to the fitness around  $\phi = 0$ :

$$F_3(\phi, a) = \frac{a^2}{(\phi + a)^2} \quad (20)$$

A visual illustration of the shape of the three transfer functions is given in Fig. 7. With these transfer functions, we can construct a single-objective fitness function that takes into account all necessary requirements of safe flocking behavior:

$$F = F^{\text{speed}} \cdot F^{\text{coll}} \cdot F^{\text{disc}} \cdot F^{\text{cluster}} \cdot F^{\text{wall}} \cdot F^{\text{corr}} \quad (21)$$

where

$$\begin{cases} F^{\text{speed}} = F_1(\phi^{\text{vel}}, v^{\text{flock}}, v^{\text{tol}}), \\ F^{\text{coll}} = F_3(\phi^{\text{coll}}, a^{\text{tol}}), \\ F^{\text{disc}} = F_3(N^{\text{disc}}, N/5), \\ F^{\text{cluster}} = F_3(N^{\text{min}}, N/5, N/5), \\ F^{\text{wall}} = F_2(\phi^{\text{wall}}, r^{\text{tol}}), \\ F^{\text{corr}} = \Theta(\phi^{\text{corr}}) \phi^{\text{corr}} \end{cases} \quad (22)$$

and  $v^{\text{tol}}$ ,  $a^{\text{tol}}$ , and  $r^{\text{tol}}$  are tolerance values for speed, collision risk, and collisions with walls and obstacles, respectively. These tolerance

values can be chosen arbitrarily, depending on the absolute and relative importance of the partial fitness components in the optimization. We chose  $v^{\text{tol}} = \frac{1.5}{4} v^{\text{flock}}$  m/s,  $a^{\text{tol}} = 0.00003$ , and  $r^{\text{tol}} = 2$  m, which gave a balanced weighting to the overall fitness function. Note that the order parameter  $\phi^{\text{corr}}$  is present in the fitness function only as a multiplicative term with a cutoff at 0 because its values are originally between  $-1$  and  $1$ .

With this method, we created a single-objective optimization scenario, which can be solved using state-of-the-art evolutionary

algorithms such as the CMA-ES (38, 53). To perform this task, we used an open-source Python library (54), with default settings (see table S6). Parameters were initialized at mid-value, with an initial SD of one-sixth of their allowed range.

**Drone setup**

Our quadcopters use the Pixhawk autopilot (55) for controlling the rotors with a slightly modified ArduPilot controller [see our open-source code that runs on the Pixhawk system at (56)]. We also used an onboard, Linux-based companion minicomputer (Odroid C1+) through which we gave desired velocity commands at 20 Hz to the autopilot. The desired velocity was calculated onboard using the flocking model presented above as the control algorithm.

We used two independent, parallel wireless modules for interagent communication in the 2.4-GHz range, both broadcasting the same status packets. One is an XBee module broadcasting through its own proprietary protocol at 1 Hz; the other one is a small universal serial bus (USB) wifi dongle (Odroid Wifi Module 0) transmitting user datagram protocol (UDP) packets through a local ad hoc wireless network at 10 Hz. The two modules are complementary in bandwidth and range (XBee being small bandwidth and longer range and Wifi being large bandwidth but shorter range). Packets contained an absolute time stamp, geodetic position, and velocity principally measured by onboard GNSS receivers and other safety-related status info about the actual state of the drone that was not relevant to the main control algorithm. Relative position and velocity were calculated by the differences of GNSS-based absolute measurements. The net payload size of a status packet was 46 bytes.

Because of the properties of the wireless media and the broadcasting transport protocols, packet delivery was unreliable; at a transmission

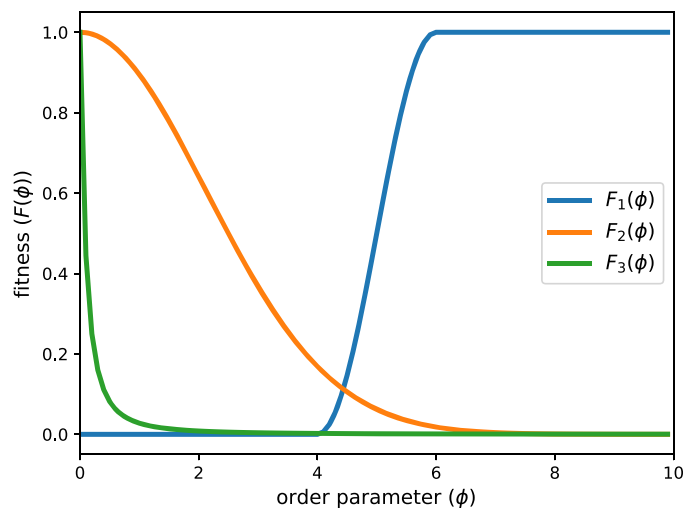


**Fig. 7. Three different types of transfer functions with a codomain of [0,1].** A global single-objective fitness value can be defined as the multiplication of several partial fitness functions based on these transfer functions.

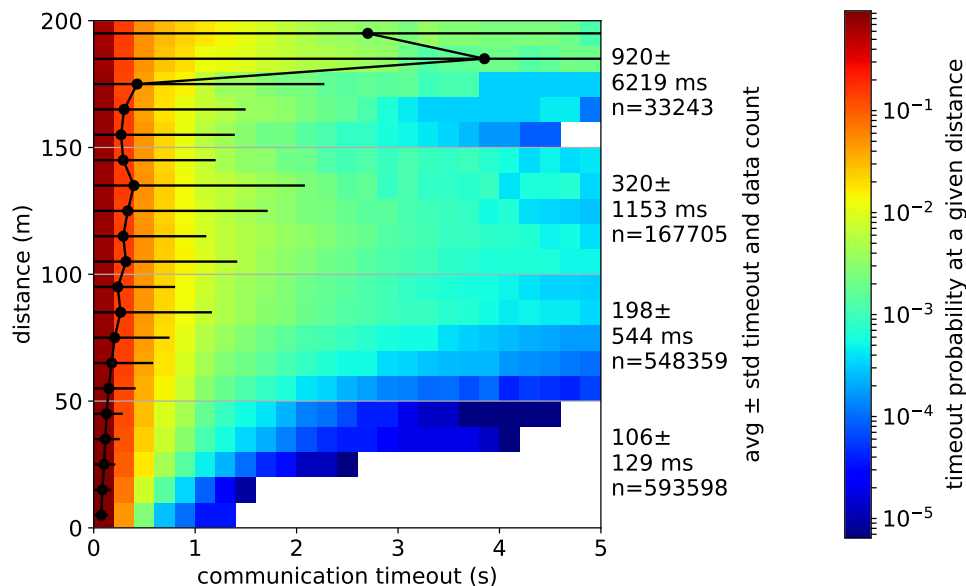


**Fig. 8. Probability distribution of the communication outages as a function of distance.** The database was gathered from a 5-min section of a general flight with 32 drones in a remote open-air setting. Each drone logged a 5-Hz sampling of the elapsed time since the reception of the last status packet from all other drones. This value [we call it timeout for simplicity but it actually also contains a small (<0.2 s) processing delay] was matched later with the position of the drones recorded accurately by each drone onboard. The distribution shows logs from all drones (1,349,490 data points in total), and it is normalized for each row (distance) separately. Color indicates timeout probability in each bin for a given distance. Average timeouts with SD and with the number of data points are indicated on the right for 50-m distance binning, whereas the black line on the plot indicates average and SD of timeout for each distance bin of 10 m. Database is very sparse and thus less accurate above 150 m, but as a general tendency, communication is most stable between close-by drones, whereas outages were more frequent and longer with increasing distance.

frequency of 10 + 1 status packets sent per second per UAV, typically only around 40 to 80% of them were received by close-by peers on average in a general flight with 30 drones, where the reception rate was dependent on many factors, such as the bandwidth usage of other nearby wireless solutions or the details of the surrounding environment. Because signal power decays quickly with space [ideally at  $1/r^2$  in open space (57)], reception from nearby agents (<20 m) was nearly perfect, whereas large communication outages started to occur at larger distances (>50 m). As an illustration of the actual communication characteristics, a detailed log of the distance dependence of the reception quality from a 5-min sample flight with 32 drones can be seen in Fig. 8. Note that the observed spatial decay fits naturally into our targeted distributed communication approach for two reasons: (i) the most critical information comes from the closest agents, which is always the most reliable, and (ii) the communication network naturally becomes scalable with flock size as the bandwidth overlap decays with distance.

There is a trivial reality gap in the communication aspects: Simulations contain constant delay and communication range, whereas the real setup was more stochastic and distance-dependent. Furthermore, in the real setup, we compensated for communication outages to some extent with linearly extrapolating neighboring drone positions using the global time stamps and velocity. With this approach, our overall aim was to have the safest real system possible and an underestimated communication quality through the model design phase to be prepared for a worst-case communication scenario. As a result, with this setup, we did not experience any mission-critical communication outage so far.

## SUPPLEMENTARY MATERIALS

robotics.sciencemag.org/cgi/content/full/3/20/eaat3536/DC1

Movie S1. Simulation of the old flocking model (algorithm A) with 100 agents.

Movie S2. Simulation of the new flocking model (algorithm B) after evolutionary optimization with 100 agents.

Movie S3. Simulation of flocking for different speeds (4 to 32 m/s), flock sizes (30 to 1000 agents), and scenarios.

Movie S4. Flight log visualization of 30 drones at 4 m/s in a diagonal flight pattern.

Movie S5. Flight log visualization of 30 drones at 6 m/s with obstacles.

Movie S6. Flight log visualization of 30 drones at 8 m/s in a circular flight pattern.

Movie S7. Summarizing documentary with simulation, flight log visualization, and footage on real flights.

Table S1. Optimized model parameter values and working ranges in simulation.

Table S2. Statistic evaluation of optimized simulations.

Table S3. Explanation of flocking model parameters.

Table S4. Model parameter values used on real drones.

Table S5. Environmental parameters of the realistic setup.

Table S6. Parameter settings of the evolutionary optimization.

## REFERENCES AND NOTES

1. P. DeLellis, G. Poverino, G. Ustuner, N. Abaid, S. Macri, E. M. Bollt, M. Porfiri, Collective behaviour across animal species. *Sci. Rep.* **4**, 3723 (2014).
2. J. Buhl, D. J. T. Sumpter, I. D. Couzin, J. J. Hale, E. Despland, E. R. Miller, S. J. Simpson, From disorder to order in marching locusts. *Science* **312**, 1402–1406 (2006).
3. A. Attanasi, A. Cavagna, L. Del Castello, I. Giardina, T. S. Grigera, A. Jelić, S. Melillo, L. Parisi, O. Pohl, E. Shen, M. Viale, Information transfer and behavioural inertia in starling flocks. *Nat. Phys.* **10**, 615–698 (2014).
4. M. Ballerini, N. Cabibbo, R. Candelier, A. Cavagna, E. Cisbani, I. Giardina, V. Lecomte, A. Orlandi, G. Parisi, A. Procaccini, M. Viale, V. Zdravkovic, Interaction ruling animal collective behavior depends on topological rather than metric distance: Evidence from a field study. *Proc. Natl. Acad. Sci. U.S.A.* **105**, 1232–1237 (2008).
5. U. Lopez, J. Gautrais, I. D. Couzin, G. Theraulaz, From behavioural analyses to models of collective motion in fish schools. *Interface Focus* **2**, 693–707 (2012).
6. H. Hildenbrandt, C. Carere, C. K. Hemelrijk, Self-organized aerial displays of thousands of starlings: A model. *Behav. Ecol.* **21**, 1349–1359 (2010).
7. C. W. Reynolds, Flocks, herds, and schools: A distributed behavioral model. *ACM SIGGRAPH Comput. Graph.* **21**, 25–34 (1987).
8. T. Vicsek, A. Zafeiris, Collective motion. *Phys. Rep.* **517**, 71–140 (2012).
9. B. T. Fine, D. A. Shell, Unifying microscopic flocking motion models for virtual, robotic, and biological flock members. *Auton. Robots* **35**, 195–219 (2013).
10. E. Méhes, T. Vicsek, Collective motion of cells: From experiments to models. *Integr. Biol.* **6**, 831–854 (2014).
11. M. Brambilla, E. Ferrante, M. Birattari, M. Dorigo, Swarm robotics: A review from the swarm engineering perspective. *Swarm Intell.* **7**, 1–41 (2013).
12. D. Floreano, R. J. Wood, Science, technology and the future of small autonomous drones. *Nature* **521**, 460–6 (2015).
13. International Organization for Standardization (ISO), *ISO 8373:2012, Robots and Robotic Devices—Vocabulary* (ISO, 2012).
14. A. E. Turgut, H. Çelikkanat, F. Gökçe, E. Şahin, Self-organized flocking in mobile robot swarms. *Swarm Intell.* **2**, 97–120 (2008).
15. F. Gökçe, E. Şahin, To flock or not to flock: The pros and cons of flocking in long-range “migration” of mobile robot swarms, in *Proceedings of The 8th International Conference on Autonomous Agents and Multiagent Systems—Volume 1* (International Foundation for Autonomous Agents and Multiagent Systems, 2009), pp. 65–72.
16. D. Helbing, I. Farkas, T. Vicsek, Simulating dynamical features of escape panic. *Nature* **407**, 487–490 (2000).
17. B. Liu, T. Chu, L. Wang, Stability and oscillation of swarm with interaction time delays, in *2007 American Control Conference (ACC’07)* (IEEE, 2007), pp. 4600–4605.
18. E. Forgoston, I. B. Schwartz, Delay-induced instabilities in self-propelling swarms. *Phys. Rev. E* **77**, 035203 (2008).
19. Z. Yang, Q. Zhang, Z. Jiang, Z. Chen, Flocking of multi-agents with time delay. *Int. J. Syst. Sci.* **43**, 2125–2134 (2012).
20. B. Lindley, L. Mier-y Teran-Romero, I. B. Schwartz, Noise induced pattern switching in randomly distributed delayed swarms, in *2013 American Control Conference (ACC’13)* (IEEE, 2013), pp. 4587–4591.
21. S. K. Armah, S. Yi, Analysis of time delays in quadrotor systems and design of control, in *Time Delay Systems* (Springer, 2017), pp. 299–313.
22. R. Olfati-Saber, Flocking for multi-agent dynamic systems: Algorithms and theory. *IEEE Trans. Automat. Contr.* **51**, 401–420 (2006).
23. R. Olfati-Saber, R. M. Murray, Consensus problems in networks of agents with switching topology and time-delays. *IEEE Trans. Automat. Contr.* **49**, 1520–1533 (2004).
24. G. Vásárhelyi, Cs. Virágh, G. Somorjai, N. Tarcai, T. Szörényi, T. Nepusz, T. Vicsek, Outdoor flocking and formation flight with autonomous aerial robots, in *2014 IEEE/RSJ International Conference on Intelligent Robots and Systems (IROS 2014)* (IEEE, 2014), pp. 3866–3873.
25. K. Kaplan, “500 drones light night sky to set record,” *iQ by Intel*, 4 November 2016; <https://iq.intel.com/500-drones-light-show-sets-record/>.
26. Ehang, China; [www.ehang.com/formation/](http://www.ehang.com/formation/).
27. M. Waibel, B. Keays, F. Augugliaro, “Drone shows: Creative potential and best practices,” *Verity Studios*, January 2017; <http://veritystudios.com/whitepaper/>.
28. “Department of Defense Announces Successful Micro-Drone Demonstration,” *U.S. Department of Defense*, 9 January 2017; [www.defense.gov/News/News-Releases/News-Release-View/Article/1044811/departement-of-defense-announcessuccessful-micro-drone-demonstration/](http://www.defense.gov/News/News-Releases/News-Release-View/Article/1044811/departement-of-defense-announcessuccessful-micro-drone-demonstration/).
29. A. Kushleyev, D. Mellinger, C. Powers, V. Kumar, Towards a swarm of agile micro quadrotors. *Auton. Robots* **35**, 287–300 (2013).
30. J. A. Preiss, W. Honig, G. S. Sukhatme, N. Ayanian, CrazySwarm: A large nano-quadcopter swarm, in *2017 IEEE International Conference on Robotics and Automation (ICRA)* (IEEE, 2017), pp. 3299–3304.
31. S. Hauert, S. Leven, M. Varga, F. Ruini, A. Cangelosi, J.-C. Zufferey, D. Floreano, Reynolds flocking in reality with fixed-wing robots: Communication range vs. maximum turning rate, in *2011 IEEE/RSJ International Conference on Intelligent Robots and Systems* (IEEE, 2011), pp. 5015–5020.
32. A. Pospischil, “Mapping ad hoc communications network of a large number fixed-wing uav swarm,” thesis, Naval Postgraduate School, Monterey, California (2017).
33. R. G. Braga, R. C. da Silva, A. C. Ramos, F. Mora-Camino, Collision avoidance based on Reynolds rules: A case study using quadrotors, in *Information Technology—New Generations* (Springer, 2018), pp. 773–780.
34. S. A. Quintero, G. E. Collins, J. P. Hespanha, Flocking with fixed-wing UAVs for distributed sensing: A stochastic optimal control approach, in *2013 American Control Conference* (IEEE, 2013), pp. 2025–2031.
35. J. L. Sanchez-Lopez, J. Pestana, P. de la Puente, R. Suarez-Fernandez, P. Campoy, A system for the design and development of vision-based multi-robot quadrotor swarms, in *2014 International Conference on Unmanned Aircraft Systems (ICUAS)* (IEEE, 2014), pp. 640–648.
36. A. E. Eiben, J. E. Smith, From evolutionary computation to the evolution of things. *Nature* **521**, 476–482 (2015).
37. A. E. Eiben, J. E. Smith, *Introduction to Evolutionary Computing* (Springer, ed. 2, 2015).

38. N. Hansen, A. Ostermeier, Completely derandomized self-adaptation in evolution strategies. *Evol. Comput.* **9**, 159–195 (2001).
39. Atlasz Supercomputer Cluster Service; <http://hpc.iig.elte.hu/>.
40. C. Virágh, G. Vásárhelyi, N. Tóth, T. Szörényi, G. Somorjai, T. Nepusz, T. Vicsek, Flocking algorithm for autonomous flying robots. *Bioinspir. Biomim.* **9**, 025012 (2014).
41. C. J. Pennycuik, S. Åkesson, A. Hedenström, Air speeds of migrating birds observed by ornithodolite and compared with predictions from flight theory. *J. R. Soc. Interface* **10**, 20130419 (2013).
42. A. Bottinelli, D. T. J. Sumpter, J. L. Silverberg, Emergent structural mechanisms for high-density collective motion inspired by human crowds. *Phys. Rev. Lett.* **117**, 228301 (2016).
43. N. Tóth, C. Virágh, D. Ábel, M. Nagy, P. L. Várkonyi, G. Vásárhelyi, T. Vicsek, Patterns, transitions and the role of leaders in the collective dynamics of a simple robotic flock. *J. Stat. Mech.* **2011**, P04010 (2011).
44. T. Vicsek, Universal patterns of collective motion from minimal models of flocking, in *2008 Second IEEE International Conference on Self-Adaptive and Self-Organizing Systems (IEEE, 2008)*, pp. 3–11.
45. J. Deseigne, S. Léonard, O. Dauchot, H. Chaté, Vibrated polar disks: Spontaneous motion, binary collisions, and collective dynamics. *Soft Matter* **8**, 5629–5639 (2012).
46. I. J. Farkas, T. Vicsek, Patterns in the collective behavior of humans. *AIP Conf. Proc.* **779**, 1–15 (2005).
47. J. L. Silverberg, M. Bierbaum, J. P. Sethna, I. Cohen, Collective motion of humans in mosh and circle pits at heavy metal concerts. *Phys. Rev. Lett.* **110**, 228701 (2013).
48. C. Virágh, M. Nagy, C. Gershenson, G. Vásárhelyi, Self-organized UAV traffic in realistic environments, in *2016 IEEE/RSJ International Conference on Intelligent Robots and Systems (IROS)*, pp. 1645–1652.
49. F. Cucker, S. Smale, Emergent behavior in flocks. *IEEE Trans. Automat. Contr.* **52**, 852–862 (2007).
50. S.-Y. Ha, T. Ha, J.-H. Kim, Emergent behavior of a cucker-smale type particle model with nonlinear velocity couplings. *IEEE Trans. Automat. Contr.* **55**, 1679–1683 (2010).
51. L. Meier, P. Tanskanen, F. Fraundorfer, M. Pollefeys, PIXHAWK: A system for autonomous flight using onboard computer vision, in *2011 IEEE International Conference on Robotics and Automation (IEEE, 2011)*, pp. 2992–2997.
52. J. Han, M. Li, L. Guo, Soft control on collective behavior of a group of autonomous agents by a skill agent. *J. Syst. Sci. Complex.* **19**, 54–62 (2006).
53. N. Hansen, S. D. Müller, P. Koumoutsakos, Reducing the time complexity of the derandomized evolution strategy with covariance matrix adaptation (CMA-ES). *Evol. Comput.* **11**, 1–18 (2003).
54. CMA-ES Python Library; <https://github.com/CMA-ES/pycma>.
55. Pixhawk AutoPilot; <https://pixhawk.org>.
56. CollMot Branch of the ArduCopter codebase on GitHub; <https://github.com/collmot/ardupilot/tree/CMCopter-3.4>.
57. S. Hayat, E. Yanmaz, R. Muzaffar, Survey on unmanned aerial vehicle networks for civil applications: A communications viewpoint. *IEEE Commun. Surv. Tut.* **18**, 2624–2661 (2016).

**Acknowledgments:** The long-exposure photo was taken by Zs. Bézsényi. We are grateful for the help of other members of the robotics team, namely, B. Badár, I. Donkó, and N. Gál, who are not present here as authors, but have made valuable contribution to make our drones fly. **Funding:** This work was partly supported by the following grants: U.S. Air Force grant no. FA9550-17-1-0037, K\_16 Research Grant of the Hungarian National Research, Development and Innovation Office (K 119467), and János Bolyai Research Scholarship of the Hungarian Academy of Sciences (BO/00219/15/6). **Author contributions:** The project was conceived by T.V. Cs.V., G.V., and T.V. developed the concept and algorithms. Cs.V. and G.V. developed the simulation. T.N. and G.V. developed the software for drones. G.S. and G.V. developed the drone hardware. A.E.E. and G.V. implemented the evolutionary optimization framework. T.N., G.S., Cs.V., and G.V. performed drone experiments. The paper was written by A.E.E., Cs.V., G.V., and T.V. **Competing interests:** The authors declare that they have no competing interests. **Data and materials availability:** The project website is <http://hal.elte.hu/drones/>. Flight logs related to the results presented are available at <https://doi.org/10.5061/dryad.mq85r61>. Source code of our robotic simulation framework is available at <https://github.com/csviragh/robotsim>. All other data needed to evaluate the conclusions in the paper are present in the paper or the Supplementary Materials.

Submitted 17 February 2018

Accepted 1 June 2018

Published 18 July 2018

10.1126/scirobotics.aat3536

**Citation:** G. Vásárhelyi, Cs. Virágh, G. Somorjai, T. Nepusz, A. E. Eiben, T. Vicsek, Optimized flocking of autonomous drones in confined environments. *Sci. Robot.* **3**, eaat3536 (2018).

## SENSORS

# Prosthesis with neuromorphic multilayered e-dermis perceives touch and pain

Luke E. Osborn<sup>1\*</sup>, Andrei Dragomir<sup>2</sup>, Joseph L. Betthausen<sup>3</sup>, Christopher L. Hunt<sup>1</sup>, Harrison H. Nguyen<sup>1</sup>, Rahul R. Kaliki<sup>1,4</sup>, Nitish V. Thakor<sup>1,2,3,5\*</sup>

Copyright © 2018  
The Authors, some  
rights reserved;  
exclusive licensee  
American Association  
for the Advancement  
of Science. No claim  
to original U.S.  
Government Works

The human body is a template for many state-of-the-art prosthetic devices and sensors. Perceptions of touch and pain are fundamental components of our daily lives that convey valuable information about our environment while also providing an element of protection from damage to our bodies. Advances in prosthesis designs and control mechanisms can aid an amputee's ability to regain lost function but often lack meaningful tactile feedback or perception. Through transcutaneous electrical nerve stimulation (TENS) with an amputee, we discovered and quantified stimulation parameters to elicit innocuous (nonpainful) and noxious (painful) tactile perceptions in the phantom hand. Electroencephalography (EEG) activity in somatosensory regions confirms phantom hand activation during stimulation. We invented a multilayered electronic dermis (e-dermis) with properties based on the behavior of mechanoreceptors and nociceptors to provide neuromorphic tactile information to an amputee. Our biologically inspired e-dermis enables a prosthesis and its user to perceive a continuous spectrum from innocuous to noxious touch through a neuromorphic interface that produces receptor-like spiking neural activity. In a pain detection task (PDT), we show the ability of the prosthesis and amputee to differentiate nonpainful or painful tactile stimuli using sensory feedback and a pain reflex feedback control system. In this work, an amputee can use perceptions of touch and pain to discriminate object curvature, including sharpness. This work demonstrates possibilities for creating a more natural sensation spanning a range of tactile stimuli for prosthetic hands.

## INTRODUCTION

One of the primary functions of the somatosensory system is to provide exteroceptive sensations to help us perceive and react to stimuli from outside of our body (1). Our sense of touch is a crucial aspect of the somatosensory system and provides valuable information that enables us to interact with our surrounding environment. Tactile feedback, in conjunction with proprioception, allows us to perform many of our daily tasks that rely on the dexterous manipulation of our hands (2). Mechanoreceptors and free nerve endings in our skin give us the means to perceive tactile sensation (2). The primary mechanoreceptors in the glabrous skin that convey tactile information are Meissner corpuscles, Merkel cells, Ruffini endings, and Pacinian corpuscles. The Merkel cells and Ruffini endings are classified as slowly adapting (SA) and respond to sustained tactile loads. Meissner and Pacinian corpuscles are rapidly adapting (RA) and respond to the onset and offset of tactile stimulation (1, 3). More recently, research has shown the role of fingertips in coding tactile information (4) and extracting tactile features (5).

A vital component of our tactile perception is the sense of pain. Although often undesired, pain provides a protection mechanism when we experience a potentially damaging stimulus. In the event of an injury, increased sensitivity can render even innocuous stimuli as painful (6). Nociceptors are dedicated sensory afferents in both glabrous and nonglabrous skin responsible for conducting tactile stimuli that we perceive as painful (6). Nociceptors, free nerve endings in the epidermal layer of the skin, act as high threshold mechanoreceptors (HTMRs) and re-

spond to noxious stimuli through A $\beta$ , A $\delta$ , and C nerve fibers (1), which enable our perception of tactile pain. It was discovered that A $\delta$  fiber HTMRs respond to both innocuous and noxious mechanical stimuli with an increase in impulse frequency while experiencing the noxious stimuli (7). It is also known that mechanoreceptor activation along with nociceptor activation helps inhibit our perception of pain, and our discomfort increases when only nociceptors are active (8), which helps to explain our ability to perceive a range of innocuous and noxious sensations. Although novel approaches have improved prosthesis motor control (9), comprehensive sensory perceptions are not available in today's prosthetic hands.

The undoubted importance of our sense of touch, and lack of sensory capabilities in today's prostheses, has spurred research on artificial tactile sensors and restoring sensory feedback to those with upper limb loss. Novel sensor developments use flexible electronics (10–12), self-healing (13, 14) and recyclable materials (15), mechanoreceptor-inspired elements (16, 17), and even optoelectronic strain sensors (18), which will likely affect the future of prosthetic limbs. Local force feedback to a prosthesis is known to improve grasping (19), but in recent years, there has been a major push toward providing sensory feedback to the prosthesis and the amputee. Groundbreaking results show that implanted peripheral nerve electrodes (20–23) and non-invasive electrical nerve stimulation methods (24) can successfully elicit sensations of touch in the phantom hand of amputees.

Recent approaches aim to mimic the biological behavior of tactile receptors using advanced skin dynamics (25) and what are known as neuromorphic (26) models of tactile receptors for sensory feedback. A neuromorphic system aims to implement components of a neural system, for example, the representation of touch through spiking activity based on biologically driven models. One reason for using a neuromorphic approach is to create a biologically relevant representation of tactile information using actual mechanoreceptor characteristics. Neuromorphic techniques have been used to convey tactile sensations for differentiating textures using SA-like dynamics for the stimulation

<sup>1</sup>Department of Biomedical Engineering, Johns Hopkins School of Medicine, 720 Rutland Avenue, Baltimore, MD 21205, USA. <sup>2</sup>Singapore Institute for Neurotechnology, National University of Singapore, 28 Medical Drive, #05-02, Singapore 117456, Singapore. <sup>3</sup>Department of Electrical and Computer Engineering, Johns Hopkins University, 3400 North Charles Street, Baltimore, MD 21218, USA. <sup>4</sup>Infinite Biomedical Technologies, Johns Hopkins University Eastern Campus, 1101 East 33rd Street, Suite E305, Baltimore, MD 21218, USA. <sup>5</sup>Department of Neurology, Johns Hopkins University, 600 North Wolfe, Baltimore, MD 21205, USA.  
\*Corresponding author. Email: losborn@jhu.edu (L.E.O.); nitish@jhu.edu or eletnv@nus.edu.sg (N.V.T.)

paradigm to an amputee through nerve stimulation (26) and for feedback to a prosthesis to enhance grip functionality (27). Although important, methods of sensory feedback have been limited to sensations of pressure (21), proprioception (23), and texture (26), even though our perception of tactile information culminates in a sophisticated, multifaceted sensation that also includes stretch, temperature, and pain.

Current forms of tactile feedback fail to address the potentially harmful mechanical stimulations that could result in damage to cutaneous tissue or, in this context, to the prosthesis itself. We investigated the idea that a sensation of pain could benefit a prosthesis by introducing a sense of self-preservation and the ability to automatically release an object when pain is detected. Specifically, we implemented a pain reflex in prosthesis hardware that mimics the functionality of the polysynaptic pain reflex found in biology (28–30). Pain serves multiple purposes in that it allows us to convey useful information about the environment to the amputee user while also preventing damage to the fingertips or cosmesis, a skin-like covering, of a prosthetic hand. It is worth noting that an ideal prosthesis would allow the user to maintain complete control and overrule pain reflexes if desired. However, in this paper, we focus on the ability to detect pain through a neuromorphic interface and initiate an automated pain reflex in the prosthesis.

We postulate that the presence of both innocuous and noxious tactile signals will help in creating more advanced and realistic prosthetic limbs by providing a more complete representation of tactile information. We developed a multilayered electronic dermis (e-dermis) and neuromorphic interface to provide tactile information to enable the perception of touch and pain in an upper limb amputee and prosthesis. We show closed-loop feedback to a transhumeral amputee through transcutaneous electrical nerve stimulation (TENS) to elicit either innocuous or painful sensations in the phantom hand based on the area of activation on a prosthesis (Fig. 1). Furthermore, we identified features of peripheral nerve stimulation, specifically pulse width and frequency, that play key roles in providing both innocuous and noxious tactile feedback. Quantifying the differences in perception of sensory feedback, specifically innocuous and noxious sensations, adds dimensionality and breadth to the type and amount of information that can be transmitted to an upper limb amputee, which aids in object discrimination. Finally, we demonstrate the ability of the prosthesis and the user to differentiate between safe (innocuous) and painful (noxious) tactile sensations dur-

ing grasping and to react appropriately using a prosthesis reflex, modeled as a polysynaptic withdrawal reflex, to prevent damage and further pain.

## RESULTS

### Biologically inspired e-dermis

Mechanoreceptors in the human body are uniquely structured within the dermis and, in the case of Meissner corpuscles (RA1) and Merkel cells (SA1), lie close to the epidermis boundary (1). RA1 receptors are often found in the dermal papillae, which lend to their ability to detect movement across the skin, and SA1 receptors tend to organize at the base of the epidermis. However, in glabrous skin, the HTMR free nerve endings extend into the epidermis (i.e., the outermost layer of skin) (1). We used this natural layering of tactile receptors to guide the multilayered approach of our e-dermis (Fig. 2A) to create sensing elements to capture signals analogous to those detected by mechanoreceptors (dermal) and nociceptors (epidermal) in healthy glabrous skin (Fig. 2B). The sensor was designed using piezoresistive (Eeonyx, Pinole, CA) and conductive fabrics (LessEMF, Latham, NY) to measure applied pressure on the surface of the e-dermis. A 1-mm rubber layer (Dragon Skin 10, Smooth-On, Easton, PA) between the artificial epidermal (top) and dermal (bottom) sensing elements provides skin-like compliance and distributes loads during grasping. There are three tactile pixels, or taxels, with a combined sensing area of about 1.5 cm<sup>2</sup> on each fingertip. The sensor layering resulted in variation of the e-dermis output during loading (Fig. 2C). The change in resistance in the tactile sensor was greater for the epidermal layer, enabling higher sensitivity. During grasping of an object, the e-dermis sensing layers, which were calibrated for a range of 0 to 300 kPa, exhibited differences in behavior. These differences can be used for extracting additional tactile information such as pressure distribution and object curvature (Fig. 2, D and E).

### Touch and pain perception

To provide sensory feedback, we used targeted TENS to extensively map and understand the perception of a transhumeral amputee's phantom limb during sensory feedback, a method we previously demonstrated in multiple amputees (24). Although the participant did not undergo any targeted muscle or sensory reinnervation during surgery, there was a natural regrowth of peripheral nerves into the remaining muscles, soft tissue, and skin around the amputation. The median and ulnar nerves were identified on the amputee's left residual limb and targeted for noninvasive electrical stimulation because these nerves innervated relevant areas of the phantom hand. The participant received more than 25 hours of sensory mapping in addition to over 150 trials of sensory stimulation experiments to quantify the perceptual qualities of the stimulation. Extensive mapping of the residual limb showed localized activation of the amputee's phantom hand (Fig. 3A).

The amputee identified multiple unique regions of activation in his phantom hand from the electrical stimulation. The participant did not report any sensory activation, other than the physical presence of the probe, of his residual limb at the stimulation sites. He indicated that the dominating perceived sensation during stimulation occurred in his phantom hand, which is supported by our previous work (24). Cutaneous receptors on the residual limb respond to physical stimuli, whereas the electrical stimulation activates the underlying peripheral nerves to activate the phantom hand. Psychophysical experiments showed the amputee's perception of changes in stimulation pulse width and frequency on his median and ulnar nerves (Fig. 3, B and C). In general,

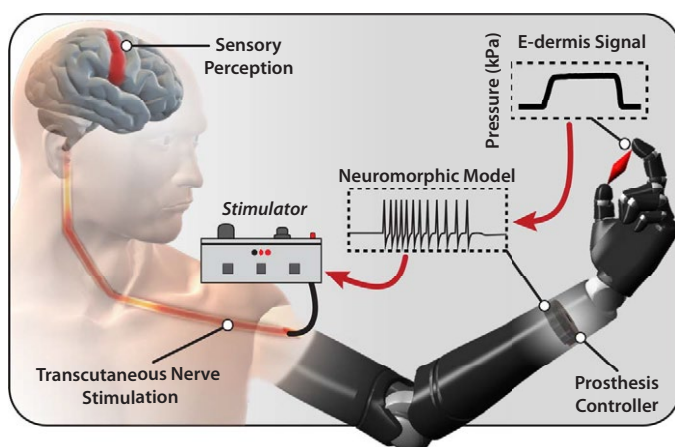


**Fig. 1. Prosthesis system diagram.** Tactile information from object grasping is transformed into a neuromorphic signal through the prosthesis controller. The neuromorphic signal is used to transcutaneously stimulate peripheral nerves of an amputee to elicit sensory perceptions of touch and pain.

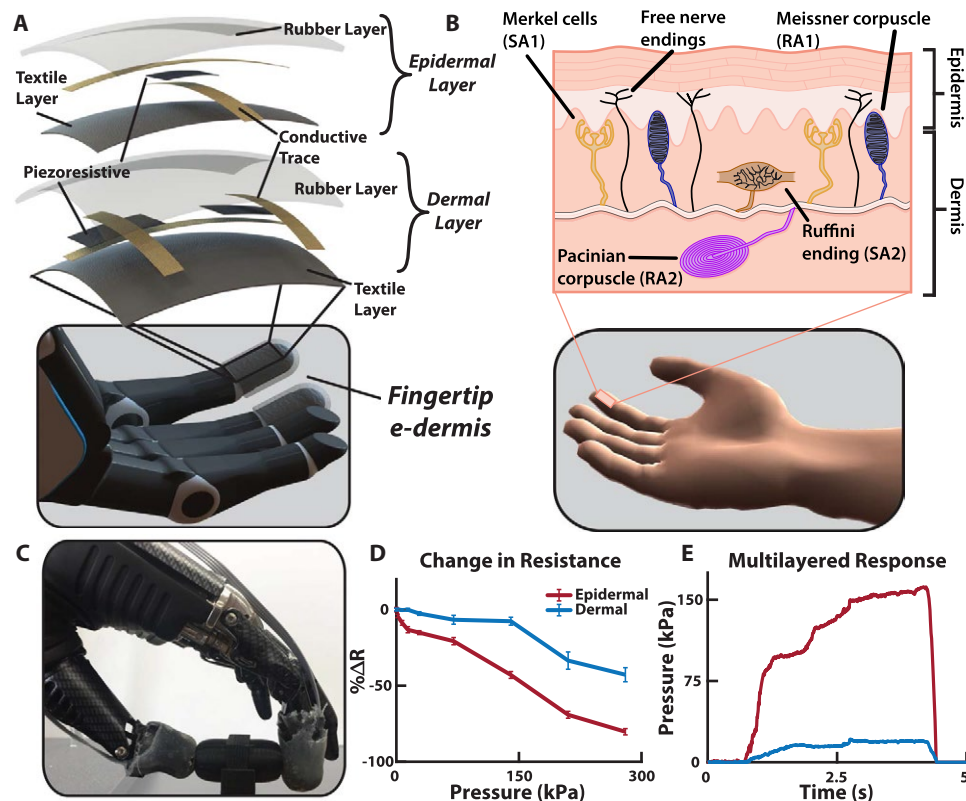


**Fig. 2. Multilayered e-dermis design and characterization.** (A) The multilayered e-dermis is made up of conductive and piezoresistive textiles encased in rubber. A dermal layer of two piezoresistive sensing elements is separated from the epidermal layer, which has one piezoresistive sensing element, with a 1-mm layer of silicone rubber. The e-dermis was fabricated to fit over the fingertips of a prosthetic hand. (B) The natural layering of mechanoreceptors in healthy glabrous skin makes use of both RA and SA receptors to encode the complex properties of touch. Free nerve endings (nociceptors) that are primarily responsible for conveying the sensation of pain in the fingertips are also present in the skin. (C) The prosthesis with e-dermis fingertip sensors grasps an object. (D) The epidermal layer of the multilayered e-dermis design is more sensitive and has a larger change in resistance compared with the dermal layer. (E) Differences in sensing layer outputs are captured during object grasping and can be used for adding dimensionality to the tactile signal.

the stimulation was perceived primarily as pressure with some sensations of electrical tingling (paresthesia) (Fig. 3D). Stability of the participant's sensory activation (fig. S1) and stimulation perceptual thresholds (fig. S2) were tracked over several months in his thumb and index fingers (median nerve) as well as his pinky finger (ulnar nerve).

Sensory feedback of noxious tactile stimuli was delivered using TENS to an amputee, and the perception was quantified. The results show that changes in both stimulation frequency and pulse width influence the perception of painful tactile sensations in the phantom hand (Fig. 3E). The relative discomfort of the tactile sensation was reported by the user on a modified comfort scale ranging from -1 (pleasant) to 10 (very intense, disabling pain that dominates the senses) (table S1). In this experiment, the highest perceived pain was rated as a 3, which corresponded to uncomfortable but tolerable pain. The most painful sensations were perceived at relatively low frequencies between 10 and 20 Hz. Higher frequency stimulation tends toward more pleasant tactile sensation, which is contrary to what might be expected when increasing stimulation frequency (31). In addition, very low frequencies generally resulted in innocuous activation of the phantom hand, whereas frequencies that were closer to the discrete detection boundary (15 to 30 Hz) resulted in the most noxious sensations in the activated region. We used electroencephalography (EEG) signals to localize and obtain an affirmation of the stimulus-associated perception. The stimulation caused activation in contralateral somatosensory regions of the

amputee's brain, which corresponded to his left hand (Fig. 3F) (32). EEG activation during stimulation is significantly higher ( $P < 0.05$ ) than baseline activity, confirming the perceived phantom hand activation experienced by the user (fig. S3 and movie S1).

### Neuromorphic transduction

As mentioned previously, a neuromorphic system attempts to mimic the behavior found in the nervous system. On the basis of the results from the sensory mapping of the participant, we developed the neuromorphic representation of the tactile signal to enable the sensation of both touch and pain. To enable direct sensory feedback to an amputee through peripheral nerve stimulation, we transformed the e-dermis signal from a pressure signal into a biologically relevant signal using a neuromorphic model. The aim for the neuromorphic model was to capture elements of our actual neural system, in this case, to represent the neural equivalent of a tactile signal for feedback to an amputee. To implement the biological activity from tactile receptors, namely, the spiking response in the peripheral nerves due to a tactile event, we used the Izhikevich model of spiking neurons (33), which provides a neuron modeling framework based on known neural dynamics while maintaining computational efficiency and easily allowing for different neuron behaviors from parameter adjustments. The Izhikevich model has been used in previous work for providing tactile feedback to an amputee through nerve stimulation (26). In our work, mechanoreceptor and nociceptor

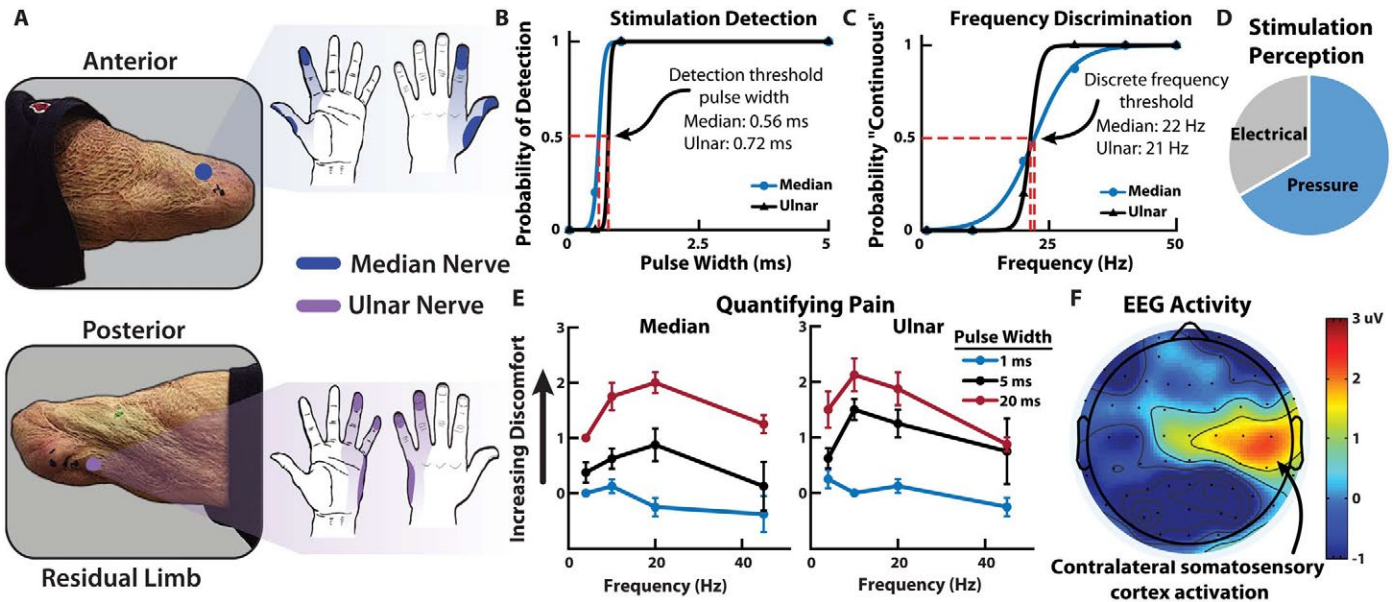


**Fig. 3. Sensory feedback and perception.** (A) Median and ulnar nerve sites on the amputee’s residual limb and the corresponding regions of activation in the phantom hand due to TENS. Psychophysical experiments quantified the perception of the nerve stimulation including (B) detection and (C) discrete frequency discrimination thresholds. In both cases, the stimulation amplitude was held at 1.4 mA. (D) The perception of the nerve stimulation was largely a tactile pressure on the activated sites of the phantom hand, although sensations of electrical tingling also occurred. (E) The quantification of pain from nerve stimulation shows that the most noxious sensation is perceived at higher stimulation pulse widths with frequencies in the range of 10 to 20 Hz. (F) Contralateral somatosensory cortex activation during nerve stimulation shows relevant cortical representation of sensory perception in the amputee participant (movie S1).

models produced receptor-specific outputs, in terms of neuron voltage, based on the measured pressure signal on the prosthesis fingertips. The mechanoreceptor model combined characteristics of SA and RA receptors through the regular and fast-spiking Izhikevich neurons, respectively, to convey more pleasant tactile feedback to the amputee. The nociceptor model used fast-spiking Izhikevich neuron dynamics to mimic the behavior of the free nerve endings.

When an object was grasped by the prosthesis, a higher number of active taxels indicated a larger distribution of the pressure on the fingertip, which was conveyed in the neuromorphic transduction as an innocuous (i.e., nonpainful) tactile sensation. Changes in the tactile signal were captured in the neuromorphic transduction by changes in stimulation frequency and pulse width to correspond to the appropriate perceived levels of touch or pain during sensory feedback. On the basis of the results from the psychophysical experiments and the quantification of pain, the perception of noxious tactile feedback was achieved through the nociceptor model (see Materials and Methods).

To demonstrate the neuromorphic representation of a tactile signal, we used three different objects, each of equal width but varying curvature, to elicit different types of tactile perceptions in the prosthesis during grasping (Fig. 4A). The objects follow a power law shape, where the radius of curvature ( $R_c$ ) was modified using the power law exponent  $n$ , which ranges between 0 and 1 and effectively defines the sharpness of the objects (see Materials and Methods). The power law exponents used were  $1/4$ ,  $1/2$ , and 1 and correspond to object 1, object 2, and object 3, respectively. The response of the fingertip taxels during object loading captured differences in object curvature based on the relative activation of all sensing elements (Fig. 4, B and C, and movie S2). As expected, the epidermal layer was the most activated taxel during loading and absorbed the largest pressure. The sharp edge of object 3 produced a highly localized pressure source on the epidermal layer of the e-dermis, which

triggered the neuromorphic nociceptor model (see Materials and Methods) (Fig. 4D).

**Prosthesis tactile perception and pain reflex**

As an extension of the body, a prosthetic hand should exhibit similar behavior and functionality of a healthy hand. The perceptions of innocuous touch and pain are valuable at both the local (i.e., the prosthetic hand) and the global (i.e., the user) levels. At the local level, a reflex behavior from the prosthesis to open when pain is detected can help prevent unintended damage to the hand or cosmesis. It should be noted that, in an ideal prosthesis, this reflex would be modulated by the user based on the perceived pain. To demonstrate a local closed-loop pain reflex, a prosthetic hand with a multilayered e-dermis on the thumb and index finger grasped, held, and released one of the previously described objects (Fig. 5, A to C). The sensor signals were used as feedback to the embedded prosthesis controller to enable differentiation of the various objects and determine pain. We used pressure distribution (Fig. 6A), contact rate (Fig. 6B), and the number of activated sensing elements per finger (Fig. 6C) as input features in a linear discriminant analysis (LDA) algorithm for object detection.

In the online pain detection task (PDT), the prosthesis grabbed, held, and released an object (movie S3). In this work, the curvature of object 3 was assumed to be considered painful during grasping. When pain was detected, a prosthesis pain reflex caused the hand to open, releasing the object. The prosthesis was able to reliably detect which object is being grasped (Fig. 7A). The prosthesis had a high likelihood of perceiving pain while grasping object 3 and a significantly less likelihood of perceiving pain for objects 2 and 1 ( $P < 0.001$ ) (Fig. 7B). The reaction time for the prosthesis to complete a reflex after perceiving pain was recorded and was similar to reaction times in healthy humans from previously published data (Fig. 7C) (28).

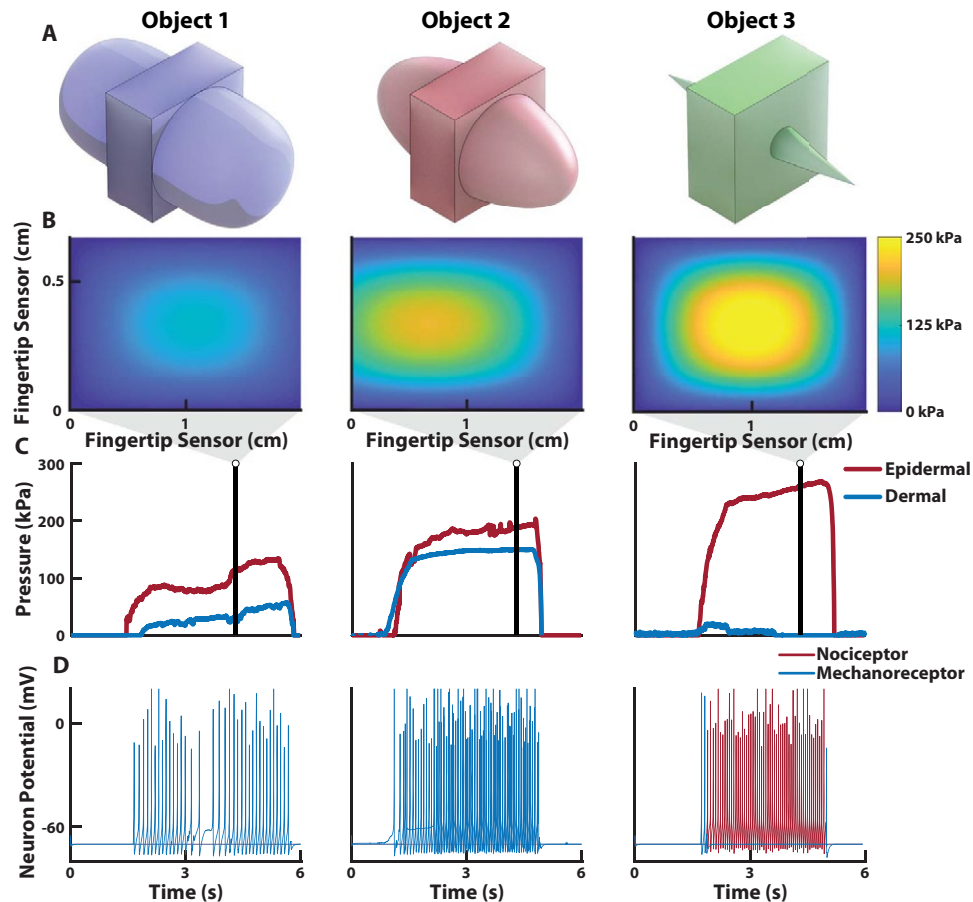


**Fig. 4. E-dermis and neuromorphic tactile response from different objects.** (A) Three different objects, with equal width but varying curvature, were used to elicit tactile responses from the multilayered e-dermis. (B) Pressure heatmap from the fingertip sensor on a prosthetic hand during grasping of each object and (C) corresponding pressure profile for each of the sensing layers. (D) The pressure profiles were converted to the input current,  $I$ , for the Izhikevich neuron model for sensory feedback to the amputee user (movie S2). Note the highly localized pressure during the grasping of object 3 and the resulting nociceptor neuromorphic stimulation pattern, which is realized through changes in stimulation pulse width and the neuromorphic model parameters.

### User tactile perception

With the added ability to perceive both innocuous and noxious tactile sensations in a single stimulation modality, an amputee user can use more realistic tactile sensations to discriminate between objects with a large or small (sharp) radius of curvature. The participant demonstrated his ability to perceive both innocuous and noxious tactile sensations by performing several discrimination tasks with a prosthetic hand. The neuromorphic tactile signal was passed from the prosthesis controller directly to the stimulator to provide sensory feedback to the amputee. The participant could reliably detect, with perfect accuracy, which of the fingers of the prosthesis were being loaded (Fig. 8A). The participant also received sensory feedback from varying levels of pressure applied to the prosthetic fingers. A light (<100 kPa), medium (<200 kPa), or hard (>200 kPa) touch, as measured by the e-dermis, presented to the prosthesis was translated to the peripheral nerves of the amputee by using the neuromorphic representation of touch (figs. S4 and S5). To demonstrate the ability of the prosthesis and user to perceive differences in object shape through variation in the comfort levels of sensory feedback, we presented each of the three objects to the prosthesis. Sensory feedback to the thumb and index finger regions of the phantom hand enabled the participant to perceive variations in the object curva-

tures, which were realized through changes in perceived comfort of the sensation. The results show an inversely proportional relationship between the radius of curvature of an object and the perceived discomfort of the tactile feedback (Fig. 8B). In addition to being able to perceive variation in sharpness of the objects, as conveyed by the discomfort in the neuromorphic tactile feedback, the participant could reliably differentiate between the three objects with high accuracy (Fig. 8C). Finally, the participant performed the PDT with his prosthesis (movie S4). The prosthesis pain reflex control was implemented during the grasping task, which resulted in the prosthesis automatically releasing an object when pain was detected (see Materials and Methods). During actual amputee use, the prosthesis pain reflex registered over half of the object 3 movements as painful, significantly more than for the other objects ( $P < 0.05$ ) (Fig. 8D).

Responses from a subjective survey of the perception of the sensory stimulation show that the amputee felt as if the tactile sensations were coming directly from his phantom hand. In addition, the participant stated that he could clearly feel the touch of objects on the prosthetic hand and that it seemed that the objects themselves were the cause of the touch sensations that he was experiencing during the experiments (table S2).

**DISCUSSION**

**Perceiving touch and pain**

Being able to quantify the perception of innocuous and noxious stimuli for tactile feedback in amputees is valuable because it enables the replacement of an extremely valuable piece of sensory information: pain. Not only does pain play a role in providing tactile context about the type of object being manipulated, but it also acts as a mechanism for protecting the body. One could argue that this protective mechanism is not necessary in a prosthesis because it is merely an external tool or piece of hardware to an amputee user. We postulate that being able to capture noxious stimuli is actually more valuable to a prosthesis because it does not have the same self-healing characteristics found in healthy human skin, although recent research has shown self-healing materials that could be used for future prosthetic limbs (13, 34). To enable an artificial sense of self-preservation, a noxious tactile signal is useful for the prosthesis to ensure that it does not exceed the limits of a cosmetic covering or the hand itself. As prosthetic limbs become more sophisticated and sensory feedback becomes more ubiquitous, there will be a need to in-

crease not just the resolution of tactile information but also the amount of useful information being passed to the user. We have identified how changing stimulation pulse width and frequencies enables a spectrum of tactile sensation that captures both innocuous and noxious perceptions in a single stimulation modality.

Our extensive phantom hand mapping, psychophysics, and EEG results support the use of TENS for providing relevant sensory information to an amputee. The EEG results are limited in that they do not provide detailed information on how changes in stimulation patterns were perceived, but they do show activation in sensory regions of the brain indicating relevant sensations in the amputee. Furthermore, the results from the user survey (table S2) showed that sensory feedback helped the amputee better perceive his phantom hand and that objects being grabbed by the prosthesis were perceived as being the source of the sensation, which helps support the neuromorphic stimulation as a valid approach for providing relevant sensory feedback.

The results from the PDT showed the ability of the prosthesis to detect pain and reflex to release the object. Object 3 was overwhelmingly detected as painful due to its sharp edge (Fig. 7B). The high success rate for detecting and preventing pain for the benchtop PDT is likely due to the controlled nature of the prosthesis grip. The likelihood of detecting object 3 as painful decreased and the chances of pain being detected for the other objects increased during the PDT with a user-controlled prosthesis (Fig. 8D); however, pain detection and reflex were still significantly more likely for object 3 ( $P < 0.05$ ). This shift in pain detection is likely due to the amputee's freedom to pick up the objects with his prosthesis in any way he chose. The variability in grasping orientation and approach for each trial resulted in more instances where object 3 was not perceived as painful by the prosthesis. The ability to handle objects in different positions and orientations raises an interesting point: The amount of pain produced is not an inherent property of an object; rather, it is dependent on the way in which it is grasped. A sharp edge may still be safely manipulated without pain if the pressure on the skin does not exceed the threshold for pain. To reliably encode both touch and pain for prostheses, tactile signals should be analyzed in terms of pressure as opposed to grip force.

The prosthesis pain reflex presented here is autonomous, but one possibility is to use the amputee's electromyography (EMG) signal as an additional input to the reflex model to enable modulation of the pain sensitivity perceived by the prosthesis. In this work, the pain sensation was not severe enough to generate a reliable EMG reflex signal, so the reflex decision was made by the prosthesis instead of the user. The time for a user to process sensory feedback and produce a voluntary contraction is over 1 s (35), which is why we implemented an autonomous prosthesis pain reflex to achieve a response time closer to what is found in

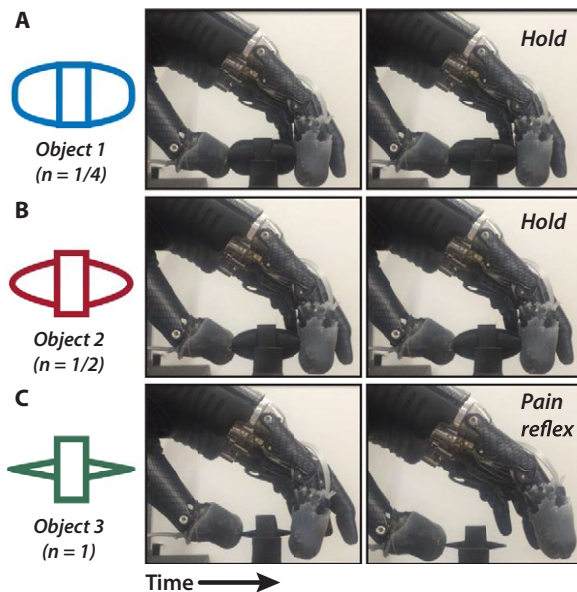


**Fig. 5. Prosthesis grasping and control.** To demonstrate the ability of the prosthesis to determine safe (innocuous) or unsafe (painful) objects, we performed the PDT. The objects were (A) object 1, (B) object 2, and (C) object 3, each of which is defined by their curvature. In the case of a painful object (object 3), the prosthesis detected the sharp pressure and released its grip through its pain reflex (movie S3).

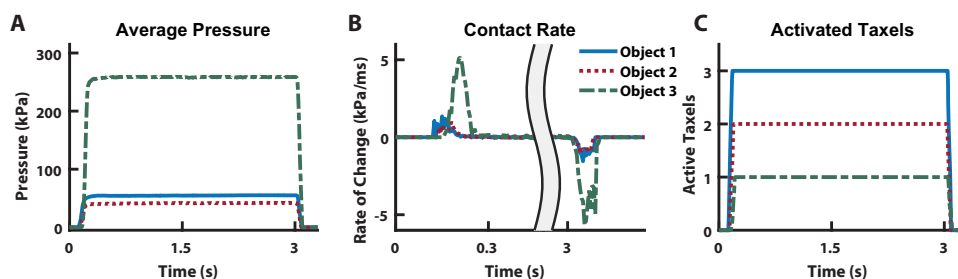


**Fig. 6. Tactile features for prosthesis perception.** To determine which object is being touched during grasping, we implemented LDA to discriminate between the independent classes. As input features into the algorithm, we used (A) sensor pressure values, (B) the rate of change of the pressure signal, and (C) the number of active sensing elements during loading.

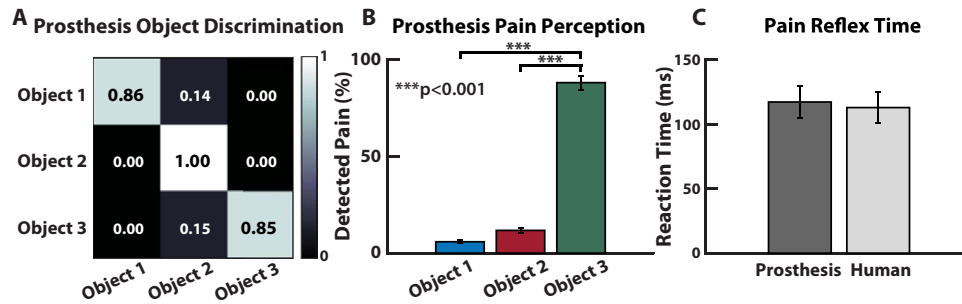


**Fig. 7. Real-time prosthesis pain perception.** (A) LDA classifier's accuracy across the various conditions and (B) percentage of trials where the prosthesis perceived pain during the online PDT. Note the high percentage of detected pain during the PDT for object 3. (C) Pain reflex time of the prosthesis, using the rate of change of the pressure signal to determine object contact and release, compared with previously published data of pain reflex time in healthy adults (28).

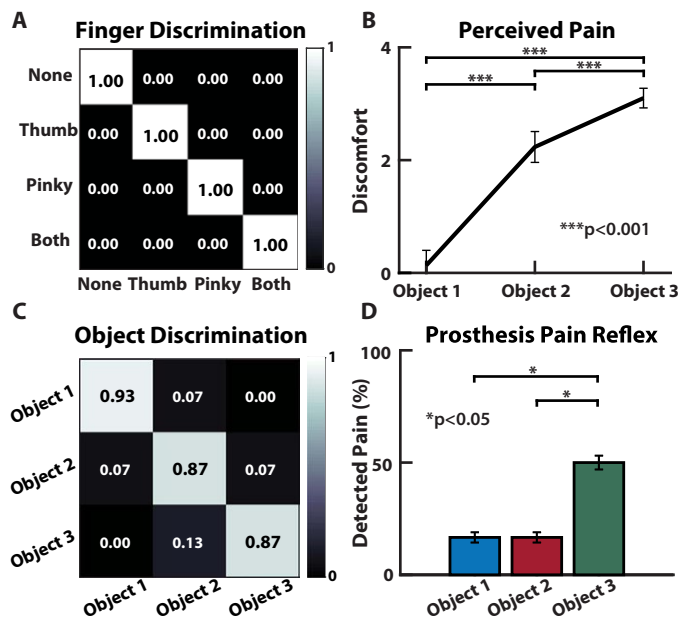


**Fig. 8. Innocuous (mechanoreception) and noxious (nociception) prosthesis sensing and discrimination in an amputee.** (A) The amputee could discriminate which region of his phantom hand was activated, if at all. (B) Perception of pain increases with decreasing radius of curvature (i.e., increase in sharpness) for the objects presented to the prosthetic hand. (C) Discrimination accuracy shows the participant's ability to reliably identify each object presented to the prosthesis based purely on the sensory feedback from the neuromorphic stimulation. (D) Results from the PDT during user-controlled movements, with pain reflex enabled.

biology (Fig. 7C). Biologically, this autonomous response is equivalent to a fast spinal reflex compared with the slower cortical response for producing a voluntary EMG signal for controlling limb movement.

Another implication of this work is the quantification of perceived noxious and innocuous tactile sensations during TENS of peripheral afferents. One might assume that an increase in discomfort would be associated with an increase in delivered charge; however, we found that the most painful sensations during tactile feedback to an amputee delivered through TENS were primarily dictated by an increase in stimulation pulse width and stimulation frequency. Specifically, frequencies that were near the discrete detection boundary (15 to 30 Hz) were perceived as more painful than higher frequencies. Changes in stimulation frequency seemed to have the largest influence on the perceptions of touch and pain, whereas pulse width affected intensity of the sensation

(Fig. 3E). Furthermore, we demonstrated real-time discrimination between object curvature based purely on perceived discomfort in tactile feedback, which was associated with sharpness of the objects by the participant.

### Neuromorphic touch

The ability of the participant to discriminate objects, specifically those that cause pain, is rooted in the neuromorphic tactile transduction and corresponding nerve stimulation. The psychophysical results illuminate the stimulation paradigms necessary to elicit tactile sensations that correspond to both mechanoreceptors and nociceptors in the phantom hand of an amputee.

More sophisticated neuron models exist and could be used to capture behavior of individual receptors and transduction (25); however, the limitation of hardware prevents the stimulation of individual afferent nerve fibers. The Izhikevich model is simplistic in its dynamics but still follows basic qualities of integrate-and-fire models with voltage nonlinearity for spike generation and extremely low computational requirements, which allow for the creation of a wide variety of neuron behaviors (33). The advantage of the neuromorphic representation of touch in our work is that we can transform signals from the multilayered e-dermis directly into the appropriate stimulation paradigm needed to elicit the desired sensory percepts in the amputee participant. Specifically, the combination of mechanoreceptor and nociceptor outputs enables additional touch dimensionality while maintaining a single modality of feedback in both physical location and stimulation type. This combination allows the user to better differentiate between objects based on their unique evoked perceptions for each object (Fig. 8, B and C).

The limitation of this work is the small study sample. Although this work is a case study with a single amputee, the extensive psychophysical experiments and stability (figs. S1 and S2) of the results over several months show promise that other amputees would experience a similar type of perception from TENS, a technique we have previously validated for activating relevant phantom hand regions in multiple amputees (24). However, the psychophysics will likely have slight differences based on age and condition of the amputation. The results are promising in that the stimulation parameters used to elicit pain or touch followed the same trend in both median and ulnar nerve sites of the amputee (Fig. 3E). This work implies that both innocuous and noxious touches can be conveyed using the same stimulation modality. In addition, we showed that it is not necessarily a large amount of injected charge into the peripheral nerves that elicits a painful sensation. Rather, a combination of stimulation pulse width and frequency at the discrete detection boundary appears to create the most noxious sensations. Additional

amputee participants who are willing to undergo nerve stimulation, sensory mapping, and psychophysical experiments to quantify their perceived pain would be needed to allow us to generalize the clinical significance to a wider amputee population. Our findings have applications not only in prosthetic limb technology but also for robotic devices in general, especially devices that rely on tactile information or interactions with external objects. The overarching idea of capturing meaningful tactile information continues to become a reality, because we can now incorporate both innocuous and noxious information in a single channel of stimulation. Whether it is used for sensory feedback or internal processing in a robot, the senses of touch and pain together enable a more complete perception of the workspace.

This study illustrates, through demonstration in a prosthesis and amputee participant, the ability to quantify and use tactile information that is represented by a neuromorphic interface as both mechanoreceptor and nociceptor signals. Through our demonstration of capturing and conveying a range of tactile signals, prostheses and robots can incorporate more complex components of touch, namely, differentiating innocuous and noxious stimuli, to behave in a more realistic fashion. The sense of touch provides added benefit during manipulation in prostheses and robots, but the sense of pain enhances their capabilities by introducing self-preservation and protection.

## MATERIALS AND METHODS

### Objectives and study design

Our objectives were to show that (i) a prosthetic hand was capable of perceiving both touch and pain through a multilayered e-dermis and (ii) an amputee was capable of perceiving the sense of both touch and pain through targeted peripheral nerve stimulation using a neuromorphic stimulation model.

### Participant recruitment

All experiments were approved by the Johns Hopkins Medicine Institutional Review Board. The amputee participant was recruited from a previous study at Johns Hopkins University in Baltimore, MD. The participant consented to participate in all the experiments and to have images and recordings taken during the experiments used for publication and presentations. At the time of the experiments, the participant was a 29-year-old male with a bilateral amputation 5 years prior, due to tissue necrosis from septicemia. The participant has a transradial amputation of the right arm and a transhumeral amputation of the left arm. The left arm was used for all sensory feedback and controlling the prosthesis in this work. After 2 months of sensory mapping, the experiments were performed on average once every 2 weeks over a period of 3 months with follow-up sessions after 2, 5, and 8 months. EEG data were collected in one session over a period of 2 hours.

### Sensory feedback

The sensory feedback experiments consisted of TENS of the median and ulnar nerves using monophasic square-wave pulses. We performed mapping of the phantom hand using a 1-mm beryllium copper (BeCu) probe connected to an isolated current stimulator (DS3, Digitimer Ltd., Hertfordshire, UK). An amplitude of 0.8 mA and frequency of 2 to 4 Hz were used while mapping the phantom hand. Anatomical and ink markers were used, along with photographs of the amputee's limb, to map the areas of the residual limb to the phantom hand. For all other stimulation experiments, we used a 5-mm disposable Ag-Ag/Cl electrode. A 64-channel EEG cap with Ag-Ag/Cl electrodes (impedance, <10 k $\Omega$ )

was used for the EEG experiment. The participant was seated, and stimulation electrodes were placed on the median and ulnar nerve sites of his residual limb. Each site was stimulated individually for a period of 2 s, followed by a 4-s delay with 25% jitter before the next stimulation. There was a total of 60 stimulation presentations with varying pulse width (1 to 20 ms) and frequencies (4 to 45 Hz) with an amplitude of 1.6 mA. A time window of 450 ms starting at 400 ms after stimulation was used to average EEG activity across trials and compared with baseline activity using methods similar to those in (36).

### Psychophysical experiments

Psychophysical experiments were performed to quantify the perception of TENS on the median, radial, and ulnar nerves of the amputee. Experiments included sensitivity detection (varying pulse width at 20 Hz), detection of discrete versus continuous stimulation (varying frequency with pulse width of 5 ms), and scaled pain discrimination. For the pain discrimination experiment, the participant used a discomfort scale that ranged from pleasant or enjoyable (-1) to no pain (0) to very intense pain (10) (table S1). Stimulation current amplitude was held at 2 mA, whereas frequency and pulse width were modulated to quantify the effect of signal modulation on perception in the participant's phantom hand. Every electrical stimulation was presented as a 2-s burst with at least 5-s rest before the next stimulation. Experiments were conducted in blocks up to 5 min with a break up to 10 min between each block. Every stimulation condition was presented up to 10 times. Psychometric functions were fit using a sigmoid link function (24).

### E-dermis fabrication

The multilayered e-dermis was constructed from piezoresistive transducing fabric (Eeonyx) placed between crossing conductive traces (stretch conductive fabric, LessEMF), similar to the procedure described in previous work (37). The piezoresistive material is pressure-sensitive and decreases in resistance with increased loading. The intersection of the conductive traces created a sensing taxel, a tactile element. Human anatomy expresses a lower density of nociceptors, compared with mechanoreceptors, in the fingertip (38). So, we designed the epidermal layer as a 1  $\times$  1 sensing array, whereas the dermal layer was a 2  $\times$  1 array (Fig. 2A). The size of the prosthesis fingertip and the available inputs to the prosthesis controller limited the number of sensing elements to three per finger. The piezoresistive and conductive fabrics were held in place by a fusible tricot fabric with heat-activated adhesive. A 1-mm layer of silicone rubber (Dragon Skin 10, Smooth-On) was poured between two sensing layers. After the intermediate rubber layer cured, the textile sensors were wrapped into the fingertip shape, and a 2-mm layer of silicone rubber (Dragon Skin 10, Smooth-On) was poured as an outer protection and compliance layer, which is known to benefit prosthesis grasping (19). The e-dermis was placed over the thumb, index, and pinky phalanges of a prosthetic hand (Fig. 1B).

### Prosthesis control

A bionic prosthetic hand (Ottobock, Duderstadt, Germany) was used for the experiments. Prosthesis movement was controlled using a custom control board, with an ARM Cortex-M processor, developed by Infinite Biomedical Technologies (IBT; Baltimore, MD). The board was used for interfacing with the prosthesis, reading in the sensor signals, controlling the stimulator, and implementing the neuromorphic model. During the user-controlled PDT, the amputee used his own prosthesis (fig. S6), a bionic hand with Motion Control wrist

and a Utah Arm 3+ arm with elbow (Motion Control Inc., Salt Lake City, UT). The amputee controlled his prosthesis using an LDA algorithm on an IBT control board for EMG pattern recognition. The electrodes within his socket were bipolar Ag-Ag/Cl EMG electrodes from IBT.

### Neuromorphic models

We implemented artificial mechanoreceptor and nociceptor models to emulate natural tactile coding in the peripheral nerve. We tuned the model to match the known characterization of TENS in the amputee to elicit the appropriate sensation. Constant current was applied during stimulation, and both pulse width and spiking frequency were modulated by the model. Higher grip force was linked to increased stimulation pulse width and frequency, which was perceived as increased intensity in the phantom hand. Innocuous tactile stimuli resulted in shorter pulse widths (1 or 5 ms), whereas the noxious stimuli produced a longer pulse width (20 ms), a major contributor to the perception of pain through TENS, as shown by the results. To create the sensation of pain, we varied the parameters of the model in real time based on the output of the e-dermis. We converted the e-dermis output to neural spikes in real time by implementing the Izhikevich neuron framework (33) in the embedded C++ software on the prosthesis control board. The output of the embedded neuromorphic model on the control board was used to control the stimulator for sensory feedback. The neuromorphic mechanoreceptor model was a combination of SA and RA receptors modeled as regular and fast-spiking neurons. The nociceptor model was made up of A $\delta$  neurons, which were modeled as fast-spiking neurons to elicit a painful sensation in the phantom hand. It should be noted that the fast-spiking neuron model was perceived as noxious with an increase in pulse width, which allows us to use the same Izhikevich neuron for both mechanoreceptors and nociceptors. The e-dermis output was used as the input current,  $I$ , to the artificial neuron model. The evolution of the membrane potential  $v$  and the refractory variable  $u$  are described by Eqs. 1 and 2. When the membrane potential reaches the threshold  $v_{th}$ , the artificial neuron spikes. The membrane potential was reset to  $c$ , and the membrane recovery variable  $u$  was increased by a predetermined amount  $d$  (Eq. 3). The spiking output was used to directly control the TENS unit for sensory feedback.

$$\frac{dv}{dt} = Av^2 + Bv + C - u + \frac{I}{RC_m} \quad (1)$$

$$\frac{du}{dt} = a(bv - u) \quad (2)$$

$$\text{if}(v \geq v_{th}), \text{ then } \begin{cases} v \leftarrow c \\ u \leftarrow u + d \end{cases} \quad (3)$$

Because we are not directly stimulating individual afferents in the peripheral nerves, we tuned the model to represent behavior of a population of neurons. The parameters used for the different receptor types were as follows:  $A = 0.04/Vs$ ;  $B = 5/s$ ;  $C = 140 V/s$ ;  $C_m = 1 F$ ;  $R = 1$ ;  $b = 0.2/s$ ;  $c = -65 mV$ ;  $d = 8 mV/s$ ;  $v_{th} = 30 mV$ ; and

$$a = \begin{cases} 0.02/s, \text{ Regular spiking (RS)} \\ 0.01/s, \text{ Fast spiking (FS)} \end{cases}$$

$A$ ,  $B$ , and  $C$ , are constants of the model,  $b$  describes the sensitivity of the recovery variable  $u$ ,  $c$  is the membrane reset voltage,  $C_m$  is the membrane capacitance, and  $R$  describes the membrane resistance of the neuron. The fast-spiking neurons fire with high frequency with little adaptation, similar to responses from nociceptors during intense, noxious stimuli (7). In the model, fast spiking is represented by a very fast recovery ( $a$ ). Values for the parameters were taken from (26) and (33).

We limited the spiking frequency of the neuromorphic model to 40 and 20 Hz for the mechanoreceptor and nociceptor models, respectively. The transition of the neuromorphic model from mechanoreceptors to nociceptors relies on the pressure measured at the fingertips of the prosthesis, the number of active sensing elements, and the SD of the pressure signal across the active taxels. The prosthesis fingertip pressure ( $P$ ) is used to determine the neuromorphic stimulation model for sensory feedback. Highly localized pressure above a threshold  $\beta$  triggers the FS model, whereas the RS model is used in cases of more distributed fingertip pressure. The following pseudocode explains how the stimulation model is chosen, where  $\beta = 150 kPa$ ,  $n$  is the number of active taxels, and  $pw$  is the stimulation pulse width:

```
if ( $P \geq \beta$  and  $n < 2$ ), then [nociceptor (A $\delta$ ) (FS:  $pw = 20 ms$ )]
else if ( $P \geq \beta$  and  $n = 2$ ), then [mechanoceptor (SA/RA) (FS:  $pw = 5 ms$ )]
else [mechanoceptor (SA/RA) (RS:  $pw = 5 ms$ )]
```

### Prosthesis pain reflex

To mimic biology, we modeled the prosthesis pain withdrawal as a polysynaptic reflex (29, 30) in the prosthesis hardware. In our model, the prosthesis controller was treated as the spinal cord for the polysynaptic reflex. The nociceptor signal was the input,  $I(t)$ , to an integrating interneuron  $\Gamma$  whose output  $I_\Gamma(t)$  was the input to an  $\alpha$  motor neuron, which triggered the withdrawal reflex through a prosthesis hand open command after  $\sim 100 ms$  of pain. Both neurons can be modeled as leaky integrate and fire with a synapse from the  $\alpha$  motor neuron causing the reflex movement (Eqs. 4 and 5, and fig. S7), similar to the EMG signals generated during a nociceptive reflex (39).

$$\text{Interneuron } (\Gamma) : \tau_m \frac{dv_\Gamma}{dt} = E + RI(t) - v_\Gamma(t) \quad (4)$$

$$\text{Alpha motor neuron } (\alpha) : \tau_m \frac{dv_\alpha}{dt} = E + RI_\Gamma(t) - v_\alpha(t) \quad (5)$$

Both neurons had time constant  $\tau_m = 10 ms$ , resting potential  $E = -60 mV$ , membrane resistance  $R = 20 ohms$ , and a spiking threshold of  $v_{th} = -40 mV$ . The time step was 5 ms, and the nociceptor signal was normalized, enveloped, and scaled by  $\beta = 0.2 mV$ . The prosthesis reflex parameters were chosen to trigger hand withdrawal after  $\sim 100 ms$  of pain to mimic the pain reflex in healthy humans (28). Fingertip pressure, the rate of contact, and the number of active sensing elements on each fingertip were used as features for an LDA algorithm to detect the different objects. Object 3 was labeled as a painful object. A taxel was considered active if it measured a pressure greater than 10 kPa. The pattern recognition algorithm was trained using sensor data from 5 trials of prosthesis grasping for each object and validated on 10 different trials.

### Object design and fabrication

We created three objects of equal size with varying edge curvatures, defined by the edge blend radius, using a Dimension 1200es 3D printer (Stratasys, Eden Prairie, MN). Each object has a width of 5 cm but

differed in curvature. Each object's curvature followed a power law, where the leading edge of the protrusions varies in blend radii and ranges from flat to sharp. The radius of curvature,  $R_c$ , of the leading edge can be modified by the body power law exponent,  $n$ , where

$$R_c = \frac{1}{|nA(n-1)|} \left[ x^{\frac{2(2-n)}{3}} + (nA)^2 x^{\frac{2(2n-1)}{3}} \right]^{\frac{2}{3}} \quad (6)$$

$A$  is the power law constant, which is a function of  $n$ , and  $x$  is the position along the Cartesian axis in physical space. The objects for this study were designed to maintain a constant width,  $w$  (fig. S8), to prevent the ability to discriminate between the objects based on overall width. The three objects used had a power law exponent,  $n$ , of  $1/4$ ,  $1/2$ , and 1 and were referred to as object 1, object 2, and object 3, respectively. More details and explanation of power law-shaped edges can be found in (40, 41).

## Experimental design

### Finger discrimination

The multilayered e-dermis was placed over the thumb and pinky finger of the prosthesis. Activation of each fingertip sensor corresponded directly to nerve stimulation of the amputee in the corresponding sites of his phantom hand. The participant was seated, and his vision was occluded. The experimenter pressed the prosthetic thumb, pinky, both, or neither in a random order. Each condition was presented eight times. The stimulation amplitude was 1.5 and 1.45 mA for the thumb and pinky sites on the amputee's residual limb, respectively. Next, the experimenter pressed the prosthetic thumb or pinky with a light (<100 kPa), medium (<200 kPa), or hard (>200 kPa) pressure (figs. S4 and S5). Each force condition was presented 10 times in a random order for each finger.

### Object discrimination

Fingertip sensors were placed on the thumb and index finger of a stationary bionic prosthetic hand. The participant was seated, and his vision of the prosthesis was occluded. A stimulating electrode was placed over the region of his residual limb that corresponded to his thumb and index fingers on his phantom hand. The experimenter presented one of the three objects on the index finger of the prosthetic hand for several seconds. The participant responded with the perceived object and the perceived discomfort based on the tactile sensation. Each block consisted of up to 15 object presentations. The participant performed three blocks of this experiment. Each object was presented randomly within each block, and each object was presented the same number of times as the other objects. The participant visually inspected the individual objects before the experiment took place, but he was not given any sample stimulation of what each object would feel like. This was done to allow the participant to create his own expectation of what each object should feel like if he were to receive sensory feedback on his phantom hand.

### Pain detection task

In the benchtop PDT, the prosthesis was mounted on a stand with the multilayered sensors on the thumb and index finger. The object was placed on a stand, and the prosthesis grabbed the object using a closed precision pinch grip. Each object was presented to the prosthesis at least 15 times in a random order. For the user-controlled PDT, the participant used his prosthesis to pick up and move one of the three objects. Each object was presented at least 10 times. The instances of prosthesis reflex were recorded. The participant took a survey at the end of the experiments (table S2).

## Data collection

Each taxel of the multilayered e-dermis was connected to a voltage divider. Sensor data were collected by the customized prosthesis controller and sent through serial communication with a baud rate of 115,200 bps to MATLAB (MathWorks, Natick, MA) on a PC for further postprocessing and plotting. Each sensing element in the e-dermis was sampled at 200 Hz. Responses from the psychophysical experiments were recorded using MATLAB and stored for processing and plotting. The prosthesis controller communicated with MATLAB through Bluetooth communication with a baud rate of 468,000 bps. Sixty-four-channel EEG data were recorded at 500 Hz by a SynAmp2 system (Compumedics Neuroscan, Charlotte, NC) and processed in MATLAB using the EEGlab Toolbox (Swartz Center for Computational Neuroscience, University of California, San Diego, San Diego, CA). EEG data were downsampled to 256 Hz and band-pass-filtered between 0.5 and 40 Hz using a sixth-order Chebyshev filter. Muscle artifacts were rejected by the Automatic Artifact Rejection (AAR) blind source separation algorithm using canonical correlation approach. Independent component analysis was performed for removal of the eye and remnant muscle artifacts to obtain noise-free EEG data. Results from data collected over multiple trials of the same experiment were averaged together. Statistical  $P$  values were calculated using a one-tailed, two-sample  $t$  test. Error bars represent the SEM, unless otherwise specified.

## SUPPLEMENTARY MATERIALS

robotics.sciencemag.org/cgi/content/full/3/19/eaat3818/DC1

Fig. S1. Sensory mapping over time.

Fig. S2. Stimulation thresholds over time.

Fig. S3. EEG activation.

Fig. S4. Amputee pressure discrimination.

Fig. S5. Average fingertip pressures.

Fig. S6. Custom prosthetic arm.

Fig. S7. Prosthesis pain reflex.

Fig. S8. Power law object edge radius of curvature.

Table S1. Scaled comfort responses.

Table S2. Amputee survey.

Movie S1. Dynamic EEG activity during nerve stimulation.

Movie S2. Neuromorphic transduction during grasping.

Movie S3. Prosthesis PDT with reflex.

Movie S4. Amputee PDT with reflex.

## REFERENCES AND NOTES

1. V. E. Abraira, D. D. Ginty, The sensory neurons of touch. *Neuron* **79**, 618–639 (2013).
2. R. S. Johansson, J. R. Flanagan, Coding and use of tactile signals from the fingertips in object manipulation tasks. *Nat. Rev. Neurosci.* **10**, 345–359 (2009).
3. A. B. Vallbo, R. S. Johansson, Properties of cutaneous mechanoreceptors in the human hand related to touch sensation. *Hum. Neurobiol.* **3**, 3–14 (1984).
4. J. Scheibert, S. Leurent, A. Prevost, G. Debrégeas, The role of fingerprints in the coding of tactile information probed with a biomimetic sensor. *Science* **323**, 1503–1506 (2009).
5. J. A. Pruszynski, R. S. Johansson, Edge-orientation processing in first-order tactile neurons. *Nat. Neurosci.* **17**, 1404–1409 (2014).
6. E. S. J. Smith, G. R. Lewin, Nociceptors: A phylogenetic view. *J. Comp. Physiol.* **A. Neuroethol Sens. Neural Behav. Physiol.** **195**, 1089–1106 (2009).
7. E. R. Perl, Myelinated afferent fibres innervating the primate skin and their response to noxious stimuli. *J. Physiol.* **197**, 593–615 (1968).
8. A. E. Dubin, A. Patapoutian, Nociceptors: The sensors of the pain pathway. *J. Clin. Invest.* **120**, 3760–3772 (2010).
9. D. Farina, I. Vujaklija, M. Sartori, T. Kapelner, F. Negro, N. Jiang, K. Bergmeister, A. Andalib, J. Principe, O. C. Aszmann, Man/machine interface based on the discharge timings of spinal motor neurons after targeted muscle reinnervation. *Nat. Biomed. Eng.* **1**, 0025 (2017).
10. D.-H. Kim, J.-H. Ahn, W. M. Choi, H.-S. Kim, T.-H. Kim, J. Song, Y. Y. Huang, Z. Liu, C. Lu, J. A. Rogers, Stretchable and foldable silicon integrated circuits. *Science* **320**, 507–511 (2008).

11. J. Kim, M. Lee, H. J. Shim, R. Ghaffari, H. R. Cho, D. Son, Y. H. Jung, M. Soh, C. Choi, S. Jung, K. Chu, D. Jeon, S.-T. Lee, J. H. Kim, S. H. Choi, T. Hyeon, D.-H. Kim, Stretchable silicon nanoribbon electronics for skin prosthesis. *Nat. Commun.* **5**, 5747 (2014).
12. C. Larson, B. Peele, S. Li, S. Robinson, M. Totaro, L. Beccai, B. Mazzolai, R. Shepherd, Highly stretchable electroluminescent skin for optical signaling and tactile sensing. *Science* **351**, 1071–1074 (2016).
13. C.-H. Li, C. Wang, C. Keplinger, J.-L. Zuo, L. Jin, Y. Sun, P. Zheng, Y. Cao, F. Lissel, C. Linder, X.-Z. You, Z. Bao, A highly stretchable autonomous self-healing elastomer. *Nat. Chem.* **8**, 618–624 (2016).
14. B. C.-K. Tee, C. Wang, R. Allen, Z. Bao, An electrically and mechanically self-healing composite with pressure- and flexion-sensitive properties for electronic skin applications. *Nat. Nanotechnol.* **7**, 825–832 (2012).
15. Z. Zou, C. Zhu, Y. Li, X. Lei, W. Zhang, J. Xiao, Rehealable, fully recyclable, and malleable electronic skin enabled by dynamic covalent thermoset nanocomposite. *Sci. Adv.* **4**, eaq0508 (2018).
16. B. C.-K. Tee, A. Chortos, A. Berndt, A. K. Nguyen, A. Tom, A. McGuire, Z. C. Lin, K. Tien, W.-G. Bae, H. Wang, P. Mei, H.-H. Chou, B. Cui, K. Deisseroth, T. N. Ng, Z. Bao, A skin-inspired organic digital mechanoreceptor. *Science* **350**, 313–316 (2015).
17. K.-Y. Chun, Y. J. Son, E.-S. Jeon, S. Lee, C.-S. Han, A self-powered sensor mimicking slow- and fast-adapting cutaneous mechanoreceptors. *Adv. Mater.* **30**, 1706299 (2018).
18. H. Zhao, K. O'Brien, S. Li, R. F. Shepherd, Optoelectronically innervated soft prosthetic hand via stretchable optical waveguides. *Sci. Robot.* **1**, eaai7529 (2016).
19. L. Osborn, R. R. Kaliki, A. B. Soares, N. V. Thakor, Neuromimetic event-based detection for closed-loop tactile feedback control of upper limb prostheses. *IEEE Trans. Haptics* **9**, 196–206 (2016).
20. E. L. Graczyk, M. A. Schiefer, H. P. Saal, B. P. Delhaye, S. J. Bensmaia, D. J. Tyler, The neural basis of perceived intensity in natural and artificial touch. *Sci. Transl. Med.* **8**, 362ra142 (2016).
21. S. Raspopovic, M. Capogrosso, F. M. Petrini, M. Bonizzato, J. Rigosa, G. Di Pino, J. Carpaneto, M. Controzzi, T. Boretius, E. Fernandez, G. Granata, C. M. Oddo, L. Citi, A. L. Ciancio, C. Cipriani, M. C. Carrozza, W. Jensen, E. Guglielmelli, T. Stieglitz, P. M. Rossini, S. Micera, Restoring natural sensory feedback in real-time bidirectional hand prostheses. *Sci. Transl. Med.* **6**, 222ra19 (2014).
22. D. W. Tan, M. A. Schiefer, M. W. Keith, J. R. Anderson, J. Tyler, D. J. Tyler, A neural interface provides long-term stable natural touch perception. *Sci. Transl. Med.* **6**, 257ra138 (2014).
23. S. Wendelken, D. M. Page, T. Davis, H. A. C. Wark, D. T. Kluger, C. Duncan, D. J. Warren, D. T. Hutchinson, G. A. Clark, Restoration of motor control and proprioceptive and cutaneous sensation in humans with prior upper-limb amputation via multiple Utah Slanted Electrode Arrays (USEAs) implanted in residual peripheral arm nerves. *J. Neuroeng. Rehabil.* **14**, 121 (2017).
24. L. Osborn, M. Fifer, C. Moran, J. Betthausen, R. Armiger, R. Kaliki, N. Thakor, Targeted transcutaneous electrical nerve stimulation for phantom limb sensory feedback, 2017 *IEEE Biomedical Circuits and Systems Conference (BioCAS)*, Torino, Italy, 19 to 21 October 2017.
25. H. P. Saal, B. P. Delhaye, B. C. Rayhaun, S. J. Bensmaia, Simulating tactile signals from the whole hand with millisecond precision. *Proc. Natl. Acad. Sci. U.S.A.* **114**, E5693–E5702 (2017).
26. C. M. Oddo, S. Raspopovic, F. Artoni, A. Mazzoni, G. Spigler, F. Petrini, F. Giambattistelli, F. Vecchio, F. Miraglia, L. Zollo, G. Di Pino, D. Camboni, M. C. Carrozza, E. Guglielmelli, P. M. Rossini, U. Faraguna, S. Micera, Intraneural stimulation elicits discrimination of textural features by artificial fingertip in intact and amputee humans. *eLife* **5**, e09148 (2016).
27. L. Osborn, H. Nguyen, R. Kaliki, N. Thakor, Prosthesis grip force modulation using neuromorphic tactile sensing, in *Myoelectric Controls Symposium* (University of New Brunswick, 2017), pp. 188–191.
28. V. Skljarevski, N. M. Ramadan, The nociceptive flexion reflex in humans—Review article. *Pain* **96**, 3–8 (2002).
29. B. Bussel, A. Roby-Brami, Ph. Azouvi, A. Biraben, A. Yakovleff, J. P. Held, Myoclonus in a patient with spinal cord transection. Possible involvement of the spinal stepping generator. *Brain* **111**, 1235–1245 (1988).
30. A. Latremoliere, C. J. Woolf, Central sensitization: A generator of pain hypersensitivity by central neural plasticity. *J. Pain* **10**, 895–926 (2009).
31. G. Chai, X. Sui, S. Li, L. He, N. Lan, Characterization of evoked tactile sensation in forearm amputees with transcutaneous electrical nerve stimulation. *J. Neural Eng.* **12**, 066002 (2015).
32. G. Schalk, J. Mellinger, Brain sensors and signals, in *A Practical Guide to Brain–Computer Interfacing with BCI2000*, G. Schalk, J. Mellinger, Eds. (Springer, 2010), pp. 9–35.
33. E. M. Izhikevich, Simple model of spiking neurons. *IEEE Trans. Neural Netw.* **14**, 1569–1572 (2003).
34. S. Terryn, J. Bancart, D. Lefeber, G. Van Assche, B. Vanderborght, Self-healing soft pneumatic robots. *Sci. Robot.* **2**, eaan4268 (2017).
35. D. D. Damian, A. H. Arita, H. Martinez, R. Pfeifer, Slip speed feedback for grip force control. *IEEE Trans. Biomed. Eng.* **59**, 2200–2210 (2012).
36. C. Hartley, E. P. Duff, G. Green, G. S. Mellado, A. Worley, R. Rogers, R. Slater, Nociceptive brain activity as a measure of analgesic efficacy in infants. *Sci. Transl. Med.* **9**, eaah6122 (2017).
37. L. Osborn, W. W. Lee, R. Kaliki, N. Thakor, Tactile feedback in upper limb prosthetic devices using flexible textile force sensors, *Fifth IEEE RAS & EMBS International Conference on Biomedical Robotics and Biomechatronics*, San Paulo, Brazil, 12 to 15 August, 2014.
38. F. Mancini, C. F. Sambo, J. D. Ramirez, D. L. Bennett, P. Haggard, G. D. Iannetti, A fovea for pain at the fingertips. *Curr. Biol.* **23**, 496–500 (2013).
39. M. Serrao, F. Pierelli, R. Don, A. Ranavolo, A. Cacchio, A. Currà, G. Sandrini, M. Frascarelli, V. Santilli, Kinematic and electromyographic study of the nociceptive withdrawal reflex in the upper limbs during rest and movement. *J. Neurosci.* **26**, 3505–3513 (2006).
40. W. F. N. Santos, M. J. Lewis, Aerothermodynamic performance analysis of hypersonic flow on power law leading edges. *J. Spacecr. Rockets* **42**, 588–597 (2005).
41. W. F. N. Santos, M. J. Lewis, Power-law shaped leading edges in rarefied hypersonic flow. *J. Spacecr. Rockets* **39**, 917–925 (2002).

**Acknowledgments:** We would like to sincerely thank the participant who volunteered and selflessly dedicated his time for this research to help enhance the current state of the art of prosthetic limb technology for the betterment of current and future users. We would like to thank B. Skeritt-Davis for help with the EEG experiment and M. Hodgson for support with the prosthesis controller and hardware. **Funding:** This work was supported in part by the Space@Hopkins funding initiative through Johns Hopkins University, the Johns Hopkins University Applied Physics Laboratory Graduate Fellowship Program, and the Neuroengineering Training Initiative through the National Institute of Biomedical Imaging and Bioengineering through the NIH under grant T32EB003383. **Author contributions:** L.E.O. and N.V.T. conceptualized the idea of quantifying and conveying pain and tactile sensory signals. L.E.O. designed the studies, developed the hardware and software, performed the experiments, analyzed the data, and wrote the paper. A.D. analyzed EEG data and assisted with writing the paper. H.H.N. assisted in collecting and analyzing data. J.L.B., C.L.H., and R.R.K. assisted in analyzing the data and writing the paper. N.V.T. supervised the experiments and assisted in designing the studies, analyzing the data, and writing the paper.

**Competing interests:** L.E.O. and N.V.T. are inventors on intellectual property regarding the multilayered e-dermis, which has been disclosed to Johns Hopkins University. N.V.T. is a cofounder and R.R.K. is the chief executive officer of IBT. This relationship has been disclosed to and is managed by Johns Hopkins University. The other authors declare that they have no competing interests. **Data and materials availability:** All data needed to evaluate the conclusions in the paper are present in the paper or the Supplementary Materials. Data and software code can be made available by materials transfer agreement upon reasonable request.

Submitted 11 March 2018

Accepted 29 May 2018

Published 20 June 2018

10.1126/scirobotics.aat3818

**Citation:** L. E. Osborn, A. Dragomir, J. L. Betthausen, C. L. Hunt, H. H. Nguyen, R. R. Kaliki, N. V. Thakor, Prosthesis with neuromorphic multilayered e-dermis perceives touch and pain. *Sci. Robot.* **3**, eaat3818 (2018).

## SOFT ROBOTS

# Peano-HASEL actuators: Muscle-mimetic, electrohydraulic transducers that linearly contract on activation

Nicholas Kellaris,<sup>1,2</sup> Vidyacharan Gopaluni Venkata,<sup>1</sup> Garrett M. Smith,<sup>1</sup> Shane K. Mitchell,<sup>1</sup> Christoph Keplinger<sup>1,2\*</sup>

Copyright © 2018  
The Authors, some  
rights reserved;  
exclusive licensee  
American Association  
for the Advancement  
of Science. No claim  
to original U.S.  
Government Works

Soft robotic systems are well suited to unstructured, dynamic tasks and environments, owing to their ability to adapt and conform without damaging themselves or their surroundings. These abilities are crucial in areas such as human-robot interaction. Soft robotic systems are currently limited by the soft actuators that power them. To date, most soft actuators are based on pneumatics or shape-memory alloys, which have issues with efficiency, response speed, and portability. Dielectric elastomer actuators (DEAs) are controlled and powered electrically and excel with muscle-like actuation, but they typically require a rigid frame and prestretch to perform effectively. In addition, DEAs require complex stacks or structures to achieve linear contraction modes. We present a class of soft electrohydraulic transducers, termed Peano-HASEL (hydraulically amplified self-healing electrostatic) actuators, that combine the strengths of fluidic actuators and electrostatic actuators, while addressing many of their issues. These actuators use both electrostatic and hydraulic principles to linearly contract on application of voltage in a muscle-like fashion, without rigid frames, prestretch, or stacked configurations. We fabricated these actuators using a facile heat-sealing method with inexpensive commercially available materials. These prototypical devices demonstrated controllable linear contraction up to 10%, a strain rate of 900% per second, actuation at 50 hertz, and the ability to lift more than 200 times their weight. In addition, these actuators featured characteristics such as high optical transparency and the ability to self-sense their deformation state. Hence, this class of actuators demonstrates promise for applications such as active prostheses, medical and industrial automation, and autonomous robotic devices.

## INTRODUCTION

Traditional mechanical systems, made from rigid components such as pistons and electromagnetic motors, excel at precise and repetitive tasks. As a result, these rigid systems have seen widespread application in areas such as industrial automation. However, they have limited adaptability, which restricts their effectiveness in unstructured and dynamic environments. Soft robotic systems, which are based on compliant materials and structures, demonstrate promise in these unpredictable situations due to their resilience, adaptability, and shock-absorbing characteristics (1–6).

Soft actuators currently explored for use in robotic systems are numerous [Hines *et al.* (7) provides a good overview of various soft actuator technologies] and include thermally responsive polymers (8), fluidic actuators (both pneumatic and hydraulic) (9–15), and dielectric elastomer actuators (DEAs) (16–19). Of these, pneumatic actuators are the most prevalent because they can achieve high actuation force and large strokes, similar to natural muscle (20). In addition, they are highly versatile, which allows them to achieve varied modes of actuation (21). However, pneumatic actuators have low efficiency (11) and experience substantial trade-offs between actuation speed and portability, with the response speed of untethered devices being low (2, 22); high-power operation requires rigid and bulky reservoirs or compressors.

Electrically powered actuators, such as DEAs, offer several advantages such as high-speed actuation, high strain (>100%) (16), silent operation, and self-sensing (23). However, DEAs are driven by high electric fields, which can lead to irreversible dielectric breakdown. The likelihood of

dielectric failure, which follows Weibull statistics, increases as electrode area is scaled up (24), reducing the reliability of DEAs for large-scale applications. Furthermore, DEAs typically require rigid and bulky frames to provide a prestretch for high-strain and high-power operation, with current freestanding DEAs limited to small strains (25–27). In addition, actuation modes are generally limited to elongation on activation, with contraction being achieved through stacked configurations (28) that require elaborate fabrication processes and large electrode areas, increasing risk of dielectric failure.

Here, we introduce Peano-HASEL actuators as a class of versatile, soft electrohydraulic transducers that feature fast linear contraction on activation, demonstrate high force production and scalability, and can be made from inexpensive materials that are compatible with industrial fabrication methods. Peano-HASEL actuators synergize the strengths of linearly contracting Peano fluidic actuators created by Niiyama *et al.* (12) and Sanan *et al.* (13), and hydraulically amplified self-healing electrostatic (HASEL) actuators recently developed by Acome *et al.* (29). Building upon the fundamental physical concepts of HASEL actuators introduced in (29), Peano-HASEL actuators use a materials system based on inextensible but flexible thin shells, thereby eliminating the need for highly stretchable electrodes and dielectrics. Peano-HASELs have several distinctive qualities: (i) They linearly contract on application of voltage without relying on prestretch, rigid frames, or stacked configurations; (ii) they are electrically powered, which grants them the advantages of DEAs such as high-speed operation and the ability to self-sense their deformation state through capacitance monitoring (23); (iii) they incorporate a liquid dielectric, which provides direct coupling of electrostatic and hydraulic forces for high-power and precise operation, without requiring external sources of compressed fluids or pumps; (iv) they can be made from a variety of materials, even allowing for highly transparent

<sup>1</sup>Department of Mechanical Engineering, University of Colorado Boulder, Boulder, CO 80309, USA. <sup>2</sup>Materials Science and Engineering Program, University of Colorado Boulder, Boulder, CO 80309, USA.

\*Corresponding author. Email: christoph.keplinger@colorado.edu

designs; and (v) they are fabricated using industrially compatible methods such as heat sealing.

## RESULTS

### Principles of operation and design

Peano-HASEL actuators operate on electrostatic and hydraulic principles, as shown in Fig. 1A. The actuator consists of a series of rectan-

gular pouches made from a flexible and inextensible shell that is filled with a liquid dielectric. Electrodes cover a portion of each pouch on either side of the actuator. When a voltage is applied, electrostatic forces displace the liquid dielectric, causing the electrodes to progressively close, such as in electrostatic “zipping” actuators (30–33). These electrostatic forces are determined by the Maxwell pressure,  $P \propto \epsilon E^2$  (34), where  $\epsilon$  is the dielectric permittivity and  $E$  is the magnitude of the electrical field. This pressure forces fluid into the uncovered portion

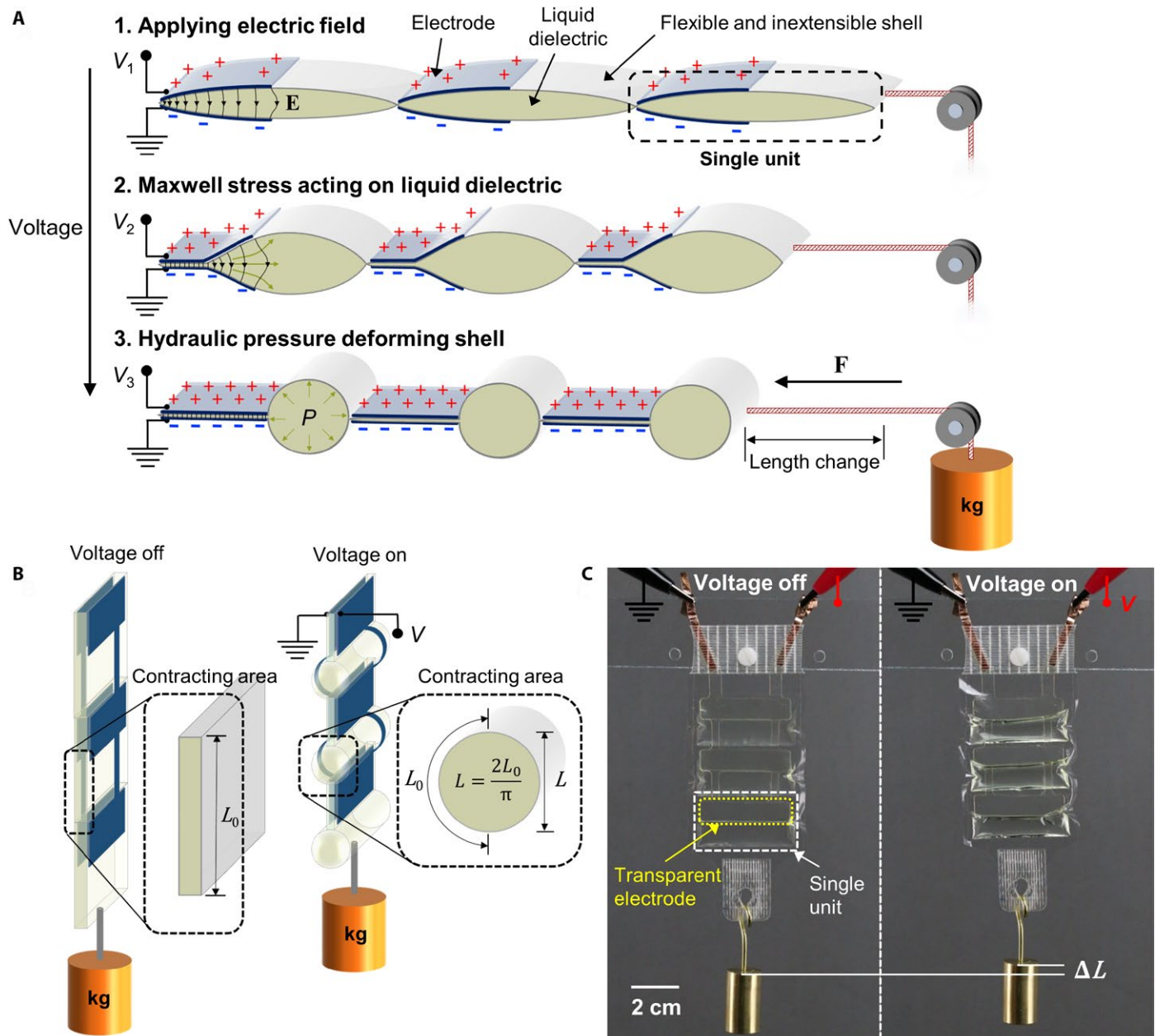


**Fig. 1. Basic components of Peano-HASEL actuators and principles of operation.** (A) Schematic side view showing the cross section of a three-unit Peano-HASEL actuator; each unit consists of a rectangular pouch made from an inextensible and flexible polymer shell, filled with a liquid dielectric. Electrodes are placed over a portion of the pouch on either side; when an increasing voltage ( $V$ ) is applied, electrostatic forces displace the liquid dielectric, causing the electrodes to progressively close. This forces fluid into the uncovered portion of the pouch, causing a transition from a flat cross section to a more circular one, which leads to a contractile force,  $F$ . (B) Schematic side view of a three-unit Peano-HASEL actuator with voltage off and voltage on. The theoretical maximum strain for the contracting area of the pouch is  $1 - \frac{2}{\pi}$  or about 36%.  $L_0$ , length of contracting area with voltage off.  $L$ , length of contracting area with voltage on. (C) Three-unit Peano-HASEL actuator shown lifting 20 g on application of 8 kV across the electrodes. This construction used transparent hydrogels as electrodes and fiberglass-reinforced tape for mounting connections.

of the pouch, causing this region to transition from a flat cross section toward a more circular one. Because the shell is inextensible, this transition results in linear contraction of the actuator. The theoretical maximum strain is  $\sim 36\%$  ( $1 - 2/\pi$ ) in the contracting area, as can be seen through simple geometric changes in cross section shown in Fig. 1B. For our design, only half of each pouch is contracting area, whereas the other half is reserved for electrodes, so the theoretical maximum overall strain is limited to  $\sim 18\%$ . Figure 1C shows a three-unit Peano-HASEL actuator with no rigid components contracting on application of 8 kV.

### Fabrication of devices

Figure 2A shows the three central components used to fabricate Peano-HASEL actuators. The shell material is a biaxially oriented polypropylene (BOPP) film that is heat sealable on one side. This material is commonly used in food packaging for its mechanical strength, as well as in commercial capacitors for its high dielectric breakdown strength of  $\sim 700 \text{ V } \mu\text{m}^{-1}$  (35). The liquid dielectric is Envirotemp FR3—a high breakdown strength vegetable-based transformer oil. Last, we use ionically conductive hydrogel electrodes (36) to provide a voltage across our actuators. These are laser cut from a polyacrylamide hydrogel swollen with an aqueous LiCl solution (37) and bonded to a thin polydimethylsiloxane (PDMS) substrate (38) for mechanical support. Figure 2 (B to F) illustrates the heat-sealing process used to construct these actuators. First, we used a heat-press (detailed in fig. S1) with a heated metal die for

sealing actuator pouches. We left gaps in the seal of each pouch to fill them with liquid dielectric. After filling, the pouches were sealed completely with a heated aluminum bar. Last, we aligned and placed the prefabricated hydrogel electrodes (described in fig. S2) on the pouches to create a completed actuator with a total weight of 5 g. We left excess BOPP on the sides of the pouches to serve as a “skirt” to prevent electrical arcing around the device during operation.

We focused on a three pouch Peano-HASEL because it allowed us to explore the behavior of connected pouches while reducing fabrication complexity. Each pouch was 4 cm wide by 2 cm high, with electrodes 3.8 cm wide by 1 cm high, covering half of the pouch height. This design made the contracting area 4 cm wide by 1 cm high; the aspect ratio 4:1 was picked to be large enough to reduce edge effects caused by the constrained sides, as found by Veale *et al.* (15) for Peano fluidic actuators. To demonstrate ease of manufacturing and compatibility with industrial production methods, we also fabricated devices with aluminum electrodes integrated on the BOPP surface using a commercial vacuum-deposition process. Our fabrication process began with metalized BOPP sheets that were etched with a KOH solution into a desired electrode pattern. The full process is detailed in fig. S3.

### Force-strain characteristics

We tested the force-strain relation for two Peano-HASEL actuators—one using hydrogel electrodes and the other using aluminum electrodes.

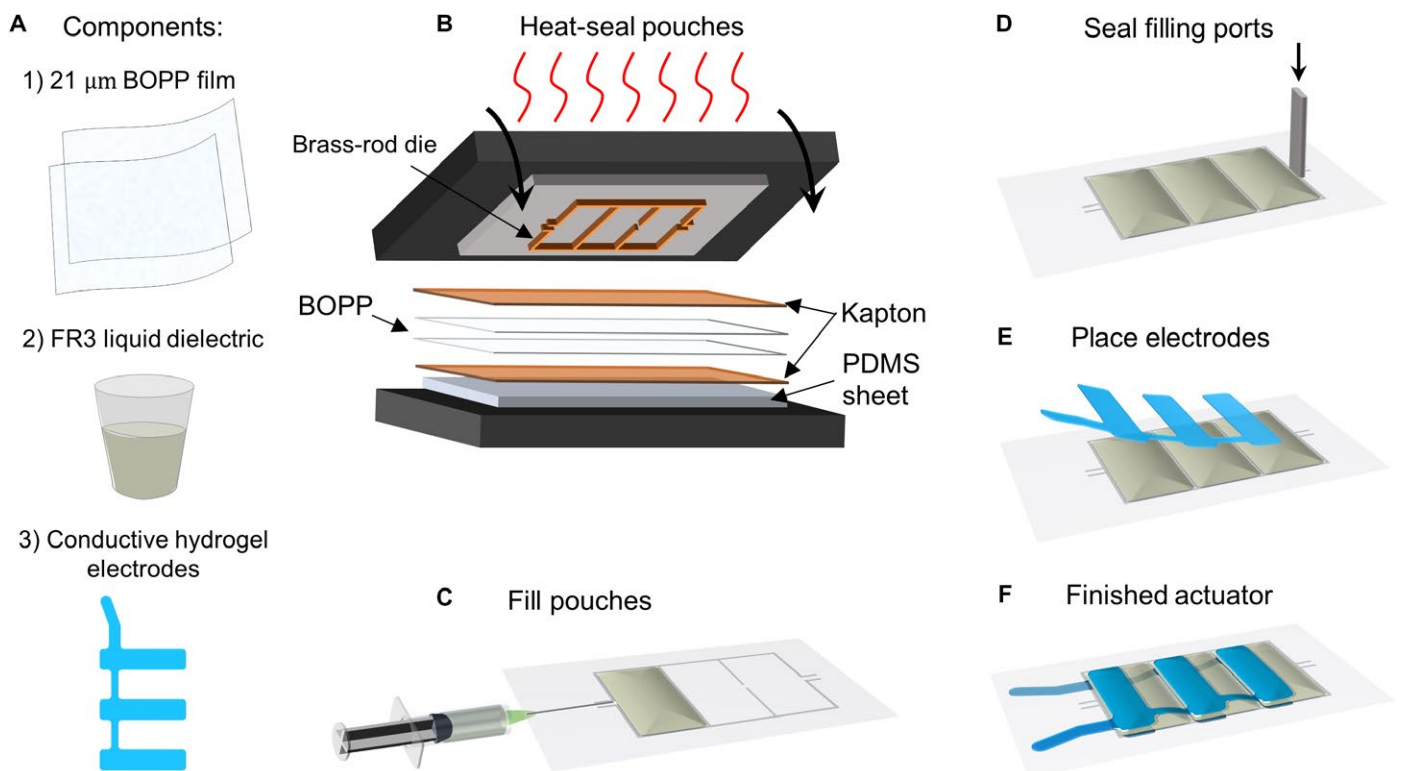


**Fig. 2. Fabrication process for Peano-HASEL actuators.** (A) Basic components of a Peano-HASEL actuator. (B) Two BOPP sheets were placed between two layers of Kapton film and sealed using a heated brass-rod die. The die was designed to give pouches (2 cm by 4 cm) with 2-mm access ports for filling with liquid dielectric. A PDMS sheet was placed below the Kapton as a load-dispersing layer. Figure S1 describes the heat-press in more detail. (C) Pouches were filled with FR3 liquid dielectric using a syringe. (D) A heated aluminum rod was used to seal the filling ports. (E) PDMS-backed hydrogel electrodes were placed on each side of the pouches. Figure S2 describes the process for fabricating these electrodes. (F) A finished actuator is shown.

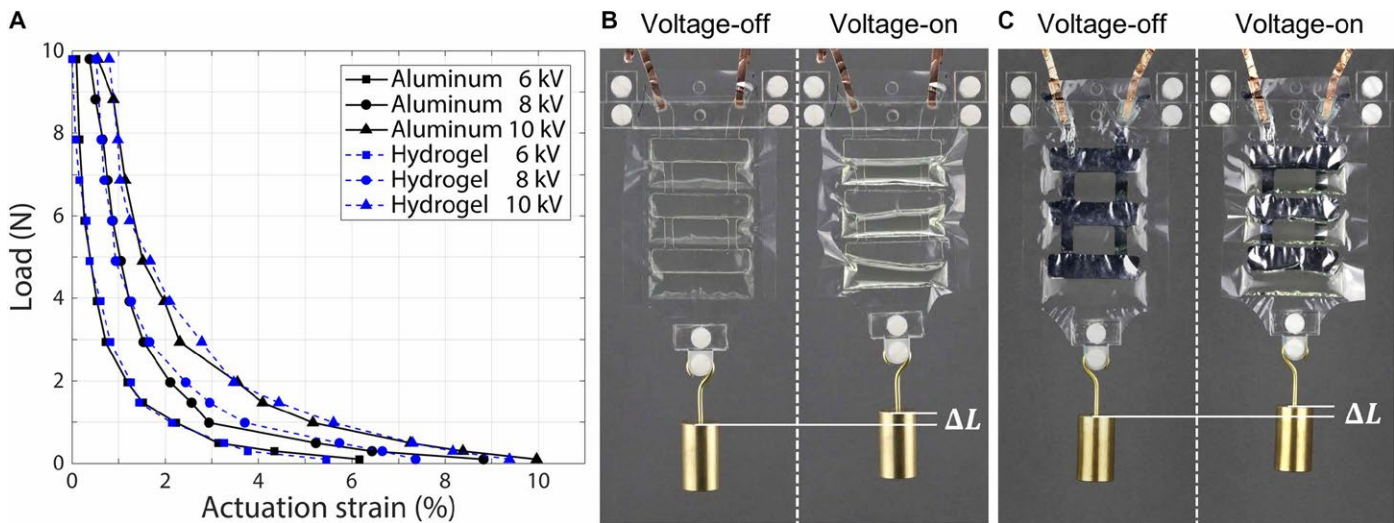


**Fig. 3. Force-strain characteristics of Peano-HASEL actuators using hydrogel and aluminum electrodes.** (A) Comparison of the force-strain curves for two Peano-HASEL actuators, one using hydrogel and the other using aluminum electrodes, revealing no difference in performance. A maximum of 10% strain was observed under a 20-g load at 10-kV applied voltage. (B) A hydrogel-electrode actuator was mounted on an acrylic stand for actuation tests and demonstrated contraction under 20-g load at 8 kV. (C) An aluminum-electrode actuator was mounted on an acrylic stand for actuation tests and demonstrated contraction under 20-g load at 8 kV.

A modified square-wave voltage signal with long rise and fall times ( $\sim 1$  s) was used to ensure consistent actuation (fig. S4). Actuators were tested at 6, 8, and 10 kV; this corresponded to maximum electric fields of 140, 190, and 240  $\text{V } \mu\text{m}^{-1}$ , respectively. The measured force-strain curves are depicted in Fig. 3A and show no difference between aluminum- and hydrogel-electrode performance, demonstrating versatility in material selection and design. The highest load applied to the actuators was 10 N (1 kg), which corresponded to the blocking force for actuators activated at 6 kV and was less than the blocking force at 8 and 10 kV. The 1-kg load resulted in a maximum cross-sectional stress of 6 MPa in the actuator. A strain of 10% was achieved at 10 kV with a 0.02-N (20 g) load. The shape of the observed force-strain relation is characteristic of Peano-fluidic actuators (12). Furthermore, the monotonic decrease in force with strain is also observed in skeletal muscle (20).

Figure 3 (B and C) shows examples of actuators with hydrogel and aluminum electrodes, respectively. Movies S1 and S2 demonstrate the dynamics of both types of actuators. Although the vacuum-deposited aluminum electrodes show promise for industrially amenable fabrication, the very thin aluminum layers used in this paper ( $\sim 30$  nm) made the electrodes vulnerable to mechanical wear and ablation during high-voltage operation (fig. S5).

### Arrays of parallel actuators for scaling up forces

A key feature of biological muscle is its massively parallelized structure, which allows for high-force generation and operational redundancy. Figure 4A demonstrates a method for efficiently stacking Peano-HASEL actuators in parallel to increase actuation force. Offsetting actuators vertically allows the expanding cross section of one actuator to nest within the pulled-in electrode area of adjacent actuators. Alternating electrode polarities ensures that adjacent electrodes are always at the same potential. Figure 4B shows a 1.4-cm-thick stack of six actuators in its inactive and active state to visualize the offset configuration. As expected, the stack demonstrated an actuation force roughly six times that of an individual Peano-HASEL actuator, as shown in Fig. 4C. Figure 4D shows this

stack, which weighs 30 g, lifting 500 g over a strain of 4.6%. Movie S3 shows several lifting cycles for this 500-g mass, as well as actuation with a filled water bottle ( $\sim 1$  kg).

### High-speed actuation

For most fluidic actuators, the limiting factor in mechanical response is the time required to pump the working fluid throughout the system. Because Peano-HASELs locally pump the fluid in each pouch, we reduce the distance the fluid must travel, which reduces actuation time. In addition, we reduce viscous loss and design complexity by avoiding the need for regulators and valves.

To elucidate the fast-actuation characteristics of Peano-HASEL actuators, we examined contraction speed under an inertial load (i.e., a hanging weight), as shown in Fig. 5A. We applied a square-wave voltage signal and measured mechanical response as a function of time for loads ranging from 10 to 500 g; Fig. 5B plots actuator response for a 100-g load. Actuators took between 12 ms (for a 10-g load) and 18 ms (for a 500-g load) from initial contraction  $t_s$  to their equilibrium strain  $t_e$  as we varied the loads between 10 and 500 g. The total load is the hanging weight (e.g., 10 g) plus the mass of the lower mounting piece (4 g). Performance parameters, such as peak strain rate and specific power, were calculated between  $t_s$  and  $t_e$ . Calculations are described in the Supplementary Materials; fig. S6A shows the relevant parameters for these calculations, and fig. S6 (B to E) shows the data produced for a 100-g load.

Peak strain rate as a function of load is shown in Fig. 5C; we see a generally hyperbolic relation for these actuators, which resembles the force-velocity relation for mammalian muscle under isotonic contraction (39). Values varied between 140 and 890%  $\text{s}^{-1}$  depending on the load; our maximum strain rate was nearly two times the maximum achievable strain rate in mammalian skeletal muscle (500%  $\text{s}^{-1}$ ) (40). By comparison, DEAs have demonstrated peak strain rates between 450 and 4500%  $\text{s}^{-1}$  for acrylic elastomers and up to 34,000%  $\text{s}^{-1}$  for silicone elastomers (41); however, these numbers are for radially expanding DEAs that require prestretch and do not act on external loads.

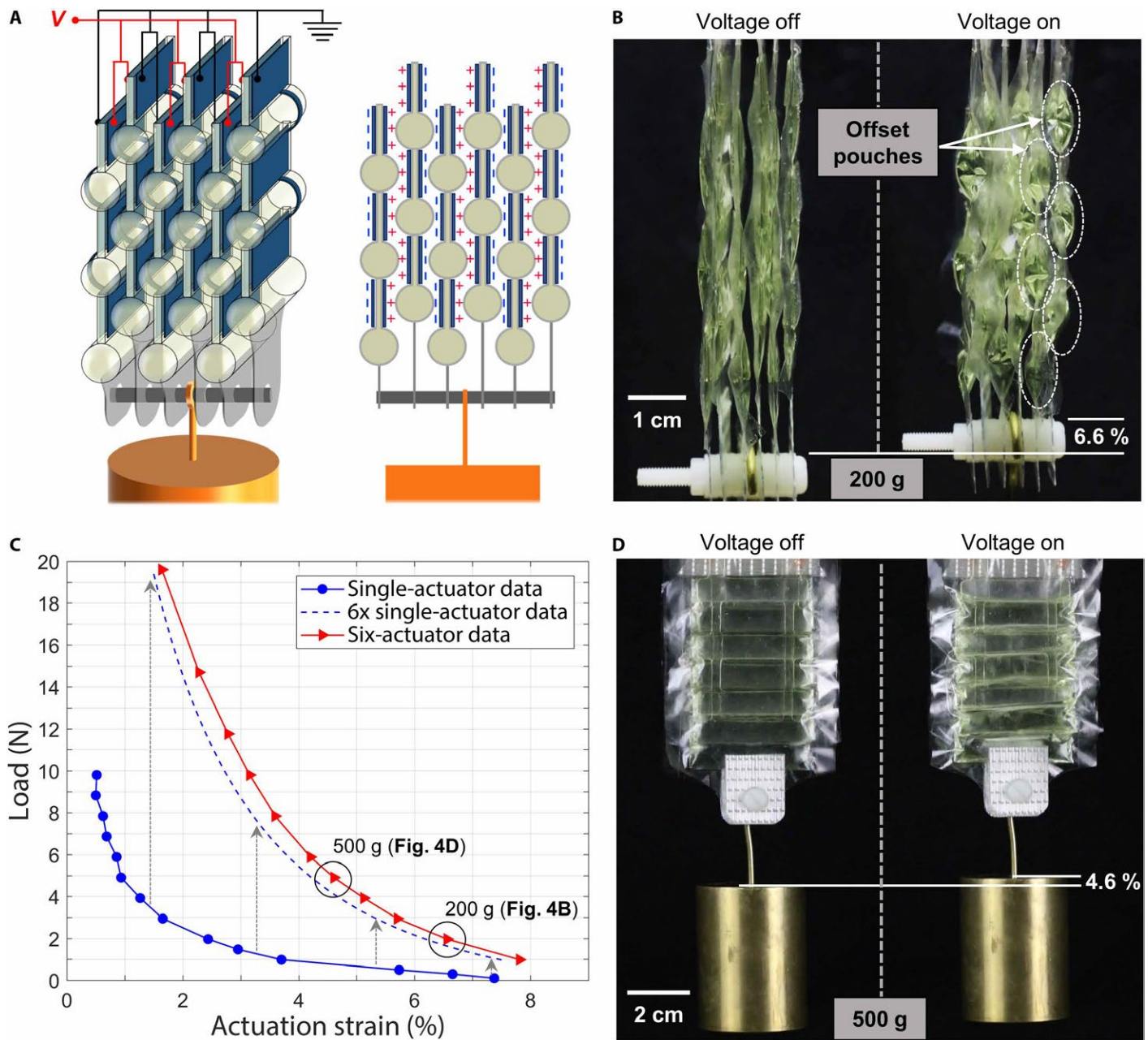


**Fig. 4. Scaling up forces with arrays of Peano-HASEL actuators.** (A) Peano-HASEL actuators arranged in parallel to scale up force generation in a compact array. Actuators are stacked such that adjacent actuators are vertically offset by half of the pouch height. Electrode polarity alternates (as shown on the right) such that electrodes facing each other from adjacent actuators are always at the same potential. (B) Six actuators shown contracting 6.6% under a 200-g load at 8 kV. The white ovals show the offset pouches in the two rightmost actuators. (C) Comparison of the force-strain characteristics for one actuator to an array of six. Single-actuator data were projected upward by multiplying the load by six (dashed line) to estimate expected performance for an array of six actuators. The array of six actuators slightly outperforms expected results, demonstrating the ability to effectively scale up actuation force. (D) Six actuators shown contracting 4.6% under a 500-g load at 8 kV.

Specific power was calculated during these contraction cycles and is shown in Fig. 5D. From this plot, we see that peak specific power was greatest during contraction with a 100-g load. The maximum value of  $160 \text{ W kg}^{-1}$  is comparable to mammalian skeletal muscle, which falls between 50 (typical) and  $284 \text{ W kg}^{-1}$  (maximum) (41). The average specific power during contraction was above  $50 \text{ W kg}^{-1}$  for all but the lowest load.

To further explore the fast actuation characteristics of fabricated Peano-HASEL actuators, we created a custom stand for mounting

the actuators (fig. S7A), with elastic bands to provide a nearly constant restoring force at a range of frequencies (Fig. 5E). Tests were conducted at various frequencies using a reversing-polarity square wave (fig. S7B). Actuation strain (normalized to maximum actuation at low frequency) is plotted as a function of frequency in Fig. 5F. Tests were performed with FR3 medium-viscosity liquid dielectric, as well as a low-viscosity mineral oil (Drakeol 7), to test viscosity dependence of the system. FR3 has a viscosity of 50 cSt at  $40^\circ\text{C}$ , whereas Drakeol 7 has a viscosity of  $\sim 12 \text{ cSt}$  at  $40^\circ\text{C}$ . With FR3, the

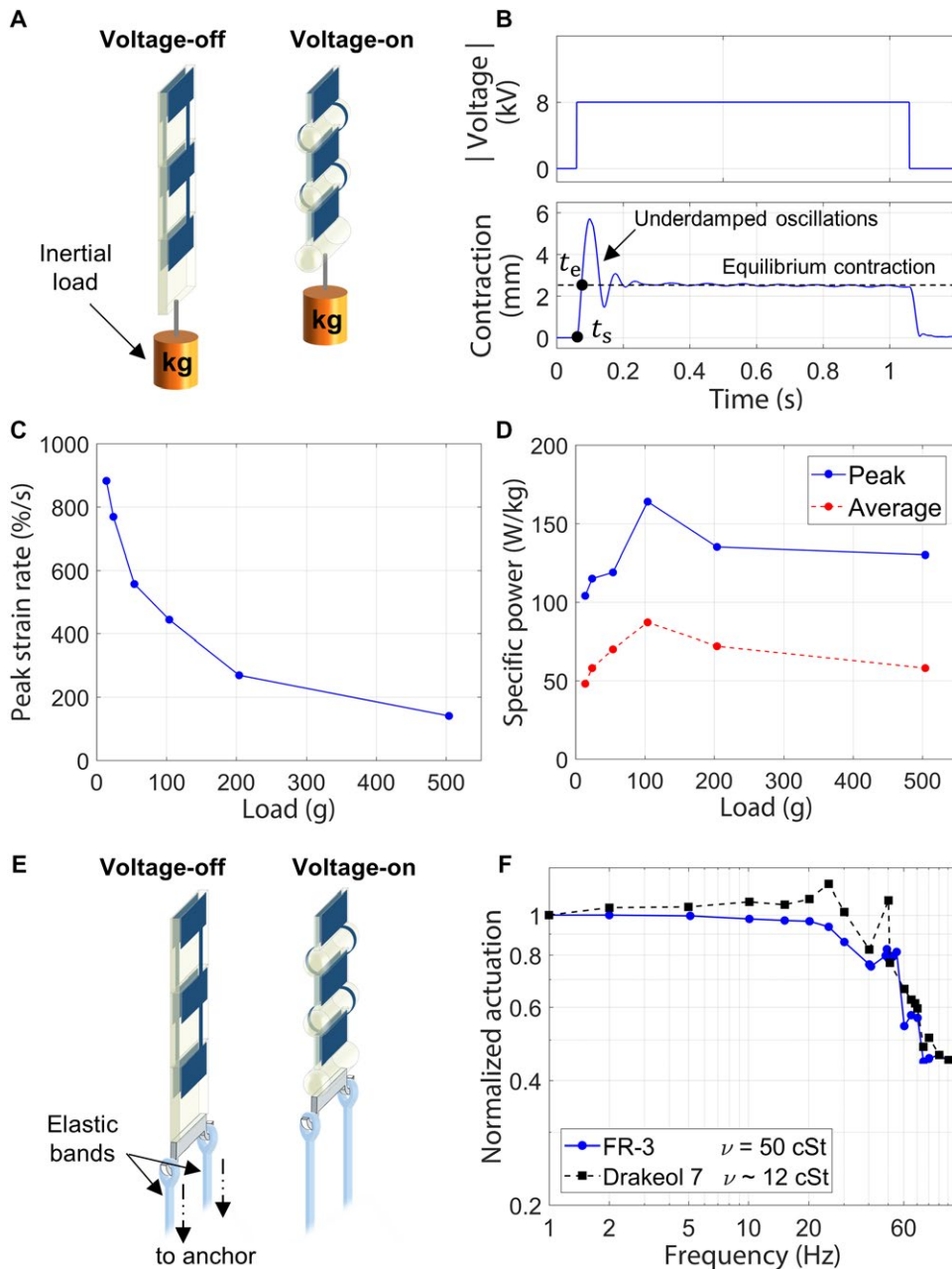


**Fig. 5. High-speed performance of Peano-HASEL actuators.** (A) Schematic of the test setup for determining contraction characteristics. The minimum cross section of the actuator used for testing was (40 mm by 0.042 mm) corresponding to a maximum static stress of 2.9 MPa with a 500-g load. (B) An 8-kV square wave was applied to the actuator. The resulting contraction response was measured, where  $t_s$  and  $t_e$  correspond to the time of initial contraction and equilibrium contraction, respectively. Underdamped oscillations were observed after initial contraction. The small oscillations observed after 0.3 s correspond to out-of-plane swinging of the load and are not part of the characteristic response. (C) Peak strain rate during contraction as a function of load. (D) Peak and average specific power as a function of load. (E) Schematic of the test setup for frequency response. Elastic bands were attached to the bottom of the actuator and tensioned to provide a constant 1-N restoring force. (F) Frequency response curves for Peano-HASEL actuators filled with liquid dielectrics of different viscosities. The actuator filled with FR3 liquid dielectric showed a nearly flat response up to 20 Hz. The lower viscosity Drakeol 7 allowed maximum actuation at higher frequencies.

three-unit actuator had a cutoff frequency of more than 40 Hz and actuated with >90% maximum actuation up to 25 Hz. Movie S4 shows the performance of an FR3-filled actuator at several frequencies from 1 to 50 Hz. With Drakeol 7, we see undiminished actuation up

to 30 Hz. The flat frequency profile below cutoff is attractive for simple control when used in robotic systems. Various resonance peaks can be seen in the data and are likely a result of the elastic bands used during testing. These results indicate that frequency characteristics depend on the viscosity of the liquid dielectric. Actuation speed should similarly depend on pouch geometry and size and can be improved by future optimization efforts.

### Demonstration of fast and precise actuation

To illustrate fast and precisely controlled actuation of Peano-HASEL actuators in a robotic application, we constructed a 7:1 acrylic lever arm connected to two actuators in a parallel configuration (Fig. 6A) and applied a variety of voltage signals. Applying a 13-kV voltage step allowed fast contraction to throw a table tennis ball 24 cm into the air (Fig. 6B). To demonstrate controllable static displacement, voltage was increased from 1 to 12 kV in 1-kV increments, with 0.75-s hold time at each voltage, with three illustrative voltages shown in Fig. 6C. Movie S5 shows the full demonstration of actuation, which includes progressive voltage steps, sinusoidal actuation, and the 13-kV voltage step. Figure S8 shows the voltage profile used for the demonstration. The fast and controllable actuation of Peano-HASEL actuators is largely due to the near-incompressibility of liquids, which generally leads to higher bandwidth and better static position control than equivalent pneumatic systems (42).

The control of autonomous mechanical systems requires sensory feedback. Because Peano-HASEL actuators are variable capacitors, their capacitance state can provide information on their deformation state. Keplinger *et al.* (23) has shown previously that by continuously monitoring the capacitance of DEAs, one can glean information on the mechanical deformation of the system. We adopted this method for Peano-HASEL actuators, using the setup described by Acome *et al.* (29) to self-sense deformation; the basic idea relies on superimposing a low-voltage ac signal onto the high-voltage dc actuation signal and then analyzing

the electrical impedance of the system. The position of the actuator was optically tracked while applying an actuation voltage signal similar to fig. S8; these data were compared to the changing capacitance signal, with the results shown in Fig. 7. Capacitance data were multiplied

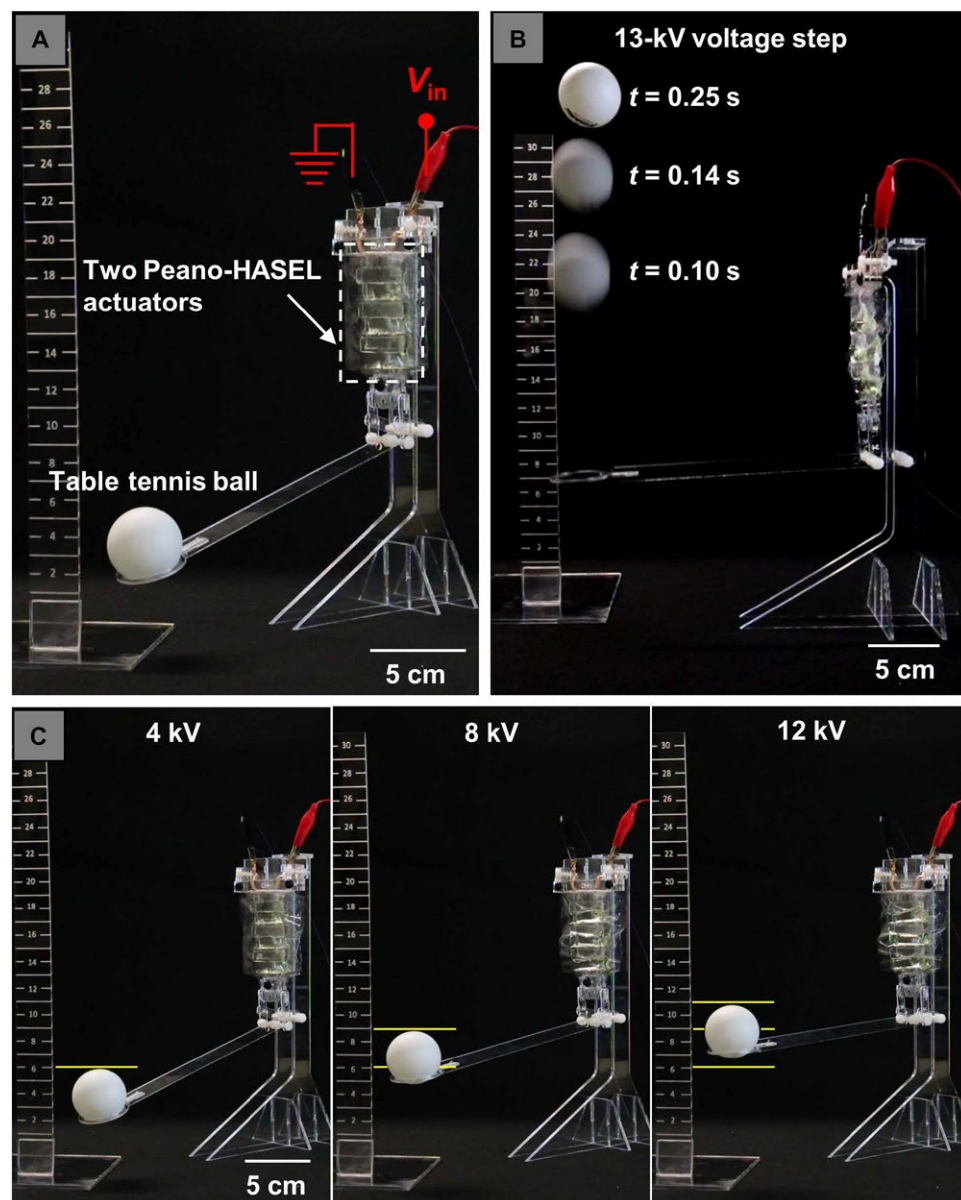


**Fig. 6. Demonstration of high-speed and precise actuation.** (A) A lever-arm setup was connected to two Peano-HASEL actuators in parallel for demonstrating fast and controllable actuation. (B) By applying a 13-kV voltage step, these actuators contracted fast enough to throw a ping-pong ball 24 cm into the air. Labeled times are measured from the start of contraction. (C) Incrementing voltage allowed controllable actuation of the arm, as shown in the progression of images with increasing voltage left to right. The yellow lines mark the position of the top of the ball for comparison. The ruler to the left of each picture shows 1-cm increments for scale.

by a constant scaling factor to allow comparison with the optical data. Reasonable agreement was observed between the two data sets. The observed discrepancy implies a nonlinear relationship between capacitance and strain. Experimental determination of this nonlinearity would enable calibration of capacitive data and allow for precise dynamic information on the deformation state of the actuator, mimicking the proprioceptive nature of biological systems.

### An imperceptible actuator

Using BOPP films and PDMS/hydrogel electrodes allows construction of an actuator that is highly transparent when submerged in an

index-matched liquid. Figure 8A shows a Peano-HASEL actuator in air. Submersion in Drakeol 19 mineral oil (Fig. 8B) led to a substantial reduction in light dispersion and high transparency. Figure 8C shows this actuator contracting with a 10-g load. Movie S6 shows the process of submerging the actuator followed by actuation while fully submerged. Peano-HASELs have the potential to be virtually invisible and operable in water by (i) fully encapsulating and insulating the electrodes and (ii) using a liquid dielectric with an index of refraction that matches water.

### Actuator lifetime

Lifetime tests were performed for two actuators—one at 6 Hz and the other at 50 Hz—with the same setup used for testing frequency response. Actuator failure occurred after ~20,000 cycles in both cases. No observable decrease in actuation was measured before electrical breakdown, which occurred through the heat seal of the actuators near the electrodes. These results are presented in fig. S9 for the 6-Hz test. Although these results are promising, actuator lifetime may be improved through optimization of materials and pouch geometries.

### DISCUSSION

Here, we have introduced a class of artificial muscle actuators based on electrohydraulic operating principles. Peano-HASEL actuators are versatile and provide many muscle-mimetic properties, including contraction on activation, muscle-like specific power, and the potential for highly parallelized stacking for increased force generation. In some areas, such as peak strain rate and frequency response, they exceed the performance of mammalian skeletal muscle.

Compared with current fluidic actuators and DEAs, Peano-HASELs exhibit several promising qualities. First, Peano-

HASEL actuators linearly contract on activation without stacks, pre-stretch, or frames, which makes them unique in the field of electrostatic actuators. Second, by locally displacing liquid dielectrics, Peano-HASEL actuators reduce viscous loss within the system, increase their response speed, and achieve high positional control. Further, their flat frequency response until cutoff and minimal elasticity lead to simpler kinematics for actuator control and modeling. In addition, the ability of Peano-HASEL actuators to self-sense their deformation state through capacitance monitoring mimics the proprioceptive nature of muscle. In contrast to hydrostatically coupled DEAs, where electric fields are applied across elastomers (43), Peano-HASELs

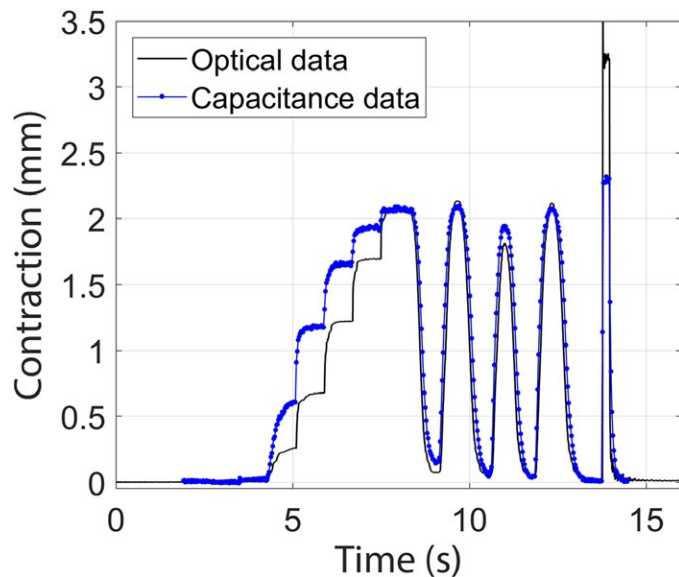


**Fig. 7. Self-sensing of actuator position.** Plot of dimensionless capacitance and optically tracked position data for a single actuator under the influence of a varying voltage signal. Capacitance data were multiplied by a constant scale factor to provide agreement with position data; no other calibration was performed.

apply electric fields through a deformable structure containing a liquid dielectric, which does not have to rely on highly stretchable electrodes and dielectrics. The resulting flexibility in material selection enables Peano-HASELs to be low cost, versatile, and compatible with roll-to-roll industrial fabrication processes such as heat sealing and vacuum-deposition of electrodes. Currently, hydrogel-electrode actuators can be made for  $\sim$ \$0.10 in materials, which should reduce considerably for large-scale fabrication. Last, actuator characteristics are largely independent of the constituent materials—assuming they meet certain criteria such as flexibility and high breakdown strength—therefore, design can be tailored for attractive properties like high transparency.

Moving forward, there are many opportunities to explore new materials, geometries, and methods of fabrication to improve performance and resolve current limitations of Peano-HASEL actuators. One outstanding issue is their inability to consistently self-heal because of the thin BOPP layer, which can puncture after dielectric breakdown events, allowing fluid to leak out. With next-generation materials, these actuators should achieve the same self-healing properties shown by Acome *et al.* (29) for HASEL actuators. An existing hurdle for electrostatic actuators is the requirement of high electric fields, which typically means providing voltages of several kilovolts. Operational voltages can be reduced by improving the design of actuators through the use of dielectrics with high permittivity, reducing the thickness of dielectric layers and exploring alternate geometries. However, there are already several commercial options for supplying and controlling high voltage that are readily available: XP Power and Pico Electronics produce several ultraminiature high-voltage dc-dc converters that can produce up to 10 kV using a 5-V input; IXYS manufactures metal oxide semiconductor field-effect transistors, and Voltage Multipliers Inc. produces optocouplers for fast switching of high-voltage signals. In addition, several groups have created their own high-voltage control systems (44–46). As it stands, the combination of properties for Peano-HASEL actuators

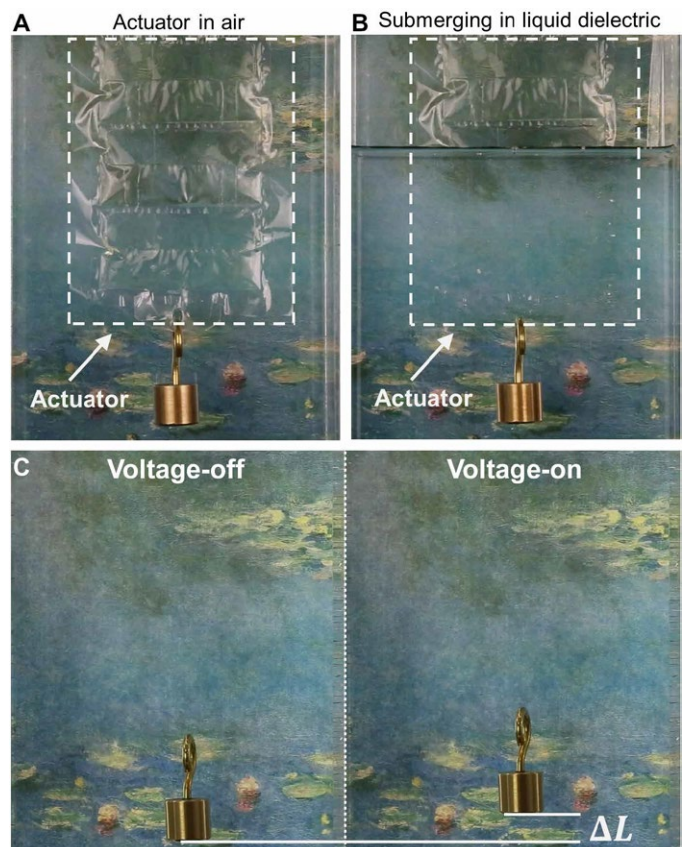


**Fig. 8. Invisible Peano-HASEL actuators.** (A) A Peano-HASEL actuator was suspended in an acrylic box with a colorful background (Claude Monet's Water Lilies). (B) The acrylic box was filled with a liquid dielectric (Drakeol 19). The submerged portion of the actuator is nearly invisible. (C) Submerged actuator with a suspended 10-g weight and no applied voltage. On application of 8 kV, the actuator contracted and lifted the weight.

shown in this study highlights their promise for next-generation soft robotic systems.

## MATERIALS AND METHODS

### Actuator materials

The inextensible shell was made from one-side metalized, one-side heat sealable, 21- $\mu$ m BOPP obtained from Impex Global (MSB 20 film). Measurements confirmed the dielectric breakdown strength of our BOPP film to be  $\geq 650$  V  $\mu$ m $^{-1}$  (as shown in fig. S10) after our KOH etch, which was in agreement with the literature value (35). Our liquid dielectric was Envirotemp FR3 transformer oil, which was purchased from Cargill. As stated, two types of electrodes were tested: Aluminum electrodes were made during manufacture of the BOPP film through a vacuum-deposition process; hydrogel electrodes were prepared according to Keplinger *et al.* (36) and Bai *et al.* (37) and bonded to a PDMS backing. To promote strong bonding between the hydrogel and PDMS backing, we applied a benzophenone treatment to the PDMS (38), as described in the Supplementary Materials.

We used two methods to mount actuators for testing. The first consisted of fiberglass-reinforced packaging tape (pictured in Fig. 1C) for an actuator design with no rigid components. The second used

acrylic frames to provide a consistent mounting position and load-bearing points.

### Testing methods

For actuation tests, frequency tests, and contraction speed tests, contraction was measured with Tracker video analysis software (version 4.96). All tests used reversing-polarity voltage signals to minimize what appeared to be charge accumulation on the BOPP actuators. These signals were generated using custom LabVIEW VIs (version 15.0.1f2) and fed into a Trek Model 50/12 high-voltage amplifier through an NI 6212 data acquisition system (DAQ). Low-speed tests used a Canon EOS 6D DSLR camera to provide data for optical tracking, whereas high-speed tests (frequency and contraction speed) used a Vision Research Phantom v710 high-speed camera. More detail on actuator materials, fabrication, and testing methods may be found in the Supplementary Materials.

### SUPPLEMENTARY MATERIALS

robotics.sciencemag.org/cgi/content/full/3/14/ear3276/DC1

Materials and Methods

Fig. S1. Heat-press used for sealing BOPP pouches.

Fig. S2. Fabrication process for Peano-HASEL actuators with hydrogel electrodes.

Fig. S3. Fabrication process for Peano-HASEL actuators with aluminum electrodes.

Fig. S4. Voltage signal with reversing polarity used during force-strain tests.

Fig. S5. Example of damage to aluminum electrodes after voltage cycling.

Fig. S6. High-speed contraction of Peano-HASEL actuators.

Fig. S7. Experimental setup used for frequency response tests of Peano-HASEL actuators.

Fig. S8. Full actuation signal for lever arm tests.

Fig. S9. Lifetime test for Peano-HASEL actuators.

Fig. S10. Dielectric breakdown tests for KOH-etched BOPP film.

Movie S1. Demonstration of actuation characteristics.

Movie S2. Actuation using integrated aluminum electrodes.

Movie S3. Scaling up forces with Peano-HASEL actuators.

Movie S4. Frequency response of Peano-HASEL actuators.

Movie S5. Demonstration of precise and rapid actuation.

Movie S6. Transparent Peano-HASEL actuators.

References (47, 48)

### REFERENCES AND NOTES

- E. W. Hawkes, L. H. Blumenschein, J. D. Greer, A. M. Okamura, A soft robot that navigates its environment through growth. *Sci. Robot.* **2**, eaan3028 (2017).
- M. T. Tolley, R. F. Shepherd, B. Mosadegh, K. C. Galloway, M. Wehner, M. Karpelson, R. J. Wood, G. M. Whitesides, A resilient, untethered soft robot. *Soft Robot.* **1**, 213–223 (2014).
- H. Yuk, S. Lin, C. Ma, M. Takaffoli, N. X. Fang, X. Zhao, Hydraulic hydrogel actuators and robots optically and sonically camouflaged in water. *Nat. Commun.* **8**, 14230 (2017).
- C. Larson, B. Peele, S. Li, S. Robinson, M. Totaro, L. Beccai, B. Mazzolai, R. Shepherd, Highly stretchable electroluminescent skin for optical signaling and tactile sensing. *Science* **351**, 1071–1074 (2016).
- S. Kim, C. Laschi, B. Trimmer, Soft robotics: A bioinspired evolution in robotics. *Trends Biotechnol.* **31**, 287–294 (2013).
- Y. Cao, T. G. Morrissey, E. Acome, S. I. Allec, B. M. Wong, C. Keplinger, C. Wang, A transparent, self-healing, highly stretchable ionic conductor. *Adv. Mater.* **29**, 1605099 (2017).
- L. Hines, K. Petersen, G. Z. Lum, M. Sitti, Soft actuators for small-scale robotics. *Adv. Mater.* **29**, 1603483 (2017).
- C. S. Haines, M. D. Lima, N. Li, G. M. Spinks, J. Foroughi, J. D. W. Madden, S. H. Kim, S. Fang, M. J. de Andrade, F. Göktepe, Ö. Göktepe, S. M. Mirvakili, S. Naficy, X. Lepó, J. Oh, M. E. Kozlov, S. J. Kim, X. Xu, B. J. Swedlove, G. G. Wallace, R. H. Baughman, Artificial muscles from fishing line and sewing thread. *Science* **343**, 868–872 (2014).
- F. Ilievski, A. D. Mazzeo, R. F. Shepherd, X. Chen, G. M. Whitesides, Soft robotics for chemists. *Angew. Chem. Int. Ed.* **123**, 1930–1935 (2011).
- D. Yang, M. S. Verma, J.-H. So, B. Mosadegh, C. Keplinger, B. Lee, F. Khashai, E. Lossner, Z. Suo, G. M. Whitesides, Buckling pneumatic linear actuators inspired by muscle. *Adv. Mater. Technol.* **1**, 1600055 (2016).
- M. A. Meller, M. Bryant, E. Garcia, Reconsidering the McKibben muscle: Energetics, operating fluid, and bladder material. *J. Intell. Mater. Syst. Struct.* **25**, 2276–2293 (2014).
- R. Niiyama, D. Rus, S. Kim, Pouch motors: Printable/inflatable soft actuators for robotics, in *Proceedings of the 2014 IEEE International Conference on Robotics and Automation (ICRA)* (IEEE, 2014), pp. 6332–6337.
- S. Sanan, P. S. Lynn, S. T. Griffith, Pneumatic torsional actuators for inflatable robots. *J. Mech. Robot.* **6**, 031003 (2014).
- A. J. Veale, I. A. Anderson, S. Q. Xie, The smart Peano fluidic muscle: A low profile flexible orthosis actuator that feels pain. *Proc. SPIE* **9435**, 94351V (2015).
- A. J. Veale, S. Q. Xie, I. A. Anderson, Characterizing the Peano fluidic muscle and the effects of its geometry properties on its behavior. *Smart Mater. Struct.* **25**, 065013 (2016).
- R. Pelrine, R. D. Kornbluh, Q. Pei, J. Joseph, High-speed electrically actuated elastomers with strain greater than 100%. *Science* **287**, 836–839 (2000).
- P. Brochu, Q. Pei, Advances in dielectric elastomers for actuators and artificial muscles. *Macromol. Rapid Commun.* **31**, 10–36 (2010).
- S. Rosset, H. R. Shea, Small, fast, and tough: Shrinking down integrated elastomer transducers. *Appl. Phys. Rev.* **3**, 031105 (2016).
- G.-Y. Gu, J. Zhu, L.-M. Zhu, X. Zhu, A survey on dielectric elastomer actuators for soft robots. *Bioinspir. Biomim.* **12**, 011003 (2017).
- F. Daerden, D. Lefeber, Pneumatic artificial muscles: Actuators for robotics and automation. *Eur. J. Mech. Environ. Eng.* **47**, 11–21 (2002).
- P. Polygerinos, N. Correll, S. A. Morin, B. Mosadegh, C. D. Onal, K. Petersen, M. Cianchetti, M. T. Tolley, R. F. Shepherd, Soft robotics: Review of fluid-driven intrinsically soft devices; manufacturing, sensing, control, and applications in human-robot interaction. *Adv. Eng. Mater.* **19**, 1700016 (2017).
- M. Wehner, R. L. Truby, D. J. Fitzgerald, B. Mosadegh, G. M. Whitesides, J. A. Lewis, R. J. Wood, An integrated design and fabrication strategy for entirely soft, autonomous robots. *Nature* **536**, 451–455 (2016).
- C. Keplinger, M. Kaltenbrunner, N. Arnold, S. Bauer, Capacitive extensometry for transient strain analysis of dielectric elastomer actuators. *Appl. Phys. Lett.* **92**, 192903 (2008).
- S. Diahm, S. Zelmat, M.-L. Locatelli, S. Dinculescu, M. Decup, T. Lebey, Dielectric breakdown of polyimide films: Area, thickness and temperature dependence. *IEEE Trans. Dielectr. Electr. Insul.* **17**, 18–27 (2010).
- M. Duduta, R. J. Wood, D. R. Clarke, Multilayer dielectric elastomers for fast, programmable actuation without prestretch. *Adv. Mater.* **28**, 8058–8063 (2016).
- M. Vatankhah-Varnoosfaderani, W. F. M. Daniel, A. P. Zhushma, Q. Li, B. J. Morgan, K. Matyjaszewski, D. P. Armstrong, R. J. Spontak, A. V. Dobrynin, S. S. Sheiko, Bottlebrush elastomers: A new platform for freestanding electroactuation. *Adv. Mater.* **29**, 1604209 (2017).
- X. Niu, H. Stoyanov, W. Hu, R. Leo, P. Brochu, Q. Pei, Synthesizing a new dielectric elastomer exhibiting large actuation strain and suppressed electromechanical instability without prestretching. *J. Polym. Sci. Part B Polym. Phys.* **51**, 197–206 (2013).
- G. Kovacs, L. Düring, S. Michel, G. Terrasi, Stacked dielectric elastomer actuator for tensile force transmission. *Sens. Actuators A* **155**, 299–307 (2009).
- E. Acome, S. K. Mitchell, T. G. Morrissey, M. B. Emmett, C. Benjamin, M. King, M. Radakovitz, C. Keplinger, Hydraulically amplified self-healing electrostatic actuators with muscle-like performance. *Science* **359**, 61–65 (2018).
- L. Maffli, S. Rosset, H. R. Shea, Zipping dielectric elastomer actuators: Characterization, design and modeling. *Smart Mater. Struct.* **22**, 104013 (2013).
- A. S. Chen, H. Zhu, Y. Li, L. Hu, S. Bergbreiter, A paper-based electrostatic zipper actuator for printable robots, in *Proceedings of the 2014 IEEE International Conference on Robotics and Automation (ICRA)* (IEEE, 2014), pp. 5038–5043.
- M. P. Brenner, J. H. Lang, J. Li, A. H. Slocum, Optimum design of an electrostatic zipper actuator. *NSTI Nanotech 2004* **2**, 371–374 (2004).
- A. A. Sathe, E. A. Groll, S. V. Garimella, Analytical model for an electrostatically actuated miniature diaphragm compressor. *J. Micromech. Microeng.* **18**, 035010 (2008).
- Z. Suo, Theory of dielectric elastomers. *Acta Mech. Sol. Sin.* **23**, 549–578 (2010).
- J. Ho, R. Jow, *Characterization of high temperature polymer thin films for power conditioning capacitors* (No. ARL-TR-4880, Army Research Laboratories, 2009).
- C. Keplinger, J.-Y. Sun, C. C. Foo, P. Rothenmund, G. M. Whitesides, Stretchable, transparent, ionic conductors. *Science* **341**, 984–987 (2013).
- Y. Bai, B. Chen, F. Xiang, J. Zhou, H. Wang, Z. Suo, Transparent hydrogel with enhanced water retention capacity by introducing highly hydratable salt. *Appl. Phys. Lett.* **105**, 151903 (2014).
- H. Yuk, T. Zhang, G. A. Parada, X. Liu, X. Zhao, Skin-inspired hydrogel–elastomer hybrids with robust interfaces and functional microstructures. *Nat. Commun.* **7**, 12028 (2016).
- A. V. Hill, The heat of shortening and the dynamic constants of muscle. *Proc. R. Soc. B Biol. Sci.* **126**, 136–195 (1938).
- I. W. Hunter, S. Lafontaine, A comparison of muscle with artificial actuators, in *Proceedings of the IEEE 5th Technical Digest, Solid-State Sensor and Actuator Workshop* (IEEE, 1992), pp. 178–185.
- J. D. W. Madden, N. A. Vandesteeg, P. A. Anquetil, P. G. A. Madden, A. Takshi, R. Z. Pytel, S. R. Lafontaine, P. A. Wieringa, I. W. Hunter, Artificial muscle technology: Physical principles and naval prospects. *IEEE J. Ocean. Eng.* **29**, 706–728 (2004).

42. M. Focchi, E. Guglielmino, C. Semini, A. Parmiggiani, N. Tsagarakis, B. Vanderborght, D. G. Caldwell, Water/air performance analysis of a fluidic muscle, in *Proceedings of IEEE/RSJ 2010 International Conference on Intelligent Robots and Systems (IROS)* (IEEE, 2010), pp. 2194–2199.
43. F. Carpi, G. Frediani, D. De Rossi, Hydrostatically coupled dielectric elastomer actuators. *IEEE/ASME Trans. Mech.* **15**, 308–315 (2010).
44. T. Li, G. Li, Y. Liang, T. Cheng, J. Dai, X. Yang, B. Liu, Z. Zeng, Y. Luo, T. Xie, W. Yang, Fast-moving soft electronic fish. *Sci. Adv.* **3**, e1602045 (2017).
45. B. M. O'Brien, E. P. Calius, T. Inamura, S. Q. Xie, I. A. Anderson, Dielectric elastomer switches for smart artificial muscles. *Appl. Phys. A* **100**, 385–389 (2010).
46. A. Marette, A. Poulin, N. Basse, S. Rosset, D. Briand, H. Shea, Flexible zinc–tin oxide thin film transistors operating at 1 kV for integrated switching of dielectric elastomer actuators arrays. *Adv. Mater.* **29**, 1700880 (2017).
47. E. M. Mount III, C. A. Bishop, Figure 2.2.1 in *Metallizing Technical Reference* (Association of International Metallizers, Coaters and Laminators, 2012).
48. Impex Global, *Metallized BOPP Film* (Technical Data Sheet); [www.impexfilms.com/wp-content/uploads/2017/01/63\\_2METOPP70-120.pdf](http://www.impexfilms.com/wp-content/uploads/2017/01/63_2METOPP70-120.pdf).

**Acknowledgments:** We thank S. Humbert for the use of high-speed camera equipment (Phantom v710 and high-power tungsten flood lights). Special thanks to Impex Global for providing samples of BOPP film and to Penreco for providing samples of Drakeol 7 and Drakeol 19 mineral oil for actuator construction and testing. **Funding:** This work was sponsored by start-up funds from the University of Colorado Boulder. G.M.S. acknowledges financial support from the Undergraduate Research Opportunity Program at the University of

Colorado Boulder. **Author contributions:** C.K. conceived and supervised the research. N.K., V.G.V., and S.K.M. designed the Peano-HASEL actuators. N.K. and V.G.V. developed fabrication methods for actuators. G.M.S., V.G.V., and N.K. fabricated actuators. N.K., V.G.V., and G.M.S. designed experiments/demos and collected data. S.K.M. performed dielectric breakdown tests on BOPP. V.G.V. and N.K. analyzed data from force-strain tests and high-speed video for frequency and contraction tests. N.K. designed and revised supplementary and main text figures with contributions from all authors. G.M.S. designed and revised supplementary videos. V.G.V. drafted and revised supplemental text. N.K., C.K., V.G.V., and S.K.M. drafted and revised the manuscript with contributions from G.M.S. **Competing interests:** The authors declare that they have no competing financial interests. N.K., S.K.M., and C.K. are listed as inventors on a U.S. provisional patent application (62/474,814) submitted by the University of Colorado Boulder that covers fundamental principles and designs of Peano-HASEL actuators. **Data and materials availability:** All data needed to support the conclusions of this manuscript are included in the main text or supplementary materials. Contact C.K. for materials.

Submitted 2 November 2017

Accepted 20 December 2017

Published 5 January 2018

10.1126/scirobotics.aar3276

**Citation:** N. Kellaris, V. Gopaluni Venkata, G. M. Smith, S. K. Mitchell, C. Keplinger, Peano-HASEL actuators: Muscle-mimetic, electrohydraulic transducers that linearly contract on activation. *Sci. Robot.* **3**, eaar3276 (2018).

# THIS IS NOT SCIENCE FICTION

This is captivating, impactful *Science*

Contact us today to discuss pricing options for adding any of these journals to your collection of *Science* resources.

#### Institutional Licensing

ScienceMag.org/request | scienceonline@aaas.org  
1-866-265-4152 (USA) | +1-202-326-6730 (outside USA)

**Science**  
AAAS

**Science  
Advances**

**Science  
Immunology**

**Science  
Robotics**

**Science  
Signaling**

**Science  
Translational  
Medicine**



*Science* Webinars help you keep pace with emerging scientific fields!

Stay informed about scientific breakthroughs and discoveries.

Gain insights into current research from top scientists.

Take the opportunity to ask questions during live broadcasts.

 Get alerts about upcoming free webinars.

**Sign up at: [webinar.sciencemag.org/stayinformed](https://webinar.sciencemag.org/stayinformed)**

## BIOMIMETICS

# A biorobotic adhesive disc for underwater hitchhiking inspired by the remora suckerfish

Yueping Wang,<sup>1\*</sup> Xingbang Yang,<sup>1,2\*</sup> Yufeng Chen,<sup>3\*</sup> Dylan K. Wainwright,<sup>4</sup> Christopher P. Kenaley,<sup>5</sup> Zheyuan Gong,<sup>1</sup> Memin Liu,<sup>1</sup> Huan Liu,<sup>6</sup> Juan Guan,<sup>7</sup> Tianmiao Wang,<sup>1</sup> James C. Weaver,<sup>3</sup> Robert J. Wood,<sup>3†</sup> Li Wen<sup>1†</sup>

Remoras of the ray-finned fish family Echeneidae have the remarkable ability to attach to diverse marine animals using a highly modified dorsal fin that forms an adhesive disc, which enables hitchhiking on fast-swimming hosts despite high magnitudes of fluid shear. We present the design of a biologically analogous, multimaterial biomimetic remora disc based on detailed morphological and kinematic investigations of the slender sharksucker (*Echeneis naucrates*). We used multimaterial three-dimensional printing techniques to fabricate the main disc structure whose stiffness spans three orders of magnitude. To incorporate structures that mimic the functionality of the remora lamellae, we fabricated carbon fiber spinules (270  $\mu\text{m}$  base diameter) using laser machining techniques and attached them to soft actuator-controlled lamellae. Our biomimetic prototype can attach to different surfaces and generate considerable pull-off force—up to 340 times the weight of the disc prototype. The rigid spinules and soft material overlaying the lamellae engage with the surface when rotated, just like the discs of live remoras. The biomimetic kinematics result in significantly enhanced frictional forces across the disc on substrates of different roughness. Using our prototype, we have designed an underwater robot capable of strong adhesion and hitchhiking on a variety of surfaces (including smooth, rough, and compliant surfaces, as well as shark skin). Our results demonstrate that there is promise for the development of high-performance bioinspired robotic systems that may be used in a number of applications based on an understanding of the adhesive mechanisms used by remoras.

## INTRODUCTION

Since Aristotle's time, humans have been fascinated by the remarkable structure of the remora's adhesive disc (1). The eight species of remoras within the ray-finned fish family Echeneidae have the remarkable ability to "hitchhike," or adhere, to a wide range of biological and nonbiological surfaces, including boat hulls, sharks and rays, teleost fishes, cetaceans, sea turtles, and even human divers (2). In the case of dolphins, for example, remoras can remain attached while hosts leap out of water and spin with high rotational speeds (3). This hitchhiking behavior affords remoras easier access to food from messy-eating hosts and host parasites and protection from predators (4). The greatest advantage of this behavior is the reduced energy expenditure associated with movement: By attaching to swimming hosts, remoras can be transported over large distances with minimal effort (5). This hitchhiking behavior and corresponding energy savings are enabled by an adhesive disc on the remora's cranium—a modified dorsal fin that represents one of the most extraordinary adaptations within the vertebrates (Fig. 1A) (6, 7).

Although some mechanisms of adhesion in biological systems have been well documented, the van der Waals forces used by geckos (8) or the capillary forces by tree frogs (9, 10), terrestrial gastropods (11), and beetles (12, 13) are of limited utility in underwater envi-

ronments. In contrast to their terrestrial counterparts, adhesion mechanisms in aquatic species, such as in the clingfish's suction disc, often rely on a disc's ability to conform to a surface and create a seal (14, 15). The remora's complex disc system, by comparison, is unique and is composed of integumentary structures and musculoskeletal linkages, including a soft disc lip to maintain a seal in addition to rotating, spinule-covered lamellae in the disc interior to aid in attachment. As a result, the biomechanical basis of this high-performance adhesive behavior has recently attracted growing attention (3, 6, 16).

In many recent studies, biologically inspired robotic platforms (17–20), state-of-the-art three-dimensional (3D) printing technologies (21–23), and soft robotic systems (24–29) have been developed to investigate biomechanical questions related to the locomotion of jumping, swimming, and crawling. In an expansion of this previous work, we fabricated and tested a biomimetic remora disc. In contrast to previous studies that focused primarily on anatomical descriptions, our current efforts focused on the fabrication of a synthetic composite remora disc and therefore permitted a detailed investigation of remora morphological features (i.e., the soft lamella tissue overlay, rigid spinules, and rotatable motion of the lamellae) and their related effects on underwater adhesion under controlled experimental conditions.

Inspired by morphological and kinematic analyses of the adhesive disc from the slender sharksucker, *Echeneis naucrates*, we created a multimaterial 3D-printed prototype that contains composite lamellae lined with ca. 1000 of at-scale carbon fiber spinules, which were fabricated through laser machining; the lamella pitching motion is controlled by lightweight, compliant, soft pneumatic actuators. A detailed description of our design and fabrication workflow is provided in Materials and Methods. Using our remora disc prototype, we investigated the effect of morphological and kinematic features on the disc's adhesive performance on surfaces of different roughness. On the basis of

<sup>1</sup>School of Mechanical Engineering and Automation, Beihang University, Beijing, China. <sup>2</sup>School of Biological Science and Medical Engineering, Beihang University, Beijing, China. <sup>3</sup>John A. Paulson School of Engineering and Applied Sciences and Wyss Institute for Biologically Inspired Engineering, Harvard University, Cambridge, MA 02138, USA. <sup>4</sup>Museum of Comparative Zoology, Harvard University, Cambridge, MA 02138, USA. <sup>5</sup>Department of Biology, Boston College, Boston, MA 02215, USA. <sup>6</sup>School of Chemical Science and Engineering, Beihang University, Beijing, China. <sup>7</sup>School of Material Science and Engineering, Beihang University, Beijing, China.

\*These authors contributed equally to this work.

†Corresponding author. Email: liwen@buaa.edu.cn (L.W.); rjwood@eecs.harvard.edu (R.J.W.)

the experimental results from these studies (such as disc chamber pressure, pull-off force, and frictional force), we further combined the biomimetic adhesive disc prototype with an underwater vehicle to explore remora-like applications of our system by transitioning from swimming to attached states on a variety of surfaces.

**RESULTS**

**Morphology of the biological remora disc**

Within the remora disc interior (Fig. 1A), consecutive rows of slightly overlapping lamellae are distributed in a bilaterally symmetrical fashion (Fig. 1B). The number of rows of lamellae varies across remora species,

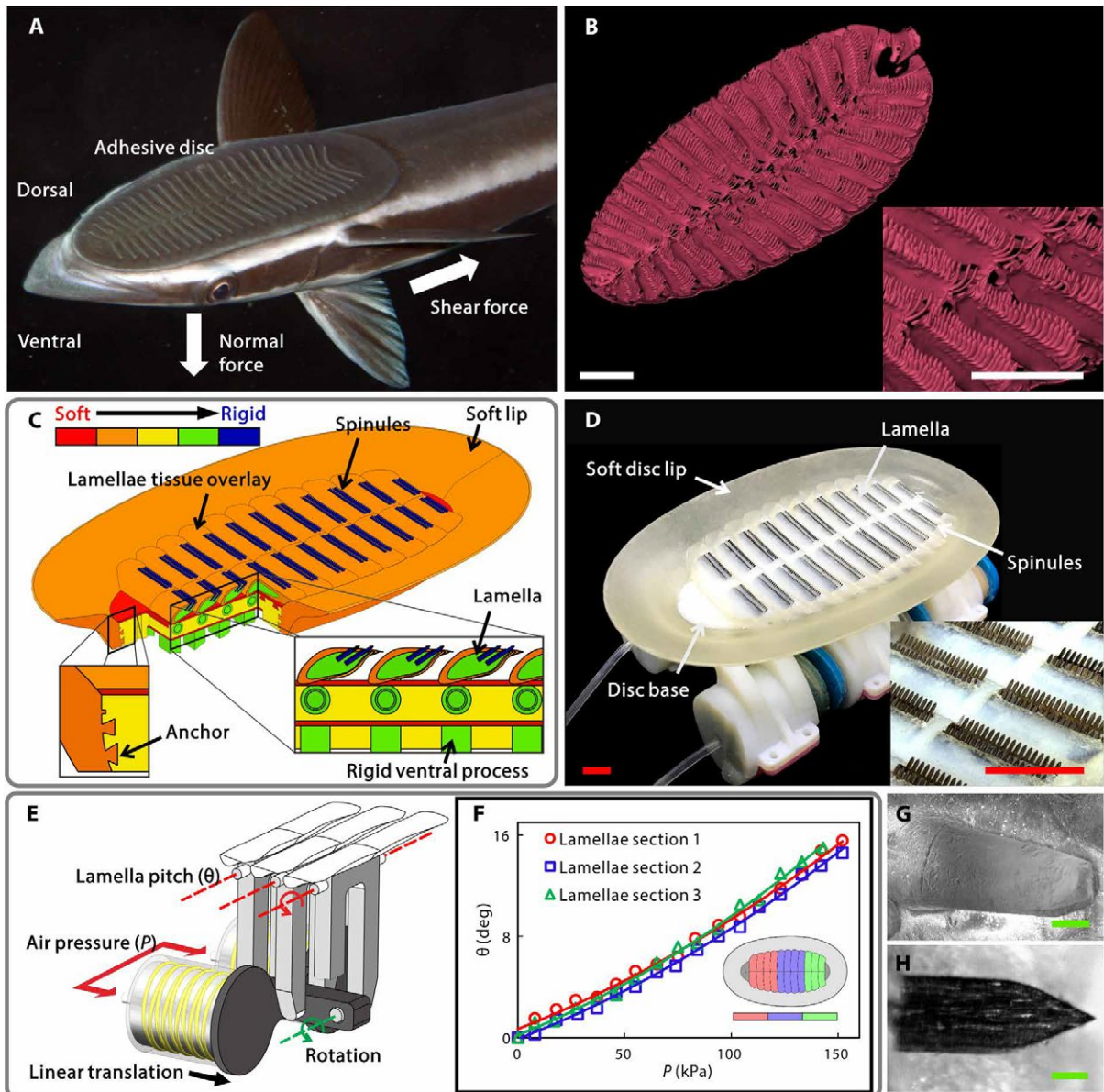


**Fig. 1. Morphology structure of the remora's adhesive disc and our biomimetic prototype design with mechanical elements and mechanisms.** (A) Dorsolateral view of the slender sharksucker, *E. naucrates*. The arrows indicate the direction of friction and pull-off force. [Photo credit: Klaus M. Stiefel.] (B) 3D reconstructed model of the remora disc based on microCT data (resolution, 35  $\mu\text{m}$ ). (Inset) Closer image of the lamellae and rows of spinules. Scale bars, 10 mm. (C) CAD model of the biomimetic remora disc. The principal elements of the disc were assigned multiple materials represented by different colors. The spinules have the greatest stiffness (blue), and the materials in the main body include a fully rigid material [e.g., the ventral process and the lamella plate (green)], a medium rigid material [e.g., the disc base (yellow)], and a flexible material [e.g., the disc lip and soft lamella tissue overlay (orange)]. From the cross-sectional view, the edge of the rigid disc base penetrates into the soft lip and forms a cross-connected anchor-like structure (left inset). (Right inset) The biomimetic lamellae are composed of both a rigid skeleton (green) and a soft lamella tissue overlay (orange). For more data about the stiffness of the materials, refer to table S5. (D) Photograph of the biomimetic remora adhesive disc prototype (disc pad length, 127 mm; width, 62 mm). Scale bars, 10 mm. (Inset) A higher-magnification view showing the rows of composite lamellae embedded with carbon fiber spinules. (E) Drive mechanism for lamella pitch motions, which translates the linear movement of the soft actuators (driven by a pneumatic system) into the rotational movement of the lamellae. Animation of the lamella pitching motion can be seen in movie S3. Lateral view of the actuated disc prototype is provided in movie S4. (F) Pitch angle  $\theta$  of the three sections of the biomimetic disc lamellae (actuated by three pairs of actuators) versus the input air pressure  $P$ . (G) ESEM image of higher-magnification views of a single biological spinule. (H) Optical microscopy image of a single carbon fiber spinule fabricated by laser machining. Scale bars, 100  $\mu\text{m}$  (G and H).

with different species having between 10 and 30 rows of lamellae in total (30). These lamellae are partially covered by a thin layer of soft tissue that connects laterally with the soft fleshy lip surrounding the disc (2, 31). Through integration with the lamella ventral process, erector and depressor muscles that lie beneath the disc base can rotate the lamellae up or down, in a similar manner by which teleost fish can rotate their spiny dorsal fins to an erect or depressed state (2, 32–34). Each lamella row has two to three rows of small rigid spines called spinules (Fig. 1B, inset), and thus, an entire remora disc can contain more than a thousand of these fine structures. The biological spinules have a cone-shaped geometry with an average diameter of 270  $\mu\text{m}$  at their base, a height of approximately 500  $\mu\text{m}$ , and a spacing of 250  $\mu\text{m}$  between adjacent spinules (Fig. 1G). Detailed morphological data on body length, disc dimensions (length, width, and area), mean spanwise length of perpendicular lamellae, lamella spacing, and other disc components are included in table S1.

### Biomimetic remora disc prototype

On the basis of the morphological features of the natural remora disc, we successfully fabricated a biologically inspired, multimaterial structural analog (Fig. 1D). The disc prototype was 127 mm long and 72 mm wide, with a mass of 129 g. The prototype contained a soft lip at the periphery and 11 consecutive rows of overlapped lamellae made of composite materials, each of which contained a linear array of rigid carbon fiber spinules (Fig. 1D). The remora disc prototype was made of a fully rigid material for the skeletal elements (e.g., ventral process and mechanical linkages), a less rigid material for the disc base (e.g., lamella plates and disc base), and a flexible material to allow surface conformation (e.g., disc lip and the soft tissue enveloping the lamella plate) (Fig. 1C). The material stiffness of the 3D-printed disc components spanned three orders of magnitude from flexible to rigid (1.1 to 3000 MPa; table S5). Two rows of laser-cut carbon fiber spinules were installed on the top edge of the lamellae at an angle of 33.7° relative to the horizontal plane, identical to the spinule angle found in *E. naucrates*. Each carbon fiber spinule was 270  $\mu\text{m}$  and terminates in a sharp tip (Fig. 1H).

To mimic the functions of the lamella erector and depressor muscles of the biological remora disc, we used pneumatic, fiber-reinforced soft actuators that connected with the ventral process of the biomimetic lamellae and moved linearly when pressurized pneumatically (Fig. 1E and movie S3). The linear elongation of the soft actuator was converted to the lamella pitching motion through a linkage bar mechanism. The relationship between the lamella pitch angle and the air pressure of the soft actuator was quantified experimentally (Fig. 1F). Upon pressurization, the lamella pitch angle could be precisely controlled between 0° (a biological lamellae's default “down” state) and 16° (a biological lamellae's fully “raised” state) based on the input pneumatic pressure (from 0 to 160 kPa). A comprehensive list of the prototype disc's physical parameters is provided in table S2.

### Biological and biomimetic remora disc kinematics

Observations of the disc functionality revealed that live remoras can actively raise up or fold down rows of lamellae in the center of the adhesive disc, creating a suction seal to the substrate with the soft outer lip. The length, adhesive disc area, and mass of live remoras are in the range of 273 to 324 mm, 11.0 to 19.0  $\text{cm}^2$ , and 54.9 to 86.9 g, respectively (table S1). We found that remoras fold down their lamellae while sliding along a surface, with the marker point (labeled A in Fig. 2) on the lamellae moving posteriorly up to an amplitude,  $\Delta d$  (the displacement of marker points projected on the  $x$  axis), of 0.32 mm (Fig. 2).

Remoras that intend to stop and adhere to a surface raise up their lamellae, with the marker point moving anteriorly up to an amplitude of 0.25 mm (Fig. 2A). A demonstration of the lamella movement in a live remora is demonstrated in movie S2. We used a nondimensional parameter ( $u$ ;  $u = \Delta d/L$ , where  $L$  represents the distance between two adjacent lamellae) to account for the difference in disc lengths between different remoras and the biomimetic prototype disc to evaluate the lamella pitch motion during attachment. The dimensionless amplitude  $u$  of the lamella movement varied significantly for different attachment events (Fig. 2C and fig. S8A). Experimental results show that  $u$  ranges from  $2.3 \times 10^{-2}$  to  $13.7 \times 10^{-2}$  for the folding down of the lamellae and from  $2.0 \times 10^{-2}$  to  $14.8 \times 10^{-2}$  for the raising up. Statistical analysis showed no significant difference in the dimensionless amplitude ( $u$ ) between raising up and folding down motions of the lamellae [analysis of variance (ANOVA),  $df = 73$ ,  $F = 0.08$ ,  $P = 0.78$ ] (Fig. 2E).

By pressurizing and depressurizing the three pairs of soft actuators in sequence, the disc prototype can mimic the natural lamella movement (raising and folding) during attachment events. Both tilted 45° top view and side view of the disc prototype are provided in movie S4. Undulation of the lamellae through a differential in actuator timing was developed and is shown in movie S4 for demonstration purposes. For ease of visualization, each of these two motions was performed while the disc prototype was attached to a transparent glass surface underwater (movie S4).

The biomimetic lamellae of our prototype produced pitch motion amplitudes ( $u = 0$  to  $14.8 \times 10^{-2}$ ) that covered the range of moving amplitudes of biological lamellae (Fig. 2E). The kinematic profiles of three motion sequences during both raising up (Fig. 2D) and folding down (fig. S8B) lamella movements are quite similar to those found in the biological remora (Fig. 2C and fig. S8A). A comparison of raising and folding motions between the live remora and the biorobotic prototype is available in movie S5.

To further characterize the movement of the biomimetic lamellae, we fabricated a second prototype with a clear disc edge that permitted visualization of the contact between the lamellae and the substrate using a microlens digital camera (section S6). This experimental approach was essential because lateral-view visualization was impossible to achieve in the live remora experiments. Using this second prototype, we were able to visualize the transition of lamellae (with spinules) from a folded ( $u = 0$ , lamella pitch angle  $\theta = 0$ ) to a raised configuration ( $u = 14.8 \times 10^{-2}$ ,  $\theta = 16^\circ$ ) while in contact with a smooth surface (Fig. 2H). The marker point on the biomimetic lamellae moved anteriorly with an amplitude ( $\Delta d$ ) of 1.04 mm. The soft tissue overlay and rigid spinules made no contact with the smooth surface in the folded-down state ( $u = 0$ ). However, in the raised-up state, the lamella soft tissue overlay and the rigid spinules engaged with the surface. The contact zone between the lamella soft tissue overlay (the translucent component) and the smooth substrate is indicated in Fig. 2H.

The lamella pitch motion induced negative pressure between the disc interior and the ambient environment. By gradually raising up the lamellae, that is, increasing  $\theta$  from 0° to 16°, the pressure of the prototype chamber varied from 0 to  $-3$  kPa when the disc was attached to a smooth substrate (fig. S9).

### Force results

The biomimetic remora disc generates considerable pull-off force in the ambient underwater environment (fig. S6), measuring up to  $436.6 \pm 16.0$  N (error values are  $\pm 1$  SEM) on the smooth surface (Fig. 3A), which was approximately 340 times the weight of the disc prototype (0.129 kg). The pull-off forces ( $F_d$ ) varied with different substrate roughness. The

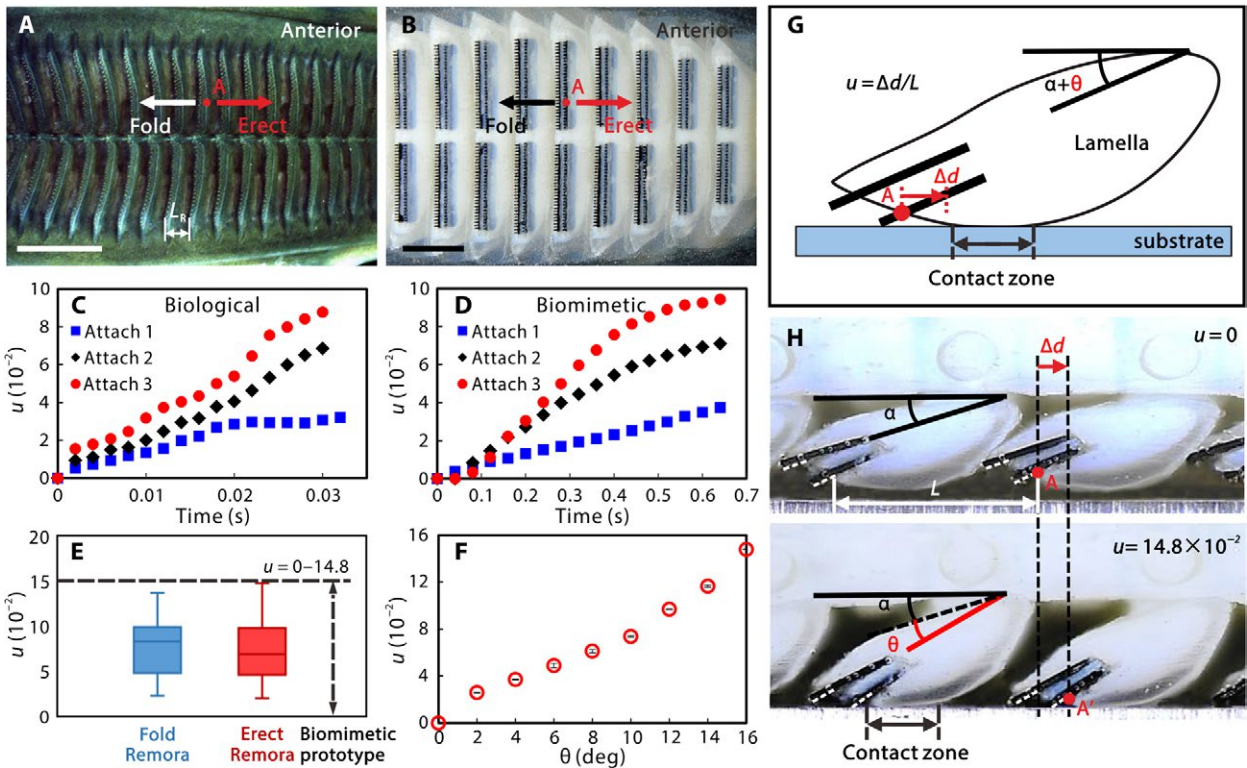


**Fig. 2. Lamella kinematics of the adhesive disc in a live remora and a biorobotic disc prototype.** (A) Dorsal view of a live remora’s adhesive disc ( $L_R$  represents the distance between two adjacent lamellae of the live remora) and (B) the biomimetic remora disc prototype attached to a transparent glass substrate. The representative marker point A on the lamella moves anteriorly when the lamellae are raised up and moves posteriorly when the lamellae are folded down. The displacement profiles of the representative marker points for the lamellae of a live remora (C) and the biomimetic prototype (D) were provided in the raised state ( $u = \Delta d/L$ , where  $L$  represents the distance between two adjacent biomimetic lamellae of the prototype and  $\Delta d$  is the displacement of marker point projected in the  $x$  axis shown in fig. S1B, which is calculated by instantaneous  $x$  value of marker point subtracting the initial  $x$  value of marker point). The original point indicates the initial position of the marker point. Profiles for folding down are provided in fig. S8. (E) Statistical analysis of lamella kinematics for the remora and biomimetic disc. The lamella rotational range of the biomimetic disc ( $u = 0$  to  $14.8 \times 10^{-2}$ ; indicated by black dashed line) is greater than that found in live remoras for both erect and fold motions and can be actively controlled within that range. (F) Dimensionless amplitude  $u$  of the disc prototype versus lamella pitch angle ( $\theta$ ). (G) Schematic view of the lamellae interacting with a substrate.  $\alpha$  denotes the angle between the disc lamellae (at the initial fold state) and the horizontal plane, whereas  $\theta$  denotes the lamella dynamic pitch angle. The contact zone between the lamella soft tissue overlay and the substrate is also illustrated. (H) Contact visualization between the biomimetic lamellae and a smooth substrate from side views. Lamellae are composed of both a rigid material (white) and a soft tissue overlay (translucent). Side view of lamellae with the spinules raised from the initial folded state ( $u = 0$ ; top) to the erected state ( $u = 14.8 \times 10^{-2}$ ,  $\theta = 16^\circ$ ; bottom) while in contact with a smooth surface. When the lamellae are raised, the marker point A moved to A’ with displacement  $\Delta d$  (1.04 mm) in the direction of the vector arrows.

disc prototype produced  $163.7 \pm 3.8$  N on real shark skin (from the shortfin mako, *Isurus oxyrinchus*) and  $117.8 \pm 0.7$  N on synthetic rough surfaces (surface roughness  $R_a = 200 \mu\text{m}$ ). The pull-off stress  $\sigma_z$  ( $\sigma_z = F_d/A$ , where  $A$  represents the area of the disc pad) ranged from  $15.8 \pm 0.1$  kPa on rough surfaces to  $58.4 \pm 2.1$  kPa on smooth surfaces. We also observed that the disc volume and the pressure differential between the inside and outside of the disc chamber increased during the pull-off process (fig. S10). The edges of the soft disc lip deformed toward the center of the disc, eventually caving inward and causing the attachment to fail; both pressure and force values dropped to zero once adhesive failure occurred. The disc lamellae also lost contact with the substrate during application of ventrally directed normal forces, suggesting that the normal adhesion force could be primarily attributed to the suction generated by sealing of the soft lip.

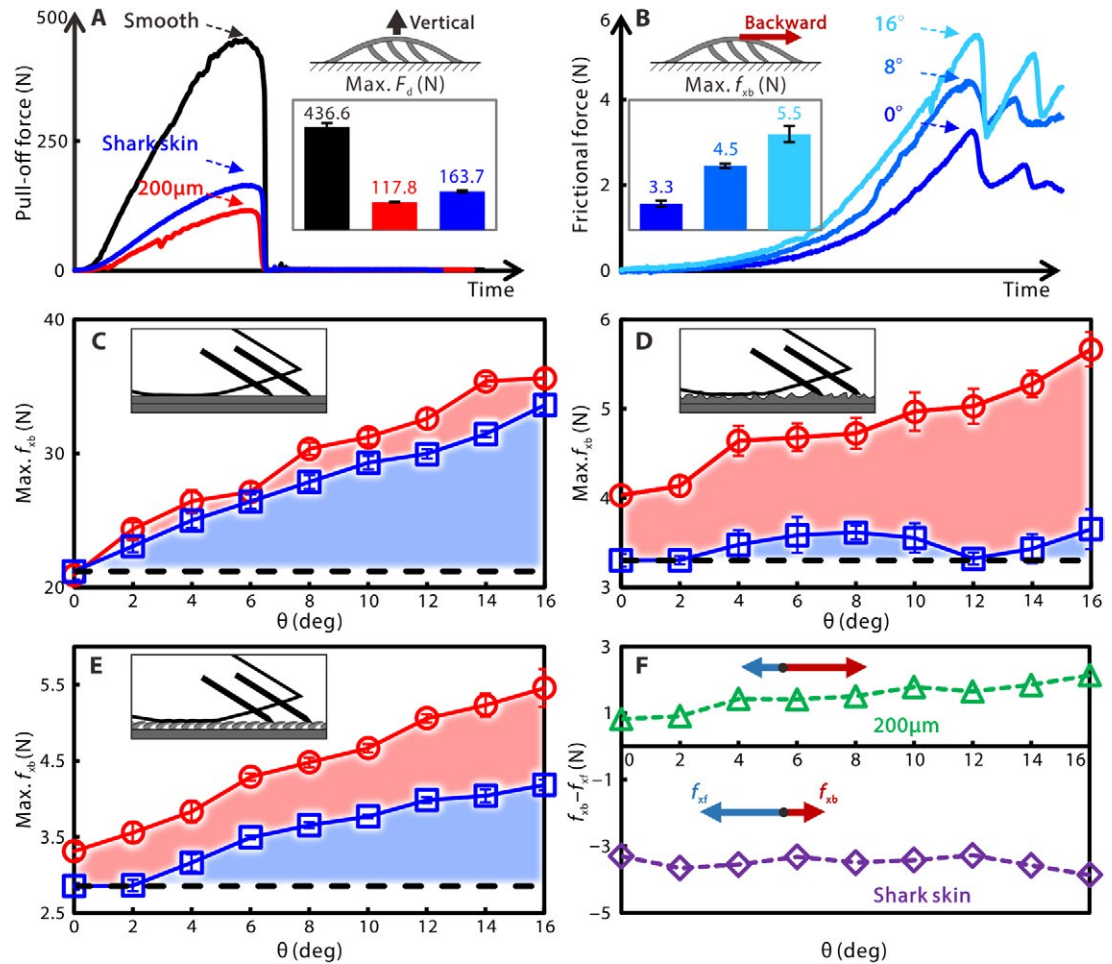
We further investigated the effects of both the lamella pitch angle (which correlates with the height change of the lamellae) and the presence of rigid spinules on the adhesive performance of the disc

on surfaces of different roughness. In particular, we focused on the role of these structures in the generation of frictional forces during the application on the posteriorly directed forces, a scenario that models fluid drag experienced by a remora when its host is swimming. The instantaneous posterior frictional forces and maximum frictional force of the disc prototype over a range of different lamella pitch angles on the rough surface ( $R_a = 200 \mu\text{m}$ ) are shown in Fig. 3B. On smooth surfaces ( $R_a = 0 \mu\text{m}$ ), the average frictional enhancement for all pitch angles ( $\theta$ ) was 8.1 N for the lamellae with spinules and 6.3 N for the lamellae without spinules (Fig. 3C). From the color-shaded area in Fig. 3C, the contribution of the lamella soft tissue overlay to the frictional enhancement is significant, and the spinules do not contribute appreciably to frictional forces on smooth surfaces. Conversely, on the rough surface ( $R_a = 200 \mu\text{m}$ ), the average frictional enhancement is 1.49 N for the prototype with spinules and 0.17 N in the spinule-free control (Fig. 3D). In contrast, in trials on the real shark skin surface (average roughness  $R_a = 120 \mu\text{m}$ ), the prototype generated

**Fig. 3. Adhesive ability of the bio-robotic remora disc prototypes.**

(A) Pull-off force time series ( $F_d$ ) of the bio-robotic disc prototype with artificial spinules on a smooth surface ( $R_a = 0 \mu\text{m}$ ; black), a real shark skin surface ( $R_a = 120 \mu\text{m}$ ; blue), and a rough surface ( $R_a = 200 \mu\text{m}$ ; red). (Inset) Vertically directed pull-off forces ( $\text{Max. } F_d$ ) on three surfaces; colors correspond to those in the time history curves.

(B) Posteriorly directed backward frictional forces ( $f_{xb}$ ) of the disc prototype at different lamella pitch angles  $\theta$  ( $0^\circ$ ,  $8^\circ$ , and  $16^\circ$ ) on the real shark skin versus time during a representative trial. (Inset) Maximum static frictional forces ( $\text{Max. } f_{xb}$ ) at  $\theta = 0^\circ$ ,  $8^\circ$ , and  $16^\circ$  from left to right. (C to E) Backward frictional forces ( $f_{xb}$ ) of the bio-robotic disc prototypes with both lamellae and carbon fiber spinules (red) and lamellae without the artificial spinules (blue) as a function of  $\theta$  ( $0^\circ$  to  $16^\circ$ ) on different surfaces. The dashed gray line represents the control prototype without lamellae and spinules. The blue shaded area indicates the contribution of the soft lamella tissue overlay to the frictional force. The red shaded area indicates the contribution of the rigid spinules to the frictional force. (C) Smooth surface. (D) Rough surface ( $R_a = 200 \mu\text{m}$ ). (E) Real shark skin surface (*I. oxyrinchus*;  $R_a \approx 120 \mu\text{m}$ ). (F) Anisotropic force ( $f_{xb} - f_{xt}$ ) of the disc prototype with carbon fiber spinules versus  $\theta$  on the rough surface (green) and the shark skin surface (purple).



1.58 N of frictional force with spinules and 0.70 N in the spinule-free control. These results suggest that remoras rely on both the soft tissues of the lamellae and the rigid spinules to enhance the friction force on different surfaces in response to posteriorly directed forces, such as those induced by fluid drag during attachment.

We also found that the lamella pitch motion could significantly enhance the frictional force of the disc prototype. The frictional force with spinules nearly monotonically increased with the lamella pitch angle  $\theta$  on all three tested surfaces: smooth, rough, and real shark skin (Fig. 3). On the smooth surface, the frictional force of the disc prototype with spinules (red) was almost identical to that without spinules (gray) at  $\theta = 0^\circ$  but was enhanced 0.7 times at  $\theta = 16^\circ$  with a frictional stress of  $\sigma_{xb} = 4.77 \text{ kPa}$  ( $\sigma_{xb} = f_{xb}/A$ , where  $A$  represents the disc area) (Fig. 3C). For the disc prototype with spinules, the backward frictional force ( $f_{xt}$ ) increased from  $20.93 \pm 0.468 \text{ N}$  to  $35.62 \pm 0.579 \text{ N}$  when the lamellae were raised from  $\theta = 0^\circ$  to  $16^\circ$  (ANOVA,  $df = 8$ ,  $F = 399.51$ ,  $P = 1.963 \times 10^{-7}$ ). On the rough surface, the frictional force of the prototype with spinules was 16% greater than that of the control at  $\theta = 0^\circ$  and 55% greater when the lamellae were fully erected to  $\theta = 16^\circ$  with a frictional stress of  $\sigma_{xb} = 0.758 \text{ kPa}$  (Fig. 3D). The backward frictional force ( $f_{xt}$ ) of the prototype with spinules increased from  $4.03 \pm 0.102 \text{ N}$  to  $5.67 \pm 0.193 \text{ N}$  when the lamellae were raised from  $0^\circ$  to  $16^\circ$  (ANOVA,  $df = 14$ ,

$F = 32.42$ ,  $P = 7.37 \times 10^{-5}$ ). On the real shark skin, the frictional force of the prototype with spinules was 16% larger than that of the control at  $\theta = 0^\circ$  and increased up to 31% at  $\theta = 16^\circ$  with a frictional stress of  $\sigma_{xb} = 0.730 \text{ kPa}$  (Fig. 3E). The backward frictional force of the prototype with spinules increased from  $3.31 \pm 0.092 \text{ N}$  to  $5.46 \pm 0.248 \text{ N}$  when the lamella angle increased from  $0^\circ$  to  $16^\circ$  (ANOVA,  $df = 10$ ,  $F = 76.09$ ,  $P = 1.10 \times 10^{-5}$ ).

The roles of rigid spinules and lamella soft tissue overlay on the frictional anisotropy of the biomimetic remora disc with spinules depend on the properties of the host surface. On the isotropic rough surface ( $R_a = 200 \mu\text{m}$ ), the forward frictional force ( $f_{xt}$ ) increased from  $3.21 \pm 0.095 \text{ N}$  to  $3.53 \pm 0.047 \text{ N}$  when the lamellae were raised from  $\theta = 0^\circ$  to  $16^\circ$  (ANOVA,  $df = 9$ ,  $F = 10.98$ ,  $P = 0.0106$ ; fig. S11), and the frictional anisotropy (defined as  $f_{xb}/f_{xt}$ ) of the disc prototype was 1.26 at  $\theta = 0^\circ$  and 1.61 at  $\theta = 16^\circ$  (Fig. 3F). On the anisotropic real shark skin surface, the forward frictional force ( $f_{xt}$ ) increased from  $6.61 \pm 0.107 \text{ N}$  to  $9.31 \pm 0.117 \text{ N}$  (ANOVA,  $df = 9$ ,  $F = 288.61$ ,  $P = 1.42 \times 10^{-7}$ ; fig. S11), and the frictional anisotropy on the shark skin was 0.5 at  $\theta = 0^\circ$  and 0.59 at  $\theta = 16^\circ$  (Fig. 3F). Our results therefore suggest that the lamella pitch motion enhances the forward ( $f_{xt}$ ) and the backward ( $f_{xb}$ ) frictional forces of the prototype on both isotropic and anisotropic rough surfaces. The backward force had a larger magnitude than the forward force on the isotropic surface ( $f_{xb}/f_{xt} > 1$ ), whereas on the anisotropic real shark skin,

the opposite was true ( $f_{xb}/f_{xf} < 1$ ). For remoras, these results suggest that, when they adhere to sharks and other anisotropic surfaces, they are even better at resisting shear force (caused by inertial or external impact) along the anterior direction than the drag force generated in their common attachment direction (water moving from head to tail).

### Underwater attachment and hitchhiking

To explore the potential of our prototypes for integration into autonomous platforms capable of repetitive adhesion, we mounted the biomimetic disc to an underwater remotely operated vehicle (ROV) and demonstrated its performance by executing transitions from free-swimming to stable attachments. The biomimetic disc prototype with artificial spinules was mounted to the underwater vehicle via four springs and four soft fiber-reinforced pneumatic actuators (Fig. 4A). The four springs provided passive alignment between the disc and the overhanging surfaces, and the soft fiber-reinforced actuators could exert a 20-N preload upon pressurization.

The attachment of the disc-containing vehicle was realized in three steps: (i) The vehicle was propelled to an overhanging surface from the bottom of the tank (1.2 m in length, 0.8 m in width, and 1 m in height). (ii) Once the remora disc prototype contacted the surface, the soft actuators were pressurized and generated a preload to push the disc against the surface from below, allowing the artificial spinules to achieve better contact with the local surface asperities. The springs permitted the soft lip of the disc to align with the surface and ensure a dependable suction seal. (iii) All disc lamellae were raised up to increase the capacity for overcoming the external force along the shear directions (Fig. 4B, inset, and movie S6, inset). Last, the vehicle's propellers were switched off to confirm a successful attachment event. To demonstrate system robustness, we repeated the attachment experiments 10 times and observed a 100% success rate, with each attempt taking less than 4 s on average to achieve a stable attachment. For each trial, a significant portion of the time was spent in the swimming phase from the tank bottom to the surfaces located 40 cm above. For demonstration, we also show the underwater vehicle with the remora disc prototype detaching from the substrate and transiting back into the swimming mode (Fig. 4B).

We also varied thrust directions of the three propellers (running at the full speed of 5580 rpm) to create twist ( $0.45 \pm 0.02$  N-m), propulsive ( $6 \pm 0.5$  N), and pull ( $4 \pm 0.3$  N) forces that simulated disturbances encountered by a live remora and complicated flow fields that may be encountered by a disc-equipped underwater vehicle (Fig. 4C). Our underwater vehicle performed robust attachments on a range of natural and artificial surfaces, including noncompliant smooth (Plexiglas), compliant rough [ $R_a \approx 200$   $\mu\text{m}$ ; fabricated using silicone elastomer (Elastosil M4601, Wacker Chemie AG, München, Germany)], and real shark skin ( $R_a \approx 120$   $\mu\text{m}$ ; Fig. 4D) surfaces, demonstrating the utility of a self-propelled, hitchhiking underwater vehicle (movie S6).

### DISCUSSION

In this study, we designed and fabricated a biologically inspired, multimaterial prototype modeled upon the disc morphology and lamellar kinematics of the remora sharksucker, *E. naucrates*. The fabrication and actuation of the prototype has several attractive features, and it offers the chance to investigate diverse adhesive disc designs both within and outside of the diversity of forms seen in nature (2, 6). In this way, our prototype provides a platform for investigating the roles of different structural features in remora adhesion while at the same

time creating devices that reversibly adhere to a diversity of surfaces underwater.

Using multimaterial 3D printing and laser micromachining to fabricate the disc permits the biologically relevant design of components that varied considerably in Young's modulus from soft (1 MPa for the disc lip and lamella soft tissue overlay) to very rigid (200 GPa for the carbon fiber spinules). Producing spinule-covered, multimaterial lamellae (soft tissue covering the rigid lamella plate) that overlap with undercuts and overhangs is a significant challenge from a traditional design and fabrication perspective (Fig. 1C). This complex morphology is a distinctive characteristic of natural remora discs (2) and has been achieved through the use of multimaterial 3D printing and laser micromachining. In addition, the overlapping arrangement of lamellae, which permits more contact with the substrate (Fig. 2H), is a key design feature to enhance friction [Fig. 3C; (35)]. Our fabrication process also enables rapid design iteration with little additional cost to change morphological features, including the shape, size, and mechanical stiffness of the components of the remora disc prototype. Such a modular and modifiable system represents great potential as a tool to examine the adhesive contributions of the diverse disc morphologies and lamellar kinematic patterns represented by the eight species within the family Echeneidae that adhere to a wide range of different hosts (2, 6).

With our disc prototype, we were able to mimic the raising and folding movements of the lamellae by controlling lamella pitch with soft pneumatic actuators. Although the pitch amplitudes of the soft-actuated biomimetic disc prototype exceeded the pitch range of the biological lamellae, they can be controlled precisely and, thus, be constrained within the range of biologically relevant values (Fig. 2E).

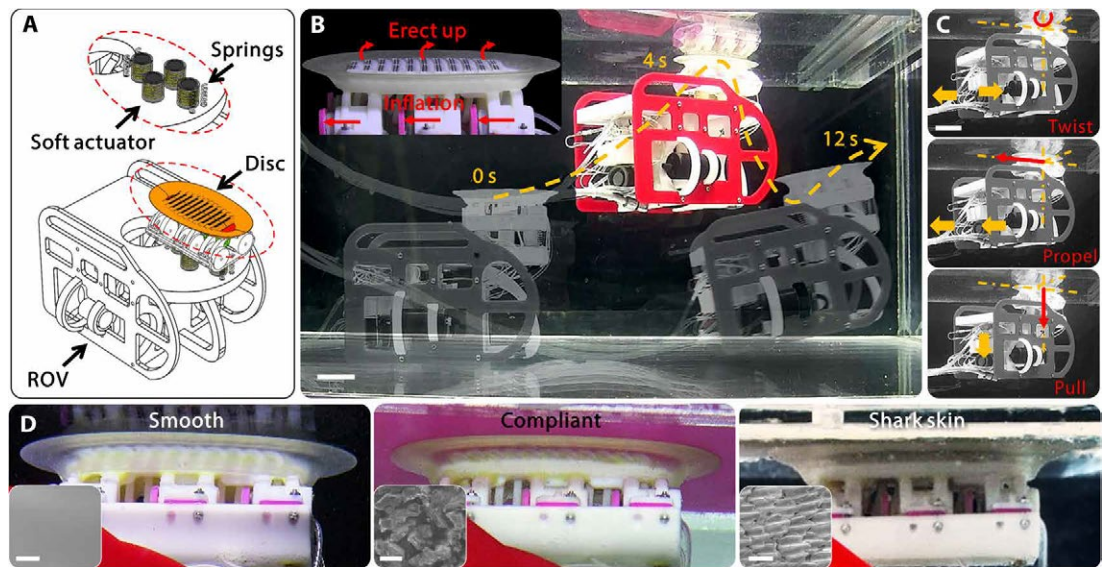
Because the mechanical properties of the remora disc soft tissues (fleshy disc lip and soft lamella overlay) are similar to those of fish skin (Young's modulus of 0.5 MPa) (2, 36), we were unable to precisely match the mechanical properties of the disc prototype (e.g., the soft tissue overlay that surrounds the overhanging rigid lamella plate and the soft tissue that connects the disc lip and the lamellae) to their biological analogs using current multimaterial 3D printing approaches. However, improvements in 3D printing technology in the future may allow for the reproduction of more flexible materials in the range of biological soft tissues for the production of more lifelike prototypes. In addition, we demonstrated disc detachment with a simplified engineering approach (by pumping water into the disc to eliminate the chamber pressure differential) to achieve a remora-like hitchhiking behavior. However, understanding the detachment behavior of remoras would require additional comprehensive studies that include morphological and kinematic measurements of live remoras. The ability to incorporate the detachment capability into the disc prototype with a new biologically inspired mechanism in the future would complete our current disc design.

Our biomimetic disc prototype demonstrated the ability to attach to a variety of surfaces, including smooth (epoxy resin), rough (epoxy resin), compliant rough (silicone elastomer), and real shark skin ( $R_a = 120$   $\mu\text{m}$ ), and enabled an underwater ROV with the ability to hitchhike onto these surfaces. Through the fabrication process and the experiments conducted on the disc prototype, we investigated the function of different morphological disc features on adhesion.

First, the soft disc lip functions as a suction seal that contributes directly to produce a considerable pull-off force up to 438 N (approximately 340 times the weight of the disc prototype). The remora disc prototype showed similar pull-off stress (58.7 kPa) on the smooth

**Fig. 4. Attachment of an underwater vehicle using the biorobotic remora disc.** (A) The remora disc prototype is connected to the ROV via four springs with low stiffness and four soft silicone pneumatic elastomer actuators. The ROV contains three propellers with a motor power rating of 300 W for each. The mass of the robot is 1.46 kg.

(B) Frames of attachment of the robot from movie S6 at various time instants. The ROV with the remora disc prototype performs a successful transition from a swimming mode (propelled by rotors) to the attachment mode (4 s) on a smooth glass surface. For demonstration purposes, we also show the remora disc ROV detaching from the surface and transitioning back into the swimming mode (12 s). For simplification, we used a syringe to pump water into the chamber for balancing the pressure difference between the interior and exterior of the disc chamber for detachment. Scale bar, 50 mm. (C) Remora disc ROV after successful attachment to the surface and attachment against propelling, twisting, and pulling. Scale bar, 50 mm. (D) As with the isolated disc prototype studies, the ROV can successfully attach to various surfaces, including smooth (Plexiglas; left), compliant rough (silicone elastomer; middle), and real shark skin (right). Scale bars, 200  $\mu\text{m}$ .



surface compared with commercial suction cups (50 to 80 kPa). However, the remora disc prototype produced substantially greater pull-off stress (15.8 to 21.9 kPa on surface of roughness  $R_a = 200 \mu\text{m}$ ) relative to commercially available suction cups on rough surfaces [which fail to stick to surfaces with  $R_a > 21.8 \mu\text{m}$ ; (14)]. Second, by raising the spinule-covered composite lamellae in the disc interior, similar to its biological counterparts, the frictional force can be significantly enhanced on both smooth and rough surfaces, up to 1.7 and 1.4 times, respectively. Third, our prototype experimental data demonstrated that the rigid spinules and the soft tissue overlaying the lamellae work in concert and contribute differentially to enhancing frictional forces during remora attachment on surfaces with different roughness. For example, on the smooth surface, we observed that prototypes with and without spinules generate similar amounts of posteriorly directed frictional forces. In contrast, for adhesion to the rough surface ( $R_a \approx 200 \mu\text{m}$ ), spinules contributed more to the frictional force than the soft tissue overlay made of soft material (Fig. 3D). On the real shark skin, a common natural host surface for *E. naucrates* [ $R_a \approx 120 \mu\text{m}$ ; (30)], both the lamella soft tissue overlay and the rigid spinules play essential roles (Fig. 3E, inset). A friction theoretical model was developed to evaluate the spinule contribution to the shear force (31), suggesting that spinules are primarily responsible for friction enhancement on rough surfaces, which agrees with our current finding. To summarize, the frictional force on the disc prototype can be significantly increased because of the combination of the rigid spinules and the lamella soft tissue overlay in response to different surface roughness. On rougher surfaces, the disc prototype always produced higher frictional forces with spinules than without spinules.

We consider hitchhiking as an effective strategy for reducing energy expenditure during transport or movement of small underwater robots. Like robotic propulsion, live fishes (including remoras) require body muscular power to generate thrust during swimming (37–39), whereas nearly zero muscular power is needed when attaching to a sub-

strate (2, 40). The shape of the remora is similar to that of a streamlined body, with a low drag coefficient well suited for hitchhiking (39). For example, a 35-cm remora attached to a 2 m/s swimming (3) bottlenose dolphin (*Tursiops truncatus*) with a relatively smooth surface ( $R_a < 20 \mu\text{m}$ ) would incur only 0.27 N of drag (39). Our disc prototype can produce a frictional force on a smooth surface, which is up to 132 times the drag experienced by a remora attached to a host swimming at 2 m/s (39). Attached to a real shark skin substrate, our disc prototype produced frictional forces up to 34 times the estimated drag force of 0.16 N for a 35-cm remora attached to a shortfin mako (*I. oxyrinchus*), a host with rough skin ( $R_a \approx 120 \mu\text{m}$ ), swimming at an average cruising speed of 1.5 m/s.

This adhesive technology also offers possible utility for gripping applications underwater [e.g., in a dynamic tanker docking engineering system as described in (16)] or in air (movie S7), which requires adhesive forces in both the normal and shear directions. As demonstrated here, the attachment dynamics of our remora disc prototype thus permits high-performance underwater adhesion. Coupled with a platform of streamlined shape, such a system could markedly reduce transport and movement costs and increase mission durations for autonomous underwater vehicles.

## MATERIALS AND METHODS

### Morphology and kinematics of the biological remora disc

To reveal the structural details of the remora skeletal system, we scanned, segmented, and reconstructed a preserved remora (*E. naucrates*) adhesive disc using microcomputed tomography (microCT) (movie S1). Using an environmental scanning electron microscope (ESEM), we also measured the geometries of more than 30 spinule samples from remora discs. More details on the morphological measurements can be found in section S2. All the live remoras used in this study were handled in accordance with the Regulations for the Administration of Affairs Concerning Experimental Animals issued by the Institutional

Animal Care and Use Committee of Beijing. To characterize the lamella kinematics, we quantified their movement using high-speed videography (Fig. 2A and fig. S1). Because the lamella movement was not visible from a side-view camera, we extracted the movement data ( $x$  axis) of marker points to analyze the lamellar kinematics from dorsal-view images (Fig. 2, A and B). More detailed descriptions on lamella locomotion analysis are found in section S1.

### Design and fabrication of the remora disc

On the basis of the previously described morphological and kinematic features, we developed a computer-aided design (CAD) model for the fabrication of the disc prototype (Fig. 1C). The primary components were designed by mimicking the dominant geometries of the natural lamella plate and disc base of microCT-scanned remora specimens. In lateral view, the spinule tips overlap with the base of the adjacent posterior lamellae (the right inset image in Fig. 1C). The biomimetic disc lip surrounds the disc base as an anchoring structure to enhance the surface area of the bonding interface (the left inset image in Fig. 1C). In addition, a soft tissue connects the lateral aspects of the lamellae to the disc lip (fig. S5C). More detailed descriptions on the design and fabrication of the disc main body, the carbon fiber spinules, and the soft actuators that erect or fold the lamellae are provided in section S3.

### Forces and pressure measurements of the prototypes

We investigated the effects of pitchable lamellae and rigid spinules on the adhesive performance of the disc while in contact with surfaces of different roughness in water. We tested each disc prototype on two nonbiological rigid surfaces, one smooth and one rough surface [ $R_a \approx 200 \mu\text{m}$ ; by both molding and casting with epoxy resin material (EpoxAcast 650, Smooth-On Inc., PA); fabrication details are provided in section S5], and on real shark skin ( $R_a \approx 120 \mu\text{m}$ ; preparation details are provided in section S5) (fig. S7). To measure the pull-off force ( $F_d$ ) and the frictional force ( $f_d$ ), we tested the submerged prototype with a multiple-axis force transducer mounted to a robotic arm (fig. S6). To evaluate the differential contribution of lamella soft tissue overlay and rigid spinules in the generation of frictional force on surfaces of different roughness, we fabricated two biorobotic remora disc prototypes: one with the lamella soft tissue only (i.e., without spinules; fig. S5A) and another with biomimetic spinules (fig. S5B). Using these disc prototypes, we further determined the pull-off force and static frictional force as a function of the lamella pitch angle  $\theta$  ( $0^\circ$  to  $16^\circ$ ). More detailed descriptions on forces and pressure measurements of the prototypes are provided in section S5.

### SUPPLEMENTARY MATERIALS

robotics.sciencemag.org/cgi/content/full/2/10/ean8072/DC1

Text

Fig. S1. Experimental setup for remora locomotion observation during attachment and schematic diagrams of lamella kinematic analysis.

Fig. S2. Design details of the lamella plates and the artificial spinules.

Fig. S3. Fabrication procedures of the whole remora disc prototype.

Fig. S4. Design and fabrication of the soft actuators.

Fig. S5. Two prototypes (disc with lamellae only without spinules and disc with lamellae and with spinules) tested in this study.

Fig. S6. Experimental setup of forces and pressure measurements.

Fig. S7. ESEM images of three substrates and setup for the side-view contact visualization.

Fig. S8. Dimensionless amplitude of the lamellae's marker point  $u$  versus time for the folding down motions of a live remora and the biomimetic remora disc.

Fig. S9. The fully ambient pressure differential of the prototype chamber versus the lamella pitch angle ( $\theta$ ) when the disc was attached to a smooth substrate.

Fig. S10. Pressure of the chamber during a complete pull-off process.

Fig. S11. Forward frictional forces on the (A) shark skin surface and (B) rough surface ( $R_a = 200 \mu\text{m}$ ).

Table S1. Morphological parameters of three individual remoras and their adhesive discs.

Table S2. Physical parameters of the disc prototype and the lamellae.

Table S3. Length of the artificial spinule plates of the disc prototype.

Table S4. Geometry of a single laser-cut biomimetic spinule and the spinule plate.

Table S5. Stiffness of the components in the biomimetic prototype.

Movie S1. Demonstration of a remora's adhesive disc in the microCT data.

Movie S2. Remora lamella motion recorded by a high-speed camera (erect up and fold down).

Movie S3. Animation of lamella pitching mechanism.

Movie S4. Lamella motion of the biomimetic adhesive disc.

Movie S5. Lamella motion comparison between the biological and biomimetic adhesive disc (erect up and fold down, on the transparent glass surface).

Movie S6. Demonstration of the underwater attachment of the biorobotic remora disc via an underwater robotic system.

Movie S7. Demonstration of the biorobotic remora disc gripping a variety of items in air.

References (41–43)

### REFERENCES AND NOTES

1. A. Günther, XLII.—On the history of *Echeneis*. *J. Nat. Hist.* **5**, 386–402 (1860).
2. B. A. Fulcher, P. J. Motta, Suction disk performance of *Echeneid* fishes. *Can. J. Zool.* **84**, 42–50 (2006).
3. D. Weihs, F. E. Fish, A. J. Nicastrò, Mechanics of remora removal by dolphin spinning. *Mar. Mamm. Sci.* **23**, 707–714 (2007).
4. R. F. Cressey, E. A. Lachner, The parasitic copepod diet and life history of diskfishes (*Echeneidae*). *Copeia* **2**, 310–318 (1970).
5. J. F. Steffensen, J. P. Lomholt, Energetic cost of active branchial ventilation in the sharksucker, *Echeneis naucrates*. *J. Exp. Biol.* **103**, 185–192 (1983).
6. R. Britz, G. D. Johnson, Ontogeny and homology of the skeletal elements that form the sucking disc of remoras (*Teleostei*, *Echeneoidei*, *Echeneidae*). *J. Morphol.* **273**, 1353–1366 (2012).
7. M. Friedman, Z. Johanson, R. C. Harrington, T. J. Near, M. R. Graham, An early fossil remora (*Echeneoidea*) reveals the evolutionary assembly of the adhesion disc. *Proc. R. Soc. B* **280**, 20131200 (2013).
8. K. Autumn, Y. A. Liang, S. T. Hsieh, W. Zesch, W. P. Chan, T. W. Kenny, R. Fearing, R. J. Full, Adhesive force of a single gecko foot-hair. *Nature* **405**, 681–685 (2000).
9. D.-M. Drotlef, L. Stepien, M. Kappl, W. J. P. Barnes, H.-J. Butt, A. del Campo, Insights into the adhesive mechanisms of tree frogs using artificial mimics. *Adv. Funct. Mater.* **23**, 1137–1146 (2013).
10. W. Federle, W. J. P. Barnes, W. Baumgartner, P. Drechsler, J. M. Smith, Wet but not slippery: Boundary friction in tree frog adhesive toe pads. *J. R. Soc. Interface* **3**, 689–697 (2006).
11. J. H. Lai, J. C. del Alamo, J. Rodríguez-Rodríguez, J. C. Lasheras, The mechanics of the adhesive locomotion of terrestrial gastropods. *J. Exp. Biol.* **213**, 3920–3933 (2010).
12. D. Dodou, P. Breedveld, J. C. F. de Winter, J. Dankelman, J. L. van Leeuwen, Mechanisms of temporary adhesion in benthic animals. *Biol. Rev.* **86**, 15–32 (2011).
13. D. Labonte, W. Federle, Scaling and biomechanics of surface attachment in climbing animals. *Philos. Trans. R. Soc. Lond. B Biol. Sci.* **370**, 20140027 (2015).
14. D. K. Wainwright, T. Kleinteich, A. Kleinteich, S. N. Gorb, A. P. Summers, Stick tight: Suction adhesion on irregular surfaces in the northern clingfish. *Biol. Lett.* **9**, 20130234 (2013).
15. P. Ditsche, D. K. Wainwright, A. P. Summers, Attachment to challenging substrates—Fouling, roughness and limits of adhesion in the northern clingfish (*Gobiesox maendricus*). *J. Exp. Biol.* **217**, 2548–2554 (2014).
16. T. I. Wolff, “The design and fabrication of a biomimetic lifting aid,” thesis, University of Twente, Enschede, Overijssel (2017).
17. C. Li, T. Zhang, D. I. Goldman, A terradynamics of legged locomotion on granular media. *Science* **339**, 1408–1412 (2013).
18. E. Kizilkan, J. Struëben, A. Staubitz, S. N. Gorb, Bioinspired photocontrollable microstructured transport device. *Sci. Robot.* **2**, eaak9454 (2017).
19. U. Çulha, F. İda, Enhancement of finger motion range with compliant anthropomorphic joint design. *Bioinspir. Biomim.* **11**, 026001 (2016).
20. J.-S. Koh, E. Yang, G.-P. Jung, S.-P. Jung, J. H. Son, S.-I. Lee, P. G. Jablonski, R. J. Wood, H.-Y. Kim, K.-J. Cho, Jumping on water: Surface tension-dominated jumping of water striders and robotic insects. *Science* **349**, 517–521 (2015).
21. M. Wehner, R. L. Truby, D. J. Fitzgerald, B. Mosadegh, G. M. Whitesides, J. A. Lewis, R. J. Wood, An integrated design and fabrication strategy for entirely soft, autonomous robots. *Nature* **536**, 451–455 (2016).
22. L. Wen, J. C. Weaver, G. V. Lauder, Biomimetic shark skin: Design, fabrication and hydrodynamic function. *J. Exp. Biol.* **217**, 1656–1666 (2014).

23. M. M. Porter, D. Adriaens, R. L. Hatton, M. A. Meyers, J. McKittrick, Why the seahorse tail is square. *Science* **349**, aaa6683 (2015).
24. H.-T. Lin, G. G. Leisk, B. Trimmer, GoQBot: A caterpillar-inspired soft-bodied rolling robot. *Bioinspir. Biomim.* **6**, 026007 (2011).
25. S. A. Morin, R. F. Shepherd, S. W. Kwok, A. A. Stokes, A. Nemiroski, G. M. Whitesides, Camouflage and display for soft machines. *Science* **337**, 828–832 (2012).
26. D. Rus, M. T. Tolley, Design, fabrication and control of soft robots. *Nature* **521**, 467–475 (2015).
27. N. W. Bartlett, M. T. Tolley, J. T. Overvelde, J. C. Weaver, B. Mosadegh, K. Bertoldi, G. M. Whitesides, R. J. Wood, A 3D-printed, functionally graded soft robot powered by combustion. *Science* **349**, 161–165 (2015).
28. S.-J. Park, M. Gazzola, K. S. Park, S. Park, V. Di Santo, E. L. Blevins, J. U. Lind, P. H. Campbell, S. Dauth, A. K. Capulli, F. S. Pasqualini, S. Ahn, A. Cho, H. Yuan, B. M. Maoz, R. Vijaykumar, J.-W. Choi, K. Deisseroth, G. V. Lauder, L. Mahadevan, K. K. Parker, Phototactic guidance of a tissue-engineered soft-robotic ray. *Science* **353**, 158–162 (2016).
29. M. A. Graule, P. Chirarattananon, S. B. Fuller, N. T. Jafferis, K. Y. Ma, M. Spenko, R. Kornbluh, R. J. Wood, Perching and takeoff of a robotic insect on overhangs using switchable electrostatic adhesion. *Science* **352**, 978–982 (2016).
30. B. O'Toole, Phylogeny of the species of the superfamily Echeneoidea (Perciformes: Carangoidei: Echeneidae, Rachycentridae, and Coryphaenidae), with an interpretation of echeneid hitchhiking behaviour. *Can. J. Zool.* **80**, 596–623 (2002).
31. M. Beckert, B. E. Flammang, J. H. Nadler, Remora fish suction pad attachment is enhanced by spinule friction. *J. Exp. Biol.* **218**, 3551–3558 (2015).
32. P. B. Moyle, J. J. Cech, *Fishes: An Introduction to Ichthyology* (Prentice Hall, 1996).
33. B. C. Jayne, A. F. Lozada, G. V. Lauder, Function of the dorsal fin in bluegill sunfish: Motor patterns during four distinct locomotor behaviors. *J. Morphol.* **228**, 307–326 (1996).
34. V. Pavlov, B. Rosental, N. F. Hansen, J. M. Beers, G. Parish, I. Rowbotham, B. A. Block, Hydraulic control of tuna fins: A role for the lymphatic system in vertebrate locomotion. *Science* **357**, 310–314 (2017).
35. B. Lorenz, B. A. Krick, N. Rodriguez, W. G. Sawyer, P. Mangiagalli, B. N. J. Persson, Static or breakloose friction for lubricated contacts: The role of surface roughness and dewetting. *J. Phys. Condens. Matter* **25**, 1–22 (2013).
36. A. P. Summers, J. H. Long Jr., Skin and bones, sinew and gristle: The mechanical behavior of fish skeletal tissues. *Fish Physiol.* **23**, 141–177 (2005).
37. L. C. Rome, D. Swank, D. Corda, How fish power swimming. *Science* **261**, 340–343 (1993).
38. J. C. Liao, D. N. Beal, G. V. Lauder, M. S. Triantafyllou, Fish exploiting vortices decrease muscle activity. *Science* **302**, 1566–1569 (2003).
39. M. Beckert, B. E. Flammang, E. J. Anderson, J. H. Nadler, Theoretical and computational fluid dynamics of an attached remora (*Echeneis naucrates*). *Zoology* **119**, 430–438 (2016).
40. S. L. Hora, The adhesive apparatus of the “sucking fish”. *Nature* **115**, 48 (1925).
41. T. L. Hedrick, Software techniques for two- and three-dimensional kinematic measurements of biological and biomimetic systems. *Bioinspir. Biomim.* **3**, 1–6 (2008).
42. M. Scherge, S. Gorb, S. N. Gorb, *Biological Micro- and Nanotribology* (Springer Science & Business Media, 2001).
43. J. N. Israelachvili, *Intermolecular and Surface Forces: Revised Third Edition* (Academic Press, 2011).

**Acknowledgments:** We thank X. Ling and L. Bao for their contribution to this work and G. Lauder for providing comments to this paper. **Funding:** This work was supported by the National Science Foundation of China support projects (grant nos. 61403012 and 61633004 to L.W.), the Wyss Institute for Biologically Inspired Engineering, NSF Postdoctoral Fellowship in Biology award no. 1103761 (to C.P.K.), and NSF Graduate Research Fellowship 2014162421 (to D.K.W.). **Author contributions:** C.P.K., R.J.W., and L.W. conceived the project. Y.W., Y.C., and L.W. designed and fabricated the biomimetic remora disc. Y.W., C.P.K., D.K.W., H.L., J.C.W., and L.W. characterized the morphology of the biological remora disc. X.Y., Y.W., Z.L., C.P.K., and L.W. conducted the kinematics of the remora disc. Y.W., X.Y., Y.C., D.K.W., and L.W. conducted the adhesive measurements and analyzed the data. Z.G., Z.L., and L.W. conducted underwater robot attachment experiments. L.W. and X.Y. prepared the manuscript, and all authors provided feedback during subsequent revisions. **Competing interests:** Patents have been submitted to the Chinese Patent Office, describing the remora-inspired underwater adhesive disc. Y.W., Y.C., and L.W. are authors of patent application 201710309248X. **Data and materials availability:** Please contact L.W. for data and other materials.

Submitted 22 May 2017

Accepted 28 August 2017

Published 20 September 2017

10.1126/scirobotics.aan8072

**Citation:** Y. Wang, X. Yang, Y. Chen, D. K. Wainwright, C. P. Kenaley, Z. Gong, Z. Liu, H. Liu, J. Guan, T. Wang, J. C. Weaver, R. J. Wood, L. Wen, A biorobotic adhesive disc for underwater hitchhiking inspired by the remora suckerfish. *Sci. Robot.* **2**, ean8072 (2017).

## HUMANOIDS

# Design principles of a human mimetic humanoid: Humanoid platform to study human intelligence and internal body system

Yuki Asano,\* Kei Okada, Masayuki Inaba

Many systems and mechanisms in the human body are not fully understood, such as the principles of muscle control, the sensory nervous system that connects the brain and the body, learning in the brain, and the human walking motion. To address this knowledge deficit, we propose a human mimetic humanoid with an unprecedented degree of anatomical fidelity to the human musculoskeletal structure. The fundamental concept underlying our design is to consider the human mechanism, which contrasts with the conventional engineering approach used in the design of existing humanoids. We believe that the proposed human mimetic humanoid can be used to provide new opportunities in science, for instance, to quantitatively analyze the internal data of a human body in movement. We describe the principles and development of human mimetic humanoids, Kenshiro and Kengoro, and compare their anatomical fidelity with humans in terms of body proportions, skeletal structures, muscle arrangement, and joint performance. To demonstrate the potential of human mimetic humanoids, Kenshiro and Kengoro performed several typical human motions.

## INTRODUCTION

For at least the last two millennia, human beings have endeavored to understand the systems and mechanisms that make up the human body, such as the principles of muscle control, the sensory nervous system that connects the brain and the body, the mechanisms of learning in the brain, and the accomplishment of the simple act of walking. In recent years, technology has developed to the point where humanoid robots that mimic human body structures are now being constructed, and these enable us to study the systems in the human body by making humanoids or through experimental trials in the real world. However, a limitation of conventional humanoids is that they have been designed on the basis of the theories of conventional engineering, mechanics, electronics, and informatics. They are also primarily intended for engineering-oriented applications, such as task achievement in daily life, personal assistance, or disaster response. By contrast, our intent is to design a humanoid based on human systems—including the musculoskeletal structure, sensory nervous system, and methods of information processing in the brain—to support science-oriented goals, such as gaining a deeper understanding of the internal mechanisms of humans.

Our research team has successfully developed musculoskeletal robots (1–5), and it seems possible to use these to our stated purpose because they imitate the human musculoskeletal structure, support the flexible body and behaviors of humans, and support human-style muscle actuation using tendon-driven actuators. However, those musculoskeletal robots are not accurate enough for our purpose from an anatomical point of view, such as body proportions, muscle arrangements, and joint structures, although their actuation does mimic human muscle contraction. Other research teams have also successfully developed musculoskeletal robots from an anthropomorphic point of view (6–12). The body structures and shapes of their robots were inspired from humans, and they provided effective

schemes for controlling and modeling those kinds of robots. However, their robots were not capable of performing whole-body motions because they did not have tendon-driven legs for supporting their weight.

Therefore, we propose a human mimetic humanoid that provides a high degree of anatomical fidelity to the human structure and is capable of whole-body motions. We believe that such a human mimetic humanoid can provide new opportunities to advance science, such as in the field of musculoskeletal physical simulation, to capture and quantitatively analyze the internal data of a moving human body using the sensors of a human mimetic humanoid. Here, we detail the design principles of an anatomically correct human mimetic humanoid in the following areas: (i) body proportions, (ii) skeletal structures, (iii) muscle arrangement, and (iv) joint performance.

We also describe the development of the Kenshiro and Kengoro humanoids as examples. The human mimetic design concept is the common concept for each humanoid. Kenshiro is the first humanoid developed based on the concept, and then Kengoro was developed with a lot of improvements for a higher degree of fidelity to humans. These humanoids have anatomically correct musculoskeletal structures in their bodies, so that we can evaluate the fidelity of the musculoskeletal structures relative to that of a human. A design overview of the proposed human mimetic humanoid is shown in Fig. 1.

## RESULTS

In this section, we describe the anatomical fidelity of Kenshiro and Kengoro and evaluate how accurately their musculoskeletal structure mimics that of a human in the four specific areas of interest.

### Body proportion fidelity

The body proportions of Kenshiro and Kengoro were designed by using human statistical data (13–16) as the design target, so that the humanoids would have more human-like body proportions, and the link lengths of Kenshiro and Kengoro were designed on the basis of the corresponding lengths in a human body. To evaluate

Copyright © 2017  
The Authors, some  
rights reserved;  
exclusive licensee  
American Association  
for the Advancement  
of Science. No claim  
to original U.S.  
Government Works

Department of Mechano-Informatics, Graduate School of Information Science and Technology, University of Tokyo, Hongo 7-3-1, Bunkyo-ku, Tokyo 113-8656, Japan.

\*Corresponding author. Email: asano@jsk.imi.i.u-tokyo.ac.jp

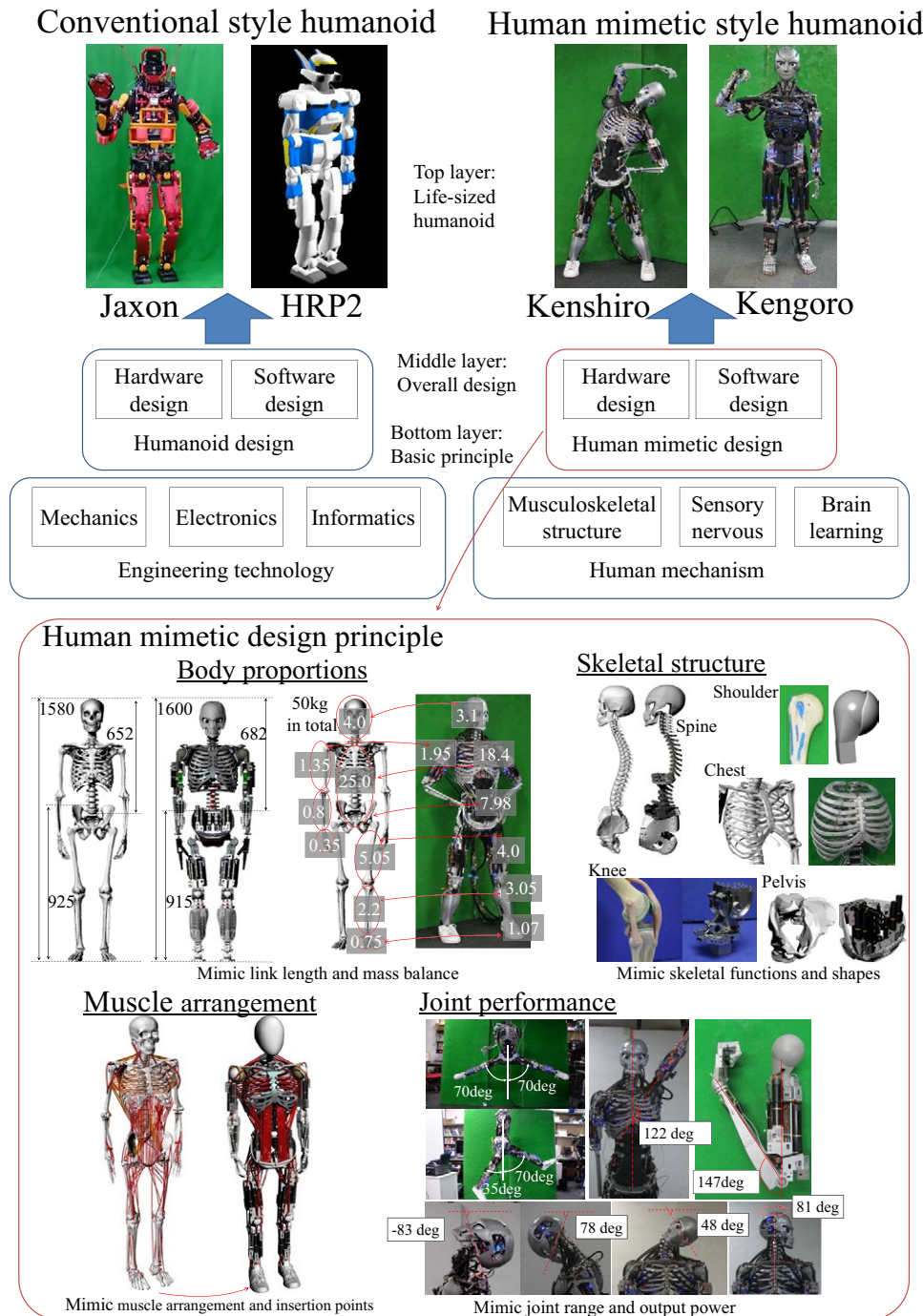


**Fig. 1. Basic design concept of human mimetic humanoid.** Human mimetic humanoids were designed on the basis of the mechanisms in the human body, in contrast to conventional humanoids designed based on the theory of engineering. In the design of a human mimetic humanoid, the same body proportions and musculoskeletal structures as those of an average human were used as design specifications.

their human mimetic body proportions, we conducted a link length comparison between Kenshiro, Kengoro, and an average human using the body segments shown in Table 1. Note that the ratio of the human link length and weight has been reported in several studies. The results indicated that the average link lengths in Kenshiro and Kengoro versus a human were 101 and 99.3%, respectively.

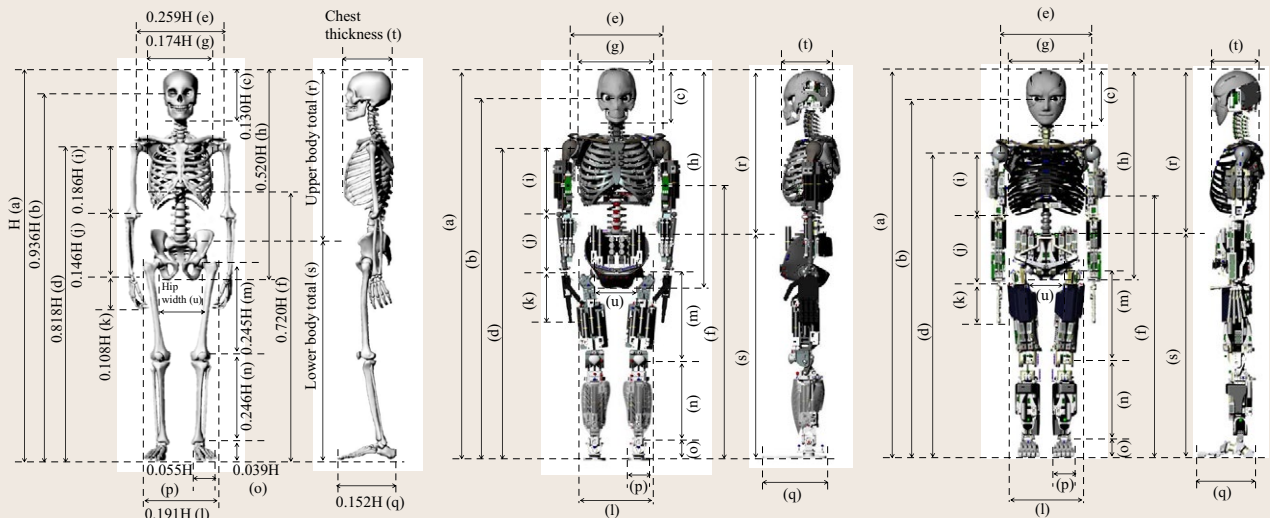
A comparison of the mass distribution properties between Kenshiro, Kengoro, and an average human was also conducted. The results of this comparison are presented in Table 2, where it can be seen that Kenshiro and Kengoro exhibited an average of 115 and 116% of the mass of an average human, respectively. Thus, we confirmed that the assembled humanoids exhibited high fidelity from the mass distribution point of view.

**Skeletal structure fidelity**

In terms of the skeletal structure evaluation, we compared the number of degrees of freedom (DOFs) between a human and several humanoids, including Kenshiro and Kengoro. In a human, 548 joint DOFs have been identified; when excluding the face and hands, there are 419 DOFs based on the number of bone connections according to their functional classification (17). Each joint may include one, two, or three DOFs. The comparison of joint DOFs, excluding those of the face and hands based on the data of Kenshiro, Kengoro, or other life-sized humanoids (3, 4, 18–25), is shown in Fig. 2. These humanoids can be largely separated into two groups. The first group (that is, the axial-driven group) is composed of ordinary humanoids with actuators at each joint to move their structural links, and the number of joint DOFs is 27 to 35. Examples of this group include the HRP2 or ASIMO humanoids. The second group (that is, the tendon-driven group) is composed of tendon-driven humanoids with human-inspired musculoskeletal structures that have a relatively large number of joint DOFs (55 to 114). The use of multiple spine joints is one of the most important factors required to approach the flexibility of a human, and the number of DOFs of current humanoids is limited by whether the humanoid has spinal flexibility. Kenshiro has 64 DOFs, which is just 15% of the 419 DOFs possessed by a human. Multiple spine joints and a yaw rotational DOF in the knee joint are the reason for the relatively larger number of whole-body DOFs compared with other humanoids. Kengoro has 114 DOFs, which

is 27% of the number possessed by humans and is the largest number of DOFs among life-sized humanoids. When hand DOFs are included, Kengoro is equipped with 174 DOFs. Multiple DOFs in its end effectors are considered the reason for the increased number of DOFs. End effectors are a challenging topic in humanoid robotics, and a large gap remains in this area between humanoids and humans.

**Table 1. Link length comparison between Kenshiro, Kengoro, and an average human.** The body segments of each are indicated for comparison purposes. Human anthropometry data were obtained from (47) based on (48). The human length proportions were calculated, assuming the same body height as Kenshiro and Kengoro. The proportional values for *r-u* were not provided, whereas those of Kenshiro and Kengoro are described in the referenced information. Dash entries indicate excluded data.



Sign	Part	Length (mm)			Length (mm)		
		Human	Kenshiro*	Ratio (%)	Human	Kengoro*	Ratio (%)
<i>a</i>	Body height	1600	1600	100	1670	1670	100
<i>b</i>	Eye height	1500	1470	98.5	1560	1540	98.8
<i>c</i>	Head	208	227	109	217	237	109
<i>d</i>	Shoulder height	1310	1270	97.3	1370	1310	95.8
<i>e</i>	Shoulder width	414	372	89.9	432	395	91.4
<i>f</i>	Chest height	1150	1130	98.6	1200	1140	94.6
<i>g</i>	Chest width	278	306	110	291	328	113
<i>h</i>	Trunk with head	831	897	108	868	901	104
<i>i</i>	Upper arm	297	270	90.9	311	270	86.9
<i>j</i>	Forearm	233	236	101	244	292	120
<i>k</i>	Hand	173	- <sup>†</sup>	-	180	161	89.4
<i>l</i>	Hip width(trochanter)	305	309	101	319	293	91.8
<i>m</i>	Thigh	391	348	89.0	409	384	93.8
<i>n</i>	Shank	393	343	87.4	411	348	84.7
<i>o</i>	Foot	62.3	74.3	119	65.1	79.2	122
<i>p</i>	Foot width	87.9	90.0	102	91.8	90.1	99.0
<i>q</i>	Foot length	243	260	107	254	241	94.9
<i>r</i>	Upper body total	-	682	-	-	745	-
<i>s</i>	Lower body total	-	915	-	-	924	-
<i>t</i>	Chest thickness	-	211	-	-	203	-
<i>u</i>	Hip width (joint)	-	168	-	-	151	-
		Average( <i>b-q</i> )		101	Average( <i>b-q</i> )		99.3

\* The distances between the parts were measured on geometrical 3D models. † The hand was excluded from the list because Kenshiro does not have hands.

**Table 2. Link weight comparison between Kenshiro, Kengoro, and an average human.** The human data used in this comparison were reported in (49) based on the data of (27) and (50). Each human link weight was calculated assuming the same body weight as Kenshiro and Kengoro.

Name	Ratio of segment weight (%)	Weight (kg)			Weight (kg)			
		Human	Kenshiro	Ratio (%)	Human	Kengoro	Ratio (%)	
Body weight	100	51.9	51.9	100	56.5	56.5	100	
Head*	8.0	4.15	3.10	74.7	4.52	2.6	57.5	
Trunk†	50.0	26.0	26.3	102	28.3	26.0	91.9	
Upper trunk‡	–	–	18.4	–	–	17.3	–	
Pelvis	–	–	7.98	–	–	8.64	–	
Upper arm	2.70	1.40	1.95	139	1.53	2.19	144	
Forearm	1.60	0.830	1.16	140	0.904	1.54	170	
Hand	0.70	0.363	– <sup>§</sup>	–	0.396	0.3	75.9	
Thigh	10.1	5.24	4.0	76.3	5.71	5.07	88.8	
Shank	4.4	2.28	3.05	134	2.49	3.53	142	
Foot	1.5	0.779	1.07	137	0.85	1.34	158	
		Average			115	Average		116

\*The heads of Kenshiro and Kengoro include their necks. †Trunk includes upper trunk and pelvis. ‡Upper trunk includes spine, chest, and shoulder blade. §Kenshiro does not possess a hand.

Body part	The number of joint DOFs					
	Human	HRP2	Kenshiro			Kengoro
Spine	73	4	lumber 11, neck 13			40
Arms	26	12	collar 3, blade 3, shoulder 3, elbow 1, radioulnar 1 (passive), wrist 2 (passive)			26
Hands	126	2	each finger 6			60
Legs	12	12	hip 3, knee 2, ankle 2			16
Feet	140	0	heel 3, lisfranc 3, each finger 2			32
Others	171	0				0
Total	548	30				174

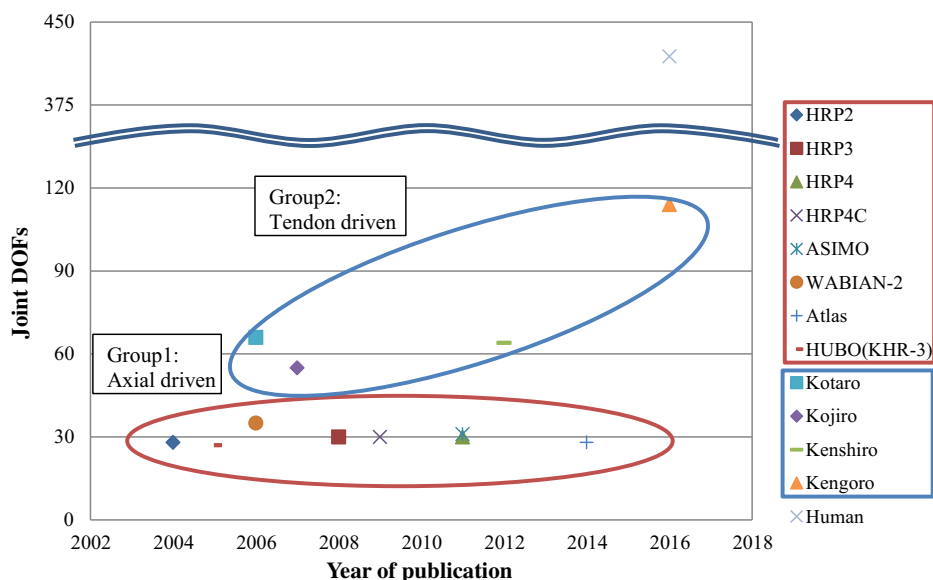


**Fig. 2. Joint DOF comparison between several humanoids and an average human.**

**Muscle arrangement fidelity**

A human mimetic muscle arrangement means that muscle actuators are placed and arranged so that they replicate muscle origin and insertion points based on human anatomy. This arrangement enables the naming of muscle actuators in a musculoskeletal humanoid to match that in humans, which, in turn, increasing the plausibility of the muscle data obtained from the movement of the human mimetic humanoid. A comparison of the number of synonymous muscles between humans and several musculoskeletal robots, including Kenshiro and Kengoro, is presented in Table 3. Human muscles important for whole-body motions and joint movements were counted. The muscles for face or organs are eliminated from the number. In the table, the count is not based on the muscle (actuator) number but the name of the muscle, because there are cases where Kenshiro and Kengoro are equipped with multiple muscle actuators that represent a single muscle. For example, Kenshiro is equipped with two muscle actuators that represent the gastrocnemius muscle to ensure enough muscle output. In the spine, Kenshiro and Kengoro have a higher number of muscle relationships than other robots. In the arm, excluding the inner muscles of

**Table 3. Muscle fidelity evaluation.** The number of muscles was counted based on the muscle names corresponding to those of the human. The numbers of muscles in the musculoskeletal robots developed by (12, 51, 52) are described in the comparison.

	Number of muscles/Ratio to human					
	Human	Athlete robot*	Pneumat-BS	Anthrob <sup>†</sup>	Kenshiro	Kengoro
Spine	34	–	2	–	10	10
Ratio (%)	100	–	5.88	–	29.4	29.4
Arm (without hand)	37	–	3	9	10	19
Ratio (%)	100	–	8.10	24.3	27.0	51.4
Leg (without foot)	42	7	16	–	21	24
Ratio (%)	100	16.7	38.0	–	50.0	57.1
Whole body (without hand and foot)	106	–	22	–	40	52
Ratio (%)	100	–	20.8	–	37.7	49.1
Whole body (with hand and foot)	133	–	22	–	40	53
Ratio (%)	100	–	16.5	–	30.1	39.1

\*Legged robot †One-armed robot

the hand, Kenshiro and Kengoro are equipped with 27.0 and 51.4%, respectively, of the muscles of humans. Kengoro has a larger number of muscles than Kenshiro, because the muscles for its forearm and wrist contribute to increasing the number of muscles. In the leg, excluding the inner muscles of the foot, Kenshiro and Kengoro are equipped with 50.0 and 57.1% of the muscles of humans. In the entire body comparison, excluding the inner muscles of the hand and the foot, the muscle fidelity of Kenshiro and Kengoro are 37.7 and 49.1%, respectively, in that of humans. On the basis of these results, we confirmed that the human mimetic humanoids Kenshiro and Kengoro have the largest rate of muscle fidelity with respect to humans when compared to the other humanoids. Nevertheless, when the muscles of the hands and feet are included, the fidelity decreases to 30.1% for Kenshiro and 39.1% for Kengoro. These results are due to the muscles for the end effectors being a large part of the entire muscle ratio of humans. Thus, end effectors are quite important for humans in their daily lives. This suggests that it is essential to develop human mimetic end effectors to move humanoid robotics forward.

### Joint performance fidelity

A joint range comparison between Kenshiro, Kengoro, and an average human was conducted. Note that the joint range of a human has been reported in (17, 26, 27). The mechanical joint range of Kenshiro and Kengoro were examined using geometrical computer-aided design models or actual movement of the real robot, and the neck, spine, shoulder, elbow, hip, knee, and ankle joint ranges were compared. The results are shown in Fig. 3. We confirmed that almost all the joint ranges of Kenshiro and Kengoro are similar to those of humans, indicating that these humanoids can achieve flexible human-like postures. In particular, the spherical joints in the shoulder and hip enable joint movements over a wide range. A multijointed spine is a human mimetic joint that enables human-like flexible poses. In the humanoid, a human-like wide range of motion can be achieved because of the human mimetic muscle arrangement. A redundant muscle arrangement

ensures sufficient joint torque near the joint limit, where the stability of the joint tends to decrease because of insufficient constraint force.

## DISCUSSION

### Summary

Here, we described our work on human mimetic humanoids, whose musculoskeletal systems are as close as possible to that of a human. We proceeded with the study based on the idea that the features crucial for improving humanoids are hidden behind the structure and motion processes of humans. Hence, we incorporated elements that facilitate fidelity with the human musculoskeletal system. To realize these humanoid systems, we mimicked human musculoskeletal structures based on our knowledge of anatomy. In terms of the design principles of the human mimetic humanoid, our design centered around four key areas—body proportion, skeletal structure, muscle arrangement, and joint performance—and the humanoids Kenshiro and Kengoro were developed on this basis. We conducted an evaluation of their design by comparing them with humans or existing humanoids and confirmed that the two humanoids have great anatomical fidelity to humans.

### Flexibility or rigidity

A conventional design approach is based on the improvement of rigidity that makes a humanoid rigid and structurally strong. It is better for controlling of humanoids in accurate positions; however, with those approaches, humanoids tend to be bulky. On the other hand, a flexible part in the body, such as the spine, is helpful for producing human-like flexible motions, but it tends to be structurally weak. We think that there is a trade-off between flexibility (weakness) and rigidity (strength). We believe that incorporating flexibility inspired from living things is more important than rigidity to make humanoids more human-like. Therefore, we incorporated flexibility of humans into the structure of our humanoids.

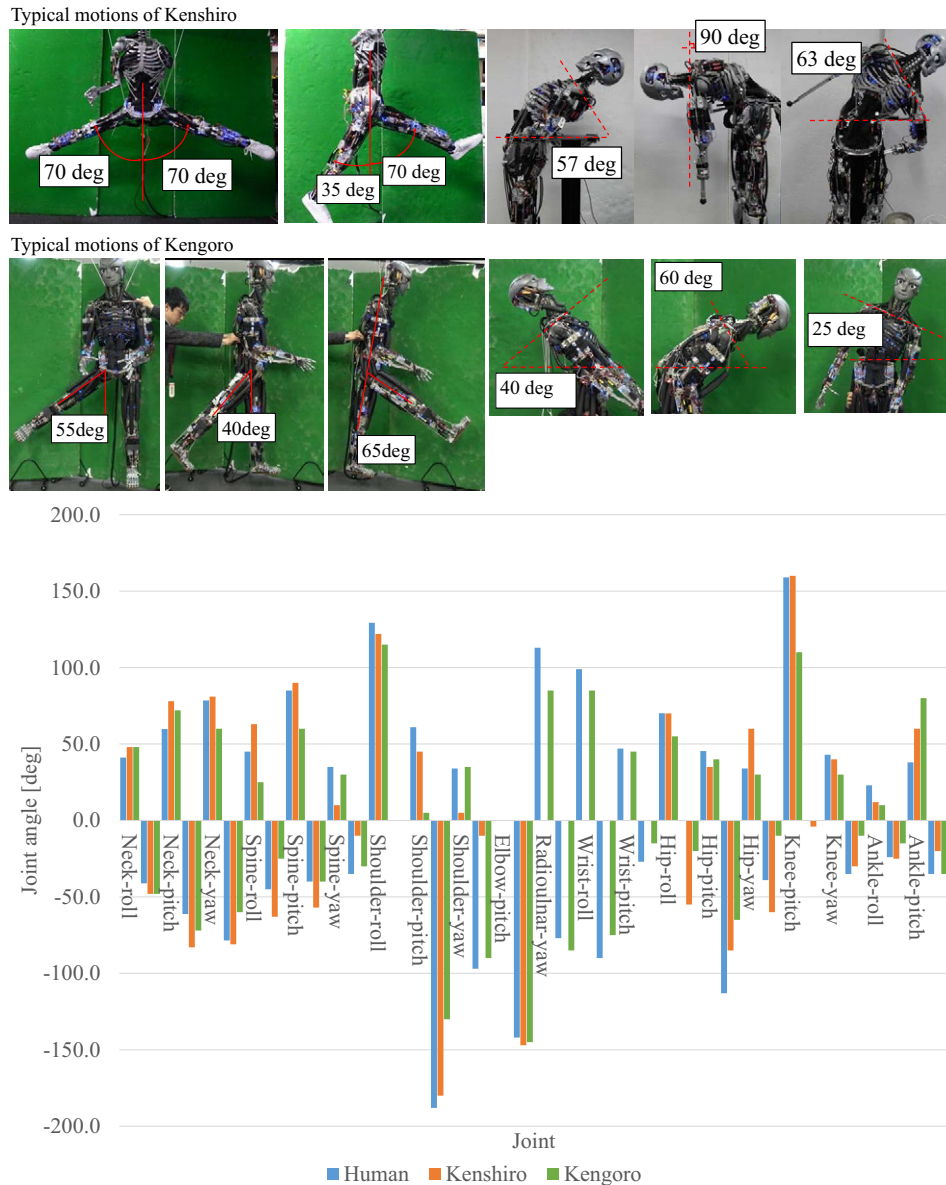


Fig. 3. Joint range comparison of Kenshiro, Kengoro, and an average human.

### Future applications

We believe that human mimetic humanoids have the potential to be used in several new applications that have not been considered previously. For example, human body musculoskeletal simulators can be used to obtain information related to the invisible internal body of humans by evaluating sensory data received from human mimetic humanoids in the real world. This type of simulator can also be used to verify hypotheses regarding human control by applying control programs artificially implemented from the human system, because human mimetic humanoids have structures quite close to those of humans. These tools can be used to provide a deeper understanding of the human mechanism. In addition, other practical applications are also possible. An interesting application is active crash test dummies used during car crash testing, because current dummies can only measure passive behavior. A human mimetic humanoid enables the replication of human reflective behavior by muscle actuation.

One research group has suggested the possibility that a musculoskeletal humanoid can be used in medicine, such as to grow tissue grafts (28). If a humanoid can replicate human movements, then the resulting muscle contribution analysis or sensory data obtained during motion will benefit athletes or sports trainers. In addition, human-shaped robotic limbs are also expected to be used in other fields, such as for artificial limbs or tele-operated human agents.

### MATERIALS AND METHODS

#### Four design principles

We are concentrating on the capability of whole-body motions by our human mimetic humanoids to achieve our goals (for example, a physical musculoskeletal simulator in the real world for motion analysis of humans). To satisfy the requirement and emulate human, similarity of kinematics and dynamics between a human and the humanoid are quite important. We considered comprehensively following factors for developing human mimetic humanoids and decided that the four principles should be our focus.

Similar link lengths and mass distributions (in other words, body proportions) to humans provide similar kinematics and dynamics. Sensory data obtained from those humanoid movements have high correlations to those of humans. In addition, strong similarity also enables these humanoids to fit in the environment for humans, such as using tools, wearing clothes for humans, or getting in a car.

A high degree of anatomical fidelity in skeletal structures is effective for emulating human body characteristics. Human joints are not only single-axis rotation

joints, but also are rolling-sliding joints that are composed of a combination of rotation and sliding movement between the bones (for example, knee joint). Spine joints with multiple vertebrae are effective to make various human-like postures and flexible upper body movement. Human-like multiple DOFs in the entire body are effective for adaptive environmental contact or movement under environmental constraint.

On the basis of the basic equations for tendon-driven robots  $\tau = {}^tGT$  and  $\tau = {}^tJF$  (where  $\tau$  is joint torque,  $T$  is muscle tension,  $F$  is end-effector force,  $G$  is muscle Jacobian, and  $J$  is Jacobian), muscle-joint-operational state mappings are necessary to control musculoskeletal robots. Muscle arrangements are important for deciding those mapping characteristics. Anatomically correct muscle arrangements can provide muscle contribution in correct tendency during the whole-body motions.

Joint performances are related to the above-mentioned three properties and decide humanoid performance in terms of whole-body

motion. Joint range and output power were determined by skeletal structures and by a combination of joint moment arm and muscle output power, respectively. Similar joint range and joint output power are essential for useful analyses of human motions by the humanoid.

### How to design a human mimetic humanoid

To develop a humanoid with human body proportions, the use of statistical data is important. Similar studies were conducted for the development of the HRP4 (20) and HRP4-C (21) humanoids. In our case, the design priority was to achieve bone lengths and limb shapes similar to those of humans. With this priority in mind, the components, muscle actuators, skeletal structure, and electrical components were designed and placed by trial and error.

The skeletal structure of the human mimetic humanoid was designed to imitate the skeletal shape, joint structure, and joint DOFs of humans. During the design process, we first studied human skeletal structures and extracted essential human skeletal mechanisms and functions that were considered useful for humanoids. Then, we simplified the biologically complex human joint structures into mechanical humanoid structures by extracting and focusing on certain functions. In addition, we considered mechanical designs or elements that enabled us to realize the important functions.

To develop a human mimetic humanoid with a human mimetic muscle arrangement, the humanoid should be equipped with as many muscle actuators as possible; however, trade-offs must be considered between the number of muscle actuators and the available design space. To overcome this challenge, we adopted a dense arrangement of muscle actuators. By modularizing the muscle actuators, we were able to effectively implement many muscles in the entire body. Muscle insertion points of the humanoids are decided according to those of humans. However, a muscle expressed by a wire can only emulate just a point insertion, not regional attachment. Planar muscle is adopted to emulate regional attachment or multiple points to more correct emulation of the human.

### Development of Kenshiro

Kenshiro incorporated human mimetic musculoskeletal structures based on the knowledge of human anatomy that we obtained (1, 29–31). Figure 4 shows the body specification of Kenshiro. For Kenshiro development, the target body parameters were those of an around average 13-year-old Japanese male, which is 158 cm and 50 kg. It was important that the body have the multi-DOFs structure of a human because this provides flexibility and adaptability to the environment. Kenshiro was equipped with several unique joints inspired by those of humans, such as multiple spine joints (32), screw-home mechanisms (33), and open-sphere joints (34). The spine joints provide a wide range of motion to the upper body. The screw-home mechanism in the knee provides not only the pitch DOF, but also the yaw DOF that enables the movement of the toe while the femur is under constraint in the sitting posture. The open-sphere joint in the shoulder enables the joint to have a wide range of motion by adhesion of muscle and bones. These structures allowed the robot to achieve human-like behavior and contribute to increased flexibility. The skeletal structure of Kenshiro is mainly made of machined aluminum alloy (A5052). For several parts that require three-dimensional (3D) complex form, we made those parts by 3D printing. For example, covers and blade bone are made of acrylonitrile butadiene styrene (ABS) plastic and stainless steel [420SS, bronze (40%)] respectively. The ribs are made by lost wax casting process with aluminum (AC4C) material.

A muscle actuator is composed of an electrical motor, mechanical parts, a wire, and sensors, which are mechanically assembled and modularized for easy use. We arranged these over the entire body of Kenshiro to achieve muscle arrangements similar to those of humans. Motors are brush-less dc (BLDC), and the output of those is 100 W for almost all muscles and 40 W for narrow parts of the body. Muscle length, tension, and temperature can be obtained from the sensors. The wire in the muscle actuator is wound by a motor to replicate muscle contraction. It is a chemical wire named Dyneema, which is strong against friction. Planar muscles that replicate the planar surface of human muscles were used in the spine and neck joints. In terms of muscle control, the behavior of muscle actuators can be made similar to human muscle behavior by implementing artificial motor controls inspired by the characteristics of human muscles. We also implemented muscle-tendon complex control to provide muscle flexibility (35) and muscle cooperation for sharing load over redundant muscles (36).

Balance control was implemented by using distributed force sensors and human-like joint structures on the body. We implemented a balancing strategy for the musculoskeletal humanoid that relied on muscle tension and the spine (37). To control the musculoskeletal humanoid, a muscle Jacobian that expresses the relationship between muscle length and joint angle is necessary. A machine learning-based approach to obtain the muscle Jacobian was proposed, and it enabled bidirectional conversion between the muscle length and joint angle (38). To overcome large robot-model errors, learning using real sensor data, but not simulation data, is preferable.

### Development of Kengoro

In the design process of Kengoro, we adopted the idea of multi-functional skeletal structures to achieve both humanoid performance and human-like proportions and devised sensor-driver-integrated muscle modules for improved muscle control. Figure 5 shows the body specifications of Kengoro. To demonstrate the effectiveness of these body structures, we conducted several preliminary movements using Kengoro.

Kengoro is the successor version of Kenshiro and is also a human mimetic humanoid designed with anatomical fidelity to humanoids (39). One of the design goals of Kengoro was to achieve actions involving contact with the environment that required a flexible body and adaptability to the environment. Thus, multi-DOFs in not only the spine, but also in end effectors are important, because humans naturally contact the environment with their hands and feet. On this basis, Kengoro was equipped with human mimetic five-fingered hands and feet. The foot has multi-DOFs and multisensors to facilitate natural adaptation to the ground (40). The toe actuation was powerful enough to perform tip-toe standing with support by hands for balancing. The toe is actuated by a muscle connected to a 90-W motor placed on the lower leg link. In addition, the hand can hold the weight of its body, because a large grasping force can be generated by the muscles in its forearm (41). The forearm is composed of a radio-ulnar joint with a tilted joint axis and expands the variety of possible hand motions, such as that in sports or dexterous tasks (42). From a physiological point of view, a skeletal structure with artificial perspiration was developed to release the heat of the motors (43). The skeletal structure of Kengoro is composed of a combination of extra super duralumin (A7075) and carbon fiber-reinforced plastic for more strength and lightness. Several parts of the body, such as the outer cover, were made by 3D printing, as with Kenshiro. LiFe batteries were embedded into the skeletal structures of legs, and they enabled movement for about 20 min without any power cables.

*Human mimetic humanoid "Kenshiro" (2012-)*

Specification  
 Height: 160 [cm]  
 Weight: 51.9 [kg]  
 DOFs: 64  
 Muscle actuators: 87

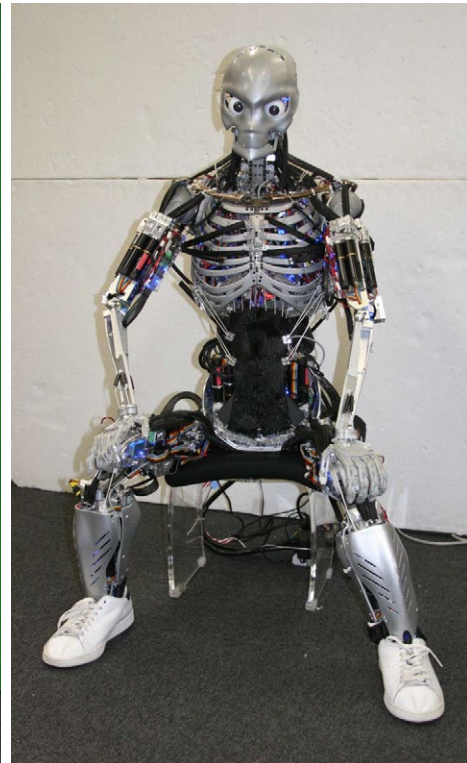
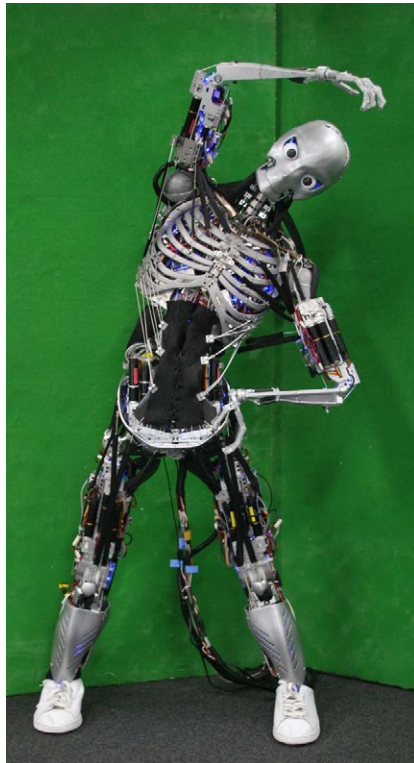
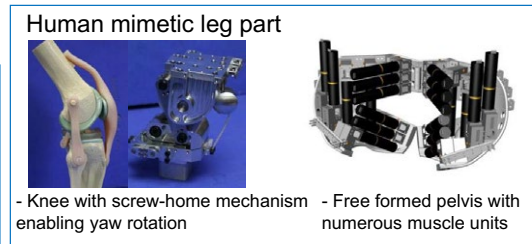
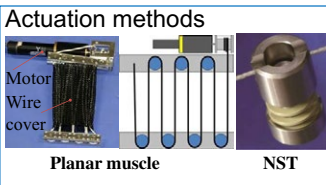
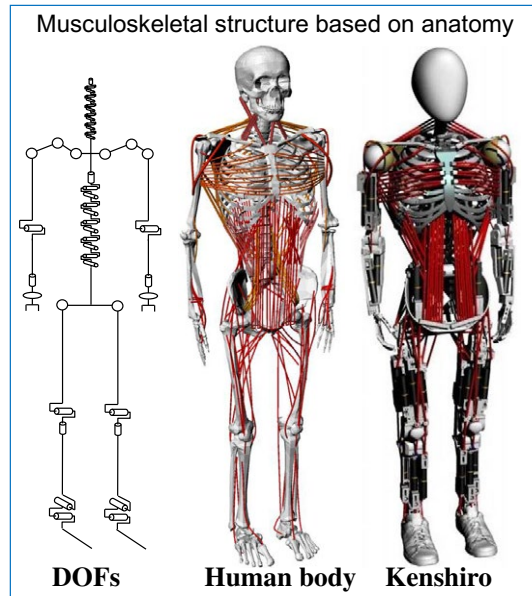
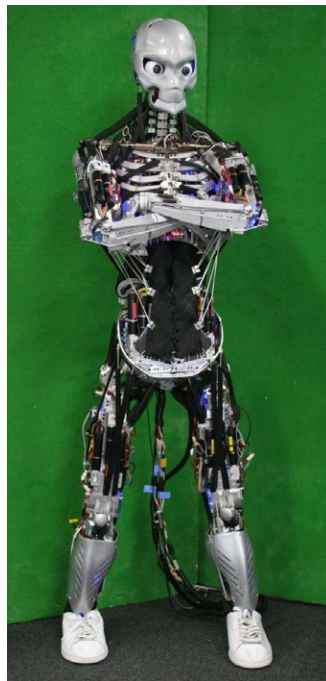
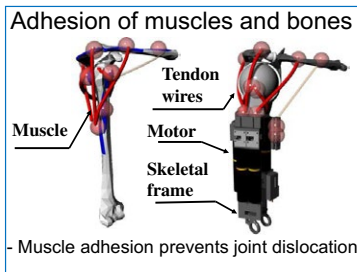
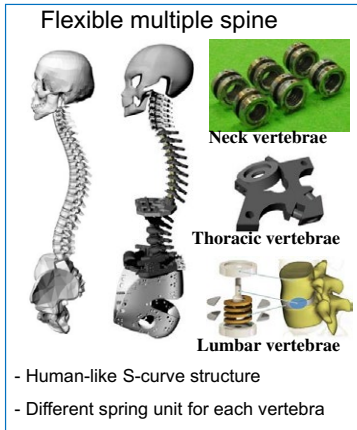


Fig. 4. Human mimetic humanoid Kenshiro.

### Human mimetic humanoid “Kengoro” (2016-)



Fig. 5. Human mimetic humanoid Kengoro.

Muscle control using force was achieved using two types of sensor-driver-integrated muscle modules (42, 44). This is an all-in-one integrated module composed of electrical motor, motor driver, and sensors for force control. Motors were BLDC and those outputs were 90, 100, or 120 W for fundamental muscles. For narrow parts of the body, such as the forearm, 60-W BLDC motors were adopted. The use of this module provided active flexibility to Kengoro. Not only muscle space, but also joint-space torque controller for flexible and adaptive environmental contact was implemented (45). On the basis of human reciprocal innervation that suppresses co-contraction in muscle antagonism, we implemented antagonist inhibition control that contributed to arm movement in a wide range of motions (46).

## SUPPLEMENTARY MATERIAL

robotics.sciencemag.org/cgi/content/full/2/13/eaq0899/DC1

movie S1. Movements of Kengoro.

movie S2. Motion comparison between Kenshiro and Kengoro.

## REFERENCES AND NOTES

1. Y. Nakanishi, S. Ohta, T. Shirai, Y. Asano, T. Kozuki, Y. Kakehashi, H. Mizoguchi, T. Kurotobi, Y. Motegi, K. Sasabuchi, J. Urata, K. Okada, I. Mizuuchi, M. Inaba, Design approach of biologically-inspired musculoskeletal humanoids. *Int. J. Adv. Robot. Syst.* **10**, 1–13 (2013).
2. M. Inaba, I. Mizuuchi, R. Tajima, T. Yoshikai, D. Sato, K. Nagashima, H. Inoue, Building spined muscle-tendon humanoid. *Robot. Res.* **6**, 113–127 (2003).
3. I. Mizuuchi, T. Yoshikai, Y. Sodeyama, Y. Nakanishi, A. Miyadera, T. Yamamoto, T. Niemela, M. Hayashi, J. Urata, Y. Namiki, T. Nishino, M. Inaba, Development of musculoskeletal humanoid Kotaro, in *Proceedings of the 2006 IEEE International Conference on Robotics and Automation* (IEEE, 2006), pp. 82–87.
4. I. Mizuuchi, Y. Nakanishi, Y. Sodeyama, Y. Namiki, T. Nishino, N. Muramatsu, J. Urata, K. Hongo, T. Yoshikai, M. Inaba, An advanced musculoskeletal humanoid Kojiro, in *Proceedings of the 2007 7th IEEE-RAS International Conference on Humanoid Robots* (IEEE, 2007), pp. 294–299.
5. Y. Nakanishi, T. Izawa, M. Osada, N. Ito, S. Ohta, J. Urata, M. Inaba, Development of musculoskeletal humanoid Kenzoh with mechanical compliance changeable tendons by nonlinear spring unit, in *Proceedings of the 2011 IEEE International Conference on Robotics and Biomimetics* (IEEE, 2011), pp. 2384–2389.
6. O. Holland, R. Knight, The anthropomimetic principle, in *Proceedings of the AISB06 Symposium on Biologically Inspired Robotics* (2006), pp. 1–8.
7. D. Gamez, R. Newcombe, O. Holland, R. Knight, Two simulation tools for biologically inspired virtual robotics (2006), in *Proceedings of the IEEE 5th Chapter Conference on Advances in Cybernetic Systems* (IEEE, 2006), pp. 85–90.
8. H. Gravato Marques, M. Jantsch, S. Wittmeier, O. Holland, C. Alessandro, A. Diamond, M. Lungarella, Rob Knight, ECCE1: The first of a series of anthropomimetic musculoskeletal upper torsos, in *Proceedings of the 2010 IEEE-RAS International Conference on Humanoid Robots* (IEEE, 2010), pp. 391–396.
9. A. Diamond, R. Knight, D. Devereux, O. Holland, Anthropomimetic robots: Concept, construction and modelling. *Int. J. Adv. Robot. Syst.* **9**, 1–14 (2012).
10. S. Wittmeier, C. Alessandro, N. Bascarevic, K. Dalamagkidis, D. Devereux, A. Diamond, M. Jantsch, K. Jovanovic, R. Knight, H. G. Marques, P. Milosavljevic, B. Mitra, B. Svetozarevic, V. Potkonjak, R. Pfeifer, A. Knoll, O. Holland, Towards anthropomimetic robotics: Development, simulation, and control of a musculoskeletal torso. *Artif. Life* **19**, 171–193 (2013).
11. M. Jantsch, C. Schmalzer, S. Wittmeier, K. Dalamagkidis, A. Knoll, A scalable joint-space controller for musculoskeletal robots with spherical joints, in *Proceedings of the 2011 IEEE International Conference on Robotics and Biomimetics* (IEEE, 2011), pp. 2211–2216.
12. M. Jantsch, S. Wittmeier, K. Dalamagkidis, A. Panos, F. Volkart, A. Knoll, Anthrob - A printed anthropomimetic robot in *Proceedings of the 2013 13th IEEE-RAS International Conference on Humanoid Robots* (IEEE, 2013), pp. 342–347.
13. M. Kouchi, M. Mochimaru, H. Iwasawa, S. Mitani, Anthropometric database for Japanese population 1997-98 *Japanese Industrial Standards Center* (AIST, MITI, 2000).
14. M. Kouchi, M. Mochimaru, 2006: AIST/HQL human size-shape database 2003 (AIST H18PRO-503, 2006).
15. Y. Nakamura, K. Yamane, G. Suwa, O. Kondou, M. Kouchi, K. Kawachi, M. Mochimaru, 2008: Skeletal shape data of adult male (AIST H20PRO-905, 2008).
16. MEXT. Statistical data of junior high school students H24, 2012.
17. D. A. Neumann, *Kinesiology of the Musculoskeletal System: Foundations for Physical Rehabilitation*, (Mosby, 2002).
18. K. Akachi, T. Isozumi, M. Hirata, S. Ohta, M. Ishizaki, "Development of the Humanoid Robot, HRP-2" (in Japanese) (Technical Report Kawada Gihou Vol. 23, 2004).
19. K. Kaneko, K. Harada, F. Kanehiro, G. Miyamori, K. Akachi, Humanoid Robot HRP-3, in *Proceedings of the 2008 IEEE/RSJ International Conference on Intelligent Robots and Systems* (IEEE, 2008), pp. 2471–2478.
20. K. Kaneko, K. Akachi, F. Kanehiro, G. Miyamori, M. Morisawa, A. Hayashi, N. Kanehiro, Humanoid robot HRP-4-humanoid robotics platform with lightweight and slim body, in *Proceedings of the 2011 IEEE/RSJ International Conference on Intelligent Robots and Systems* (IEEE, 2011), pp. 4400–4407.
21. K. Kaneko, F. Kanehiro, M. Morisawa, K. Miura, S. Nakaoka, S. Kajita, Cybernetic human HRP-4C, in *Proceedings of the 2009 9th IEEE-RAS International Conference on Humanoid Robots* (IEEE, 2009), pp. 7–14.
22. Y. Ogura, H. Aikawa, K. Shimomura, A. Morishima, H.-o. Lim, A. Takanishi, Development of a new humanoid robot WABIAN-2, in *Proceedings of the 2006 IEEE International Conference on Robotics and Automation* (IEEE, 2006), pp. 76–81.
23. M. Hirose, K. Ogawa, Honda humanoid robots development. *Philos. Trans. A Math. Phys. Eng. Sci.* **365**, 11–19 (2007).
24. M. Fallon, S. Kuindersma, S. Karumanchi, M. Antone, T. Schneider, H. Dai, C. Porez D'Arpino, R. Deits, M. DiCiccio, D. Fourie, T. Koolen, P. Marion, M. Posa, A. Valenzuela, K.-T. Yu, J. Shah, K. Iagnemma, R. Tedrake, S. Teller, "An architecture for online affordance-based perception and whole-body planning." (Technical Report MIT-CSAIL-TR-2014-003, MIT Computer Science and Artificial Intelligence Lab. CSAIL, 2014).
25. I.-W. Park, J.-Y. Kim, J. Lee, J.-H. Oh, Mechanical design of humanoid robot platform KHR-3(KAIST humanoid robot - 3: HUBO), in *Proceedings of the 2005 5th IEEE-RAS International Conference on Humanoid Robots* (IEEE, 2005), pp. 321–326.
26. A. D. Glanville, G. Kreezer, The maximum amplitude and velocity of joint movements in normal male human adults. *Human Biol.* **9**, 197–211 (1937).
27. W. T. Dempster, "Space requirements of the seated operator." (Technical Report WADC-TR-55-159, Wright-Patterson Air Force Base, 1955).
28. P.-A. Mouthuy, A. Carr, Growing tissue grafts on humanoid robots: A future strategy in regenerative medicine? *Sci. Robot.* **2**, eaam5666 (2017).
29. Y. Nakanishi, Y. Asano, T. Kozuki, H. Mizoguchi, Y. Motegi, M. Osada, T. Shirai, J. Urata, K. Okada, M. Inaba, Design concept of detail musculoskeletal humanoid "Kenshiro" - toward a real human body musculoskeletal simulator, in *Proceedings of the 2012 12th IEEE-RAS International Conference on Humanoid Robots* (IEEE, 2012), pp. 1–6.
30. Y. Asano, H. Mizoguchi, T. Kozuki, Y. Motegi, M. Osada, J. Urata, Y. Nakanishi, K. Okada, M. Inaba, Lower thigh design of detailed musculoskeletal humanoid "Kenshiro", in *Proceedings of the 2012 IEEE/RSJ International Conference on Intelligent Robots and Systems* (IEEE, 2012), pp. 4367–4372.
31. T. Kozuki, H. Mizoguchi, Y. Asano, M. Osada, T. Shirai, U. Junichi, Y. Nakanishi, K. Okada, M. Inaba, Design methodology for thorax and shoulder of human mimetic musculoskeletal humanoid Kenshiro - a thorax with rib like surface, in *Proceedings of the 2012 IEEE/RSJ International Conference on Intelligent Robots and Systems* (IEEE, 2012), pp. 3687–3692.
32. T. Kozuki, M. Yotaro, K. Kawasaki, Y. Asano, T. Shirai, S. Ookubo, Y. Kakiuchi, K. Okada, M. Inaba, Development of musculoskeletal spine structure that fulfills great force requirement in upper body kinematics, in *Proceedings of the 2015 IEEE/RSJ International Conference on Intelligent Robots and Systems* (IEEE, 2015), pp. 2768–2773.
33. Y. Asano, H. Mizoguchi, T. Kozuki, Y. Motegi, J. Urata, Y. Nakanishi, K. Okada, M. Inaba, Achievement of twist squat by musculoskeletal humanoid with screw-home mechanism, in *Proceedings of the 2013 IEEE/RSJ International Conference on Intelligent Robots and Systems* (IEEE, 2013), pp. 4649–4654.
34. T. Kozuki, Y. Motegi, T. Shirai, Y. Asano, J. Urata, Y. Nakanishi, K. Okada, M. Inaba, Design of upper limb by adhesion of muscles and bones—Detail human mimetic musculoskeletal humanoid Kenshiro, in *Proceedings of the 2013 IEEE/RSJ International Conference on Intelligent Robots and Systems* (IEEE, 2013), pp. 935–940.
35. T. Kozuki, T. Shirai, Y. Asano, Y. Motegi, Y. Kakiuchi, K. Okada, M. Inaba, Muscle-tendon complex control by "tension controlled muscle" and "non-linear spring ligament" for real world musculoskeletal body simulator Kenshiro, in *Proceedings of the 2014 IEEE International Conference on Biomedical Robotics and Biomechanics* (IEEE, 2014), pp. 875–880.
36. Y. Asano, T. Shirai, T. Kozuki, Y. Motegi, Y. Nakanishi, K. Okada, M. Inaba, Motion generation of redundant musculoskeletal humanoid based on robot-model error compensation by muscle load sharing and interactive control device, in *Proceedings of the 2013 IEEE-RAS International Conference on Humanoid Robots* (IEEE, 2013), pp. 336–341.
37. Y. Asano, S. Ookubo, T. Kozuki, T. Shirai, K. Kimura, S. Nozawa, Y. Kakiuchi, K. Okada, M. Inaba, Spine balancing strategy using muscle ZMP on musculoskeletal humanoid Kenshiro, in *Proceedings of the 2015 International Symposium on Robotics Research* (Springer, 2015), pp. 1–16.

38. S. Ookubo, Y. Asano, T. Kozuki, T. Shirai, K. Okada, M. Inaba, Learning nonlinear muscle-joint state mapping toward geometric model-free tendon driven musculoskeletal robots, in *Proceedings of the 2015 IEEE-RAS International Conference on Humanoid Robots* (IEEE, 2015), pp. 765–770.
39. Y. Asano, T. Kozuki, S. Ookubo, M. Kawamura, S. Nakashima, T. Katayama, I. Yanokura, T. Hirose, K. Kawaharazuka, S. Makino, Y. Kakiuchi, K. Okada, M. Inaba, Human mimetic musculoskeletal humanoid Kengoro toward real world physically interactive actions, in *Proceedings of the 2016 IEEE-RAS International Conference on Humanoid Robots* (IEEE, 2016), pp. 876–883.
40. Y. Asano, S. Nakashima, T. Kozuki, S. Ookubo, I. Yanokura, Y. Kakiuchi, K. Okada, M. Inaba, Human mimetic foot structure with multi-DOFs and multi-sensors for musculoskeletal humanoid Kengoro, in *Proceedings of the 2016 IEEE/RSJ International Conference on Intelligent Robots and Systems* (IEEE, 2016), pp. 2419–2424.
41. S. Makino, K. Kawaharazuka, M. Kawamura, Y. Asano, K. Okada, M. Inaba, High-power, flexible, robust hand: Development of musculoskeletal hand using machined springs and realization of self-weight supporting motion with humanoid, in *Proceedings of the 2017 IEEE/RSJ International Conference on Intelligent Robots and Systems* (IEEE, 2017), pp. 1187–1192.
42. K. Kawaharazuka, S. Makino, M. Kawamura, Y. Asano, K. Okada, M. Inaba, Human mimetic forearm design with radioulnar joint using miniature bone-muscle modules and its applications, in *Proceedings of the 2017 IEEE/RSJ International Conference on Intelligent Robots and Systems* (IEEE, 2017), pp. 4956–4962.
43. T. Kozuki, H. Toshinori, T. Shirai, S. Nakashima, Y. Asano, Y. Kakiuchi, K. Okada, M. Inaba, Skeletal structure with artificial perspiration for cooling by latent heat for musculoskeletal humanoid Kengoro, in *Proceedings of the 2016 IEEE/RSJ International Conference on Intelligent Robots and Systems* (IEEE, 2016), pp. 2135–2140.
44. Y. Asano, T. Kozuki, S. Ookubo, K. Kawasaki, T. Shirai, K. Kimura, K. Okada, M. Inaba, A sensor-driver integrated muscle module with high-tension measurability and flexibility for tendon-driven robots, in *Proceedings of the 2015 IEEE/RSJ International Conference on Intelligent Robots and Systems* (IEEE, 2015), pp. 5960–5965.
45. M. Kawamura, S. Ookubo, Y. Asano, T. Kozuki, K. Okada, M. Inaba, A joint-space controller based on redundant muscle tension for multiple DOF joints in musculoskeletal humanoids, in *Proceedings of the 2016 IEEE-RAS International Conference on Humanoid Robots* (IEEE, 2016), pp. 814–819.
46. K. Kawaharazuka, S. Makino, M. Kawamura, Y. Asano, K. Okada, M. Inaba, Antagonist inhibition control in redundant tendon-driven structures based on human reciprocal innervation for wide range limb motion of musculoskeletal humanoids. *IEEE Robot. Autom. Lett.* **2**, 2119–2126 (2017).
47. D. A. Winter, *Biomechanics and Motor Control of Human Movement* (John Wiley & Sons, Inc., ed. 4, 2009).
48. R. Drillis, R. Contini, “Body segment parameters” (Technical Report 1166–03, New York University, School of Engineering and Science, Research Division, New York under contract with Office of Vocational Rehabilitation, Department of Health, Education and Welfare, September 1966).
49. L. K. Osterkamp, Current perspective on assessment of human body proportions of relevance to amputees. *J. Am. Diet. Assoc.* **95**, 215–218 (1995).
50. C. E. Clauser, J. T. McConville, J. W. Young, “Weight, volume, and center of mass of segments of the human body” (Technical Report AMRL-TR-69-70, US Air Force, Wright-Patterson Air Force Base, Ohio, August 1969).
51. R. Niiyama, S. Nishikawa, Y. Kuniyoshi, Athlete robot with applied human muscle activation patterns for bipedal running, in *Proceedings of the 2010 IEEE-RAS International Conference on Humanoid Robots* (IEEE, 2010), pp. 498–503.
52. K. Ogawa, K. Narioka, K. Hosoda, Development of whole-body humanoid “Pneumat-BS” with pneumatic musculoskeletal system, in *Proceedings of the 2011 IEEE/RSJ International Conference on Intelligent Robots and Systems* (IEEE, 2011), pp. 4838–4843.

**Acknowledgments:** We thank the members of the Jouhou System Kougaku (JSK) robotics laboratory in the University of Tokyo, to which the authors belong. We thank all who were involved with the development of Kenshiro and Kengoro. In particular, T. Kozuki, Y. Nakanishi, S. Ookubo, M. Osada, H. Mizoguchi, Y. Motegi, S. Nakashima, T. Katayama, M. Kawamura, K. Kawaharazuka, S. Makino, A. Fujii, T. Makabe, and M. Onitsuka were deeply involved with the development. We extend our appreciation to collaborators of the development: K. Kawasaki, T. Shirai, K. Kimura, K. Sasabuchi, I. Yanokura, T. Kurotobi, M. Sugiura, T. Hirose, J. Urata, and Y. Kakiuchi. **Funding:** This work was partially supported by Japan Society for the Promotion of Science KAKENHI grant numbers 21220004, 26220003, and 16H06723. **Author contributions:** Y.A. investigated the proposed approach, developed the Kenshiro and Kengoro hardware, implemented the related software, performed the experiments with colleagues, wrote the paper, and directed this research. K.O. provided assistance in implementing the software system, maintained the infrastructure software used in this research, and provided forward-looking advice. M.I. assisted by investigating the key idea of this research, provided the environment for conducting this research, and provided forward-looking advice. **Competing interests:** A patent (no. P2017-144512A) related to this work has been submitted to the Japan Patent Office. The authors declare that they have no other competing interests. **Data and materials availability:** All data needed to evaluate the study are available in the paper. Please contact Y. Asano for other data and materials.

Submitted 30 September 2017

Accepted 6 December 2017

Published 20 December 2017

10.1126/scirobotics.aaq0899

**Citation:** Y. Asano, K. Okada, M. Inaba, Design principles of a human mimetic humanoid: Humanoid platform to study human intelligence and internal body system. *Sci. Robot.* **2**, eaaq0899 (2017).

## SOFT ROBOTS

# A soft robot that navigates its environment through growth

Elliot W. Hawkes,<sup>1,2,\*</sup> Laura H. Blumenschein,<sup>2</sup> Joseph D. Greer,<sup>2</sup> Allison M. Okamura<sup>2</sup>

Across kingdoms and length scales, certain cells and organisms navigate their environments not through locomotion but through growth. This pattern of movement is found in fungal hyphae, developing neurons, and trailing plants, and is characterized by extension from the tip of the body, length change of hundreds of percent, and active control of growth direction. This results in the abilities to move through tightly constrained environments and form useful three-dimensional structures from the body. We report a class of soft pneumatic robot that is capable of a basic form of this behavior, growing substantially in length from the tip while actively controlling direction using onboard sensing of environmental stimuli; further, the peak rate of lengthening is comparable to rates of animal and robot locomotion. This is enabled by two principles: Pressurization of an inverted thin-walled vessel allows rapid and substantial lengthening of the tip of the robot body, and controlled asymmetric lengthening of the tip allows directional control. Further, we demonstrate the abilities to lengthen through constrained environments by exploiting passive deformations and form three-dimensional structures by lengthening the body of the robot along a path. Our study helps lay the foundation for engineered systems that grow to navigate the environment.

## INTRODUCTION

Growth as a method for navigating the environment is found in fungal hyphae with diameters as small as a few micrometers (1) as well as in vines with girths as large as a meter (2–4). These organisms grow from their tips, increase length hundreds of times, and continually control growth direction based on environmental stimuli. Because lengthening from the tip, or apical extension, involves no relative movement of the body with respect to the environment, the body can lengthen along constrained paths without friction from sliding against the environment (Fig. 1A). Further, because each movement of the tip results in a directionally controlled lengthening of the body, the body forms into a three-dimensional (3D) structure along the path of the tip. These capabilities enable natural cells and organisms to grow through tightly packed tissue or abiotic materials and form structures with functions ranging from signal pathways to conduits for delivery (Fig. 1B) (5–7).

Although roboticists have successfully recreated movement through the environment using locomotion, defined as the translation of the body from one location to another (8)—flying (9), running (10), swimming (11, 12), cytoplasmic streaming (13), slithering (14), and leaping (15)—navigating the environment through growth is challenging in artificial systems. The work on soft continuum manipulators (16–20) and tendril-like robots (21, 22) has laid a foundation that has been built upon by the recent development of root-inspired robots and endoscopes that either enter a new part of the environment without changing length (23, 24) or extend one to five body lengths by adding material at rates of 1 to 10 mm/min to move through granular media (25, 26). However, tip-based length change on the order of thousands of percent with directional control at rates comparable to those of animal locomotion is still an open challenge.

We describe two principles that help enable a basic recreation of this behavior in an artificial system. First, an inverted, compliant, thin-walled

vessel will lengthen from the tip by everting when pressurized. We present our implementation of this principle, and report results showing lengthening at the tip with length change of thousands of percent, and speeds comparable to animal locomotion. Second, the tip of the vessel steers along a path when the relative lengths of the sides of the vessel are controlled while everting. We present our implementation of this principle and show results of a soft robot lengthening toward a light, autonomously controlling direction with feedback from an onboard camera at the tip. Last, we show examples of the abilities of this type of robot body, demonstrating navigation through constrained environments and the formation of structures from the lengthening body.

## RESULTS

The first principle, which is based on the eversion of a thin membrane driven by internal pressure, enables lengthening at the tip with substantial elongation and at a relatively high speed. The internal pressure forces the inverted material to evert at the tip while pulling more material from the base through the core of the body (Fig. 2A). This principle is used to deploy invaginated appendages by a variety of invertebrates such as the *Sipunculus nudus*, which everts a proboscis for defense (27). An analog of this method of lengthening, continuous eversion as found in cytoplasmic streaming, is the inspiration for robotic whole-skin locomotion (13). In our system, we implement the principle with a thin membrane of polyethylene driven by a pneumatic pump that pressurizes the interior of the soft robot body (Fig. 2, A and B, and movie S1). The design is scalable; wall stresses remain constant during geometric scaling of a thin-walled vessel, meaning that the ratio of wall thickness to diameter can be maintained. We have tested diameters ranging from 1.8 mm to 36 cm (some shown in movies S3 and S4). The thin-walled, pressurized design enables not only lengthening at the tip but also substantial length change: Very little volume of precursor wall material results in a very large volume of pressurized body. Further, unlike lengthening invertebrates, we store the precursor material in a spool, allowing length change to be

<sup>1</sup>Department of Mechanical Engineering, University of California, Santa Barbara, CA 93106, USA. <sup>2</sup>Department of Mechanical Engineering, Stanford University, Stanford, CA 94305, USA.

\*Corresponding author. Email: ewhawkes@engineering.ucsb.edu

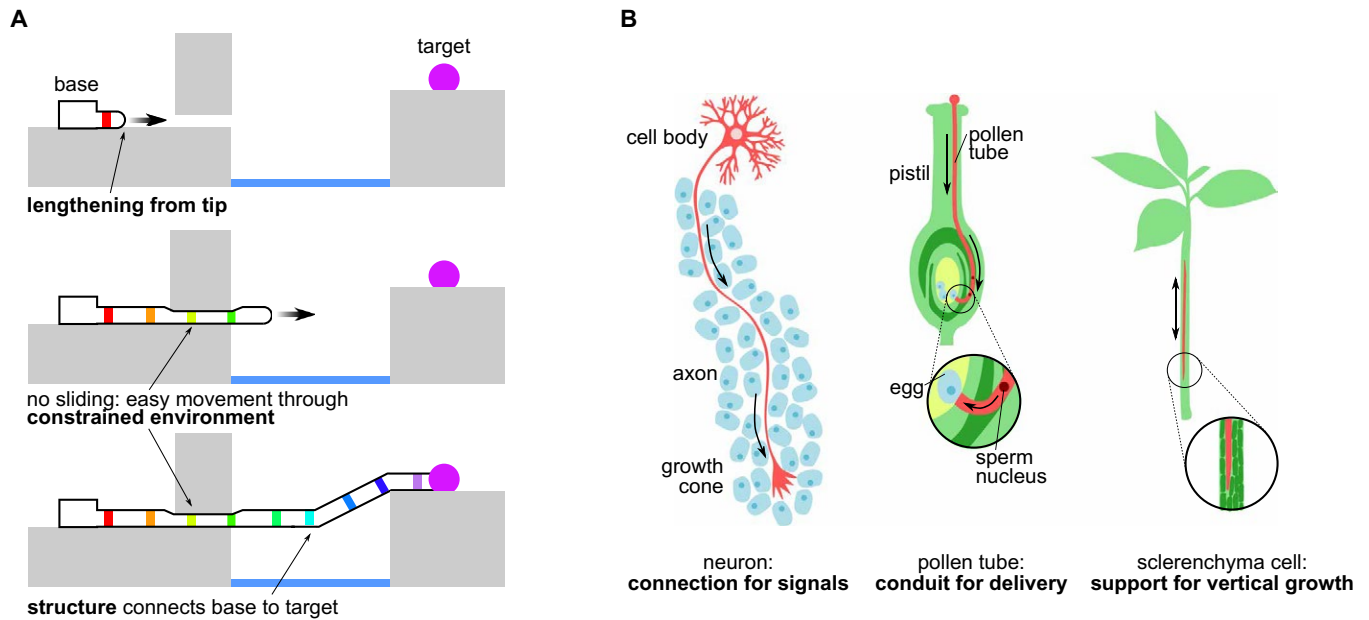


**Fig. 1. Substantial lengthening from the tip with directional control enables a body to pass through a constrained environment and create a structure along its path of growth.** (A) A body lengthens from its tip toward a target. Because only the tip moves, there is no relative movement of the body with respect to the environment (colored bands do not move). This results in the capability to move with no sliding friction through a constrained environment. As the tip moves, the body forms into a structure in the shape of the tip's path. (B) Examples of biological systems that grow to navigate their environments. Neurons grow through constrained tissue to create structures that act as signal pathways. Pollen tubes lengthen through pistil tissue to build conduits to deliver sperm to the ovary. Sclerenchyma cells grow within the xylem and phloem to create supporting structures.

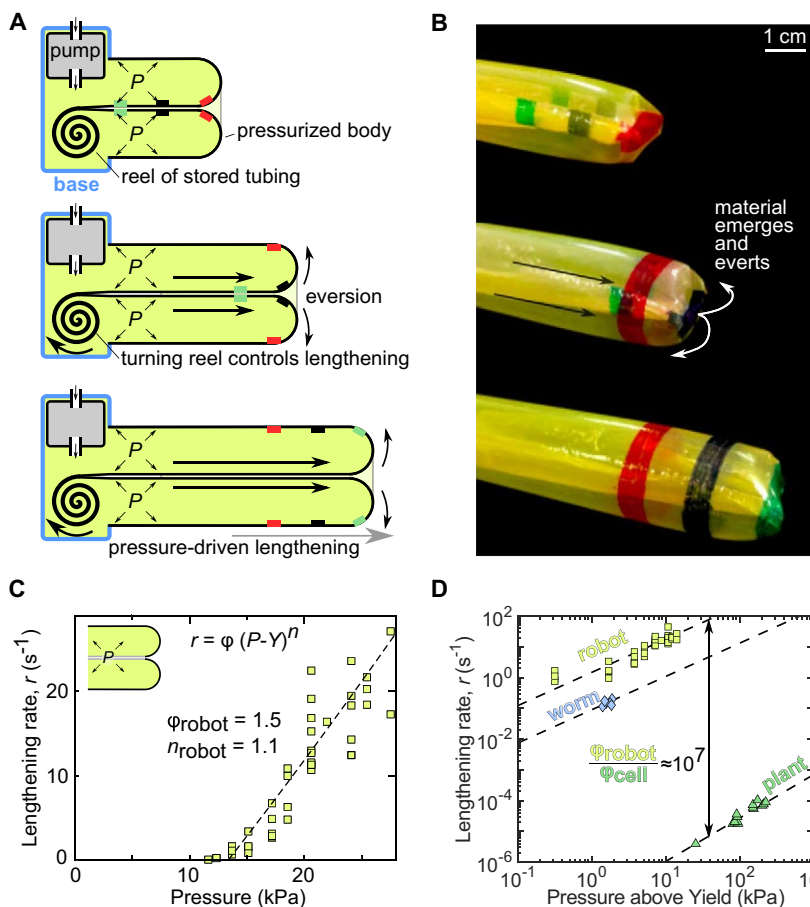


**Fig. 2. Principle of pressure-driven eversion enables lengthening from the tip at rates much higher than those found in plant cell growth.** (A) Implementation of principle in a soft robot. A pump pressurizes the body, which lengthens as the material everts at the tip. This material, which is compacted and stored on a reel in the base, passes through the core of the body to the tip; the rotation of the reel controls the length of the robot body. (B) Images of the lengthening body. The body diameter is 2.5 cm. (C) The relationship between lengthening rate ( $r$ ) and internal pressure ( $P$ ) shows a characteristic viscoplastic behavior: no extension below a yield pressure ( $Y$ ) followed by a monotonic relationship between rate and pressure with a power term ( $n$ ) close to 1. (D) Data show the relationship between rate and pressure above yield for the soft robot, worms with an everting proboscis (*S. nudus*), and a plant cell (*Nitella mucronata*). The extensibility  $\phi$  (inverse viscosity) of a soft robot body is roughly seven orders of magnitude higher than that of the plant cell, resulting in a lengthening rate that is roughly five orders of magnitude higher. The extensibility of the soft robot body is slightly higher than the worm, which uses the same principle for lengthening.

much greater than the 100% length change seen in these creatures. Although the number of turns that the soft robot body makes affects the maximum length (Supplementary Text and fig. S2), on paths with only a few turns, our system, initially 28 cm, has extended to a length of 72 m, limited by the amount of the plastic membrane on the spool (movie S1).

This principle of lengthening based on pressure-driven eversion also results in relatively fast lengthening, especially when compared to organisms that use growth to

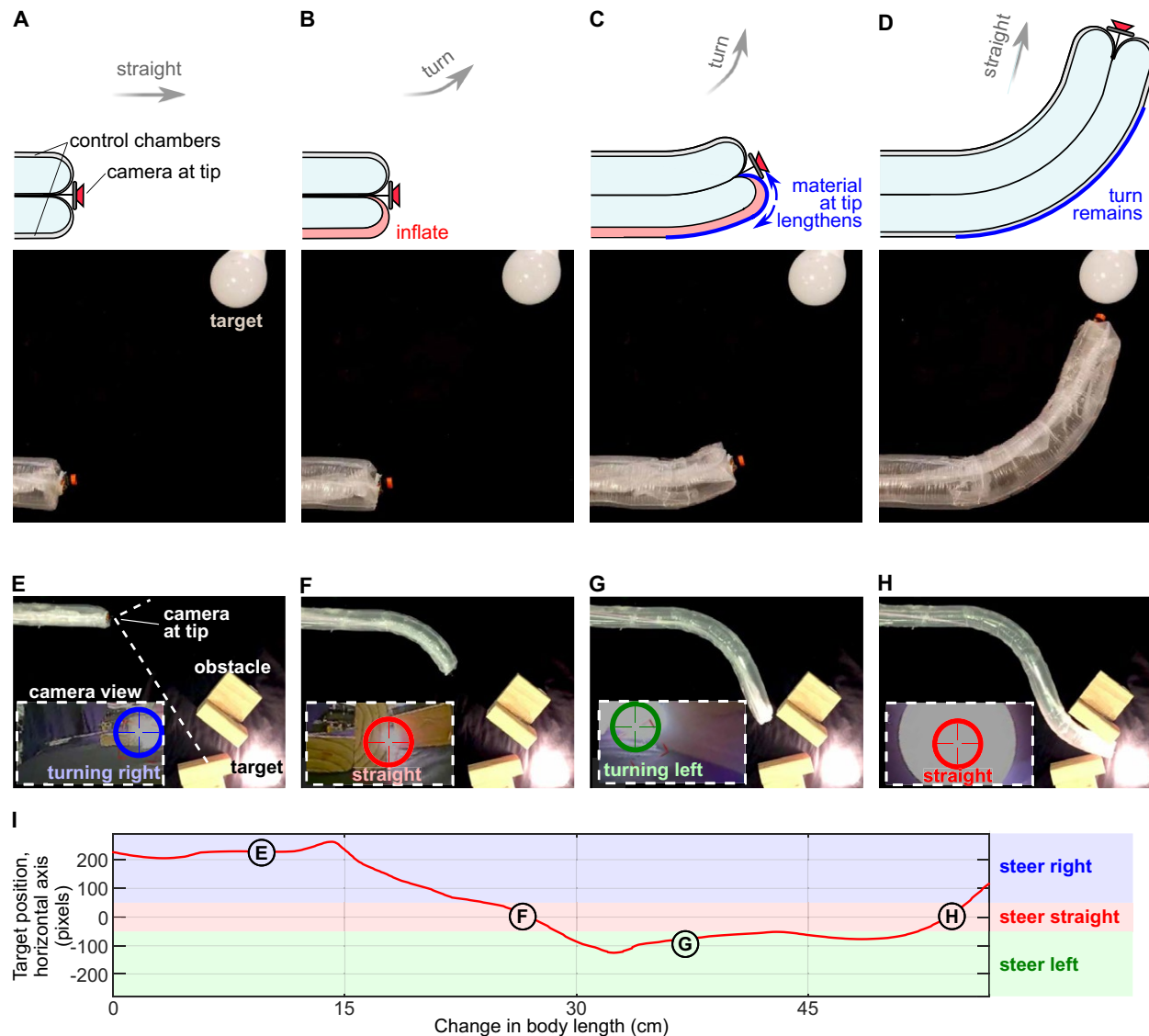


**Fig. 3. Principle of asymmetric lengthening of tip enables active steering.** (A) Implementation in a soft robot uses small pneumatic control chambers and a camera mounted on the tip for visual feedback of the environment. The camera is held in place by a cable running through the body of the robot. (B) To queue an upward turn, the lower control chamber is inflated. (C) As the body grows in length, material on the inflated side lengthens as it everts, resulting in an upward turn (see Materials and Methods and Fig. 5 for details). (D) Once the chamber is deflated, the body again lengthens along a straight path, and the curved section remains. (E) A soft robot can navigate toward light using a tip-mounted camera. Inset: The view from the camera shows the target to the right. Electronically controlled solenoid valves inflate the control chamber on the left side of the robot body, resulting in the tip reorienting to the right and forming a right turn. (F) The target is straight ahead, and the robot steers straight. (G) The target is to the left, and the robot steers left. (H) The robot reaches the target. (I) Position of the target along the horizontal axis of the camera as the robot lengthens toward the target.

navigate their environments, such as certain fungi and plants. To understand the behavior of the rate of lengthening in our system, we measured the rate as we varied the internal pressure (Fig. 3C). Because of the energy losses caused by everting the membrane, we see a behavior characteristic of a Bingham plastic, in which there is a minimum required pressure before yield, and a monotonic relationship between the rate of lengthening and pressure (28). This is the same behavior observed in growing plant cells, which soften and then stretch because of internal pressure before new material is added to rethicken the walls (29–32). In plants, the relationship between rate and pressure is described using an inverse viscosity, termed “extensibility,”  $\phi$  (fig. S5; see Supplementary Text for

discussion) (33, 34). Our system has an extensibility that is seven orders of magnitude higher than in plants and only one order of magnitude higher than in invertebrates that use the same mechanism of lengthening (Fig. 3, C and D). Our peak bursting pressure is lower than that in a plant cell, resulting in a maximum rate of lengthening roughly five orders of magnitude higher than that in plant cells, with a maximum speed over short distances of 10 m/s. Although our implementation allows for considerably faster tip movement than that of natural cells, real-time branching, as seen in fungal hyphae in a mycelium (1, 35), is not currently possible. However, a handful of preset branches are possible (fig. S4), and because the robot body is inexpensive and disposable, many

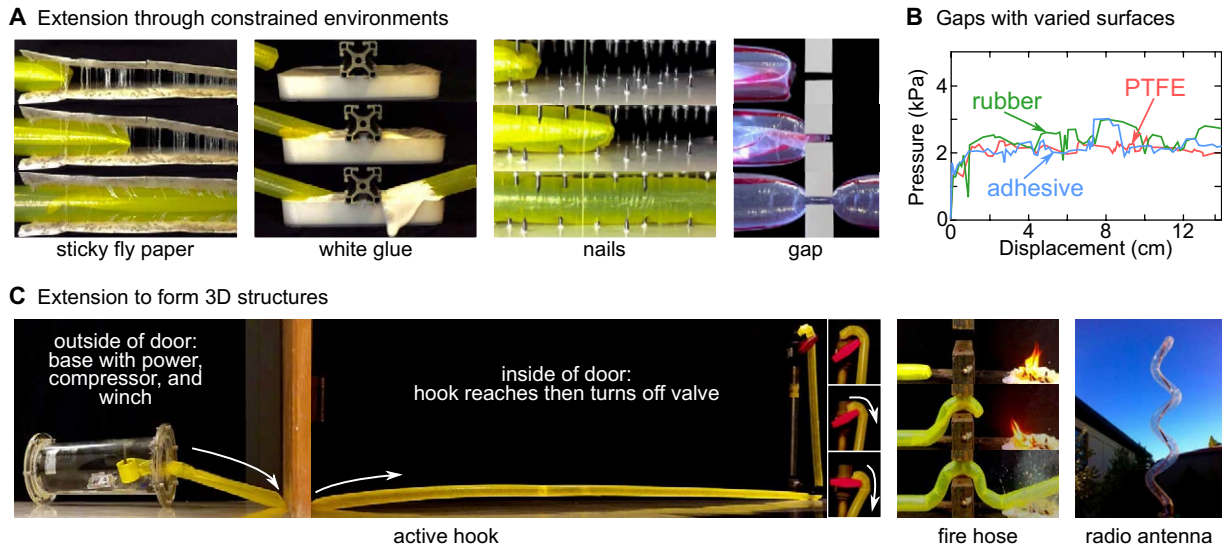


**Fig. 4. Growth enables a soft robot to move its tip through constrained environments and to form 3D structures defined by the path of its tip.** (A) A soft robot lengthens through various challenging constrained environments without active control. Instead, the robot passively deforms to navigate the obstacles. Yellow bodies, 2.5-cm diameter; clear bodies, 8-cm diameter. (B) The pressure required to lengthen through the gap remains relatively constant, despite vastly different surface properties of the material surrounding the gap and different displacements within the gap. Setup is shown in fig. S1. (C) The soft robot demonstrates the ability to lengthen into useful 3D structures.

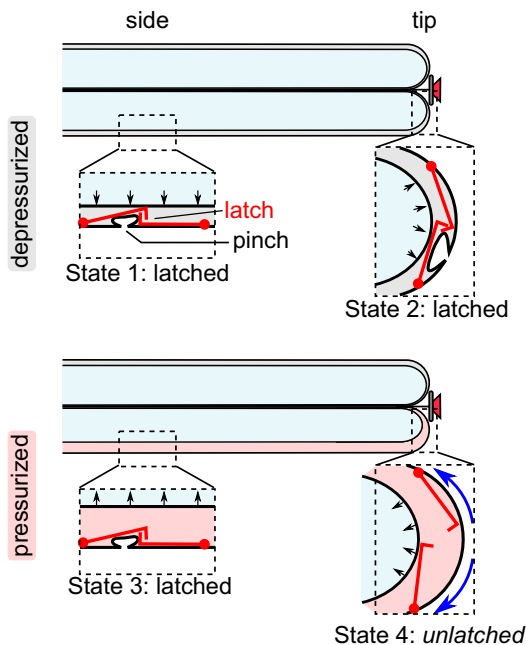


**Fig. 5. Details of an implementation of a mechanism within the control chambers for selective lengthening of the sides of the soft robot.** A series of latches are manufactured into the control chambers shown in Fig.3 (A to D). Each latch crosses pinched material, such that when released, the side lengthens. There are four total states. State 1: When the control chamber is depressurized and the latch is on the side, the latch remains closed. State 2: When the control chamber is depressurized and the latch is at the tip, the latch remains closed. (When a control chamber is depressurized, the pressure from the main chamber keeps the latch closed regardless of whether the latch is on the side or at the tip.) State 3: When the control chamber is pressurized and the latch is on the side, the latch remains closed. State 4: When the control chamber is pressurized and the latch is at the tip, the latch opens. (When the control chamber is pressurized, the latch remains closed if it is along a side, due to the shape of the interlocking of the latch, but the latch opens if it is at the tip because the high curvature overcomes the interlocking.)

parallel bodies, like a single branched body, could cover large areas for search and rescue applications (see Materials and Methods for manufacturing details).

The second principle that we leverage in our design enables the active control of direction and is based on setting the relative lengths of either side of the body at the tip as the body grows in length. This principle of directional control is found in tip-growing cells such as pollen tubes (36), fungal hyphae (1), rhizoids of algae (37), and root hairs (7). In our system, we implement this principle by selectively allowing one side of the robot body to lengthen with respect to the other side as the body everts from the tip (Fig. 3, A to D). Small control chambers that run along the side of the robot body act as the control input; when one of these chambers is inflated, the section of the robot body that is everting from the tip on that side will be lengthened. For example, when the left channel is inflated, the left side of the tip lengthens, resulting in a right turn (see Materials and Methods and Fig. 5 for details). Thus, by controlling the relative pressures of these control chambers, steering is achieved (movie S2). This method of turning is efficient and simple; it requires neither the addition of energy (beyond the control signal) nor any bulky actuators to bend an existing segment. Rather, the turn is created at the same time as the segment, using the energy stored in the pressurized fluid of the main chamber. Each turn is permanent, thus control of direction is nonholonomic (38), like in a steering car or growing pollen tube. Our implementation results in much faster changes in direction than the chemical diffusion of natural cells [less than a second for our system in contrast to roughly a minute for pollen tubes (39)]. However, our implementation has closely packed discrete sections that can be lengthened (Fig. 5), resulting in a digital system, which sacrifices some resolution that an analog system affords. To demonstrate our implementation, a soft robot navigates to a light using an onboard tip-mounted camera with closed-loop active control (Fig. 3, E to H, and movie S2).

In addition to demonstrating tip growth, substantial length increase, high-speed tip motion, and directional control, the presented class of

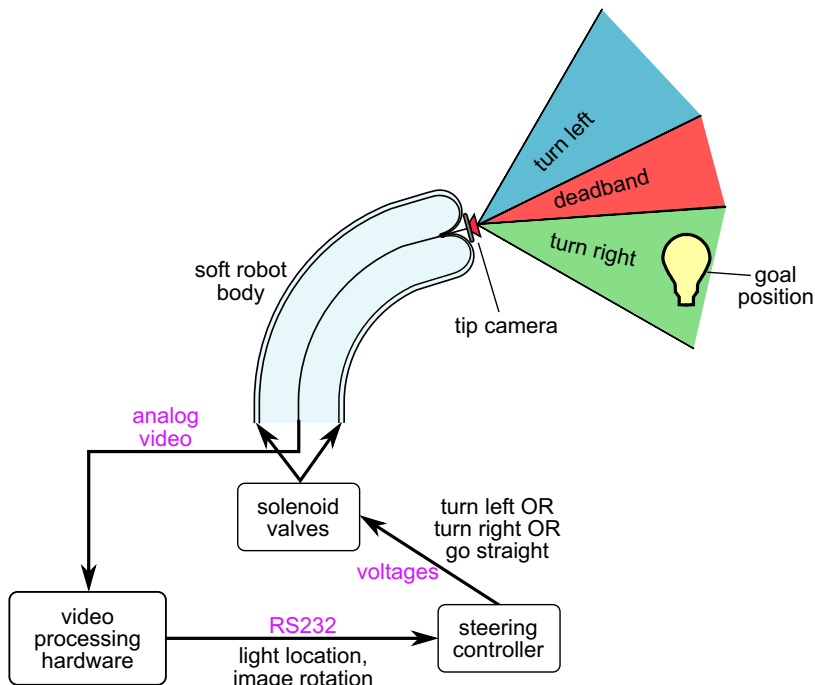


**Fig. 6. Overview of active steering control system.** Hardware components and a physical depiction of the steering task are shown. Electrical signal formats are labeled in purple, and their semantic meanings are labeled in black.

soft robot shows some of the capabilities of natural cells and organisms that navigate by growth: movement through tightly constrained environments and the creation of 3D structures with the lengthening body. We tested our system by lengthening a soft robot body through challenging constrained environments (Fig. 4A and movie S3) and demonstrated its insensitivity to surface characteristics (Fig. 4B): It takes no more pressure to grow between two adhesive surfaces than between two polytetrafluoroethylene (PTFE) surfaces. Its ability to passively deform aids in its ability to move through constrained spaces and adapt to the environment. We also demonstrated 3D structures created by lengthening a preformed body: an active hook, a fire hose, and a radio antenna (Fig. 4C and fig. S3), as well as a structure that lengthens across land and water and another that pulls a cable through a dropped ceiling (movie S4). Like the natural examples of structure creation (Fig. 1B), a variety of purposes are demonstrated: the fire hose demonstrates delivery (like pollen tubes), the structure of the antenna demonstrates support (like sclerenchyma cells), and the cable-pulling structure demonstrates connecting remote locations (like neurons).

## CONCLUSION

Growth is an intriguing method for navigating the environment and is found across kingdoms and scales in nature. Although limited in range, it allows access to constrained environments and enables the creation of 3D structures along the path of movement. We demonstrated basic versions of these capabilities in a class of pressure-driven soft robot and presented robot bodies that range across two orders of magnitude in diameter. This type of robot body can lengthen by thousands of percent from its tip, and its peak rate of extension is comparable to that of animal or robot locomotion. Further, we demonstrated active control of direction with onboard sensing, enabling response to an environmental stimulus. Our

results help pave the way for engineered systems to exploit growth as a paradigm for navigating constrained environments while forming potentially useful 3D structures.

## MATERIALS AND METHODS

### Construction

A lengthening soft robot comprises two main components: the extending body and the base (Fig. 2A). Along the length of the extending body are control chambers that can be selectively inflated by the solenoid valves. There are chambers along two sides (for creating 2D shapes during lengthening) or three sides (for creating 3D shapes during extension). When a chamber is inflated during lengthening, the material at the tip of the inflated control chamber side lengthens. This creates a turn in the direction away from the inflated control chamber (Fig. 3, A to D).

Although a variety of implementations can realize this behavior, we describe the one used for the robot shown in Fig. 3. Within each control chamber is a continuous row of latches, with each latch roughly 2 cm long (body diameter is 3.8 cm). Each engaged latch crosses pinched wall material; in this way, the side lengthens when the latch is opened without requiring the material to stretch (Fig. 5). The opening of the latches is controlled by the pressure in its control chamber as well as the location of the latch. When a control chamber is not pressurized, the pressure from the main chamber keeps the latches closed. However, when the control chamber is pressurized, a latch can open, but only if it is at the tip of the robot body. When at the tip, the curvature causes the latch to release and the section to lengthen. In contrast, if the latch is on a straight section, it remains closed because of the interlocking of the latch. The latches are manufactured from a combination of sheet steel and polypropylene and attached to the outer wall using a soft viscoelastic adhesive (TrueTape LLC). The latches can also be produced by 3D printing for large-batch fabrication. The latches can be reset after lengthening for a reusable system.

The change in the steering angle  $\theta$  that a single closed latch will cause can be described by  $\theta = \frac{l}{d}$ , where  $l$  is the length removed by the pinch and  $d$  is the diameter of the robot body. This relationship is derived by assuming that the pinched and unpinched sides of the robot body lie on concentric circles, with the body diameter being the difference in the radius between the two curves.

The other component of the robot is the base. One implementation of the base (shown in Fig. 4C) is a cylindrical airtight acrylic vessel (28 cm long, 18 cm in diameter), containing a 6-V battery-powered air compressor (Ingersoll Rand B01HG0FTAM) that crosses the vessel boundary. Note that most testing was done with an off-board air supply. When turned on, the compressor increases the mass of the air inside the vessel, resulting in a force that tends to lengthen the robot body. A spool of thin-walled polyethylene tubing (50- to 80- $\mu\text{m}$  wall thickness; Elkay Plastics) supplies new material for lengthening, and a winching motor (Maxon) can control the rate and the direction that the spool turns. Electronically controlled solenoid valves selectively pressurize the control chambers of the robot body.

### Active steering control with onboard sensing

A simple task was created to demonstrate real-time steering control of the soft robot using onboard sensing. The objective of the task was

to steer the tip of the soft robot in two dimensions to a goal location, indicated by an illuminated light bulb (Fig. 6).

### Hardware overview

The location of the illuminated light bulb was sensed using a miniature analog camera (640 × 480, 30 frames/s) at the tip of the soft robot. The camera's cables were routed along the inside of the robot's body, and the camera was kept at the tip by applying a constant tension force to its cables. This also served as a limit to the extension rate of the robot. Air was supplied to the main chamber of the soft robot with a pressure regulator. As described above and in Fig. 3, steering was implemented by inflating the control chambers of the robot: To turn right, the left chamber is inflated; to turn left, the right chamber is inflated; and to go straight, both side chambers (or neither chamber) are inflated. Electronic solenoids were used to selectively inflate the side chambers based on the commands of the vision-based steering controller.

### Vision processing

Data from the tip camera were processed using specialized video processing hardware (SLA-2000, Sightline Applications Inc.). The video processing hardware computed both the location of the light and camera rotation about its optical axis. Light location was calculated using template-based object tracking, and camera rotation was calculated using image registration between the current and the last frame. Light location (in pixels) and camera rotation (in degrees) were communicated to the steering controller via RS-232.

### Steering controller

The soft robot was controlled to steer toward the light using a bang-bang heading controller that aligned the robot's tip heading with the ray emanating from the robot's tip to the light (Fig. 6). The light location, computed by the video processing hardware, was used to make decisions about when to turn left, turn right, or go straight. A 100-pixel deadband was designated in the center of the tip camera frame. If the light location was more than 50 pixels to the left or right of the center of the tip camera image, then the steering controller commanded a left or right turn, respectively. Otherwise, the robot was commanded to go straight. Camera rotation relative to the robot body was estimated by integrating frame-to-frame rotation information. The estimated rotation was used to transform the location of the light into the robot coordinate frame so that a left-right steering decision could be made.

## SUPPLEMENTARY MATERIALS

robotics.sciencemag.org/cgi/content/full/2/8/eaan3028/DC1

Text

Fig. S1. Experimental arrangement for collection of data shown in Figs. 2 and 4 and fig. S2.

Fig. S2. Additional experimental results from tests to determine full model for soft robot lengthening.

Fig. S3. Modeling of a helical antenna formed with a soft robot.

Fig. S4. Extension of a soft robot body with preset pattern of branching.

Fig. S5. Viscoplastic relationships for natural extending systems.

Movie S1. Lengthening.

Movie S2. Steering.

Movie S3. Constrained environments.

Movie S4. Forming structures from the body.

References (40, 41)

## REFERENCES AND NOTES

- R. R. Lew, How does a hypha grow? The biophysics of pressurized growth in fungi. *Nat. Rev. Microbiol.* **9**, 509–518 (2011).
- D. Weigel, G. Jürgens, Stem cells that make stems. *Nature* **415**, 751–754 (2002).
- K. C. Vaughn, A. J. Bowling, Biology and physiology of vines. *Hortic. Rev.* **38**, 1–21 (2011).
- Historical Royal Palaces, The Great Vine; www.hrp.org.uk/hampton-court-palace/visit-us/top-things-to-see-and-do/the-great-vine.
- E. W. Dent, F. B. Gertler, Cytoskeletal dynamics and transport in growth cone motility and axon guidance. *Neuron* **40**, 209–227 (2003).
- R. Palanivelu, D. Preuss, Pollen tube targeting and axon guidance: Parallels in tip growth mechanisms. *Trends Cell Biol.* **10**, 517–524 (2000).
- A. S. Nezhad, A. Geitmann, The cellular mechanics of an invasive lifestyle. *J. Exp. Bot.* **64**, 4709–4728 (2013).
- R. M. Alexander, *Principles of Animal Locomotion* (Princeton Univ. Press, 2003).
- K. Y. Ma, P. Chirarattananon, S. B. Fuller, R. J. Wood, Controlled flight of a biologically inspired, insect-scale robot. *Science* **340**, 603–607 (2013).
- S. Seok, A. Wang, M. Y. Chuah, D. Jin Hyun, J. Lee, D. M. Otten, J. H. Lang, S. Kim, Design principles for energy-efficient legged locomotion and implementation on the MIT Cheetah Robot. *IEEE/ASME Trans. Mechatronics* **20**, 1117–1129 (2015).
- Z. Wang, G. Hang, J. Li, Y. Wang, K. Xiao, A micro-robot fish with embedded SMA wire actuated flexible biomimetic fin. *Sensor. Actuat. A Phys.* **144**, 354–360 (2008).
- A. D. Marchese, C. D. Onal, D. Rus, Autonomous soft robotic fish capable of escape maneuvers using fluidic elastomer actuators. *Soft Robot.* **1**, 75–87 (2014).
- D. W. Hong, M. Ingram, D. Lahr, Whole skin locomotion inspired by amoeboid motility mechanisms. *J. Mech. Robot.* **1**, 011015 (2008).
- H. Marvi, C. Gong, N. Gravish, H. Astley, M. Travers, R. L. Hatton, J. R. Mendelson III, H. Choset, D. L. Hu, D. I. Goldman, Sidewinding with minimal slip: Snake and robot ascent of sandy slopes. *Science* **346**, 224–229 (2014).
- J.-S. Koh, E. Yang, G.-P. Jung, S.-P. Jung, J. H. Son, S.-I. Lee, P. G. Jablonski, R. J. Wood, H.-Y. Kim, K.-J. Cho, Jumping on water: Surface tension-dominated jumping of water striders and robotic insects. *Science* **349**, 517–521 (2015).
- J. F. Wilson, D. Li, Z. Chen, R. T. George Jr., Flexible robot manipulators and grippers: Relatives of elephant trunks and squid tentacles, in *Robots and Biological Systems: Toward a New Bionics?* P. Dario, G. Sandini, P. Aebischer, Eds. (Springer, 1993), pp. 474–479.
- G. Immega, K. Antonelli, The KSI tentacle manipulator, in *Proceedings of 1995 IEEE International Conference on Robotics and Automation (IROS)* (IEEE, 1995), pp. 3149–3154.
- R. Cieslak, A. Morecki, Elephant trunk type elastic manipulator—A tool for bulk and liquid type materials transportation. *Robotica* **17**, 11–16 (1999).
- H. Tsukagoshi, A. Kitagawa, M. Segawa, Active hose: An artificial elephant's nose with maneuverability for rescue operation, in *Proceedings of the IEEE International Conference on Robotics and Automation (IROS)* (IEEE, 2001), pp. 2454–2459.
- W. McMahan, B. A. Jones, I. D. Walker, Design and implementation of a multi-section continuum robot: Air-octor, in *Proceedings of the IEEE/RSJ International Conference on Intelligent Robots and Systems (IROS)* (IEEE, 2005), pp. 2578–2585.
- J. S. Mehling, M. A. Diftler, M. Chu, M. Valvo, A minimally invasive tendril robot for in-space inspection, in *Proceedings of the First IEEE/RAS-EMBS International Conference on Biomedical Robotics and Biomechanics (BioRob)* (IEEE, 2006), pp. 690–695.
- M. B. Wooten, I. D. Walker, A novel vine-like robot for in-orbit inspection, in *Proceedings of the 45th International Conference on Environmental System (ICES)*, 2015, pp. 1–11.
- A. Sadeghi, A. Tonazzini, L. Popova, B. Mazzolai, Robotic mechanism for soil penetration inspired by plant root, in *Proceedings of the IEEE International Conference on Robotics and Automation (ICRA)* (IEEE, 2013), pp. 3457–3462.
- T. Rösch, A. Adler, H. Pohl, E. Wettschreck, M. Koch, B. Wiedenmann, N. Hoepffner, A motor-driven single-use colonoscope controlled with a hand-held device: A feasibility study in volunteers. *Gastrointest. Endosc.* **67**, 1139–1146 (2008).
- A. Sadeghi, A. Tonazzini, L. Popova, B. Mazzolai, A novel growing device inspired by plant root soil penetration behaviors. *PLOS ONE* **9**, e90139 (2014).
- E. Del Dottore, A. Mondini, A. Sadeghi, V. Mattoli, B. Mazzolai, Circumnutations as a penetration strategy in a plant-root-inspired robot, in *Proceedings of the IEEE International Conference on Robotics and Automation (ICRA)* (IEEE, 2016), pp. 4722–4728.
- E. Zuckerkandl, Coelomic pressures in *Sipunculus nudus*. *Biol. Bull.* **98**, 161–173 (1950).
- E. C. Bingham, *Fluidity and Plasticity* (McGraw-Hill, 1922).
- J. Dumais, S. L. Shaw, C. R. Steele, S. R. Long, P. M. Ray, An anisotropic-viscoplastic model of plant cell morphogenesis by tip growth. *Int. J. Dev. Biol.* **50**, 209–222 (2006).
- A. Geitmann, M. Steer, The architectural and properties of the pollen tube cell wall, in *The Pollen Tube: A Cellular and Molecular Perspective*, R. Malhó, Ed. (Springer, 2006), pp. 177–200.
- D. J. Cosgrove, Growth of the plant cell wall. *Nat. Rev. Mol. Cell Biol.* **6**, 850–861 (2005).
- T. I. Baskin, Anisotropic expansion of the plant cell wall. *Annu. Rev. Cell Dev. Biol.* **21**, 203–222 (2005).
- J. A. Lockhart, An analysis of irreversible plant cell elongation. *J. Theor. Biol.* **8**, 264–275 (1965).
- P. B. Green, R. O. Erickson, J. Buggy, Metabolic and physical control of cell elongation rate: *In vivo* studies in *Nitella*. *Plant Physiol.* **47**, 423–430 (1971).
- L. L. M. Heaton, E. López, P. K. Maini, M. D. Fricker, N. S. Jones, Growth-induced mass flows in fungal networks. *Proc. Biol. Sci.* **277**, 3265–3274 (2010).
- M. W. Steer, J. M. Steer, Pollen tube tip growth. *New Phytol.* **111**, 323–358 (1989).
- Z. Hejnowicz, B. Heinemann, A. Sievers, Tip growth: Patterns of growth rate and stress in the *Chara* rhizoid. *Z. Tierpsychol.* **81**, 409–424 (1977).

38. R. J. Webster III, J. S. Kim, N. J. Cowan, G. S. Chirikjian, A. M. Okamura, Nonholonomic modeling of needle steering. *Int. J. Robot. Res.* **25**, 509–525 (2006).
39. H. Takeuchi, T. Higashiyama, Tip-localized receptors control pollen tube growth and LURE sensing in *Arabidopsis*. *Nature* **531**, 245–248 (2016).
40. M. Kaneko, T. Yamashita, K. Tanie, Basic considerations on transmission characteristics for tendon drive robots, in *Proceedings of the Fifth International Conference on Advanced Robotics, Robots in Unstructured Environments (ICAR)* (IEEE, 1991), pp. 827–832.
41. A. A. Griffith, The phenomena of rupture and flow in solids. *Philos. Trans. R. Soc. Lon. A* **221**, 163–198 (1921).

**Acknowledgments:** We thank T. Chang, C. Lin, and J. Fan for help in designing and analyzing the antenna; D. Christensen, T. Morimoto, A. Suresh, S. Follmer, and M. Cutkosky for helpful discussions leading to design approaches; Z. Hammond, P. Slade, A. Piedra, and M. Lepert for help in designing and manufacturing soft robots; S. Sketch for input on figures; neurosurgeons G. Grant and J. Quon for consultation for potential uses in surgery; the Stanford Office of University Communications for help with filming; D. Lentink for helpful suggestions on the manuscript;

and H. Bluestone for help editing. **Funding:** This work was supported in part by the NSF (grant no. 1637446) and the NSF Graduate Research Fellowship Program. **Author contributions:** E.W.H. designed the soft robot, models, and experiments and wrote the manuscript. L.H.B. designed experiments and models, performed experiments, analyzed data, and wrote the methods. J.D.G. designed the controller and performed experiments. A.M.O. directed the project, defined the analysis, and edited the manuscript. **Competing interests:** E.W.H. and A.M.O. have a provisional patent application on the method of lengthening. **Data and materials availability:** All data are provided in the manuscript and the Supplementary Materials.

Submitted 24 March 2017

Accepted 23 June 2017

Published 19 July 2017

10.1126/scirobotics.aan3028

**Citation:** E. W. Hawkes, L. H. Blumenschein, J. D. Greer, A. M. Okamura, A soft robot that navigates its environment through growth. *Sci. Robot.* **2**, ean3028 (2017).

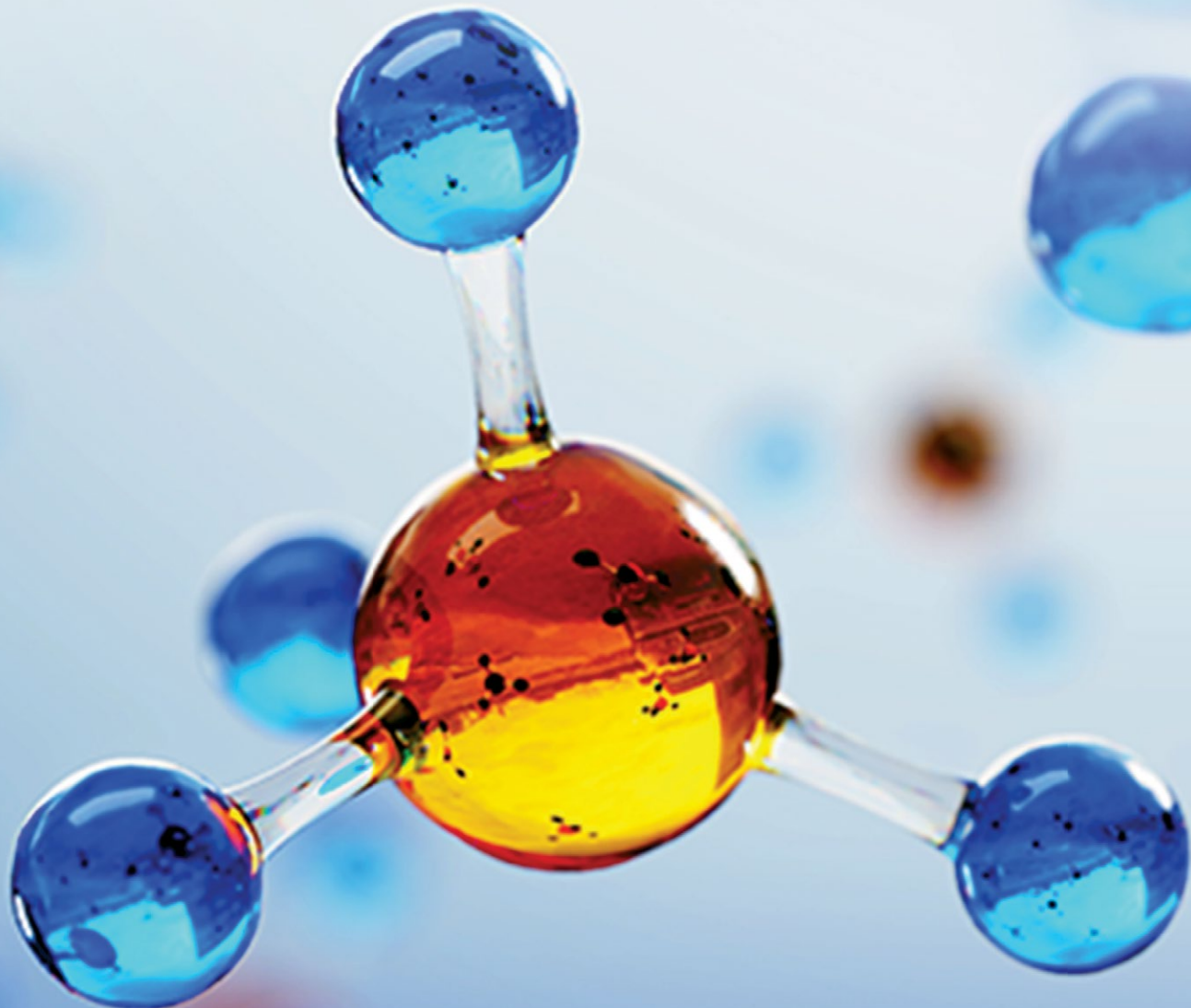
# Transforming the **Future** of **Robotics**



As a multidisciplinary online-only journal, *Science Robotics* publishes original, peer-reviewed, research articles that advance the field of robotics. The journal provides a central forum for communication of new ideas, general principles, and original developments in research and applications of robotics for all environments.

Learn more at: [ScienceRobotics.org](http://ScienceRobotics.org)

**Science  
Robotics**  
AAAS



## Publish your research in the *Science* family of journals

The *Science* family of journals (*Science*, *Science Advances*, *Science Immunology*, *Science Robotics*, *Science Signaling*, and *Science Translational Medicine*) are among the most highly-regarded journals in the world for quality and selectivity. Our peer-reviewed journals are committed to publishing cutting-edge research, incisive scientific commentary, and insights on what's important to the scientific world at the highest standards.

**Submit your research today!**

Learn more at [ScienceMag.org/journals](https://www.sciencemag.org/journals)

**Science**  
JOURNALS 